Interim Report:

SOLAR-C Plan-B

Toward understanding of the elementary structures & fundamental physical principles that govern manetized plasma

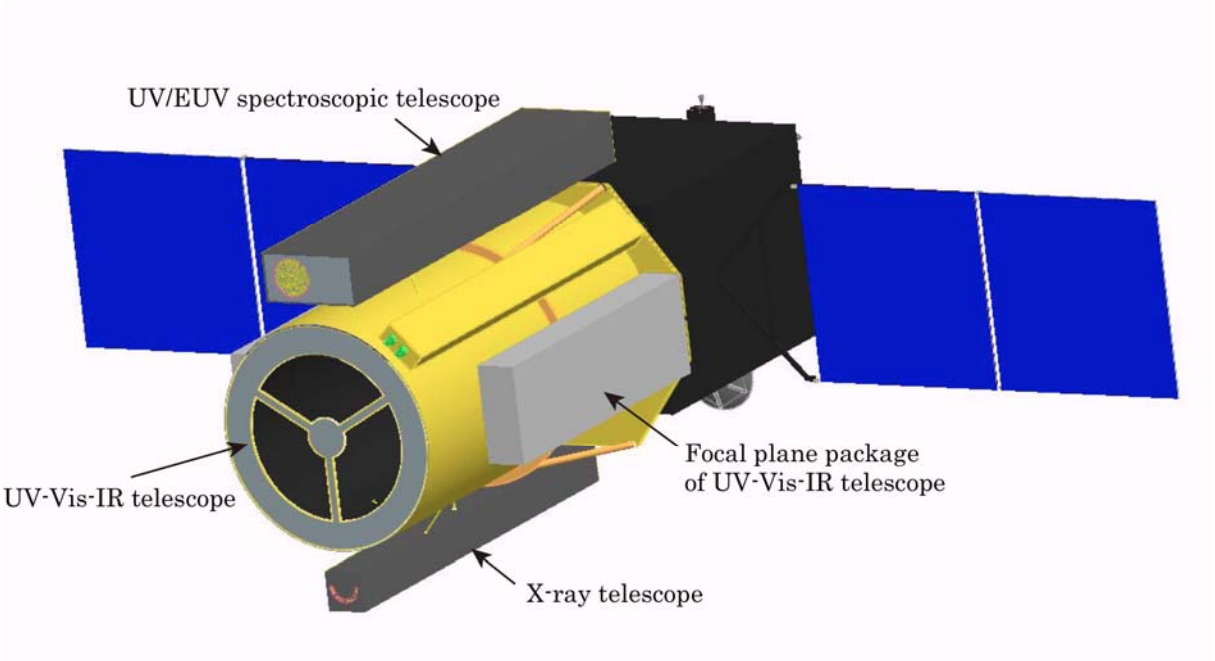

ISAS/JAXA SOLAR-C Working Group

Contents

Executive Summary

The Solar-C Plan B mission is proposed to study energy transport and dissipation of the magnetic energy governing the dynamic solar atmosphere through elementary magnetic structures. For this purpose, the plan B mission has three large state-of-art advanced telescopes that can perform for the first time high spatial resolution, high throughput, high cadence spectroscopic and polarimetric observations seamlessly covering the entire atmosphere from photosphere and chromosphere to transition region and corona.

Top-Level Science Goals

At the core of all the questions related to how the Sun floods the heliosphere with hot plasma, radiation, particles, and magnetic fields is the need **to understand the elementary structures and fundamental physical principles that govern a magnetized plasma**. Theory and laboratory experiments provide many useful insights, but the insights have been mostly triggered by new observations of the Sun's atmosphere, which is the only astrophysical plasma accessible with spatially resolving magnetic structures and dynamics.

By performing high spatial resolution imaging observations under extremely stable condition never realized so far, "Hinode" opened a new frontier in solar physics researches. For example, series of high resolution Ca II H images allow us for the first time to identify waves existing along magnetic fields, which can be considered as a key part in heating of the corona. Magnetic reconnection, which was firmly settled in solar physics with flare observations by "Yohkoh", is now used in explaining many aspects of dynamics observed in the solar atmosphere. However, details of fundamental physical processes governing the heating and dynamics in the solar atmosphere have not yet been described well with physical terms. This is because of the lack of spectroscopic measurements, which are most useful to diagnose plasma conditions. With Hinode observations, we also recognize that the chromosphere, which is the interface layer between the photosphere and corona, is the most key atmospheric layer in understanding the heating and dissipation in the magnetic atmosphere.

The outer atmosphere of the Sun (or stars) is a complicated system consisting of the photosphere, chromosphere, and the corona. The energy is built up in the magnetic atmosphere. The energy is transported via various methods, especially waves along magnetic fields. The dissipation of the magnetic energy is the central engine for causing variability in the emissions from the Sun. The energy build up, transport, and dissipation are mixed and complicated in the magnetic atmosphere, thus making it difficult to understand the governing physical processes without spectroscopic and polarimetric measurements over the entire atmosphere. Thus, the Solar-C Plan B mission is designed to make spectroscopic and polarimetric measurements over the entire atmosphere with necessary spatial and temporal resolution.

Scientific objectives of the Solar-C Plan B mission are summarized in Table 1. **As a path to exploring the fundamental physical principles**, we seek to understand:

- How **elementary structures** of the magnetic atmosphere responsible for heating and dynamics **are created and evolve** over each temperature domain of the atmosphere;
- How the energy that sustains the atmospheric structure is **transported through small elementary structures** into large-scale corona and **energizes the solar wind**; and
- How **the magnetic energy is dissipated** in the astrophysical plasma.

The solar atmosphere consists of elementary structures, one of which is magnetic flux tubes. The elementary structures shall be understood with their relationship with the magnetic field at all relevant temperatures. It is essential to quantitatively trace how they are created and evolve in association with magnetic fields and plasma flows over wide temperature domain. Magnetic field strength and direction in the chromosphere and corona, which is far above the photosphere and where the plasma is in low plasma ($\beta<1$) condition, is the crucial information to identify the magnetic structures and their roles for causing heating and dynamical nature in the atmosphere. Coronal loops are well known magnetic structures in the corona, but EUV density diagnostics suggests that coronal loops contain elemental structures that are about 10% volume of the coronal loops. The unresolved elementary structures would reflect the source of energy inputs responsible for creating the hot temperature corona.

The energy for solar activity and heating is transported from the photosphere into the corona associated with magnetic fields. The origin of the energy is the kinetic energy of the gas convection in and below the photosphere. The magnetic fields rooted on the photosphere play key roles in transporting the energy upward the chrosmosphere and corona, but we have not identified the mechanisms because of the complexity of fine structures, although some candidates have been proposed, such as high-speed upward ejections of plasma, propagation of MHD waves, and winding and braiding of magnetic fields for forming field discontinuities in the corona. It is extremely important to quantitatively evaluate how much energy is carried by waves and how the magnetic energy is dissipated in the stratified atmosphere both for heating the chromosphere and the corona and for energizing the solar wind.

A complex system of magnetic fields in the solar atmosphere triggers various types of dynamics and heating at different timescales and at different temperatures. They require the conversion of magnetic energy to heat plasma, drive flows, and accelerate particle to high energies. This conversion mechanism is “magnetic reconnection,” which may be the central engine in many solar phenomena, including the explosion of solar flares, the heating of the solar corona, and the initiation of coronal mass ejections. The solar atmosphere has a wide variety of plasma conditions; the inner corona consists of fully ionized, collisionless plasma, whereas the chromosphere is in weakly ionized plasma condition. We seek to address three important questions about magnetic reconnection. Quantitatively evaluation of fast reconnection in the weakly ionized chromosphere would be helpful to understand what plasma condition controls the energy release rate. What controls the energy distribution among thermal, kinetic, and non-thermal energies in early stage of flares? This would help to understand a wide variety of solar flares. How can reconnections in small scale develop to a large-scale flare structure?

Exploring energy transfer and dissipation governing the solar phenomena is directly linked to the space weather researches. Better understanding and predicting the space weather events are the basis on human related activities in the space. One of the important goals of solar physics research is to improve ability to predict geo-effective solar phenomena. High spatial

Table 1. Solar-C scientific objectives and required instruments

Scientific Objectives	*Specific questions to be answered*	*Section*	*Required Instruments*			
			SUVIT	*EUVS*	*XIT*	
					PC	*NI*
A. Elementary structures of the magnetic atmosphere responsible for heating and dynamics	**1. What generates dynamical chromosphere, such as jets?**	1.1.3	◎	○		
	2. What are the tunnel structures for energy transport from chromosphere to corona?	1.1.1 1.1.2 1.2.1	◎	◎		◎
	3. How are waves excited inside magnetic flux tubes?	1.1.4	◎	○		
B. Energy transport and dissipation through small-scale magnetic structures	**1. How do the observed waves behave in stratified atmosphere and contribute to the chromospheric heating?**	1.2.2	◎	◎		
	2. How much energy is carried by the waves that penetrate to the corona?	1.2.2	◎	◎		
	3. What are signatures of energy dissipation in coronal loops?	1.2.3		◎	◎	○
C. Magnetic energy dissipation: Unveil the mask of reconnection region	**1. What determines energy distribution in the energy conversion by reconnection?**	1.3.4 1.3.5		◎	◎	
	2. How can reconnections in small scale develop to a large-scale flare structure?	1.3.6	○	◎	○	
	3. Does fast reconnection really occur in the chromosphere?	1.3.3 1.3.4	◎	○		
D. Small-scale physical processes initiating large-scale phenomena regulating space weather	**1. What are the magnetic field structures during filament eruptions?**	1.4.1	◎	○	○	○
	2. How do magnetic flux and mass energy transport through the atmosphere and initiate flares and CMEs?	1.4.1	◎	◎	○	○
	3. What types of magnetic structures at the low atmosphere are origins of solar winds?	1.4.2 1.1.4 1.2.2	○	◎		

Note: [Origin] [Transport] [Dissipation]: Color indicates main physical process involved in each specific question.

Note: SUVIT = Solar UV-Visible-IR Telescope (Section 2)

EUVS = EUV/FUV high-throughput spectrometer (Section 3)

XIT = X-ray Imaging Telescope, PC= Photon counting, NI= Normal incident

and temporal resolution spectroscopic observations will much improve our knowledge about the initiation of space weather phenomena. Small-scale physical processes in the emergence of magnetic flux may play key roles in initiating the phenomena. Also, direct measurement of magnetic fields in the prominence or filaments tells how the magnetic field structures of prominences are evolved and developed to eruptions. Thus, as a goal toward the space weather researches, we seek to understand:

- How **small-scale physical processes initiate** large-scale dynamic phenomena regulating space weather.

The four science goals defined above are discussed in more details in section 1.

Scientific Measurement Requirements and Proposed Model Payloads

The following scientific measurements is required for the set of mission instruments. All of them have not yet realized in any currently operating and planned missions, and they are unique.

- **Precise polarimetric (S/N~10^{-4}) and spectroscopic measurements** for probing nature of magnetic fields both in the chromosphere and photosphere.
- **High throughput spectroscopic measurements** for probing nature of dynamics with high time resolution (0.5-1sec).
- **Seamless and simultaneous coverage of spectroscopic measurements over each temperature domain of the solar atmosphere** from chromosphere to the corona and flares for understanding the entire picture of energy transport and dissipation.
- **High spatial resolution measurements** for resolving elementary structures.

These measurement requirements are realized by the set of the following three science instruments:

1) Solar UV-Visible-IR telescope (SUVIT)

2) EUV/FUV high throughput spectroscopic telescope (EUVS)

3) X-ray imaging (spectroscopic) telescope (XIT).

EUVS will provide the crucial link between the photospheric and chromospheric magnetic field and plasma characteristics obtained by the SUVIT and the high temporal and spatial resolution diagnostics of the corona provided by the XIT. Two possibilities are considered for XIT: photon counting imaging spectroscopy telescope and ultra-high spatial resolution telescope.

Solar UV-Visible-IR Telescope

The primary purpose of the UV-Visible-IR telescope (SUVIT hereafter, Table 2) is to physically capture nature of gas dynamics and magnetic fields in the lower atmosphere, i.e., from the photosphere through the upper chromosphere, and to understand dynamical evolution of elementary structures of magnetized atmosphere. The telescope is a

diffraction-limited telescope with a **1.5 m aperture in diameter** (the size may be optimized in the future). It has potential to **resolve structures with 0.1 arcsec or better for the first time** from the space observations (Figure 1), which can reveal dynamical behaviors of the low atmosphere through elementary magnetic structures and key physics responsible for energy transfer and dissipation in the photosphere and the chromosphere.

Table 2. Key characteristics of UV-Visible-IR telescope

Item	Description
Telescope	Aplanatic Gregorian telescope equipped with an image stabilization system
Aperture diameter	φ1.5 m
Focal plane instruments	Specto-polarimeter (SP) Broadband filtergraph (BF) Narrowband filtergraph (NF)
Wavelength coverage	280 nm to 1.1 μm
Spectral lines (spectroscopic observations)	(polarimetry in the chromosphere) He I 1083 nm, Ca II 854 nm (polarimetry in the photosphere) Si I 1082.7 nm, Fe I 853.8 nm (dynamics in the chromosphere) Mg II h/k 280 nm
Spectral lines (imaging observations)	(chromosphere) Mg II h/k 280 nm, Ca II 854 nm, H I α 656 nm, Na I D 589 nm, He I D 587 nm (photosphere) Fe I TBD nm
Spatial resolution	<0.1" at UV and visible <0.2" at near-IR
Exposure time	(intensity observations) 0.1 - 1 sec (polarimetric observations) 1 – 20 sec
Spectral resolution	~120,000 with the spectro-polarimeter ~50,000 with the narrowband filtergraph
Field-of-view	180" x 180"

SUVIT will take **the first attempt to measure magnetic fields in the chromosphere from the space**. The Hinode Solar Optical Telescope measures magnetic field vectors at the thin photospheric layer with spectro-polarimetric capability with polarimetric sensitivity of ~10^{-3}, and scientists have recognized that measuring magnetic fields in the chromosphere, 1,000-2,000 km above the photosphere, is essentially important to explore the stratified magnetic atmosphere. SUVIT can diagnose magnetic fields both at the chromosphere and photosphere (Figure 1).

Polarimetric sensitivity of ~10^{-4} is needed for diagnosing the chromospheric magnetic fields with combination of the Zeeman effect and the Hanle (scattering polarization) effect. Comparing with the Hinode Solar Optical Telescope (50cm in diameter), SUVIT can accumulate **roughly one order of magnitude larger number of photons** in the same spatial sampling and in the same exposure duration. **The polarimetric sensitivity of 10^{-4} is achieved with 20 s exposure times for 0.2" pixels.**

SUVIT covers a wide wavelength region from UV (~2800 Å) to near infrared (1.1 μm), in which there are **several spectral lines best suitable for diagnosing dynamics and magnetic fields in the chromosphere as well as the photosphere.** He I 10830 Å and Ca II 8542 Å spectral lines are identified as best lines for diagnosing magnetic fields and Mg II h/k lines at 2800 Å are for diagnosing dynamics in the chromosphere.

As the focal plane instruments, two instrument capabilities are equipped to the SUVIT: **Precise spectroscopic and polarimetric measurements** allow us to determine physical parameters such as temperatures, velocities, and magnetic fields. **Imaging of intensities and magnetic fields with high temporal cadence** is another capability to capture dynamical behaviors of magnetic fields within an observing field of view. Narrow-band imager is used for polarimetric and Doppler measurements at limited number of positions in spectral lines. Broad-band imager is for best possible high spatial monochromatic images of the chromosphere and photosphere.

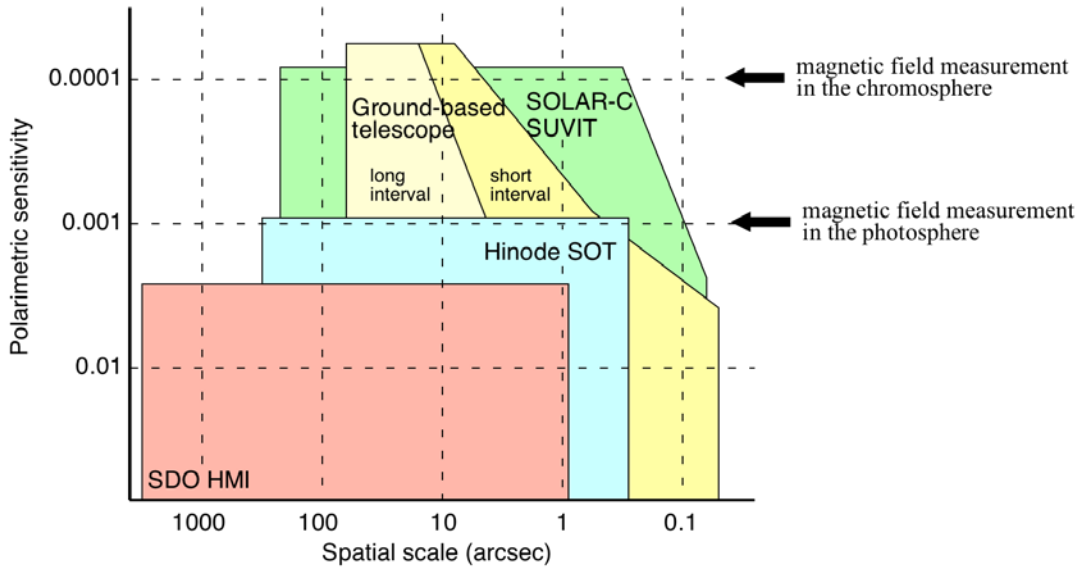

Figure 1. Spatial resolution and polarimetric sensitivity achieved with Solar-C UV-Visible-IR telescope, compared to other space-borne and ground-based large telescope.

EUV/FUV High-Throughput Spectroscopic Telescope (EUVS)

The EUV/FUV high throughput spectrometer (EUVS) is a telescope for imaging spectroscopy in the FUV-EUV region with a resolution and effective area an order of magnitude higher than currently available instruments for solar studies (Table 3, Figure 2). The spatial resolution of EUVS is **~0.3 arcsec (plate scale: 0.16 arcsec/pixel)**, which is much higher than currently operating SUMER and EIS (2-3 arcsec, 1 arcsec/pixel). This higher spatial resolution is required to spatially resolve elementary structures responsible for energy transport in the solar magnetic atmosphere. The volumetric filling factor of coronal loops derived from density sensitive line analysis suggests the existence of fine magnetic structures in order of 0.3 arcsec or ~200km. Magnetic structures in the chromosphere are also of this size, as seen as spicules. Thus, this performance allows us for the first time to trace flows of the energy from its origin (the photosphere) through the chromosphere and transition region and into the corona. Since the structures are small and dynamic, a high time cadence is necessary and consequently a high-throughput instrument is required. EUVS will have **1-5 sec** exposure for intense lines with 0.3 arcsec spatial sampling, and **0.5-1 sec or shorter exposure** for 1 arcsec sampling.

Simultaneous spectroscopic measurements sampling all temperature ranges of the solar atmosphere are essential to achieving the science goals of the Solar-C mission. EUVS is

designed to seamlessly acquire spectral lines emerging from **a wide temperature in 10^4-10^7 K**. Since lower temperature lines are mostly observed in the FUV region and higher temperature lines are in the EUV region, EUVS is designed to cover a wide wavelength range in FUV-EUV and it is something like the instrument combining EIS and SUMER.

The strawman spectrometer consists of an off-axis primary mirror and grating mirror. This optical layout minimizes the number of optical elements, resulting in high throughput performance. The spectrometer measures emission lines and continua in some numbers of wavelength windows between ~100 Å and ~1200Å. **Low-scattering optics** should be used in the spectrometer to allow us to diagnose low emission measure pixels. Many important science discoveries may be hidden in low emission measure regions, such as, reconnection outflow regions that are much fainter than flare loops, and coronal holes where solar wind acceleration and shock formation may be observed in the high corona.

Table 3. EUVS scientific characteristic

Item	Description
Instrument design	- Φ 30-40 cm, off-axis paraboloid mirror - Single grating spectrograph - Two detectors, one for EUV band and the other for long wavelength bands - Image stabilization, slit-jaw camera
Plate scale	~0.16"/pixel
Simultaneous field of view	Slit: 0.16", 0.32", 0.96"; Slot: 10", 40", 200" Slit/slot length: 200" nominal, >300" extended
Maximum raster width	+/- 75" nominal, +/- 200" extended
Wavelength bands	Four channels (Å):130-250; 510-630; 690-810; 940-1060
Exposure times	1-5 s with 0.33" spatial sampling 0.5-1 s in active regions with 1.0" spatial sampling
Velocity resolution	Doppler (centroid) shift measurement accuracy <3km/s Turbulent velocity (width) <10km/s
Temperature coverage	$10^4 - 10^7$ in active regions with $\Delta(\log T) < 0.3$

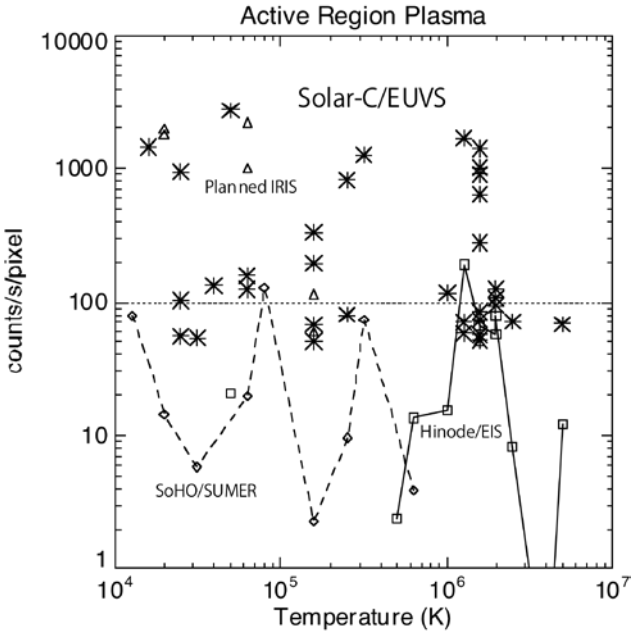

Figure 2. EUVS count rates for active region plasma, compared with currently operating telescopes (SUMER and EIS) and planned IRIS. At least 100-1200 counts are needed for spectral analysis.

X-ray Imaging (Spectroscopic) Telescope

The X-ray imaging telescope images, with spectroscopic information, the uppermost layer of the Sun, the corona, in soft X-rays or EUV to achieve comprehensive understanding on magneto-hydrodynamic processes across the entire layers of the solar atmosphere jointly with SUVIT and EUVS. The telescope should aim to (a) understand forms and mechanisms of storage and dissipation of energy transferred upwards through the photosphere and the chromosphere, (b) quantitatively understand physics of magnetic reconnection with its possible role for particle acceleration, and possibly, (c) perform diagnostics on wave phenomena in the corona. In order to pursue such scientific objectives, the telescope is required to have 1) wide coverage on coronal temperatures to observe the entire portion of single coronal loops, particularly, for the core portion of active regions, 2) high spatial resolution consistent with that for EUVS, and 3) advanced spectral diagnostic capability for quantitatively investigating physical processes in the corona.

Table 4. Outline of the photon-counting X-ray telescope

Item	Description	Remarks
Overall description	Perform imaging investigation of the X-ray corona with the following two modes. Two modes selectable (not simultaneously). (1) Photon-counting mode: Imaging spectroscopy for a limited region of interest. (2) Photon-integration mode: Imagery with the entire, or part of, the imaging array. Walter Type I (-like) grazing-incidence telescope with a segment mirror. A CMOS-APS detector to be used as the focal-plane imaging array.	
Envelope dimensions of the telescope	~40cm × 40cm × 4.5m (TBD)	Telescope plus the focal-plane camera. Includes housings.
Mirror focal length	4 m	
Angular resolution & Temporal resolution for photon counting	For photon-integration mode: ~1" (~0.5"/pixel) For photon-counting mode: For active regions and flares, generate an X-ray spectrum for spatial area whose size* ~< 2"×2" (goal) / ~4"×4" (min.) within every < 10 s (goal) / 30 s (min.)	* Spatial area size in which a spectrum with good counting statistics can be synthesized with reasonable integration time.
Field of view	For photon-integration mode*: ~13'×13' For photon-counting mode**: >~3'×3' (goal) ~80"×80" (nom.)	* Off-axis image blur not taken into account. ** Area with which photon-counting analysis can be performed.
Energy range	~0.5-5 keV* (baseline) ~0.5-~10 keV* (under study)	* Energy range above 2 keV available during flares, with photon-counting mode.
Data rate	max. 110 Mbps for 512×512 photon-counting area max. 6.9 Mbps for 128×128 photon-counting area	

A photon-counting imaging spectroscopy X-ray telescope (Table 4) is proposed, with a ultra-high spatial resolution normal incidence EUV telescope (Table 5) as another option. The photon-counting X-ray telescope will provide first-ever opportunity to perform imaging-spectroscopic investigation of the corona in soft X-ray wavelength range, by measuring energy and location of each incident X-ray photon onto the detector. In addition to

the photon-counting capability, the telescope is designed to have photon-integration capability for imaging observations (just like past solar soft X-ray telescopes) with one of the two modes to be selected for a certain period of observation. The main observational targets for the photon-counting X-ray telescope is to 1) investigate quantitatively, with spectroscopic information, structure and dynamics of magnetized plasmas around the site of magnetic reconnection, and 2) investigate temperature structure of active region corona, in particular that for high temperatures (above ~5MK). It should be noted that the photon-counting X-ray telescope provides a unique chance of investigating electron temperatures of thermal plasmas and even detecting non-thermal emission in soft X-ray wavelengths, which is mostly not visible with emission lines but should manifest itself as continuum component(s) in X-ray spectra.

The other option, ultra-high spatial resolution normal incidence EUV telescope, will focus on understanding connection between the transition region and the lower corona in collaboration with EUVS. The normal incidence telescope serves as delivering complementary observables with EUVS, providing context imagery information for EUVS with higher spatial resolution (0.2"-0.3") and wider field-of-view, and with overlapping temperature coverage. Thus, the main target of this telescope is to resolve fine, hopefully elemental, structures in the corona, study energy flows and magneto-acoustic waves as well as small-scale heatings in coronal temperature range.

Table 5. Outline of the ultra-high resolution EUV telescope (Preliminary)

Item	Description	Remarks
Overall description	Consists of two telescopes each with Cassegrain optics. Each telescope equipped with 3-sector mirrors for different wavelengths. Image stabilization system necessary.	
Optical properties	32 cm aperture diameter. TBD focal length.	
Angular resolution	0.2"-0.3" with 0.1"/pixel	
Field of view	~400" × 400"	
Wavelength Bands	171 Å, 195 Å, 211 Å, 335 Å, 94 Å and broad-UV band	TBD
Exposure time	1 s for an active region, 0.1 s for a flare	
Cadence	< 10 s	
Data rate	TBD	

Spacecraft and Mission Design

The spacecraft designed to meet required scientific performance is summarized in Table 6, and the conceptual layout is shown in Figure 3. The spacecraft is designed mainly with considering the following items.

- High pointing stability is required to realize the high spatial resolution and precise polarimetric performance. The spatial resolution of the telescopes is twice to five times higher than that of telescopes onboard Hinode. For the telescopes with angular resolution better than about 0.4 arcsec, tip-tilt mirror system is equipped inside the telescopes to

stabilize solar images on their focal plane detectors.

- High rate science telemetry is required to acquire spectroscopic and polarimetric data with high cadence and spatial resolution. The minimum requirement is that the three telescopes can acquire the data continuously with the post-compression data rate of about 8 Mbps in total. We will use an X-band telemetry system (16-QAM, 16Mbps) with 12-hour or longer duration of contacts at ground stations or a Ka-bad telemetry system (QPSK, ~80Mbps) with shorter duration of contacts at a ground station.

Table 6. Solar-C plan B mission overall characteristics

Spacecraft layout	Telescopes mounted on the optical bench, which is on the Bus module. See Figure 1.x
Weight	4930 kg (at liftoff), 2330 kg (dry weight)
Size	3.2 m x 3.2 m x 7.4 m, excluding solar array paddles
Launch vehicle	JAXA H-IIA (type 202)
Orbit	An inclined geo-synchronous orbit (Baseline) A sun-synchronous polar orbit (optional)
Power	~3,500 W (maximum)
Command & Telemetry	Uplink and housekeeping downlink: S-band Downlink: X-band 16-QAM (16Mbps) Ka-band QPSK (80Mbps, optional)
Attitude control	3-axis body pointing with high accuracy Image stabilization system in some telescopes A function to change the pointing around Z-axis for matching spectrograph slit direction to the observing target.
Science operations	Hinode operation scheme, with a final target selection around 10 to 15 minutes before the uplink in cases where this is essential for the science.

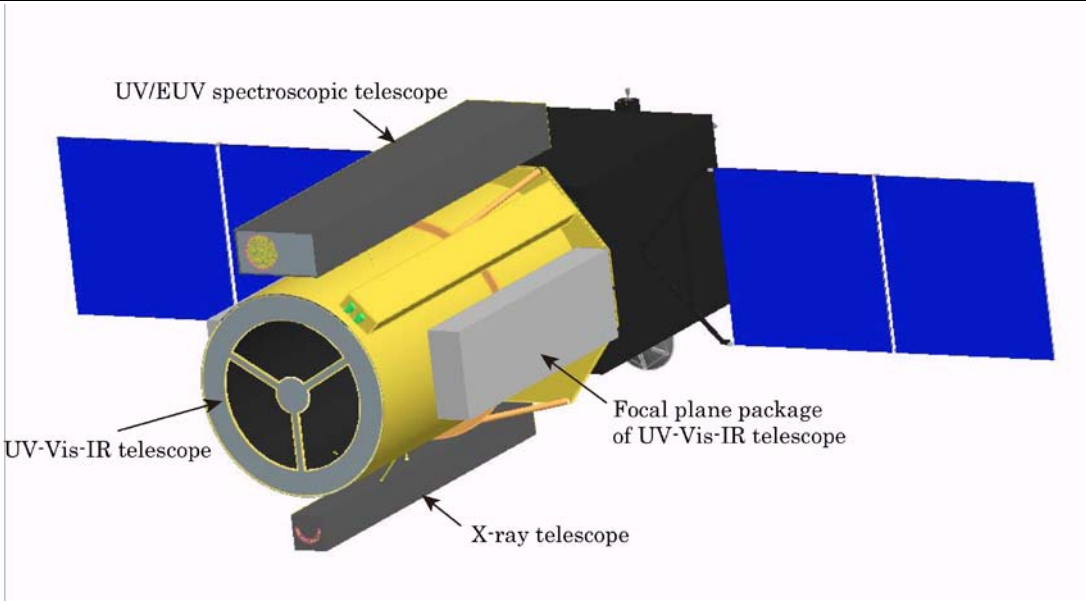

Figure 3. Solar-C plan B mission conceptual layout

- An inclined geo-synchronous orbit (GSO, altitude 36,000km, inclination < 30 deg, period 1 day) is considered as the baseline, with a sun-synchronous polar orbit as the backup. The GSO orbit provides almost uninterrupted observations of the Sun and much stable thermal environment, compared with Hinode, for minimizing the thermal deformation of the structure. It also provides long duration viewing from a ground station, allowing us to use X-band for high data rate, although the spacecraft weight and size become bigger.

- Another advantage of having a long-period downlink is that we can respond to dynamical changes on the Sun much faster, by monitoring solar images in real time. The optical and EUV spectrometers have relatively small fields of view and it is important to be able to choose the observing region as close to real-time as possible.
- The spacecraft design should utilize technical heritage from Hinode, especially the structural design and pointing related technologies for the high pointing stability and telescope alignment.

Chapter 1: Science Goals and Requirements

1.1. Understanding Small-scale Elementary Magnetic Structures

1.1.1. Elementary Structures Connecting from Photosphere to Corona

The Hinode mission provides both the first high-resolution diagnostics of the solar magnetic field and from a space platform, and is now allowing scientists to discover the processes by which the magnetic flux interacts with the solar convective flows in the lower solar atmosphere (the "photosphere"). One of major improvements on our knowledge is that horizontal oriented magnetic fields are ubiquitously distributed over the solar surface (Lites et al. 2007) and that they are dynamically evolved on the photosphere (Centeno et al. 2007, Ishikawa et al. 2007). Furthermore, Hinode has provided strong indications that the convective motions initiate outward propagating waves and dynamic reconnection events that result in heating of the plasma accompanied by significant outward mass flux (e.g., Isobe et al. 2008). One of new features revealed with Hinode observations is that many of chromospheric "Type-II" spicules show substantial transverse displacements during their short lifetimes (<100s), which is interpreted as propagation of Alfven waves along magnetic field in the chromosphere (De Pontieu et al. 2007). This observation also suggests that energy transport takes place via magnetic structures whose width is **~0.3 arcsec at the chromosphere**. Moreover, another important observational feature is that the spectral lines emitted from the corona at temperatures of 2MK show excess non-thermal line broadening at the footpoints of coronal loops, caused by weak component that is highly blue-shifted to in order of 100 km/s (Hara et al. 2008). Existence of highly blue-shifted features may suggest that numerous number of small transient energy releases, i.e., nanoflares, take place at the base of coronal loops (More details will be discussed in section 1.2).

For understanding the heating of corona and acceleration of the solar wind, it is now the most essential to quantitatively and exactly identify how the energy (such as mass flow, magnetohydrodynamic waves with fast mode, slow mode, and Alfven mode, and localized heating by nanoflares, and flux emergence) is transported to the corona through the chromosphere and transition region, which have a complex system of magnetic fields with full variety of plasma dynamics. Observations are required to distinguish the two competing theories for coronal heating, i.e., mechanical heating by upward-propagating waves, and Joule heating associated with magnetic reconnections. Quantitative identification is needed for different magnetic structures, such as active region, quiet Sun and coronal holes, because the manifestation of the energy transport is varied depending on the natures of magnetic field structures.

To distinguish transport mechanisms, it is very important challenge to resolve the dynamical nature of small-scale elementary magnetic structures in the complicated photosphere-chromosphere-corona system. Furthermore, dynamical nature and evolution of elementary structures formed in upper atmosphere is directly connected to the formation of global magnetic field structures and the magnetic energy storage and release that causes the violent dynamical events (flares and CMEs).

1.1.2. Elementary Structures of Coronal Magnetic Loops

Although the EUV images obtained by TRACE and SDO/AIA (spatial resolution about 0.5arcsec) showed thin coronal loops (Figure 1.1), it is not clear that elemental structures in corona are resolved. Aschwanden & Nightingale (2005) investigated the thermal structure of coronal loops based on the TRACE multi-filter analysis, and found that the width of the isothermal loops is 1000~2000 km. If we define the width of an elemental loop by the homogeneous temperature cross-section, we can say that TRACE resolved the elemental structure in corona. On the other hand, the EUV spectroscopic measurements with EIS on Hinode show that the volumetric filling factor of coronal loops is approximately 10% (Warren et al. 2008); With the spatial resolution of 2-3arcsec (pixel size 1arcsec), only 10% of the volume in coronal loops are filled with hot plasma. It means that a coronal loop is constructed from fine threads with the width in order of ~200 km (0.3arcsec) or less. Thus, there is the disagreement between the filling-factor analysis based on EUV spectra and the temperature analysis based on the EUV line images. Doschek et al. (2010) showed that small coronal bright points, particularly prominent in coronal holes, has internal structure in the corona, although their morphological structure are not spatially resolved with the current available instrument (Figure 1.2). Hence, to understand the elementary structures in corona, we need to resolve not only the stable structures but also the dynamic structures with high time resolution.

Figure 1.1. A magnetically active region at the edge of the Sun shows "loops" that connect one magnetic polarity to the other. A coronal image (Fe IX in 171A) from TRACE. Coronal structures seen with 0.5 arcsec spatial resolution.

The EUV spectrometer with the spatial resolution of ~0.3 arcsec, which is about one order of magnitude higher than EIS resolution, (and the normal incidence X-ray telescope with the spatial resolution of 0.2 arcsec as the second option), will be able to almost resolve coronal loops at fundamental scales. That is, spatial scales at which loops behave coherently and can be described by simple hydrodynamic models. The combination of the filling-factor analysis with the EUV spectrometer and coronal images at 0.1 arcsec pixel from the X-ray imaging telescope makes clear what the elementary structure of coronal loops is. For this purpose, the X-ray telescope with normal incidence optics may be more suitable than the photon-counting telescope.

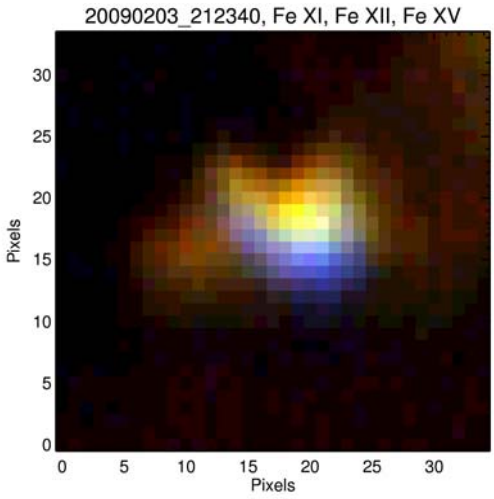

Figure 1.2. A polar coronal hole bright point in lines of Fe XI (red), Fe XII (green), and Fe XV (blue). The bright point looks like an unresolved flare seen by Yohkoh.

1.1.3. Elementary Structures in Dynamical Chromosphere

The chromosphere is the region that interfaces the gas-pressure-dominated photosphere and the magnetic-field-pressure-dominated corona, through which ionization fraction and the plasma beta change drastically. The chrompsphere forms the conduit for the upward flux of mass and energy, while most of the non-radiative energy is dissipated there to supply the heat. Hinode observations demonstrate that the chromosphere is extremely dynamic: small scale structures called as straws, jets, or fibrils cover the entire surface of the Sun, high speed chromospheric 'jets' (type-II spicules, de Pontieu etal 2007) have a width of ~0.3arcsec and change with a time scale of 10 second or less. It is obvious that the chromosphere cannot be considered as an atmospheric 'layer', but it is a wholly dynamic 3D entity that never settles to hydrostatic equilibrium. Even in the most quiet area of the Sun, i.e., in the very quiet photospheric "internetwork", the chromosphere appears to be dominated by largely acoustic shocks, which are initiated in the photosphere by the solar convection and the global p-mode oscillations. Strong "network" fields exist in the photosphere at the boundaries of the internetwork. These fields spread rapidly with height in the highly stratified chromosphere, and at some height they form a magnetic canopy over the internetwork regions. Recent observations from Hinode and other instruments have suggested that the network fields, interacting with convection, energize and structure the quiet chromosphere. Dynamic phenomena in the chromosphere are more dominating in active regions, where apparent reconnection events occur frequently, producing outward propagating jets that may be seen at coronal temperatures (e.g., Shibata et al. 2007, Figure 1.3).

High-speed jets in quiet Sun (type-II spicules) are, however, only visible near the solar limb with Hinode imaging observations, because of their insufficient optical thickness on the disk under the Hinode's Ca II H band-pass filter. In addition, Hinode provides only morphological information of such chromospheric features. With the lack of the Doppler information, the nature of the type-II spicules in quiet regions or those in sunspot penumbrae (Katsukawa et al. 2007) are still under debate. One of important question is whether they are real plasma ejections with the apparent speed along the magnetic fields or not. Without answering the question, we cannot know their physical origin. To understand the generation mechanism and consequence of this fundamental ingredient of the chromospheres, we definitely need velocity

information with better contrast and higher spatial and temporal resolutions. The proposed Solar Ultra-Violet Visible and IR telescope (SUVIT) has a large aperture (1.5 m diameter is now under study), which can achieve a spatial resolution better than 0.06arcsec in Mg II 280nm line. This UV line provides unprecedented images of fine-scale chromospheric structures with much higher contrast. The supreme spatial resolution allows us to explore plasma motions and magnetic-field behaviors inside the chromospheric structures with ~0.3arcsec width. Observations of full spectral line profiles allow us to study the real plasma flow along the magnetic fields with its acceleration and density distribution, and also to clearly identify the connectivity to their photospheric (or possibly chromospheric) root points. The high sensitivity, high-resolution Doppler images (Dopplergram) of chromospheres will for the first time detect the elementary plasma motions, which would be associated with wave shocks and magnetic reconnections, and thus provide a concrete basis of energetic in the chromosphere.

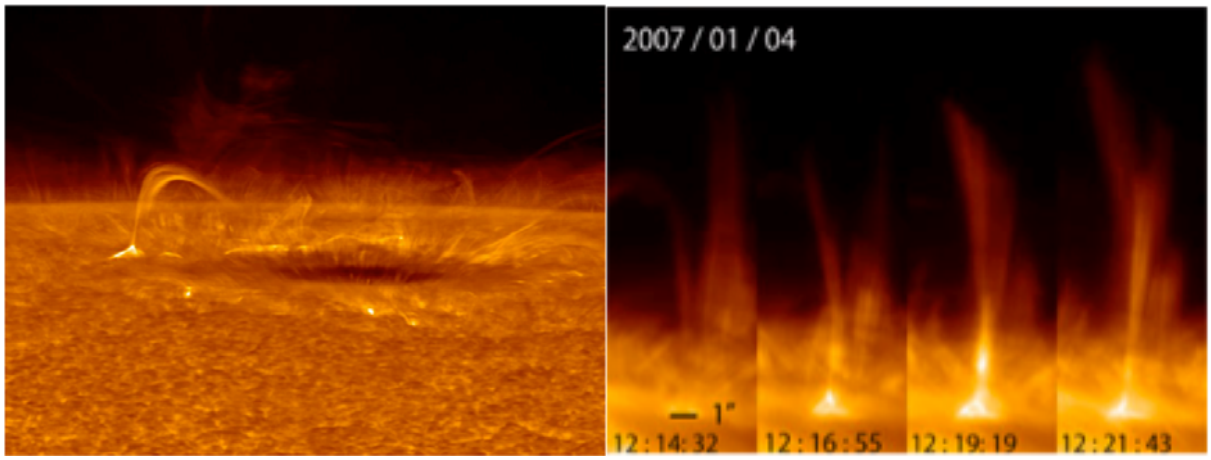

Figure 1.3. Dynamical chromosphere observed with Hinode. (Left) Dynamical chromospheric features around a large sunspot (Right) Chromospheric jets.

Ubiquitous chromospheric jets associated with cusp-shaped structures (Figure 1.3) show a hint of intermittency of plasma ejection, which infers the presence of more elementary reconnection processes. SUVIT aims to identify any non-stationary motions or intensity fluctuation in and around the reconnection site to understand the basic physics that controls the rate of fast reconnection taking place in the chromospheres (See also Section 1.3). One particular interest regarding the magnetic reconnection is the injection of magnetic helicity into the magnetic fields during the reconnection of obliquely directed two flux tubes. Spectroscopic information in a higher spatial resolution will detect the twist or twisting motions in a flux tube, which may be crucial importance for dynamics of the ejected plasma or even for global evolution of the corona. Moreover, SUVIT provides the direct measurements of the magnetic fields in particular chromospheric features like the reconnection cusp. Even with less spatial and temporal resolution in polarimetric observations, such direct information of magnetic fields at the reconnection site is of a fundamental importance to establish the reconnection models of the chromospheric dynamics. Enigmatic phenomena, such as the Ellerman bombs around sunspots (Matsumoto et al. 2008) and intermittent and recurrent occurrence of chromospheric plasma ejections from sunspot light bridges (Shimizu et al. 2009), are also important targets with a great interest relating to the magnetic field reconnection.

1.1.4. Elementary Structures in Photosphere

Photosphere is the region where the gas pressure dominates the magnetic force and, as a result, the kinetic energy of plasma is transferred into the energy of magnetic fields. The magnetic fields are discretely distributed and highly localized into tiny magnetic flux tubes. Hinode SOT aimed to resolve the magnetic flux tubes that have a size of 0.2 - 0.3 arcsec (Figure 1.4, e.g., Nagata et al. 2008), and revealed that they are continuously shaken by surrounding convective eddies, interacting with each other (merge and split), and occasionally newly formed and canceled out. These motions of magnetic elements in the photosphere are the plausible source of the generation of waves propagating upward and magnetic activities such as ubiquitous reconnections taking place in the upper atmosphere. Individual magnetic elements are detected, however, with only one or a few pixels in SOT magnetograph (Figure 1.4), and it is impossible to infer their internal structures. Thus we are still missing the information of electric currents and shape of the cross section of the flux tubes, which are of a crucial importance for understanding the real energetics of fine scale magnetic fields of the Sun. Furthermore SOT frequently observes anomalous Stokes profiles that infer the presence of unresolved magnetic structures and supersonic flows in photosphere (e.g., Shimizu et al. 2008).

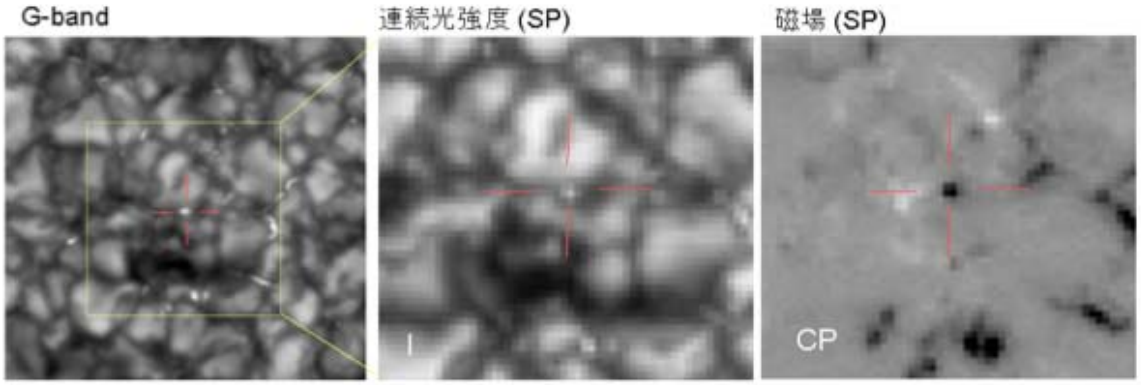

Figure 1.4. A magnetic flux tube captured with Hinode SOT.

The proposed 1.5 m telescope (SUVIT) will observe the interaction between the elementary magnetic structures and the convection in the photosphere to scrutinize the process of energy injection into the magnetic fields in much grater detail; with a 0.1arcsec spatial resolution (pixel scale dx < 0.05") and with the same photometric accuracy with SOT/Hinode (Figure 1.5), SUVIT achieves a sensitivity to the magnetic field (dBlong x $(dx)^2$) and the associated energy elements (j^2 = (dBtang x $dx)^2$) one order of magnitude higher than SOT (Figure 1.6). SUVIT will detect the twist, i.e., the electric current, of individual flux tubes and their evolutions. Temporal variation of electric current is an important signal of a small-scale energy dissipation in upper atmosphere. Interaction of flux tubes with vortices in granular convection is of particular interest for understanding the generation of electric currents and torsional waves in flux tubes. The distribution of magnetic field and velocity across the flux tube and its time variation will provide a clue to identify the mode of waves propagating along the flux tubes. Resolving possible 'hidden' magnetic polarities in a 'uni-polar' region with a higher spatial resolution is very important to understand the mechanism of ubiquitous chromospheric jets taking place over there. The most notable advantage of SUVIT is that it can continuously observe a system of magnetic flux elements in a wide field of view with a highest possible resolution, accuracy and large time coverage under a seeing-free condition. Such observation

enable us to track the evolution of foot points of the magnetic field system and, for the first time, provides a chance to capture a small scale manifestation that triggers the eruption of a magnetic system.

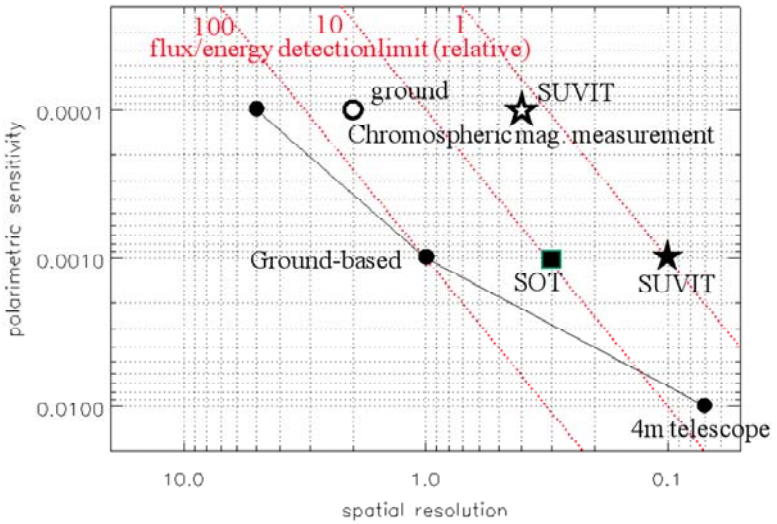

Figure 1.5. Solar-C, Hinode, and ground-based observations on the plane of the spatial resolution vs. photometric sensitivity. High S/N observations for chromospheric magnetic field are shown by open symbols. Detection limits for magnetic flux and energy element are shown by oblique dashed lines.

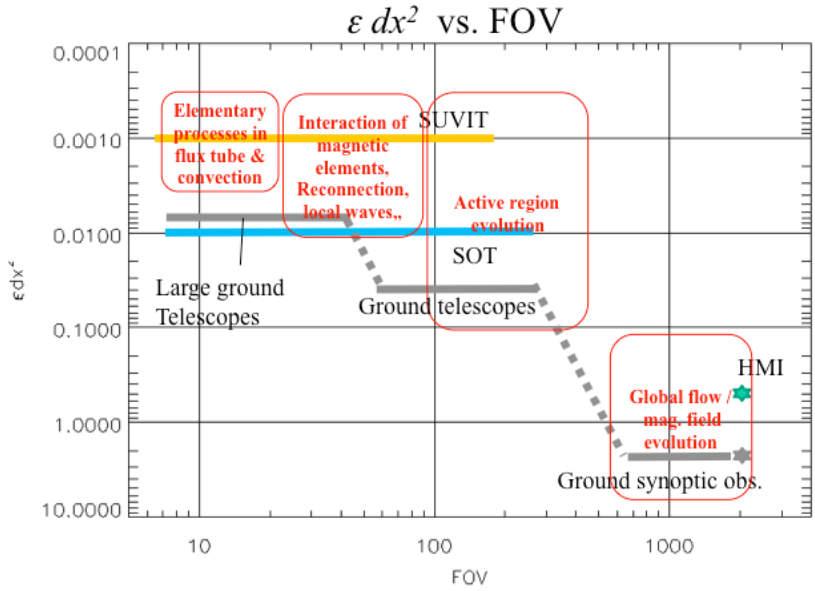

Figure 1.6. The sensitivity to the magnetic flux and energy elements (εdx^2) and the field of view (FOV) of SUVIT and other observations. The SUVIT sensitivity is compared with Hinode SOT and ground-based observations. The unit in the vertical axis is arbitrary and the horizontal axis in arcsec. The figure also shows the sensitivity range and FOV of the observations required for 4 specific science topics.

A similar argument can be applied to the Doppler measurements too; i.e., SUVIT has a 10 times higher sensitivity than SOT to the kinetic energy of gas motions. Tiny flows and shocks possibly associated with photospheric magnetic reconnections, but not resolved so far, are one

of the important targets of SUVIT observations. Observing the dynamic interactions of the magnetic fields with ubiquitous shocks generated by granular convection in the photosphere may provide a direct clue on the origin of spicules or transient phenomena in chromosphere.

These fundamental plasma processes postulated to be taking place in the high β photospheric plasma are only accessible with high accuracy spectro-polarimetric measurement at 0.1" resolution under a very stable imaging condition, which can be only realized from the space.

1.2. Understanding Energy Transport through Small-scale Structures

As briefly described in section 1.1, two non-thermal mechanisms have been debated to explain the heating of corona and acceleration of the solar wind: upward-propagating waves along the magnetic structures, and Joule heating associated with magnetic reconnections. Further observations are required to distinguish how the two mechanisms are excited in the dynamical atmosphere at the elementary structure scale, how the non-thermal energy can be transported with the mechanisms toward the chromosphere, transition region and corona, and how the transported energy can be used to heat the atmosphere and accelerating the plasma. Particularly, the energy transport through small-scale magnetic structures should be observationally understood to distinguish the roles of the two mechanisms in the heating.

1.2.1. Connecting the Chromosphere to the Corona

Hinode imaging observations revealed that substantial transverse displacements exist in many of chromospheric "Type-II" spicules (De Pontieu et al. 2007). Moreover, with coordination with measurements of EUV spectral lines oriented from the transition region (TR), a blue-red asymmetry was derived in TR spectral lines, suggesting that "Type-II" spicules transport mass towards the corona (De Pontieu et al. 2009, McIntosh & De Pontieu 2009). Furthermore, the spectral lines oriented from the corona at temperatures of 2MK show excess non-thermal line broadening at the footpoints of coronal loops, which can be seen only when the coronal loops are observed from the top (i.e., disk center view) (Hara et al. 2008). Based on these Hinode observations (Figure 1.7), quantitatively evaluating of mass and energy transport between the chromosphere, TR, and the corona at the base of coronal loops is essential to reach the conclusion for the coronal heating puzzle.

TR (transition region) is the interface connecting between 20,000 K (upper chromosphere) and 1 MK (corona). SOHO, Hinode and previous space missions have shown the TR to be a highly dynamic and structured region. SUMER high-resolution spectro-heliograms reveal that, on the quiet Sun, the lower-mid TR ($T < 700{,}000$ K) is formed by many loop-like structures 10″ to 20″ long located along and across network boundaries. Similar but fainter structures are also seen in cell centers. From these data it seems that the majority of the TR emission, particularly on the quiet Sun, may not represent a continuous transition between the chromosphere and the corona. EIS raster scans also show the transition from the small-scale TR structures to large-scale coronal loops and funnels to occur around 0.7 to 0.8 MK (Matsuzaki et al. 2007).

Of course, transition region "interface" regions must exist at the footpoints of loops or funnels reaching coronal temperatures but they appear to be responsible for only a small fraction of the TR emission. This would naturally explain the fact that the TR emits much more than it would do if it were a very thin (few tens of km) thermal layer, heated by thermal conduction from the hot corona (as in classical, static, 1-D models). On the other side, SOHO

observations have also shown the TR to be very dynamic on time scales of the order of 10 s to 100 s.

Quiet Sun TR loops also do not seem to have obvious magnetic counterparts at photospheric levels, indicating that the loop footpoints are connected to multiple magnetic elements in the photosphere via a complex system of field lines (Sanchez-Almeida et al. 2007). A similar phenomenon is also observed in moss areas, regions of enhanced EUV emission in upper TR and low coronal lines at the footpoints of 3 MK to 5 MK coronal loops in active regions. In this case their emission is mainly due to thermal conduction from the hot loops. Each footpoint of coronal loops is rooted into a uni-polar magnetic plage region, where no mixed polarity magnetic flux elements are observed at the photospheric level, suggesting a complex magnetic coupling in the upper atmosphere (Brooks et al. 2009).

Therefore, measuring magnetic fields in the higher atmosphere, i.e., chromosphere, would be crucially important for unveiling the nature of this complex coupling between loop-like structures in TR and the photosphere. At the same time, the EUV spectrometer probes all temperature ranges from the upper chromosphere up to the corona with high spatial, spectral, and temporal resolution. The TR strongly emits in the UV/EUV (160 to 2,000 Å) and lines from increasingly higher ionization stages generally fall at shorter wavelengths. The EUV spectrometer should cover a very wide spectral range at unprecedented spatial and temporal resolution, allowing, for the first time, the full characterization of this region of the solar atmosphere: from the topology and morphology of the magnetic structures to the thermodynamic state of the plasma (its motions, density, temperature and abundances) that fills these structures.

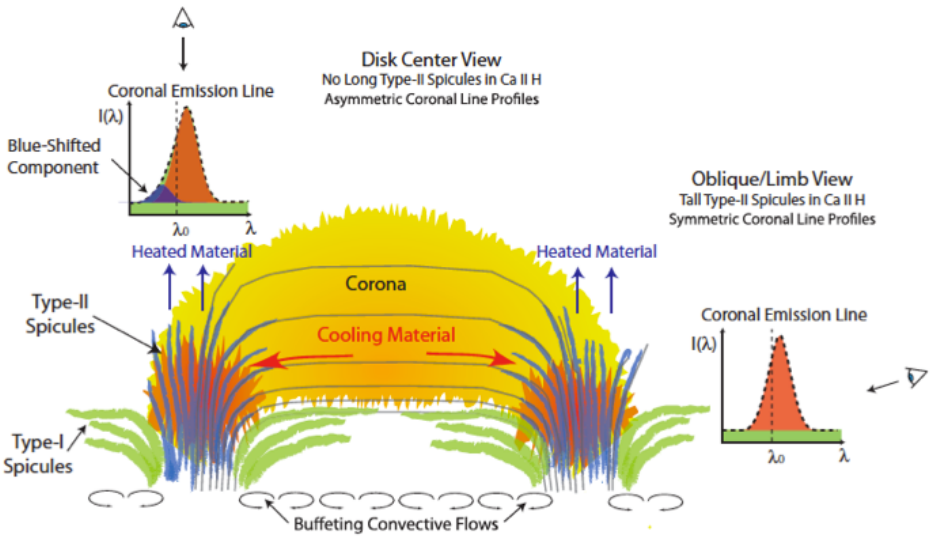

Figure 5. Mass and energy transport between the chromosphere, TR, and corona, as deduced from SOT and EIS observations. See Section 4 for details.

Figure 1.7. Schematic illustration of mass and energy transport between the chromosphere, TR, and corona for the closed loop systems (from De Pontieu et al. 2009)

1.2.2. Magnetohydrodynamic (MHD) Waves in the Solar Atmosphere

Recent observations, especially Hinode's imaging observations, have clearly revealed the presence of apparent transverse oscillations, which are affirmative evidence of the Alfven waves, in the chromosphere and corona. Wave-like oscillations are observed in a wide variety

of solar structures, such as prominence in the corona (Okamoto et al. 2007, Figure 1.8), spicules (de Pontieu et al. 2007, Figure 1.9), and Ca II H dynamical jet (Nishizuka et al. 2008) with Hinode SOT.

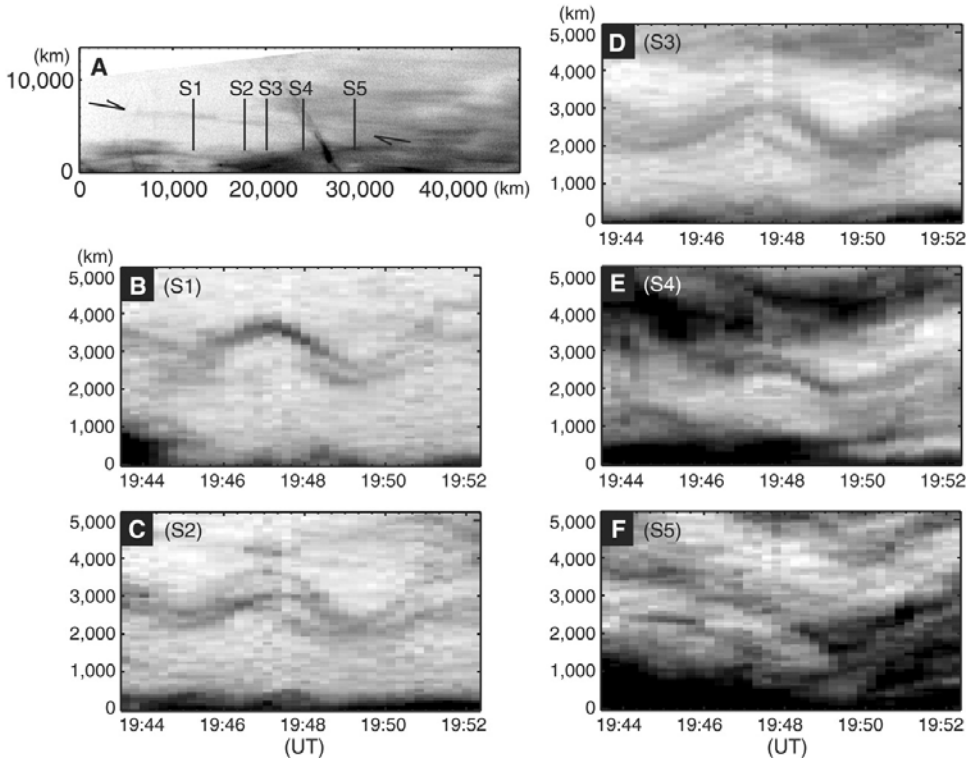

Figure 1.8. Example of a prominence thread undergoing synchronous oscillation along its entire length (from Okamoto et al. 2007)

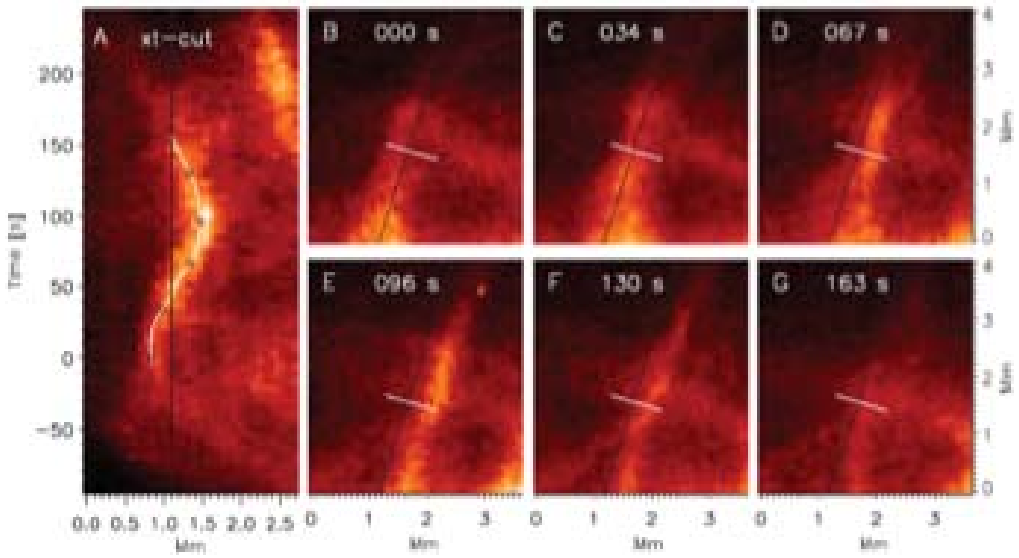

Figure 1.9. Example of the transverse displacement of a spicule (from de Pontieu et al. 2007)

However, we did not identify whether the observed waves are really propagating Alfven waves, or just standing waves in most of observations, except for ubiquitous upward waves in the corona detected with a coronagraph measurement of line-of-sight velocity fluctuations (Tomczyk et al. 2007). Thus, in order to evaluate the propagating MHD waves and their modes, observations require not only velocity and photometric measurements (Kitagawa et al 2010)

but also the measurements of the magnetic field fluctuation, as examined with photospheric magnetic-field data by Fujimura and Tsuneta (2009).

1.2.2.1. Relevance of Observed Waves for Chromospheric Energy Budget

The chromosphere's temperature is approximately 10,000 K with high density. To maintain the temperature structure of the chromosphere, it is required to input heat in the chromosphere about one order of magnitude higher than that required for heating the corona.

Recent studies show that there is insufficient acoustic wave power propagating at higher-frequencies (>5mHz) from the solar interior to heat the chromosphere (Fossum & Carlsson 2005; Carlsson et al. 2007). However, it is shown that inclined magnetic field lines at the boundaries of large-scale convective cells provide portals through which low-frequency (<5mHz) magnetoacoustic waves can propagate in the chromosphere (Suematsu 1990), and these waves provide a significant source of the energy necessary for balancing the radiative losses of the ambient chromosphere (Jefferies et al. 2006). When magnetoacoustic waves propagate upward in strongly stratified atmosphere such as the chromosphere, the waves will steep into shocks to heat the chromosphere (Carlsson & Stein 1997). Carlsson, Hansteen & Gudiksen (2010) indicates that as low-frequency magneto-acoustic shock waves interact with small magnetic elements, joule heating may be effective at these elements' edges.

It is important to observationally determine how much energy is sustained in observed waves, with identifying the mode of the waves. The energy should be measured as a function of magnetic field inclination and atmospheric height. To determine the power of magnetoacoustic waves at the lower atmosphere, we need the measurements in cadences of better than 10-20 seconds with line-of-sight velocity amplitudes of ~0.1 km/s for the photospheric lines and with ~1 km/s for chromospheric lines (e.g., Vecchio et al. 2007). High spatial resolution, 0.1-0.2 arcsec, is needed to resolve individual channels for wave propagation (Bogdan et al. 2003). Moreover, determining the importance of shocks is vital for balancing the radiative losses in the more magnetized parts of the upper chromosphere. To do this, velocity measurements with UV lines in formation temperatures between 10^4 and 10^5 K need to be coordinated with the photospheric and chromospheric measurements with visible lines. For measurements with UV lines, we need cadences of better than 20-30 seconds, which provide 6-15 measurements in one period of 3-5 minutes oscillations, and Doppler velocity measurements of better than 10 km/s (equivalent to sound speed in the upper chromosphere) with line width measurements of better than 5 km/s. It is also important to have the capability to resolve the elemental structures where the wave power is channeled. These are typically on the order of 0.3-0.4" in size, inferred from the observed width of spicules. The wide temperature coverage will allow us to track the evolution of the wave power as it propagates through the different layers of the solar atmosphere. We should note that the NASA IRIS mission, which will be launched in late 2012, will provide new information on the chromosphere, especially on the line-of-sight velocity amplitude measured with chromospheric lines, but it does not have adequate transition region and coronal coverage, nor will it measure chromospheric magnetic fields, both of them are essential to evaluate the natures of magnetoacoustic waves in the solar atmosphere.

1.2.2.2. Time Series Spectra at Different Atmospheric Layers

The problems encountered in understanding the coupling between the chromosphere and the corona are illustrated in Figure 2.2-4. The chromosphere has relatively large patches (10″ to 20″) of many thin, bright spicules (width~0.3"), and the coronal structures are narrow, isolated loops that fade at their footpoints. There is little correspondence between the two. A

comparable transition region image that can only be obtained by a rastering spectrometer would take almost two hours to complete with the current available spectrometer such as SUMER. Although the large-scale structures do not normally change on this timescale, the small-scale dynamics are much faster, and thus high-cadence spectroscopic measurements in transition region lines will make a giant step forward. Moreover, matching spatial resolutions both below (chromosphere and photosphere) and above (transition region and corona) is crucially important to trace the energy flow over the entire atmosphere.

As illustrated in Figure 1.10, spectral lines show different characteristics among chromosphere (Cauzzi et al. 2007), transition region, and corona. The chromospheric spectra have characteristic 3 to 5 min periods, the transition region brightenings occur in bursts of up to 30 min (Innes et al. 1997), while coronal variations are more diffuse. Such different characteristics would reflect the energy transport and release at each layer, but no one knows details, because this kind of time series spectra has never been recorded simultaneously with different spectral lines covering the solar atmosphere with 0.3" spatial resolution.

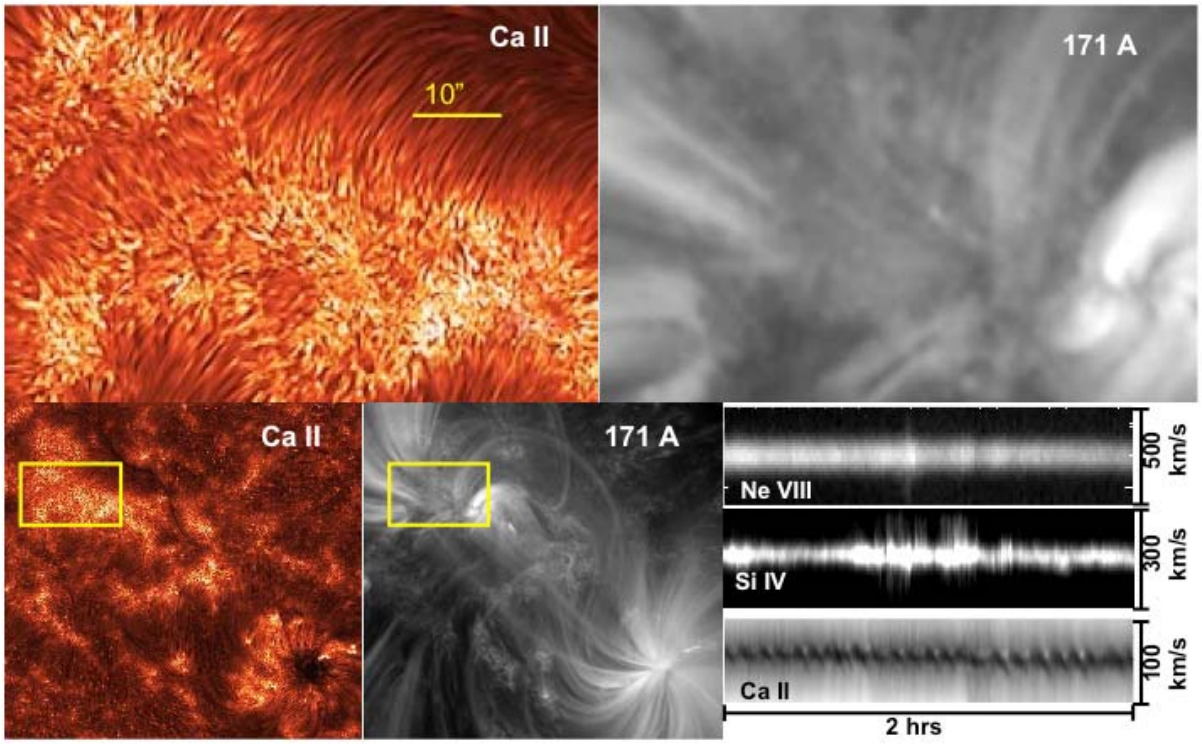

Figure 1.10. The chromosphere-corona connection. The top panels show cut-outs taken from the chromosphere (Ca II, with spatial resolution ~ 0.3") and the lower corona (171A, with spatial resolution ~1″) images. The regions are outlined in yellow. The bottom right panel shows representative time series of chromospheric (Ca II), transition region (Si IV), and lower coronal (Ne VIII) line profiles (recorded at different regions at different times).

The diffuse spectra in coronal lines is much wider than thermal line broadening due to high temperature plasma, and the extra broadening has been considered as non-thermal line broadening. The origin of the non-thermal broadening is uncertain, but it may reflect turbulent nature in the coronal loops. Hinode observations have revealed that the non-thermal line broadening is well observed at the footpoints of coronal loops and that the non-thermal broadening is more enhanced when the coronal loops are viewed from the top, suggesting that there are high-speed upflows which are not resolved spatially (Hara et al. 2008). With having

shorter exposure with ~0.3" spatial resolution, the non-thermal broadening may be partially resolved as Doppler shift signatures of jets in each elementary magnetic structure.

1.2.2.3. Alfven Waves' Contribution to Heating Corona and Accelerating Solar Winds

Alfven waves, transverse magnetohydrodynamic waves that can propagate along the magnetic field lines over large distances and transport magneto-convective energy from the photosphere into the corona, are one promising candidate for the energy source both for the acceleration of the solar wind and for the heating of the quiet corona.

Numerical simulations have been made these days to investigate the nonlinear propagation of Alfven waves in the highly stratified atmosphere. Alfven waves are significantly attenuated in the stratified atmosphere between the photosphere and transition region by various dissipation processes such as nonlinear mode conversion, Alfven wave resonance and phase mixing. Suzuki and Inutsuka (2005) showed that the limited portion of the waves is able to propagate to the corona and nonlinear low-frequency Alfven waves can simultaneously heat the corona and drive the fast solar wind. By using the temporal spectrum of the convection motions at the photosphere from Hinode observations, Matsumoto and Shibata (2010) showed that the observed convection motions generate Alfven waves and that the region between the photosphere and the transition region becomes an Alfven resonant cavity.

The currently available observations of oscillation events do not allow us to determine whether sufficient energy would remain in the waves that penetrate all the way to the corona to make a substantial contribution to the heating budget of the solar corona and/or the acceleration of the solar wind. For allowing this evaluation, observations are required to clearly identify propagating Alfven waves and their modes in the region between the photosphere and the transition region. Such observations are the measurements of the magnetic field fluctuation at the chromosphere and the simultaneous measurements of velocity and photometric information from the chromosphere to the transition region.

1.2.2.4. Specific Topics to be Addressed by New Observations

In addition to evaluating how much energy is sustained in observed waves over the atmosphere, the following questions can be newly addressed with these unique observations. All of them cannot be studied at all with currently available instruments. First, mode conversion of waves may occur around the layer where the plasma beta becomes unity (e.g., Bogdan et al. 2003). Since the beta~1 layer is around or below the middle chromosphere, we may detect the signature of mode conversion in waves. The phase relation between velocity and magnetic field fluctuations will tell how observed waves behave in stratified atmosphere, depending on magnetic structures. Secondly, high throughput performance of the proposed EUV/FUV spectroscopic telescope can allow a search for higher frequency waves and a search for wave signatures in line widths and velocity in the transition region and corona. For active region observations, the telescope will have 1-5 sec exposure time for intense spectral lines with 0.3 arcsec spatial sampling, and 0.5-1 sec exposure time for about 1 arcsec spatial sampling. Slit-and-stare measurements will provide the temporal series of spectral lines with higher cadence than 1 sec, allowing a search for higher frequency waves and thus obtaining new insights in heating of the active region corona by high frequency waves. Thirdly, we may obtain fine-scale structure of magnetic fields by measurements of vector magnetic fields at the chromosphere. We can directly study the properties of turbulent cascade or phase mixing of Alfvenic waves by these small scale magnetic structure. For instance small-scale current sheets

in the chromosphere would be an evidence for phase mixing. Anisotropic elongated structure along magnetic fields would be an evidence of cascade of Alfvenic turbulence.

1.2.3. Signatures of Energy Dissipations in the Corona

An outstanding issue that remains elusive in the formation and evolution of coronal loops is the localization of energy conversion. As an alternative to the classic nanoflare model with magnetic reconnection at coronal heights (Parker et al. 1989), it has been recently suggested that reconnection takes place in the chromosphere and is responsible for the coronal heating through the formation of jets and spicules (e.g., Aschwanden, Nightingale & Alexander 2000). As mentioned previously, recent Hinode observations indicate high-speed upward mass flows at small scale and excess non-thermal line broadening at the base of coronal loops, suggesting that the origin of coronal heating exists in the base of the coronal structures (section 1.2.1).

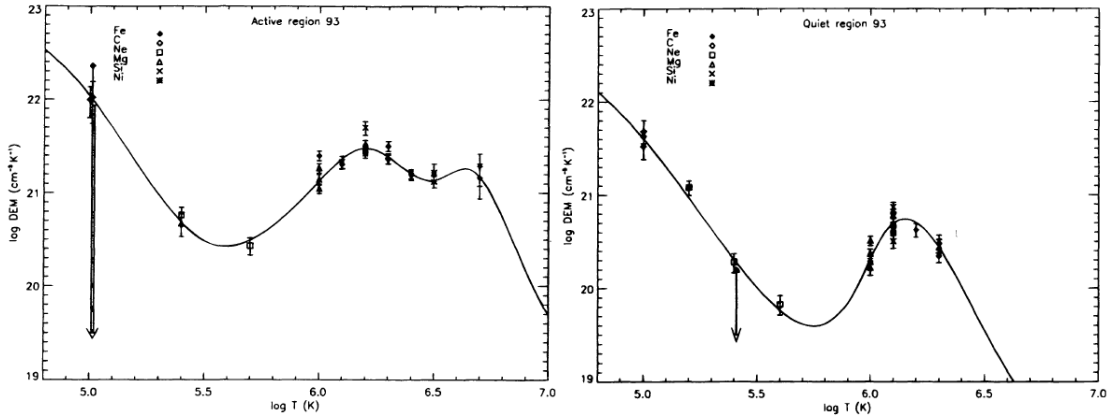

Figure 1.11. *Left:* Differential emission measure (DEM) distribution for an active region. Note no emission line is available for temperature diagnostic beyond logT = 6.7 (T = 5 MK). *Right:* DEM distribution for quiet Sun. After Brosius *et al.* 1996.

High temporal and spatial resolutions are needed to resolve the evolution of numerous, small-scale explosive events like a nanoflare "storm" (Klimchuk, 2006). This tells us whether continuous heating changing slowly compared to a cooling time or impulsive heating repeating rapidly compared to a cooling time is more significant for the coronal heating process. In addition, plasma diagnostics capabilities in the broad temperature coverage, such as measurements of the differential emission measure (DEM, Figure 1.11), electron density, or turbulent velocities, are crucial to advancing the understanding of coronal heating. Also, the pair of EUV emission lines from different atomic species allows us to estimate the thermal temperature of ions because of the difference in their thermal velocities (Imada et al. 2009). The EUV spectrometer proposed for Solar-C is the ideal instrument for the plasma diagnostic because of its sub-arcsec spatial resolution, EIS-like or better spectral resolution, wide temperature coverage from the photosphere into the corona, and high throughput. The EUV spectrometer has the diagnostic capabilities for the plasma only up to ~5 MK, because high-temperature plasma in 3-6MK is energetically dominant in active-region corona (Figure 1.11). There is also an interesting indication from Hinode XRT that there possibly exist high-temperature components whose temperature at least 5 MK (could be as high as 10 MK) diffusely distributing across the quiet Sun, even without any active regions (Ishibashi et al. 2011). High-temperature components can be created by energy dissipations in the corona.

Identification of temperatures of such components in the corona, coupled with their spatial distribution, may provide important clues on how the corona is heated, and maintains its temperature. If the proposed photon-counting X-ray telescope is selected as the X-ray imaging telescope, it will reveal high-temperature temperature components and their temporal evolution by obtaining spatially-resolved X-ray count spectra.

1.2.4. Behaviors of Magnetic Fields in Corona Explored through Seismology

It has been difficult to measure magnetic field fluctuation in the corona, which is one of key information to investigate propagating waves. However, observations of oscillations in the corona have the potential to reveal different properties of the local plasma environment. For example, kink-mode transverse oscillations of the coronal loops impulsively excited by the blast wave in a large flare (Nakariakov et al. 1999, Figure 1.12) can be recognized in the time series of coronal images and allow us to estimate the value of the local magnetic field strength. In some cases, both fundamental mode and higher harmonics are obtained, which enables us to estimate the density stratification along coronal loops.

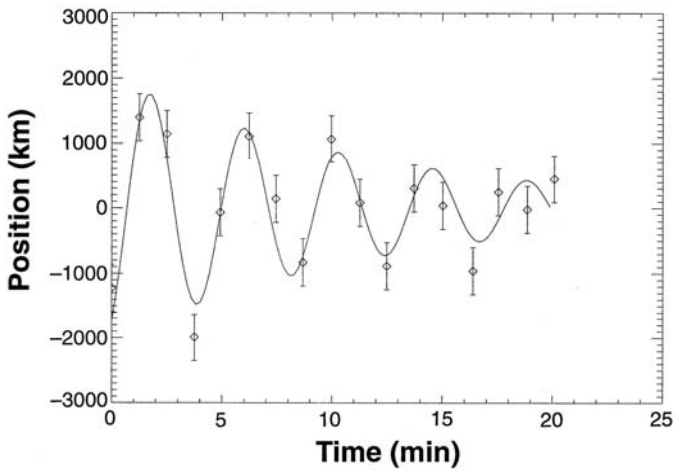

Figure 1.12. Temporal evolution of the loop displacement through the loop apex when oscillation is exited in the loop (Nakariakov et al. 1999)

The Solar-C observations will allow us to take Doppler velocity measurements of such oscillating loops. Oscillations of coronal loops during Alfven waves propagate along the loops may be measured with the proposed EUV spectrometer, which may derive local magnetic field strength as a function of the distance from the base of coronal loops. The techniques of coronal seismology require cadences of the order of 2 s (Roberts 2000) to determine radially dependent parameters. By having higher spatial resolution (~0.3”), the density and temperature can be measured in the configuration that different coronal loops are less overlapped. This allows to have better estimate on the density and the local field strength. Direct measurement of velocity is a key parameter, because linear Alfvén waves are incompressible and so do not show up as intensity perturbations. The velocity resolution needed to observe the perturbations caused by these waves is of order 10 km s^{-1} to see spatially resolved waves and 5 km s^{-1} should be these waves on smaller scales than we can resolve.

1.3. Magnetic Reconnection

1.3.1. The Solar Atmosphere as a Laboratory for Magnetic Reconnection

Magnetic reconnection is one of the most important mechanisms for the plasma heating and particle acceleration in magnetized space and astrophysical plasmas. The importance of magnetic reconnection is well discussed in many plasma environment, such as the Earth's magnetosphere (e.g., Hones, 1979; Nagai et al., 1998, 2001; Baumjohann et al., 1999; Øieroset et al., 2002; Imada et al., 2005, 2007, 2008), laboratory (e.g., Baum & Bratenahl, 1974; Ono et al., 1997; Ji et al., 1998; Yamada et al., 1997), and also the solar atmosphere. Several astronomical phenomena, such as accretion disks, proto-type stars, AGN jets, cluster of galaxies, and pulser wind, are also recently simulated and discussed with magnetic reconnection to explain dynamical natures revealed with X-ray and radio observations.

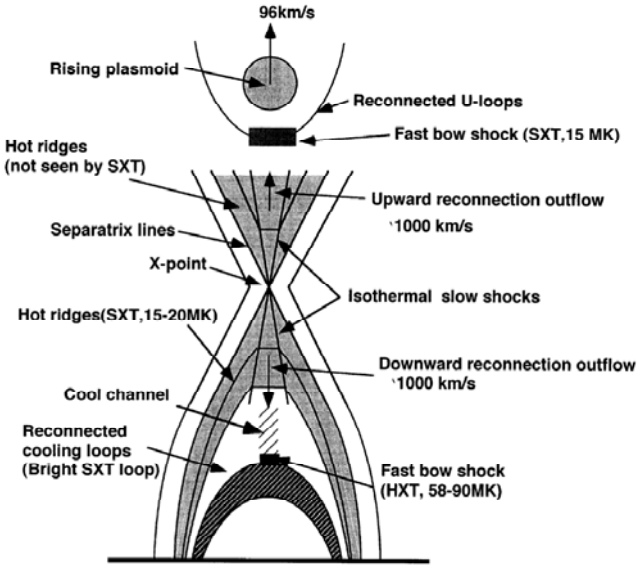

Figure 1.13. Global magnetic configuration and associated reconnection signatures in a type of solar flares (Tsuneta et al. 1997).

Magnetic reconnection is believed to be central to the energy release in solar flares, the heating of the solar corona, and the initiation of coronal mass ejections (CMEs) (Figure 1.13). It is a rapid mechanism for converting the stored magnetic energy into kinetic, thermal, non-thermal and wave/turbulence energy via magnetic dissipation process. Yohkoh X-ray observations provided some pieces of evidence for magnetic reconnection in solar flares and coronal jets, and then Hinode has revealed that magnetic reconnection occurs with various configurations of magnetic fields not only in the corona but also in the chromosphere. The energy conversion by magnetic reconnection is fundamental and essential to explain dynamical behaviors in the wide variety of plasmas in the solar atmosphere. While considerable progress has been made over the past decade, three key questions listed below have not yet been answered with observations:

1) What plasma conditions and parameters, such as collisionality or temperature, control the energy release rate of magnetic reconnection (reconnection rate)?
   → Section 1.3.2 and 1.3.3
2) What determines the energy distribution among kinetic, thermal, wave/turbulence, and especially non-thermal energy at the rapid conversion of stored magnetic energy? → Section 1.3.4 and 1.3.5
3) What is the role of 3-dimensionality in magnetic reconnection? → Section 1.3.6

Observations carried out by the Solar-C Plan B mission should be designed to answer these questions.

1.3.2. Magnetic reconnection occurring in a wide variety of plasma conditions

One of the fundamental questions in magnetic reconnection is what determines the energy release rate. It is also what fraction of released energy is converted into kinetic, thermal, non-thermal, and wave/turbulence energies. Previous studies of solar, space and laboratory plasmas challenged these questions, though they have not yet answered these questions. The solar atmosphere shows us a wide variety of plasma conditions, i.e. weakly ionized to fully ionized plasmas, and collisional to collisionless plasmas (Table 1.1), which are quite different from the plasma conditions in magnetosphere or laboratory experiments. Observational investigation of magnetic reconnection under various plasma conditions is very important for space, solar, astrophysical and laboratory plasma physics. The challenge of the Solar-C mission is to diagnose magnetic reconnection in such various plasma conditions with more direct observational information available from spectroscopic measurements in three different wavelengths (IR-visible-UV, FUV-EUV, and soft X-ray). Especially, the proposed high throughput UV/EUV spectroscopic telescope can reveal plasma dynamics in faint reconnection region with high cadence measurements, and the proposed photon-counting X-ray telescope will enable us to diagnose particle acceleration mechanism with imaging spectroscopy in X-rays. The spectro-polarimetric instrument of the proposed IR-visible-UV telescope measures the magnetic fields in the chromosphere, allowing us to understand chromospheric reconnection more detail.

Table 1.1. Typical properties of plasma in solar atmosphere

	Photosphere	Chromosphere	Inner Corona	Outer Corona (~2Rs)
Dominant pressure	Gas	Magnetic field	Magnetic field	Gas
Ionization	Neutral	Weakly ionized	Fully ionized	Fully ionized
Collisionality	Collisional	Collisional	Semi-collisionless	Collisionless

1.3.3. Magnetic reconnection in weakly ionized plasma (solar chromosphere)

1.3.3.1. Does fast reconnection really occurs in the chromospheres?

One of the most important Hinode findings is that magnetic reconnection events frequently occur in the solar chromosphere. Shibata et al. (2007) found the ubiquitous presence of chromospheric anemone jets outside sunspots in active regions. The anemone jets have an inverted Y-shape, similar to the shape of X-ray anemone jets in the corona (Figure 1.3). Their typical velocity is comparable to the local Alfven speed in the lower chromospheres, and their footpoints are located among the mixed polarity region. So they concluded that chromospheric anemone jets imply magnetic reconnection in the chromospheres.

Hinode has also discovered new types of magnetic reconnection events in the chromospheres with various magnetic field configurations (e.g. Katsukawa et al. 2007, Nishizuka et al. 2008, Shimizu et al. 2009). Shimizu et al. (2009) revealed that sunspot light bridges sometimes show recurrent occurrence of chromospheric jets. Vector magnetic field data in the photosphere suggests that a helical magnetic flux tube lying below the light bridge plays vital roles in producing jets. Katsukawa et al. (2007) also found microjets even in the sunspot penumbra, where magnetic field lines are usually not fully anti-parallel.

One of the important questions about magnetic reconnection in the solar chromosphere is whether the magnetic reconnection in the chromosphere is really fast, independent on resistivity, or not. Our current guess, which is based on Hinode observations, is ”yes”. Hinode Ca II H movies, however, do not allow us to evaluate the reconnection rate. The time cadence of the Ca II H observations is fast enough, but quantitative information, such as plasma flows, density, temperature and magnetic field, are needed. These quantitative parameters are available from the proposed IR-visible-UV telescope

1.3.3.2. Observations of Ambipolar effect in weakly ionized plasma

Chromosphere is high density, collisional and weakly ionized plasma. In such a condition, it is hard to expect fast reconnection. On the basis of the space and laboratory plasma observations, it is said that, to drive “fast reconnection”, “anomalous resistivity” should work in the diffusion region via microscopic process. To make it possible, the following two aspects should be satisfied: ion gyro radius is larger than mean free path (collisionless condition), and the width of a current sheet becomes thin comparable to ion gyro radius. However, it seems that Sweet-Parker current sheet is not so thin, and the mean free path in the lower chromosphere is smaller than ion gyro radius. If fast reconnection really occurs in the chromosphere, additional physics should be considered.

One candidate is “ambipolar effect” in the chromosphere, where the neutral hydrogen to proton density ratio is $\sim 10^4$ (i.e. Singh and Krishan 2010). Ambipolar diffusivity is effective in the chromosphere because of the ion-neutral collisions. The collision between ions and neutrals causes ambipolar diffusion, which plays a role in making a current sheet thinner and thinner in the weakly ionized plasma (e.g., Zweibel, 1988, 1989, Brandenburg & Zweibel, 1994, Chiueh, 1998). Isobe et al. (in preparation) discussed the effect of ambipolar diffusivity and showed that bursty reconnection can take place in the chromosphere (Fig 1.14). The nature of magnetic reconnection in the chromosphere is still not clear from both observational and theoretical viewpoints. The aim of the Solar-C mission with the IR-visible-UV spectro-polarimetric

observations is to measure physical parameters around the reconnection region and observationally determine the reconnection rate qualitatively and to reveal the dynamics of magnetized plasma in various configurations of magnetic field with direct observation of chromospheric vector magnetic field.

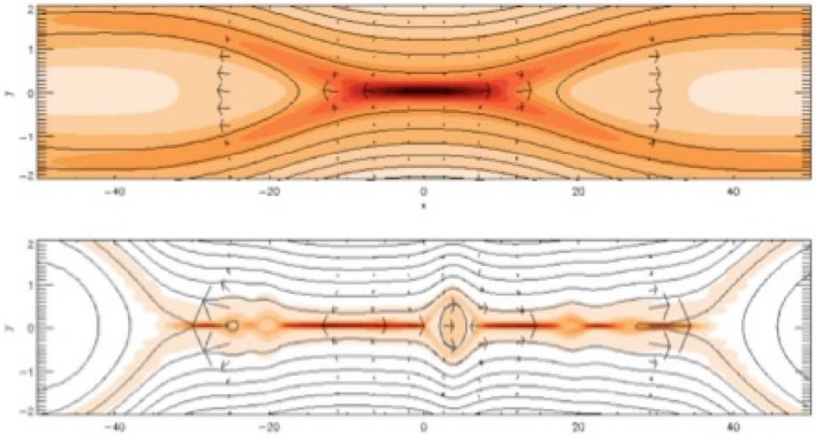

Figure 1.14. Magnetic reconnection in weakly ionized plasma (bottom) and collisionless plasma (top).

1.3.4. Magnetic reconnection in collisonless plasma (corona and transition region)

Magnetic reconnection in the solar corona has been discussed as a key mechanism involved in solar flares. Various features expected from the magnetic-reconnection model have been confirmed with modern space observations. For example, Yohkoh observed the cusp-like structure, which is predicted by the standard reconnection flare model (Tsuneta et al., 1997). Quantitative understanding in the key region of solar flares, however, is not enough so far to discuss the energy release rate or energy distribution rate of magnetic reconnection.

The primary reason why it is difficult to directly observe the magnetic reconnection region is because of its faintness. A bright cusp-like structure (flare loop) is formed during a solar flare, and the reconnection region that is believed to exist above the cusp structure is extremely faint. A large dynamic range of intensity and low-scattering performance is required to observe inside the reconnection region. Moreover, since the temperature in the reconnection region may be significantly higher than that of cusp-like flare loops (e.g., Tsuneta et al., 1997), the line spectral signature (ionization state) in the reconnection region may be different from what seen in flare loops.

1.3.4.1. What determines the energy distribution among kinetic, thermal, wave/turbulence, and non-thermal energies?

One of the important parameters for magnetic reconnection in the solar corona is how much energy is stored in the coronal magnetic fields. The stored energy can be estimated from the magnetic-field measurements at the photosphere (Top part of Fig 1.15). For example, Kubo et al. (2007) showed magnetic-field evolution of a flare productive active region with continuous series of photospheric magnetic fields by Hinode. Magara and Tsuneta (2008) calculated the magnetic helicity in the flare-productive active region and found that the helicity increases very rapidly before the flare. This quantitative analysis is very important for the estimation of stored energy before magnetic reconnection. Reconnection electric fields (reconnection rate) also can

be quantitatively estimated with Hinode (e.g. Jing et al., 2008). Therefore, we can observationally evaluate the stored magnetic field energy and its release rate, which is the top part of Fig 1.15.

To understand the energy distribution among the energies, we need to evaluate each of thermal, kinetic, non-thermal, and wave/turbulence energies during a flare. Spectroscopic observations with EIS on board Hinode enable us to evaluate thermal energy with differential emission measure analysis (e.g., Watanabe et al. 2007), kinetic energy with the Doppler velocity analysis (e.g., Asai et al., 2008), wave/turbulence energy with line broadening analysis (Imada et al. 2008), and non-thermal energy with simultaneous RHESSI hard X-ray and microwave observations (e.g. Minoshima et al. 2009, Watanabe et al. 2010).

As shown in Figure 1.15, with Hinode observations, we can know the magnetic energy stored in corona before magnetic reconnection (top part of Figure 1.15). The most part of energies can be evaluated in the post reconnection stage after the transient energy release is finished (bottom part of Figure 1.15). On the other hand, there is poor observational knowledge on the physical parameters in the reconnection region during the period when the reconnection process is on going (middle part of Figure 1.15). The inflow into the reconnection region, the plasma temperature in the reconnection region, and the temperatures and densities of the plasma jets (outflows) have not been measured quantitatively. They are key observational parameters necessary for probing reconnection process.

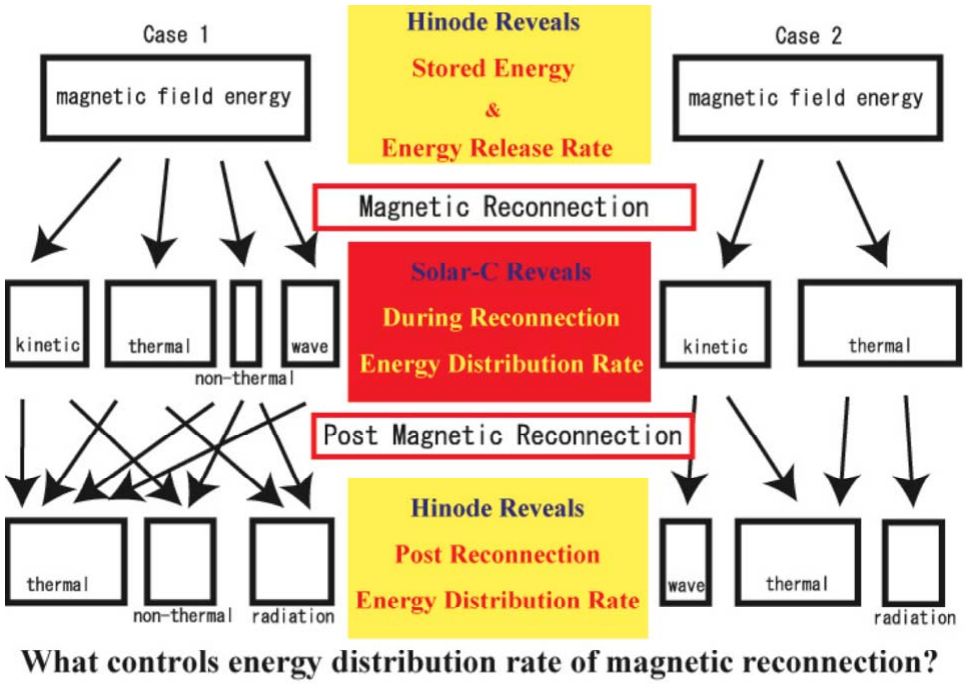

Figure 1.15. Energy distributions during magnetic reconnection.

1.3.4.2. Probing inside the reconnection region in non-ionization equilibrium

Theoretical model of steady fast reconnection, called Petchek-type reconnection, expected the formation of two slow-mode shocks elongated from the reconnection region, which play a role in heating ambient plasma. During rapid heating with slow-mode shocks, heated plasma would be in non-thermal equilibrium condition. There are typically three kind of thermal non-equilibrium conditions; 1) Non Maxwellian energy distribution, 2) different temperature in different species (e.g., Tp > Te), and 3) transient ionization condition (ionization

non-equilibrium). All of three conditions are predicted in the reconnection region, and the detection of them are a challenging target for Solar-C.

Figure 1.16 shows a calculation of non-equilibrium ionization structure in 1200 km/s jets at the down stream of magnetic reconnection region. We can clearly see that the plasma state in the downstream of slow shocks cannot reach to ionization equilibrium. The proposed high-throughput EUV spectrometer (~10 times better than the effective area of the currently available spectrometer, see Figure 3.3 in Chapter 3) can measure spectral lines with much shorter exposures, allowing detecting the transient state of non-ionization equilibrium. Such transient state tells us a history of ionization process of each ion and thus contains the information of the reconnection region. For detecting the transient ionization condition, a lot of spectral lines covering a broad range of ionization states need to be measured, which can be done only with the proposed UV/EUV spectrometer (for flare plasma, from Fe XVIII to Fe XXIV, see Appendix 3-A).

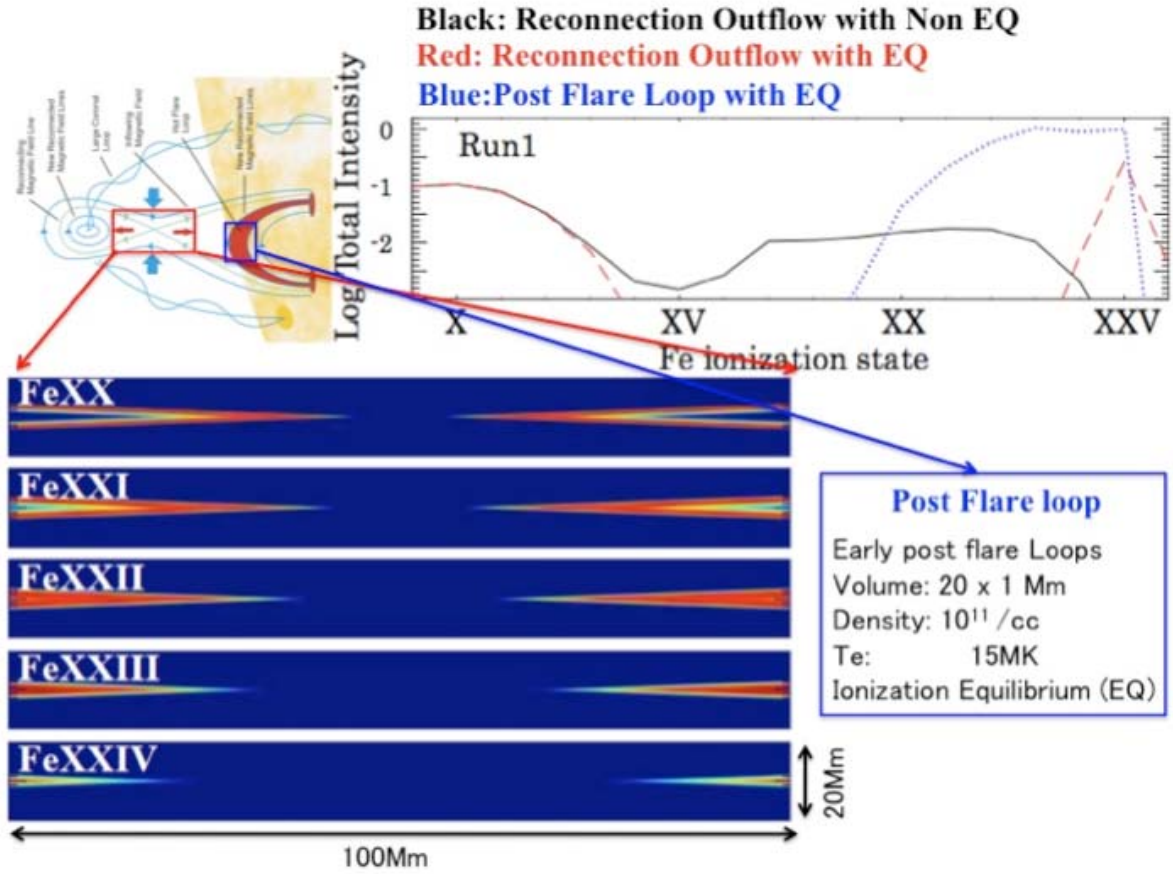

Figure 1.16. A computation of non-equilibrium ionization structure in 1200 km/s jets at the down steam of magnetic reconnection region. The following parameters are used in this computation: magnetic field 12 gauss, electron density 4.2×10^8cm-3, temperature 1MK, and plasma β 0.01 at the upstream side of the slow-mode shock and temperature 40MK at the downstream; the shock angle at the upstream and downstream is 85 deg and 2.3 deg, respectively. The upper right panel shows the total intensity of the non-equilibrium ionization structure (black line) as a function of ionization state is compared with the total intensity of post-flare loop (blue dotted line).

The signal intensity of the non-equilibrium ionization structure can be seen in contrast with the bright post-flare loop, if we choose suitable spectral lines (Fe XV ~ Fe XVIII). Bright flare

loops have typical temperature of ~10 MK and density of ~10^{11}cm^{-3}, and therefore the loops are dominantly observed with Fe XIX ~ Fe XXII. In the reconnection region, it takes ~100s to reach the ion state to higher ionization states after the energy release in a short time scale. Thus, we expect that signals exist not only in high ionization states (Fe XVIII ~ Fe XXIV) but also in low ionization states (Fe XII ~ Fe XVII).

When spectral lines with ionization states higher than Fe XIX are used for measurements, observing the early phase of solar flares is a key to success the diagnostics of the reconnection region. This is simply because bright flare loops developed during flares has higher density, say, by two orders of magnitude, than the density inside the reconnection region. This means that the spectral line intensities from the flare loops are higher by four orders of magnitude than that of the reconnection region. In the early phase, the total emission measure of flare loops is still small and thus we have possibility to detect signals from the reconnection region, when we have the spectrometer with wide dynamic range and low scattered-light optics.

In the down stream of slow-mode shocks, the ion temperature may not be same as the electron temperature. Such non-equilibrium is frequently observed in collisionless plasma condition (Baumjohann et al., 1999). To understand how much energy is given to ions and electrons respectively, we should observe both of ion and electron temperatures simultaneously. Line width of EUV spectral lines can be used to estimate ion temperature (e.g., Imada et al., 2009), but the ionization equilibrium is always assumed in the spectroscopic analysis of EUV lines, resulting in difficulty in deriving electron temperatures for transient non-equilibrium plasma. Therefore it is essential to have another measurement for deriving the electron temperature inside the magnetic reconnection region. Accurate measurements of the electron temperature can be achieved by measuring thermal bremsstrahlung emission at short wavelengths (soft X-rays) with the proposed photon-counting X-ray telescope. In contrast to the EUV line spectroscopy, the spectral shape of thermal bremsstrahlung emission directly reflects the electron temperature without depending on the ionization equilibrium.

Because of its faint structure, non-ionization equilibrium signals inside the magnetic reconnection region are not easy to detect. But the proposed UV/EUV high-throughput spectroscopic telescope has potential to detect them, because of its high-throughput performance and low scattered optics. If we can observe inside the reconnection region, then we can determine the reconnection condition by using the knowledge of non-ionization equilibrium. The ionization process is similar to the nuclear-decay process. Thus we can estimate the time passage from strong heating. The velocity, density, and ion temperature in the reconnection region can be derived from line spectroscopic analysis with the knowledge of non-ionization equilibrium plasma. Therefore, probing the magnetic reconnection region from viewpoint of non-ionization equilibrium can provide useful information on the mechanisms of the energy distribution rate.

1.3.5. Particle Acceleration coupled with Reconnection Dynamics

Yohkoh observations played an important role in revealing particle acceleration mechanism in solar flares. A loop-top hard X-ray source was discovered in a compact flare (Masuda et al. 1994), indicating that energy release and particle acceleration occurs above the post-flare loop. Using a unique technique “time-of-flight method,” Aschwanden et al. (1997) also showed that the particle acceleration occurs above the post-flare loop. It is currently believed that particles are accelerated in the current sheet and slow/fast-mode shocks coupled with the reconnection dynamics. However, we have not at all understood how particles (ions and electrons) are

accelerated. This is because of the difficulty in directly probing the acceleration region. One of the main reasons for the difficulty is the lack of dynamical range in hard X-ray observations.

Accelerated electrons radiate X-ray emissions via non-thermal bremsstrahlung process. The amplitude and energy of X-ray emissions depends on the number and energy of accelerated electrons. An impediment to fully understanding of acceleration mechanism is a dynamic range of instrumentation. The proposed photon-counting grazing-incidence X-ray telescope has dynamic range three orders of magnitude better than RHESSI. It covers the energy range from <1 to ~5 keV (goal ~10 keV), which contains thermal emission both in continuum and lines as well as non-thermal emission at the higher end of the energy range. Suprathermal electrons (~10keV) have most parts of non-thermal energy. Non-thermal signatures have been seen even below ~5 keV in many microflares (Hannah et al. 2008). Therefore, the proposed X-ray telescope may allow us to evaluate non-thermal electrons.

Another way to discuss the non-thermal energy is by determining whether the electron energy distributions are Maxwellian or not with the EUV spectroscopic measurements. Seely et al. (1987) studied the change of line intensity ratios of He- and Li-like Fe ions with non-Maxwellian electron energy distribution in the laboratory experiment. The bottom two panels of Figure 1.17 show Fe XIV lines with thermal and non-thermal equilibrium conditions. They show that intensity ratios marked with red circles changes in these two cases. Differential emission measure and electron density can affect on the intensity ratios, as well as non-thermal equilibrium state. Therefore, multiple line observations (see Appendix 3-A) can distinguish which affect on the intensity ratio. The Hinode EIS cannot perform such analysis because of poor wavelength coverage, but the proposed UV/EUV spectrometer will provide a quantum leap in our understanding of electron energy distributions and particle acceleration in the solar atmosphere.

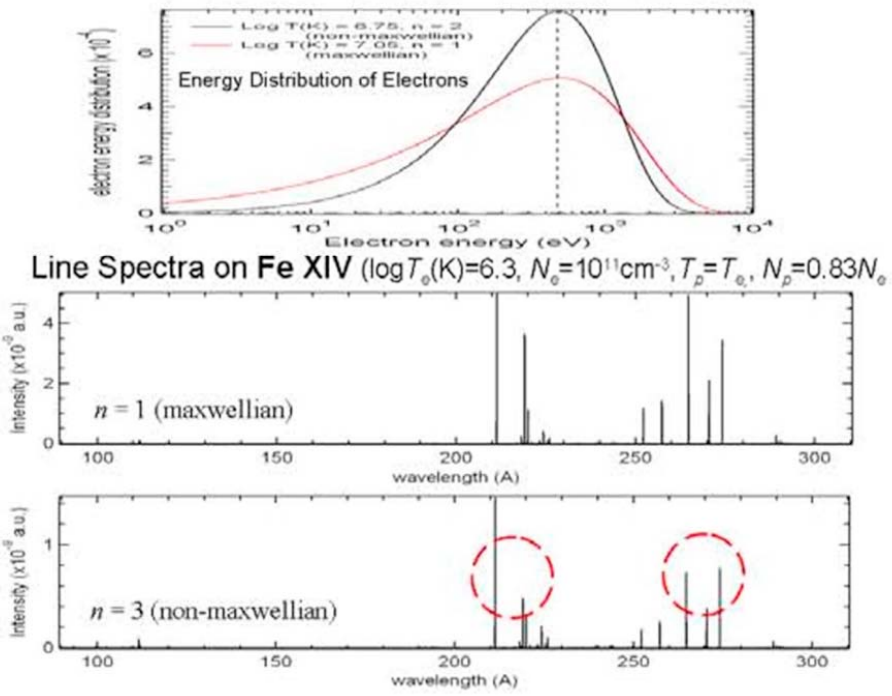

Figure 1.17. Two electron energy distributions corresponding to Te ~ 650 eV (top panel) and changes of Fe XIV line intensity ratios (bottom panel) highlighted by dotted red circles.

1.3.6. What is the role of 3-dimensionality in magnetic reconnection?

Another important question in solar flares is what is the role of 3-dimensionality in magnetic reconnection. Generally the current sheet thickness of the magnetic reconnection is in order of ion inertia/gyro radii scale (a few 10m). However, solar flares show a large (a few 100Mm) well-known flare arcade and ribbons (see Figure 1.19). The difference of scale size between current sheet thickness and current direction is roughly 7 orders of magnitude. The question is that the magnetic reconnections take place individually in current direction, or there are some causal connections for current direction. In other words, we can say that the simultaneous flare triggers happen in each current sheet and they are developed to a large flare structure, or only one local flare trigger happens and the former magnetic reconnection causes the latter magnetic reconnections. To clarify this point, we should investigate that the existence or nonexistence of the causal connection for current direction in solar flares.

One of the advantages on using the solar plasma for magnetic reconnection studies is that imaging observations of reconnection events, such as flares and jets, can provide the global picture of plasma condition and magnetic field configuration. We already have some indication from modern satellite observation, and many modeling study has been done. According to their result, flare arcades must be individually heated as large numbers of distinct loop strands in order for them to reproduce the observed emission signatures (e.g., Hori et al. 1997; Reeves & Warren 2002; Reeves, Warren, & Forbes 2007; Warren & Doschek 2005). This multi-loop model provides a good description of a coronal arcade once it has come to rest after a flare reconnection event. Some theoretical studies show that patchy reconnection (Figure 1.18) can create a large number of distinct reconnected loops which each descend individually through the corona. Although we know that each post-flare loops have different characteristics, we do not have enough information about the causal connection for each flare loops. To clarify this point, we need spectroscopic observation (Doppler shifts and line width) with high temporal resolution. If there are some relationships between each flaring loops, the information of triggers may propagate with Alfven speed. Thus at least we need temporal resolution shorter than Alfven transit time. Therefore, spectroscopic measurements with high cadence (shorter than Alfven time) can open a new window for investigating the role of 3-dimensionality in magnetic reconnection.

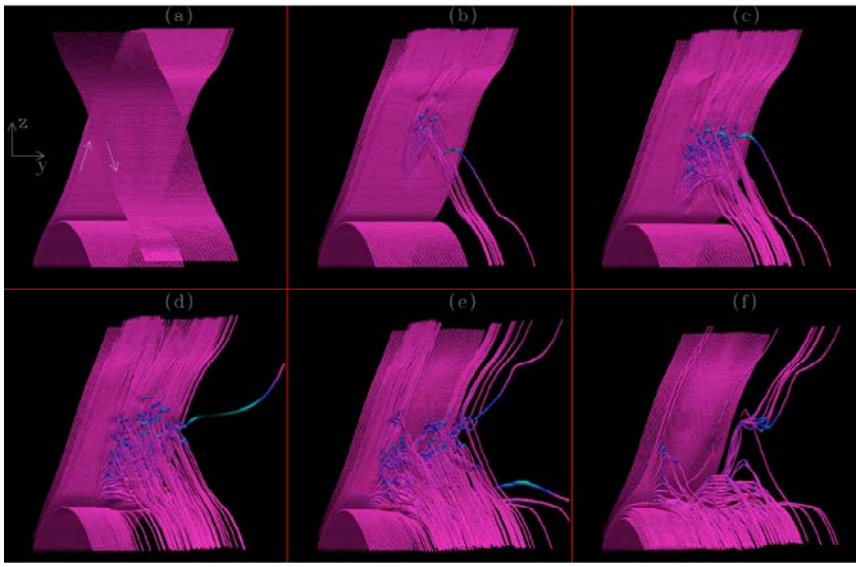

Figure 1.18. Field connectivity change predicted in patchy reconnection

1.4. Small-scale Physics Initiating Large-Scale Phenomena

1.4.1. Flares and CMEs

Solar flares and coronal mass ejections (CMEs) are manifestations of explosive energetic events at the Sun that accelerate particles. Both sources cause geo-effective particle events that endanger space assets and human explorers.

1.4.1.1. Coronal Magnetic Fields for Initiating CMEs and Flares

The start of most CMEs is associated with the eruption of a prominence/filament or sigmoid. Both prominence/filaments and sigmoids are manifestations of non-zero magnetic helicity; that is, they show evidence of non-potential magnetic fields, and thus electric currents and twisted magnetic fields. Both have been modeled as magnetic flux ropes (e.g., Rust & Kumar 1996; Titov & Demoulin 1999). Essentially all models of sigmoid formation involve twisted ropes of magnetic flux, since the twist affords a convenient method of storing energy needed for an eruption, and the appearance of the sigmoids is suggestive of writhing coronal loops (McKenzie & Canfield 2008; Savcheva & van Ballegooijen 2009).

The presence of measurably twisted fields before the eruption facilitates an estimation of the stored energy available for the eruption. The coronal magnetic fields are modeled primarily with a non-linear force free field (NLFFF) model. The magnetic fields measured at the photospheric level are currently used for this modeling, but the photospheric data are not consistent with the NLFF condition. The force-free condition is well justified in low beta plasma, which is in the corona and the upper chromosphere and is not in the photosphere. Nevertheless, precise photospheric vector magnetic field data from Hinode is currently the most key observation for NLFFF modeling of coronal fields in data-driven simulation of large flares and CMEs (e.g., Kataoka et al. 2009). The data-driven simulation will be a powerful method for understanding what triggers eruptions, flares, and CMEs. It is desirable to establish a reliable method for measuring the Poynting flux in an active region in order to calculate the available free energy for an eruption. Predicting the size of an eruption is important for space weather applications.

Magnetic fields measured in the chromosphere will be a key for improving the accuracy of NLFFF modeling. Direct chromospheric magnetic field information, e.g. Hα images can be used as additional constraint (Wiegelmann et al. 2008). Hα images show the horizontal direction of the chromospheric magnetic field vector. Direct measurements of line-of-sight chromospheric magnetic field help to serve as an additional constraint. Measurements of the magnetic field vector in the low beta chromosphere could be used directly as boundary condition for NLFFF modeling.

An important issue for NLFFF-modeling is to have sufficient large field of view that accommodates most of the connectivity within a region and its surroundings (DeRosa et al. 2009). Because of narrow field of view (200 arcsec x 200 arcsec), the high spatial resolution magnetic field data from Solar-C needs to be imbedded into a large field of view data from other spacecrafts, such as Solar Dynamic Observatory (SDO), and ground-based observatories. Therefore, for accurately estimating the magnetic field of flares and CMEs in the corona, it is most important to coordinate the Solar-C observations with instruments with wide field of view, such as SDO and ground-based observations.

1.4.1.2. Small Scale Triggers and Dynamics in Initiation

In order to accurately predict when, where, and how space weather events are initiated, we must understand the interrelationship between small-scale processes on the solar surface and large-scale magnetic structures in the solar corona. In particular, current belief is that small-scale processes (e.g., magnetic reconnection) are important as a trigger for solar flares. The solar magnetic fields control the flow of energy and formation of structures above the photosphere. Hinode observations would make much more progress in understanding the role of magnetic topology (such as quadrupolar fields in the breakout model) and small-scale photospheric flux emergence in flare and CME initiation, if Hinode captures many more flare events in coming years. Flux emergence is one of key magnetic activities in the photosphere to quickly develop magnetic topology for flare and CME initiation.

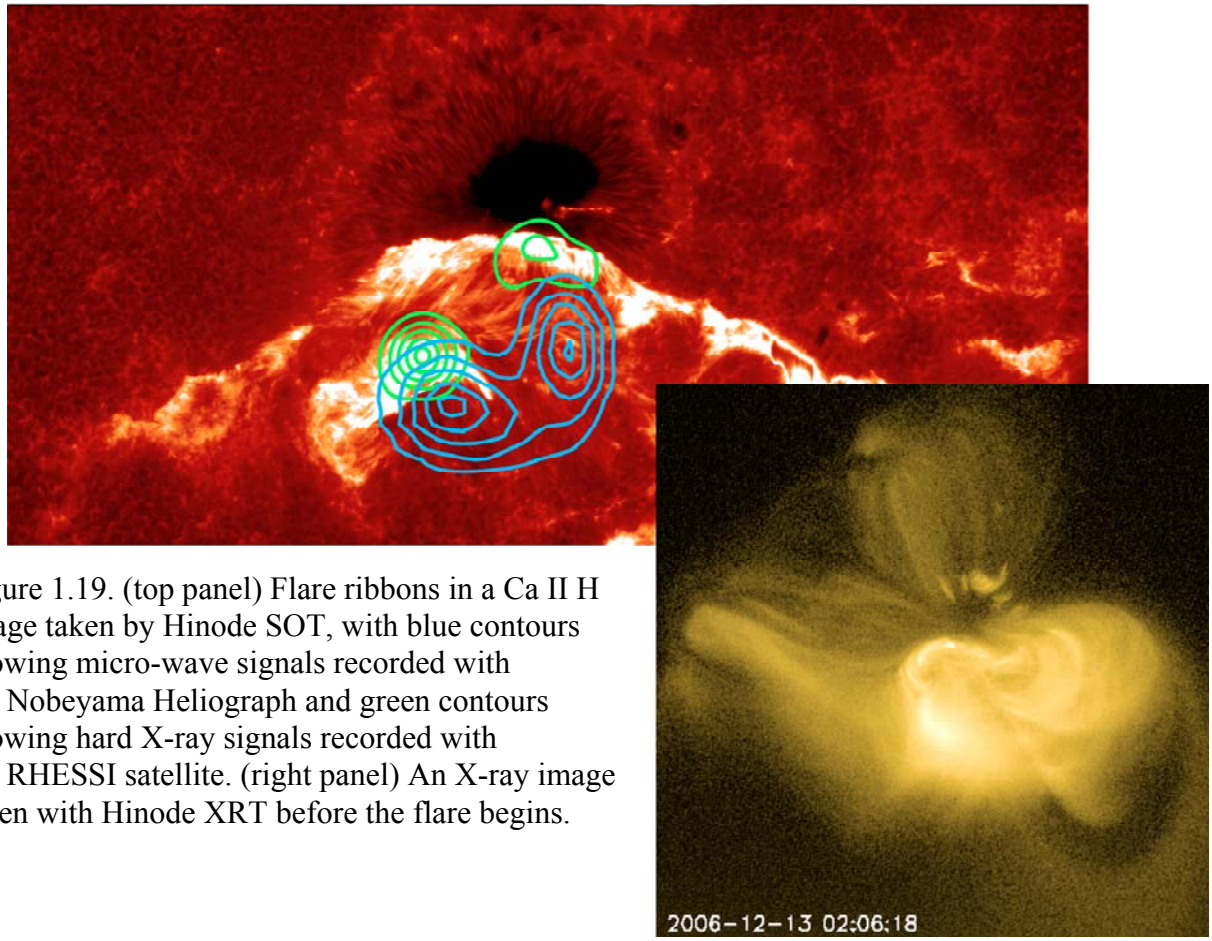

Figure 1.19. (top panel) Flare ribbons in a Ca II H image taken by Hinode SOT, with blue contours showing micro-wave signals recorded with the Nobeyama Heliograph and green contours showing hard X-ray signals recorded with the RHESSI satellite. (right panel) An X-ray image taken with Hinode XRT before the flare begins.

Measurements of magnetic fields in the higher layer, i.e., chromosphere, and mass flows over the entire atmosphere will observationally provide new insights in understanding flare and CME initiation. For example, many flares are related to newly emerging flux, and the higher the complexity and shear of the field the greater the chance of flares occurring. We do know that there is a 'time lag' from when flux emerges to when there is a response in the corona (e.g. Schmieder et al., 2004). Flux emergence can occur 6 hrs before a flare occurs. In the 13th December 2006 X-flare (Figure 1.19), the increase in coronal turbulence occurred 12 hours before the flare began (Harra et al., 2009) and 16 hours after the helicity injection rate reached a peak (Magara and Tsuneta 2008). Further work studying the detailed response of the

chromosphere and corona to emerging flux has shown that the chromospheric response occurs first (Li et al., 2007). There is also evidence that the corona shows a small increase in flows before flaring begins (Harra et al., 2010). The chromospheric emission shows small brightenings over the complex region of emerging flux. The corona behaves in a completely different way, showing the development of large-scale loops with enhanced outflows at the edges. The linkage between the chromosphere and corona nor the energy transport processes that follow the flux emergence are not understood yet. Theoretical simulations have been carried out to explain flux emergence (e.g. Cheung et al., 2008), but the full connection from below the photosphere to the corona and the linkage with magnetic reconnections in corona and chromosphere is not yet achievable.

Flare initiation studies will be partially performed with Hinode, if Hinode captures many more flare events in coming years. With this in mind, we define the Plan B science goals more specifically. Hinode can provide accurate measurements of vector magnetic fields at the photospheric level, but such maps covering a large area are available only with extremely long interval (several hours or longer). Considering the timescale of emergence of each magnetic flux (5-15 minutes to cross from the photosphere to the corona), much increase of cadence will allow us to capture details of the flux evolution. Enhanced telemetry resource about one order of magnitude larger than Hinode will increase mapping cadence to less than several tens of minutes even for a large field of view (200”x200”) with 0.2” resolution. In addition, measurements of chromospheric magnetic fields can provide the dynamical evolution of emerging flux and nearby pre-existing flux in 3D domain.

There are some signatures of changes in the corona before a CME erupts, e.g., increasing coronal flows (Baker at al., 2009). This indicates that the overlying magnetic fields are changing which reduces the stabilizing forces of the overlying magnetic field. The energy necessary to produce these changes clearly comes from magnetic fields that emerge from below the surface, but the mechanism for transporting this energy to regions above the surface is unclear, including its effect on the moment the CME is triggered. Current indications are that reconnection must be occurring in the lower atmosphere to build up the pre-eruption magnetic structure of a flux rope (Green and Kliem, 2009). But this cannot be presently modeled due to lack of spectral information in the low atmosphere. EUV/FUV spectroscopy covering from the low atmosphere to the corona can reveal the entire picture of mass flows.

1.4.1.3. Fine Magnetic Field Structures in Prominences/Filaments

A typical prominence – filament on the disk – is characterized by chromospheric cooler material (about 10,000 K) suspended at coronal heights, a configuration that can only persist if the magnetic field supports the plasma against the force of gravity. Since major flares and CMEs are sometimes accompanied by an eruption of the prominence, the formation and dynamics of the prominence is also essential to address questions of magnetic energy storage/release for a CME-like explosion.

Hinode SOT observations have revealed that prominences have very complicated geometrical configurations, and they look different in active region and quiet Sun (Figure 1.20); Active-region prominence consists of nearly horizontal threads (Okamoto et al. 2007, Merenda et al. 2007), whereas quiescent prominence has apparent vertical threads (Berger et al. 2008), although magnetic field is supposed to be oriented horizontally. Prominences are also supposed to have helical magnetic configuration to support cool materials in the corona, but there is no direct magnetic field measurements to confirm the helical configuration in prominence.

Direct measurements of magnetic fields in prominences have been required to reveal the overall magnetic field configuration in prominence and how the configuration is developed. Weak magnetic fields in prominences produce polarization signals by so-called Hanle effect and therefore magnetic field orientation can be inferred with sub-arcsec spatial resolution when the polarization profiles of chromospheric lines are measured with the proposed 1.5m telescope (SUVIT). It would be a great progress in understanding the triggers of CMEs and flares, if the magnetic fields can be measured during the eruption of prominences.

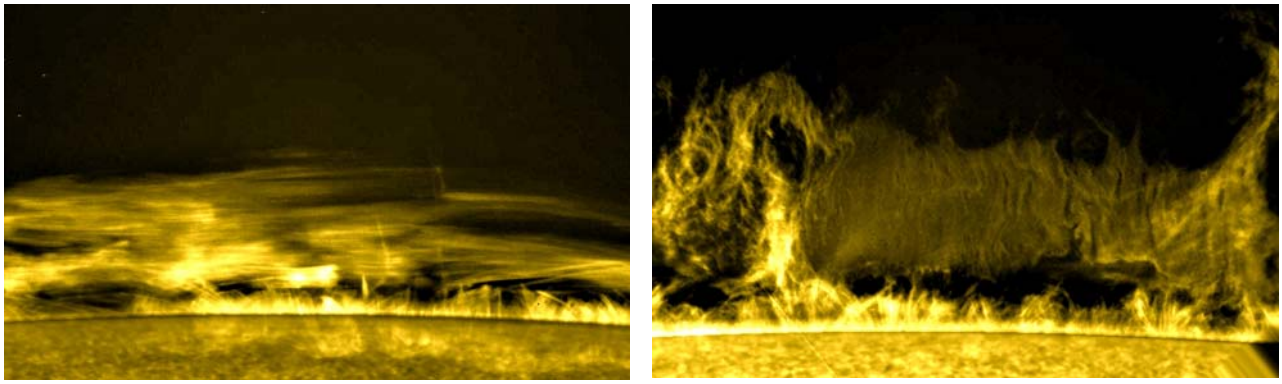

Figure 1.20. Prominences observed in an active region (left) and a quiet region (right) with Hinode. It is important to clarify how the fine structures smaller than 1 arcsec are associated with magnetic field configuration.

1.4.1.4. Solar Flare Forecasting

One of the most important goals of solar physics research is to improve our ability to predict geo-effective solar flares and CMEs. The Solar-C mission has observational capabilities to advance our understanding and prediction capability for space weather, primarily by exploring how small-scale physical processes are related to the initiation of space-weather phenomena.

It is empirically known that the occurrence rate of big solar flares correlates with some extensive quantities representing the properties of magnetic field and flow in flaring active regions. For instance, the probability for big flares to occur within 24 hours exceeds 50% in big active regions, where the extensive magnetic quantity, e.g. unsigned magnetic flux, is larger than some critical value. However, the skill score for forecasting flares is still low, and it is too difficult to predict the onset of solar flares with high reliability (Leka and Barnes 2007, Barnes and Leka 2008). It is due to the fact that the major fraction of flares occurred in moderate active regions, where the extensive quantity is lower than the critical value. The result indicates that the extensive quantities, which can be obtained by the integration over whole active region, cannot provide us sufficient information to forecast solar flares, and also suggests that the occurrence as well as the scale of solar flares is susceptible to the trigger process, which might proceed in much smaller region than the size of active region. Therefore, to identify the critical indications of flux emergence that causes flares and CMEs is crucial for developing flare prediction algorithms. If we can discriminate the small-scale activity triggering solar flares in terms of the unprecedentedly high resolution observation, it would be likely that the predictability of solar flares could be improved and that the Solar-C would greatly contribute the space weather forecast.

1.4.2. Solar Winds

1.4.2.1. Origins of Fast Solar Winds

Coronal holes (CH) are the source of the fast solar wind (Krieger et al. 1973). For polar coronal holes, Hassler et al. (1999) found regions of strong outflow lying at the boundary of magnetic network cells from observations in the λ770A Ne VIII resonance line formed at the base of the corona (T=0.63 MK). Outflows are also seen in the much cooler λ584A (Wilhelm et al., 2000) and λ10830A (Dupree et al., 1996) He I lines. Tu et al. (2005) find that the wind starts flowing between 5 Mm and 20 Mm from the measurement of C IV and Ne VIII, respectively. However, there is still a substantial lack of knowledge on which structures within coronal holes, and what physical mechanisms, are primarily responsible for the wind acceleration. Three candidates have been discussed as the structures responsible for the fast solar wind: plumes, interplumes, and jets (Figure 1.21).

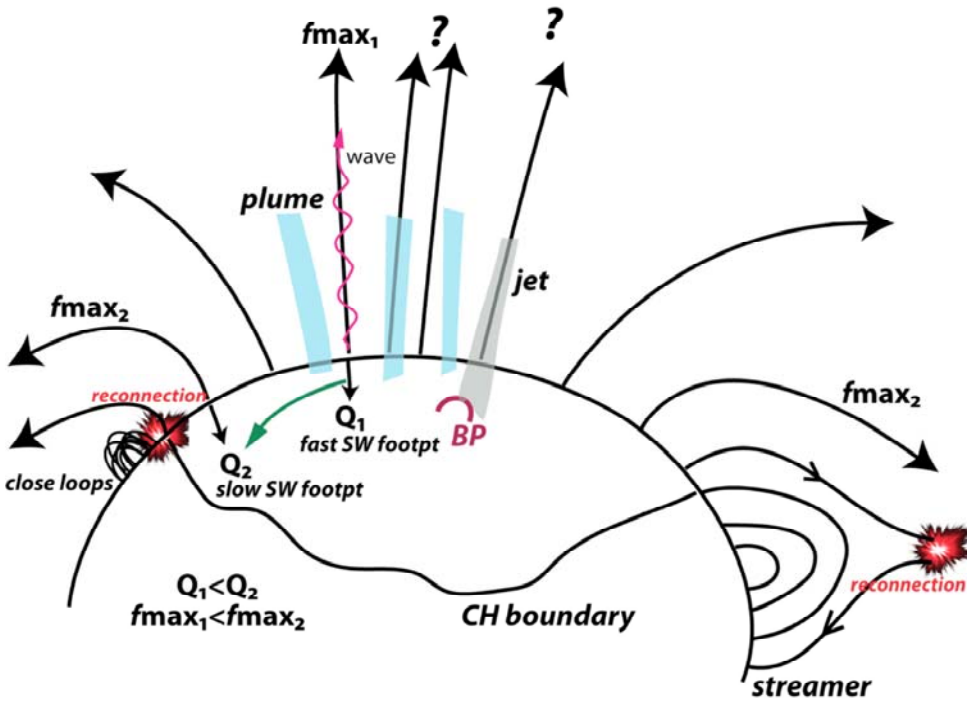

Figure 1.21. Some possible sources of the fast solar wind (plume, interplume, jet) and slow solar wind (coronal hole-steamer boundary, edge of active regions, reconnection between open field lines and close loops, reconnection at streamer stalk).

Being the most prominent feature within CHs, plumes have been and are considered as a strong candidate for the source regions of the fast wind, but theoretical models give opposite indications; Del Zanna et al. (1997) and Casalbuoni et al. (1999) show that the outflow speed in plumes can be larger or smaller than in the ambient depending on the temperature and Alfvén wave flux assumed in the two regions. VUV lines formed around 1 MK allow the study of the plumes roots on the disk where their intensity is enhanced with respect to the background CH emission. In addition to measuring Doppler shift along line of sight, Doppler dimming features seen in, for example, O VI 103.2/O VI 1037A lines allows to determine the radial component of

the plasma outflow velocity from the analysis of off-limb spectra, although some assumption on the geometry of coronal structures is necessary. From SUMER and UVCS combined data, Teriaca et al. (2003) derived the outflow vs. altitude profile in interplumes. However, the result for the plumes is controversial with very different results being present in the literature (Giordano et al. 2000; Gabriel et al. 2003, 2005; Raouafi et al. 2007). Jets are often associated to plums (Raouafi et al. 2008), which may cause different results, because the integration of signals recorded by the 36 to 48 hours' SUMER observations is required to derive reliable results. High throughput performance improved by one order of magnitude from SUMER will allow us to study time variability of outflows at timescale of a few hours. From EUV spectroscopy, plumes are known to be denser and cooler than the surrounding interplume regions (e.g., Wilhelm 2006). Spectral lines are observed to be broader in interplumes (e.g., Wilhelm, 2006; Banerjee et al. 2000) hinting at preferential energy deposition in these structures. Signatures of slow magnetoacoustic waves have also been found in both plumes (DeForest & Gurman 1998, Ofman et al. 1997; 2000) and interplume regions (Banerjee et al. 2000; 2009), and it is important to understand observational link between waves and velocity structures (see also section 1.2). Moreover, the spectroscopic analysis of chemical composition could provide a tool to establish whether plumes or interplume regions contribute significantly to the fast wind by comparing the composition of the different structures on the Sun with in situ data.

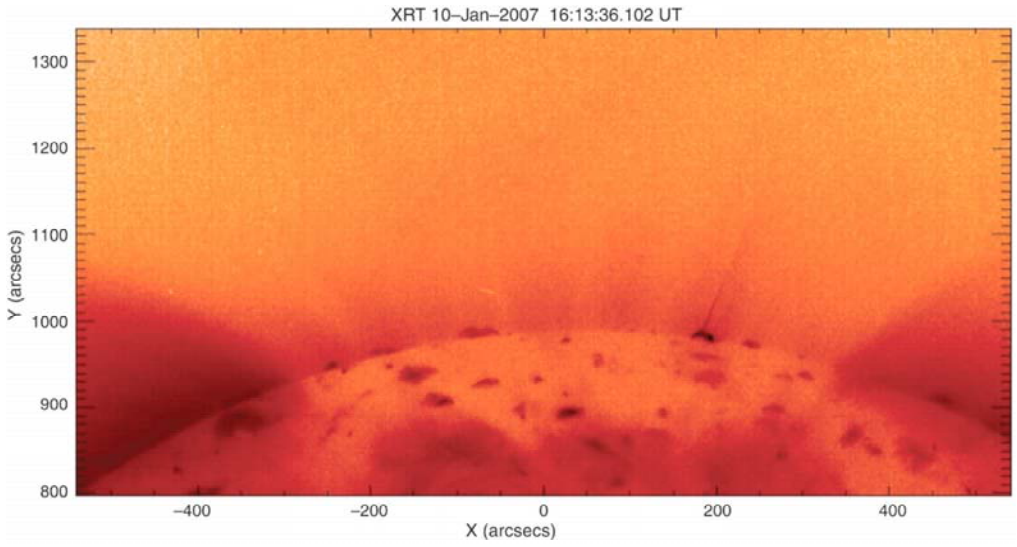

Figure 1.22. Hinode XRT false-color image of the north polar coronal hole. A typical jet is seen in the center of this image (from Cirtain et al. 2007).

The Hinode XRT has revealed a large number of jets occurring within the polar holes (Cirtain et al., 2007, Figure 1.22). Given the high velocities attained during these events (up to 800 km/s), they may be contributors to the wind. The Hinode SOT has revealed wide distribution of strong field patches in the polar regions (Tsuneta et al. 2008, Figure 1.23), by viewing the polar regions at 7 deg inclination periods with 0.3 arcsec spatial resolution. Flux emergence appears into open fields (e.g., coronal holes), resulting in jets (e.g., Shimojo and Tsuneta 2009). The standard model for jets associates the energy source with reconnection in the corona, but detailed chromospheric and transition region diagnostics are currently not available. Current observations also lack the spatial resolution to see the sub-structure of jets. Jets are important targets for close examination because they are the most likely place to observe reconnection and its related sub-structure in the corona. Because of the relatively small scale of jets, a reasonably accurate accounting of the magnetic flux budget, and the energy budget, should be

achievable with high-resolution, high-sensitivity photospheric and chromospheric magnetograms, paired with high-resolution, high-sensitivity, high-cadence coronal imagery. Such studies should enable measurements of the energy storage prior to jet eruption, the rate of energy release, and the rates of helicity transfer. In light of the Hinode observations of coronal jets, it is believed that the jets may contribute a significant amount of mass into the fast solar wind.

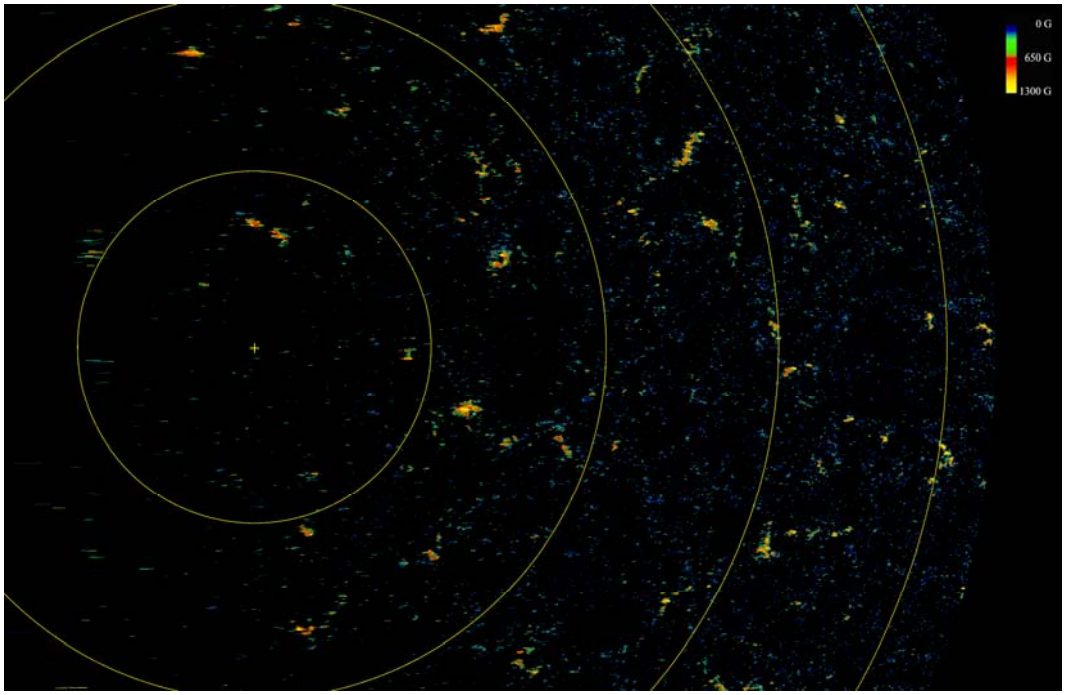

Figure 1.23. Strong patches of kG magnetic fields distribution in the polar region, reveraled with Hinode SOT magnetic field measurements (Tsuneta et al. 2008).

1.4.2.2. Origins of Slow Solar Winds

The source of the slow solar wind is even more difficult to identify than that of the fast solar wind. Sources include coronal holes boundaries, edges of the streamer belt and edges of active regions (Figure 1.21). The proposed UV/EUV spectrometer is capable of measuring relative element abundances in different atmospheric structures that can be related to in-situ measurements from Solar Orbiter and Solar Probe+. The abundances in the slow solar wind are different from in the fast solar wind. Thus, abundance measurements can be used with in-situ measurements to locate the origins of the slow solar wind. The Hinode observations have revealed the persistent flows at the edges of active regions (Figures 1.24, Sakao et al. 2007). These could provide up to 25% of the slow solar wind. Recent STEREO and Wind observations suggest that a considerable fraction of the slow solar wind is transient in nature even at solar minimum – these have small scale-sizes and low magnetic field strength. They seem to be related to coronal source surface sector boundaries (Kilpua et al., 2009) that could be dynamical changes at coronal hole boundaries or edges of helmet streamer belts. The process involved is not fully understood and it is widely debated whether these outflows are caused by waves or reconnection. Certainly the magnetic configurations involved suggest large-scale magnetic reconnection, however there is also some evidence for wave-like behavior of the outflow. The in-situ composition data for these transient slow winds seem consistent with open-field regions,

rather than closed-field regions. The proposed UV/EUV spectrometer can measure abundances throughout the atmosphere and map the differences and determine how the abundances evolve.

The active region upflow speeds derived from spectral line wavelengths vary with spectral lines formed at different temperatures, which implies that the upflows consist of fine scale structures with difference speeds. At present it is impossible to connect these flows with transition region and chromospheric structures, due to the limited wavebands and spatial resolution of Hinode EIS. If we are going to understand how these flows arise, i.e., the source of their energy, and where in the atmosphere they originate, a higher spatial resolution instrument with connectivity to lower temperatures is essential.

To make further progress, it is necessary to sort out properties of the solar wind source regions among a variety of possible source structures. It is important to 'follow' the field lines from the chromosphere, through the transition region, up into the corona by comparing and relating plasma properties such as density, temperature, line width, Doppler shift and elemental abundance, in space and time across the footpoint region of slow wind. At the same time, magnetic field extrapolations are needed to identify preferable location of magnetic reconnections in the transition region and corona and to show the connections to the heliosphere.

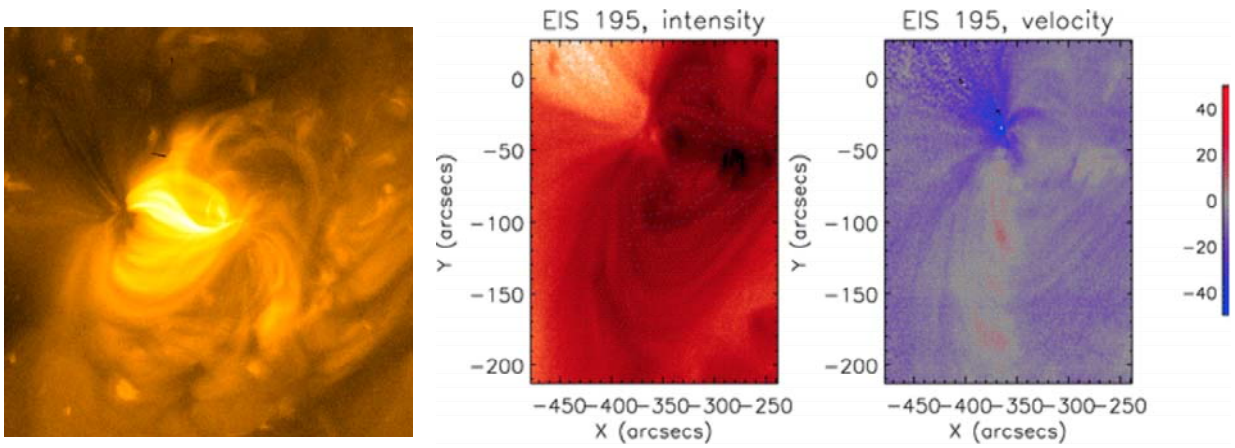

Figure 1.24. Persistent plasma outflows at the edges of action regions, revealed with Hinode observations.

Chapter 2: Solar Ultra-violet Visible and IR Telescope

2.1. Introduction

2.1.1. Solar UV-Visible-IR telescope in SOLAR-C Plan-B

The emergence of magnetic fields, its forcing by convective flows on the solar surface, and its interaction with previously-emerged magnetic flux, give rise to energetic phenomena in the solar atmosphere through magneto-hydrodynamic processes. The Hinode Solar Optical Telescope (SOT) now provides the first high-resolution diagnostics of the solar magnetic field from a space platform, and now allows discovering the processes by which magnetic flux interacts with the convective flows in the lower solar atmosphere, “photosphere”. Furthermore, Hinode and recent ground-based telescopes has provided strong indications that those photospheric dynamics initiate outward propagating waves and dynamic reconnection events that result in acceleration and heating of the plasma accompanied by significant outward energy and mass flux in the upper atmosphere, i.e. “chromosphere” and “corona”. Unfortunately, our knowledge on the magnetism of the solar chromosphere is practically inexistent notwithstanding the qualitative information provided by monochromatic images at various spectral lines sensitive to the chromosphere. Such intensity images do not provide any quantitative information on the temperatures, velocities, and magnetic fields.

In these circumstances, the primary objective of the instrument, Solar Ultra-violet Visible and IR telescope (SUVIT), is to explore dynamical nature of the magnetic solar atmosphere and physical processes responsible for making the dynamics through spectroscopic and polarimetric measurements of physical conditions (e.g. temperatures and velocities) with emphasis on magnetic fields in the chromosphere. Quantitative information on magnetic fields in the place where magnetic energies are transferred and liberated is critically important to expand our knowledge on the magnetized atmosphere although it has been significant challenges in measuring magnetic fields above the photosphere because of lower polarization signals in spectrum lines emanating from the chromosphere.

The observations also demand parallel efforts in advanced data analysis, interpretation, and modeling methods. Fortunately, at present we live in a time where rapid advancement in the analysis and modeling are taking place, and the models describe their synthetic chromosphere/corona with increasing realism (see Appendix A.3 and A.4). These theoretical advances demand new observational constraints. The present concept of SUVIT is structured to provide those specific observational constraints.

2.1.2. Science targets with the instrument

- *Magnetized solar atmospheres: how they are created and evolve.*

Hinode has demonstrated that a space-based telescope has strong benefits in precise spectro-polarimetric observations. It allows studying structures and dynamics in the photosphere, such as formation of strong flux concentration, its interaction with granular convection, and sunspots structures and dynamics associated with strong magneto-convection. The next step is to extend our quantitative knowledge of the solar atmosphere from the photosphere to the chromosphere (Fig. 2.1). In the chromosphere, magnetic pressure becomes comparable with or dominant over gas pressure (i.e. plasma beta≤ 1) while gas pressure is dominating in the photosphere. This is why measurements of magnetic fields in the atmospheric layer higher than the photosphere is demanded, which also helps to infer magnetic field configuration in coronae through magnetic field extrapolation such as potential field and force-free field modeling.

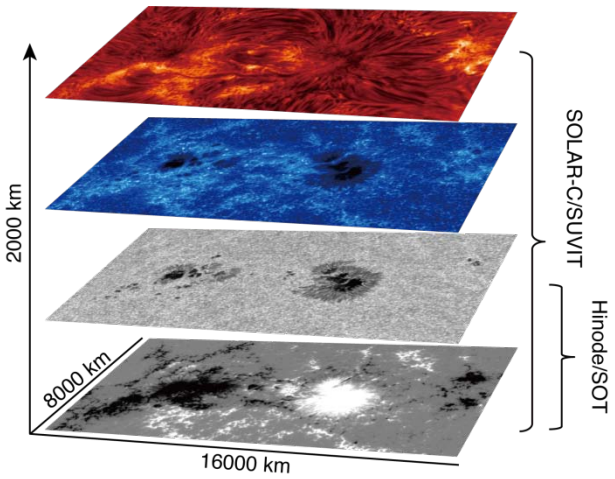

Fig. 2.1. SUVIT on SOLAR-C extends our quantitative knowledge on the magnetized solar atmosphere from the photosphere to the chromosphere.

In the quiet Sun, granular-scale horizontal field emergences are ubiquitously found in the photosphere, which were extensively studied using Hinode (Lites et al. 2008, Centeno et al. 2007, Orozco Suarez et al. 2007, Ishikawa et al. 2008). An outstanding question is how much fraction of magnetic fields keep expanding into the upper atmospheres, and how they are reconfigured to create canopy structures overlying the quiet photosphere. The observations are truly essential to know eventual history of emergent magnetic fields. High-resolution observations with Hinode and recent ground-based telescope showed super-sonic upflows and downflows ubiquitously seen at the photospheric layer. Some of them are associated with formation of strong flux tubes (e.g. Nagata et al. 2008), and some of them are associated with cancellation or disappearance of bipolar magnetic flux (e.g. Kubo et al. 2010). Driving mechanisms and ultimate consequence of the flows could be physically interpreted with SUVIT owing to combined measurements of plasma properties and magnetic fields at the multiple atmospheric layers.

A solar prominence is also an important target with SUVIT because it carries significant amount of magnetic flux and masses in coronal mass ejections (CME). In spite of the importance, its magnetic field configuration is poorly known. This is primarily because of lack of observational information on magnetic field configuration in the prominence. Hinode SOT observations revealed that structures in prominences are very complicated in the spatial scale smaller than 1000 km (Okamoto et al. 2007,

Berger et al. 2008). It is essential to understand how the fine scale structures are created and how cool materials are provided and sustained in the upper atmosphere. There are some observations of field emergence at the photospheric layer with Hinode (Okamoto et al. 2009, Lites et al. 2010), but long-term observations of the photospheric and chromospheric fields with SUVIT provide an entirely new view on formation and evolution processes of the prominences.

- *Small-scale dynamic phenomena responsible for the energy transfer.*

One of the science goals of the Solar-C plan-B is to elucidate the energy and mass transfer from the photosphere upward through the chromosphere to the corona. Although the chromosphere occupies only a very thin region in physical dimensions relative to the structure of the overlying corona, it is the region where most of the non-radiative heating takes place, and it forms the conduit for the upward flux of mass and energy.

Significant progress has already been realized in understanding the chromosphere (Fig. 2.2). Above the very quiet photospheric internetwork where the magnetic field is weakest, the chromosphere is dominated by largely acoustic shocks initiated in the photosphere and below by action of the solar convection and the p-mode oscillations (Carlsson and Stein 1997, Rutten 2007). Recent observations from Hinode and other instruments have suggested that the network fields, interacting with convection, energize and structure the chromosphere. In particular, the “type II spicules” now appear to be a candidate for channeling the upward movement of mass and energy toward the corona (De Pontieu et al. 2011). Active phenomena in the chromosphere increase within active regions, where outward propagating jets, such as chromospheric micro-jets in penumbrae (Katsukawa et al. 2007), Ellerman bombs (Georgoulis et al. 2002) and chromospheric jets (Shibata et al. 2007) around sunspots, occur frequently. In most of the active phenomena in the chromosphere, magnetic reconnection is suggested to play an essential role to energize the outward flow. But there have been no direct measurements of magnetic field configuration around the reconnection site. High-resolution observations from SUVIT would provide observations of the chromospheric magnetic field in and around these active chromospheric phenomena, and also provide the accompanying thermodynamic conditions therein. It is demanded to get knowledge on what the condition is to trigger the magnetic reconnection and how fast it dissipates magnetic energies.

Energy transfer between the atmospheric layers takes place through not only radiation and flows, but also propagation of magneto-hydrodynamic (MHD) waves. Though it has been difficult to catch signatures of waves in observational data, transverse oscillation of chromospheric structures are now ubiquitously discovered in imaging observations with Hinode thanks to its high and stable image quality (Okamoto et al. 2007, De Pontieu et al. 2007). In the photosphere signatures of propagation and reflection of MHD waves are found in spectro-polarimetric observations (Fujimura and Tsuneta 2009). Quantitative measurements of fluctuations in magnetic fields and thermodynamic parameters are essential to understand how and where the waves are generated, reflected, and dissipated. Especially it is important to know nature of waves by identifying MHD wave modes and mode conversion for subsequent shock formation, resulting in plasma heating.

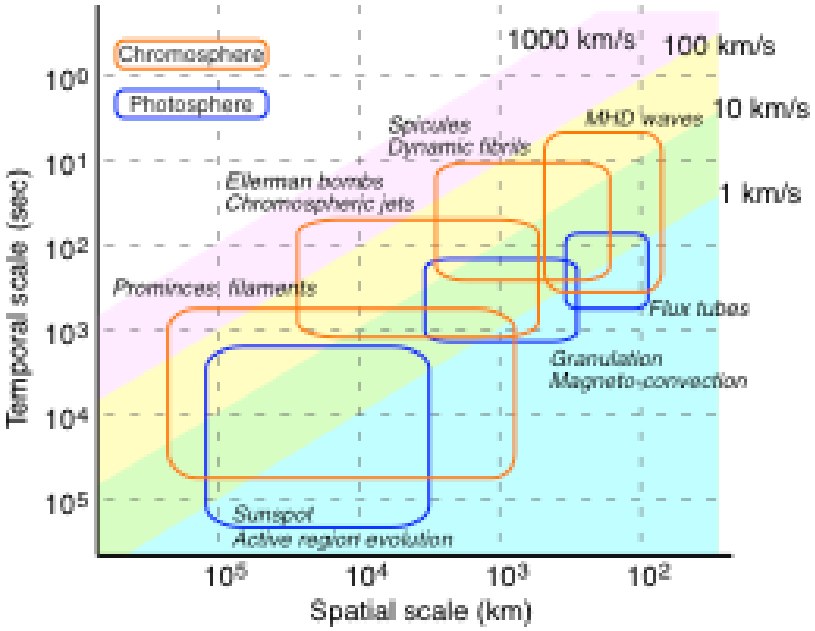

Fig. 2.2. Structures and dynamics seen in the photosphere and the chromosphere. In the chromosphere, lots of dynamics are taking place in the broad spatial and temporal range. Velocities of waves and flows are typically 10 – 100 km/s, one order of magnitude faster than typical velocities seen in the photosphere.

2.2. Basic requirements to the instrument

The science targets described above leads to basic requirements to the instrument as summarized below:

- *Polarimetric sensitivity and accuracy*

The polarimetric sensitivity in Hinode/SOT and existing ground–based telescope is typically ~10^{-3}, which is enough to get polarization signals with photospheric lines but marginal to detect the polarization signals in the chromospheric lines. For detailed measurements of the circular polarized profiles induced by the longitudinal Zeeman effect and linear polarized profiles induced by the Zeeman and Hanle effect in the field strength down to 10 gauss, we need the sensitivity of at least 10^{-4} (see A.2 and Fig. 2.23), which means we have to collect at least 10^8 photons when the sensitivity is limited with photon noise. In order to collect the number of photons with 0.2” spatial sampling and 10 to 20 sec temporal sampling, we need an aperture diameter larger than 1 m (see Fig. 2.3). It is necessary to have a strategy to minimize instrumental polarization and to remove residual polarization cross-talk with pre-flight and in-flight calibration to achieve high polarimetric accuracy.

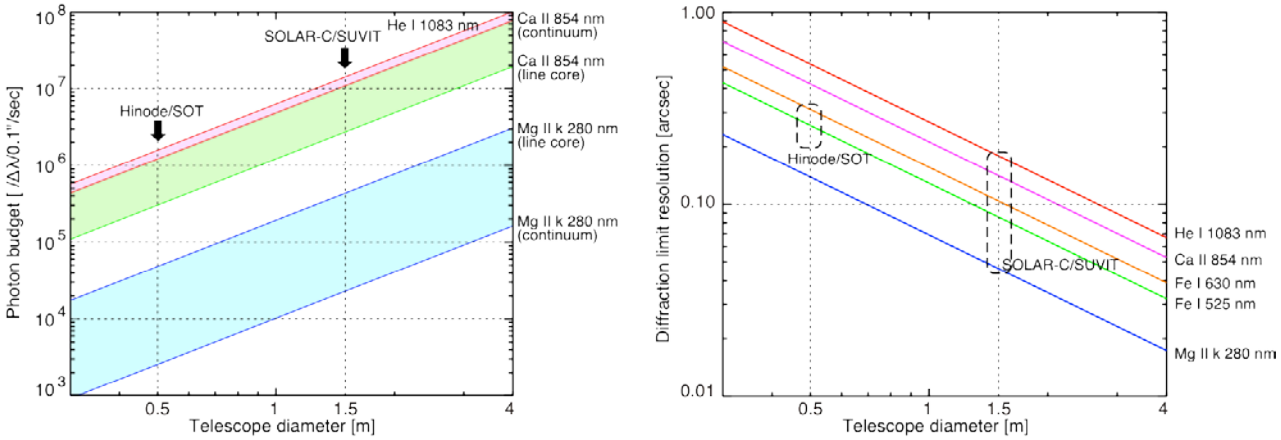

Fig. 2.3. Collectable number of photons as a function of the telescope diameter at major chromospheric lines (*right*). It is assumed that the overall efficiency of the instrument is 0.1 with the spatial sampling of 0.1", the temporal sampling of 1 sec, and the wavelength sampling of $\Delta\lambda/\lambda=2\text{x}10^5$. Diffraction-limited spatial resolution as a function of the telescope diameter (*left*).

- *Spatial resolution*

In order to resolve the structures in the chromospheres such as spicules and fibrils, whose spatial scale is smaller than 0.2", and also to detect small amplitudes of magneto-hydrodynamic waves and changes of magnetic fields associated with magnetic reconnection taking place inside the chromospheric structures, we need 0.1" resolution at the shortest wavelength (Fig. 2.2) and diffraction-limited resolution in the wavelength range longer than visible lights (0.18" at 1.1 μm in the case of φ 1.5 m, Fig. 2.3). In order to collect plenty number of photons required for the polarimetric sensitivity of 10^{-4}, we might have to mitigate the spatial sampling while keeping spatial sampling of 0.2" to 0.3" required to dissolve the elemental chromospheric structures.

- *Spectrum lines*

The He I spectrum line at 10830 Å provides the best magnetic field diagnostic by joint action of the Hanle and Zeeman effect with less affected by atmospheric stratification in the photosphere and lower chromosphere. The Ca II line at 8542 Å is the second prioritized one for magnetic field diagnostics because it has good sensitivity to the Zeeman effect in a wide range of magnetic scenarios. Simultaneous observations of a companion line, He I D3 at 5876 Å for He I 10830 Å and Ca II at 8498 Å for Ca II 8542 Å, are optional to help robustness of diagnostics. Simultaneous polarimetric measurements of a photospheric line are also important for identifying energy sources in the photosphere. There are photospheric lines available near the chromospheric lines, Fe I 8538 Å in the Ca II 8542 Å window and Si I 10827 Å in the He I 10830 Å window.

Mg II h and k lines at around 2800 Å are the best line to capture temperatures and velocities of fibril structures in the upper chromosphere because of higher opacity than Ca II lines. Because the lines are not accessible in a ground-based observation, they can be powerful tools for the diagnostics of the high atmosphere with SUVIT. See 2.3 for more details on selection of the spectral lines.

- *Temporal resolution*

We've realized ubiquitous occurrence of plasma ejection (i.e. jets) in the chromosphere and MHD waves pervading there. It is critical to resolve transit of jets and waves along and across the chromospheric structures (Fig. 2.2). The time scale of the dynamic phenomena regulated by magnetic fields is typically scaled with Alfven transit time, and is shorter than a few seconds when the Alfven velocity is 100 km/s and the spatial scale of 200 km (corresponding to 0.3 arcsec). In order to collect plenty number of photons required for the polarimetric sensitivity of 10^{-4}, we may have to mitigate the temporal sampling while keeping resolution of 20 sec (spatial scale of 200 km divided by the sound speed of 10 km/s) required to dissolve the acoustic travel time across the elemental structures.

- *Field-of-view*

When we use a 4K x 4K format with 0.05" sampling (critical sampling for the 0.1" resolution) on a detector, a field-of-view (FOV) becomes 200" x 200", which compromise most of medium-sized active regions. In force-free extrapolation of coronal magnetic fields, the FOV provides good coverage to reconstruct complex magnetic configuration at the core of a flare-productive active region though it is not enough to cover entire magnetic connectivity around the active region.

Simultaneous areal coverage in spectroscopy is also desired to track rapid chromospheric dynamics. This can be achieved by utilizing a filtergraph observation simultaneous with the spectrograph requiring slit scanning across the FOV. When the duration of the plasma ejection is 3 minutes with a velocity of 100 km/s, the plasma travels 30,000 km corresponding to 40 arcsec, which is the minimum requirement of the FOV to the narrow-band fieltergraph for imaging-spectroscopic observations.

- *Spectral resolution*

In the detailed spectro-polarimetric observation of the chromospheric lines, the minimum spectral resolution required to resolve a thermal widths of chromospheric lines is $\lambda/\Delta\lambda > 100{,}000$ corresponding to 3 km/s in a Doppler shift. In order to observe spectrum lines emanated from the photosphere, $\lambda/\Delta\lambda > 200{,}000$ corresponding to a Doppler shift of 1.5km/s is required.

2.3. Spectral lines compilation

The main properties of candidate chromospheric lines to be observed with SUVIT can be found in Table 2.1. The compilation includes spectral lines in the near-UV, visible, and near-infrared wavelength range. Several criteria have been taken into account to make the line list: they have to be formed within the chromosphere to allow the diagnosis of low β plasma; the lines should show enough sensitivity to plasma temperatures, velocities, and magnetic field vectors; and the line profiles should be interpreted through radiative transfer calculations.

Table 2.1. Candidates of chromospheric lines for SOLAR-C.

Spectral line	1.2λ/D [arcsec]	Photon budget [/Dl/0.1"□/sec]		Response height [km]		Zeeman effect			Hanle effect
		Continuum	Center	Te	V	geff	Blong [G]	Btrans [G]	
Mg II k 2796 Å	0.046	$2.5x10^4$	$2.6x10^5$	~1300	~1400	1.17	85	2100	X
Mg II h 2803 Å	0.046	$2.8x10^4$	$2.2x10^5$	~1200	~1300	1.33	73	1800	-
Ca II K 3933 Å	0.065	$5.5x10^5$	$2.9x10^5$	~1000	~1200	1.17	62	1500	X
Ca II H 3968 Å	0.065	$6.4x10^5$	$3.0x10^5$	~900	~1100	1.33	51	1200	-
H I β 4861 Å	0.080	$1.1x10^7$	$1.8x10^6$	~1500	~1000	1.00	16	1200	X
Mg I b3 5167 Å	0.085	$1.3x10^7$	$1.3x10^6$	~500	~600	2.00	3.7	220	X
Mg I b2 5172 Å	0.085	$1.3x10^7$	$1.0x10^6$	~500	~600	1.75	6.5	250	X
Mg I b1 5183 Å	0.086	$1.3x10^7$	$9.2x10^5$	~500	~600	1.25	9.6	360	X
Na I D2 5890 Å	0.097	$1.5x10^7$	$7.2x10^5$	~400	~600	1.17	4.7	290	X
Na I D1 5896 Å	0.097	$1.5x10^7$	$8.4x10^5$	~400	~500	1.33	3.4	230	-
H I α 6563 Å	0.108	$1.5x10^7$	$2.8x10^6$	~1500	~1300	1.00	9.7	680	X
Ca II 8498 Å	0.140	$1.1x10^7$	$3.3x10^6$	~700	~1000	1.07	6.3	300	X
Ca II 8542 Å	0.141	$1.1x10^7$	$2.1x10^6$	~800	~1200	1.10	6.7	340	X
Ca II 8662 Å	0.143	$1.1x10^7$	$2.1x10^6$	~700	~1100	0.83	8.4	430	X
He I 10830 Å (QS)	0.179	$1.8x10^7$	$1.7x10^7$	~1800	~1800	1.42	18	380	X
He I 10830 Å (AR)	0.179	$1.8x10^7$	$1.5x10^7$	~1800	~1800	1.42	9.3	270	X

The list contains the following information (from left to right):

1) Element and central wavelength (λ) of the transition. QS and AR stand for quiet sun and active region scenarios for the He I 10830 Å line.
2) Spatial resolution for each spectral line at the diffraction limit of a telescope of D=1.5m.
3) Photon budget estimation based upon the preliminary design of Solar-C instrument:
- The telescope consists of 5 mirrors coated with Al+MgF2.
- Spectrograph efficiency of 0.2.
- Detector efficiency of 0.5 at λ<300nm, 0.8 at λ>900nm, and typical CCD 300nm<λ<900nm.
- Spectral resolution of $\lambda/\Delta\lambda=2x10^5$ (corresponding to 1.5km/s), with Δλ the wavelength sampling.
- Spatial sampling of 0.1" per pixel.
- Temporal sampling of 1sec.

4) Geometrical height at which the sensitivity (response) of the spectral line core to temperature and velocity perturbations is dominant. The heights were calculated using the centroid of the corresponding response functions in the FALC atmospheric model (Uitenbroek 2006).
5) Sensitivity limit (1σ) to magnetic fields through the Zeeman effect. The quantities Blong and Btrans stand for the longitudinal and transverse component of the field vector detectable with the sampling shown above (/Dl/0.1"□/sec) and geff is the effective Landé factor.
6) The check boxes indicate that the spectral line is sensitive to magnetic fields through the Hanle effect.

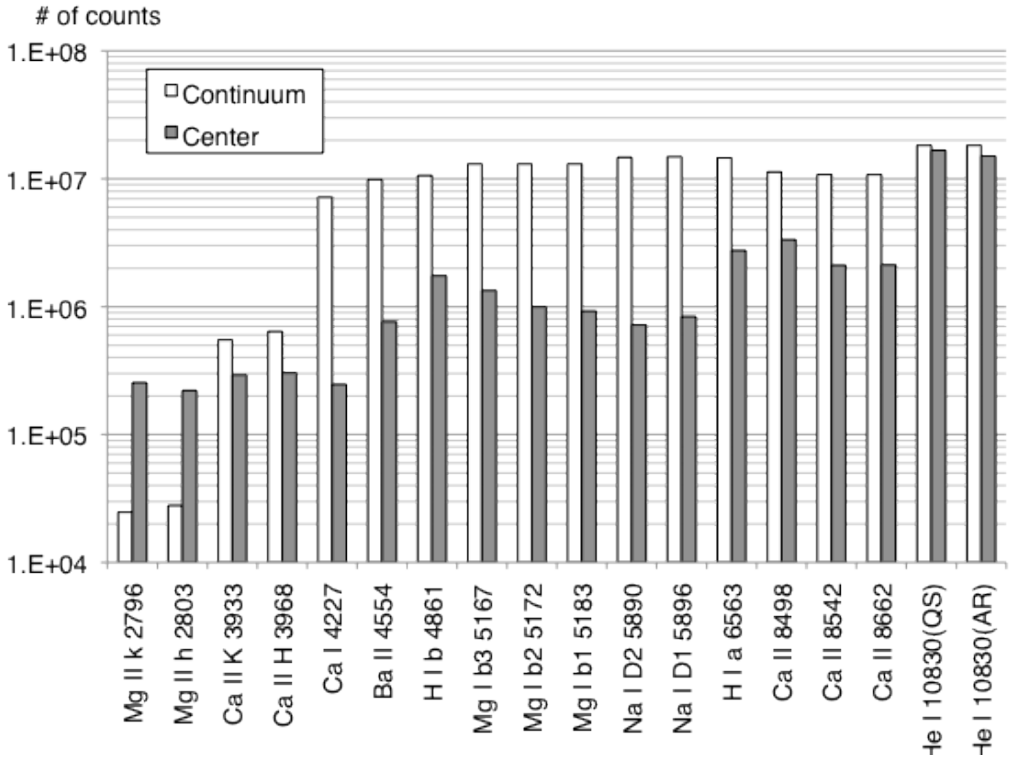

Fig. 2.4. Expected photon budged to be achieved with the 1.5mφ telescope at major chromospheric lines. See Table 2.1 for details.

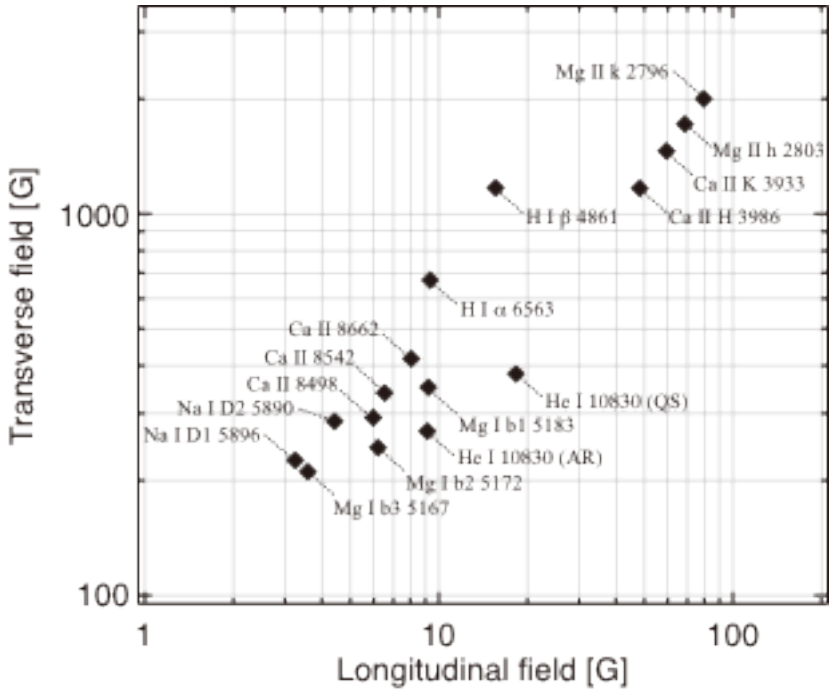

Fig. 2.5. Sensitivity of the spectral lines listed in Table 2.1 to magnetic fields through the Zeeman effect. The lower field strength means higher sensitivity.

2.3.1. Spectral lines for diagnostics of chromospheric magnetic fields

The sensitivity limit for magnetic field diagnosis through the Zeeman effect can be found in Table 2.1 and Fig. 2.5. The Na I D and Mg I b lines show good sensitivity to magnetic fields through the Zeeman effect. However, these two lines are formed low in the solar atmosphere (400 - 600 km). Therefore, they are not appropriate to diagnose the magnetic properties of the true chromospheric plasma. By contrast, the Mg II k/h and Ca II K/H lines form high in the chromosphere but their sensitivity to magnetic fields through the Zeeman effect is limited because of the short wavelengths.

The He I 10830 Å line has good sensitivity to the Zeeman effect in both, active and quiet Sun regions, although the sensitivity tends to diminish in the quiet Sun because the residual intensity decreases, i.e., the spectral line shape becomes shallow. In addition, the interpretation of the He I 10830 Å triplet is relatively easy because it is formed within a thin slab in the atmosphere. Hence, the line formation is less affected by the thermal stratification of the photosphere and lower chromosphere. Moreover, the He I 10830 Å triplet can be used for Hanle effect diagnostics. Recently, theoretical tools to model the joint action of the Zeeman and Hanle effect in the He I 10830 Å triplet have been developed satisfactorily, such that it is very powerful for magnetic field diagnostics of chromospheric and coronal structures (e.g., forward modeling and inversion code HAZEL developed by Asensio Ramos, Trujillo Bueno & Landi Degl'Innocenti 2008, see Appendix A.3.2). The longitudinal Zeeman effect at the He I 10830 Å line has a sensitivity down to 10 to 20 gauss with 0.1" spatial sampling and one second integration. We can measure transverse fields down to 0.1-100 gauss through the Hanle effect when we perform deep integration (e.g. 0.2" spatial sampling and 20 sec integration).

Table 2.2. Sensitivities (1σ) to magnetic fields at He I 10830 Å and Ca II 8542 Å.

		0.1 arcsec sampling 1 sec integration	0.2 arcsec sampling 20 sec integration
He I 10830 Å (QS)	Blong	~20 gauss	~2 gauss
	Btrans	~380 gauss (Zeeman)	~130 gauss (Zeeman) 0.1 – 100 gauss (Hanle)
He I 10830 Å (AR)	Blong	~10 gauss	~1 gauss
	Btrans	~270 gauss (Zeeman)	~90 gauss (Zeeman) 0.1 – 100 gauss (Hanle)
Ca II 8542 Å	Blong	~7 gauss	~0.8 gauss
	Btrans	~340 gauss (Zeeman)	~ 110 gauss (Zeeman)

(*) Here we assume the same instrument throughput and wavelength sampling used in Table 2.1.

The Ca II infrared triplet at about 850 nm is the second prioritized line for magnetic field diagnostics in the SUVIT on SOLAR-C. It shows good magnetic sensitivity in a wide range of magnetic scenarios, including quiet regions, which potentially remedies the weakness of the He I 10830 Å line. The longitudinal Zeeman effect especially has a good sensitivity at the Ca II 8542 Å line, and we can measure magnetic fields weaker than 10 gauss with 0.1" spatial sampling and one second integration. Of especial interest is that through the Hanle effect the linear polarization of this line is sensitive to the orientation of the magnetic field in the upper chromosphere of the quiet Sun (Manso

Sainz and Trujillo Bueno 2010) though the polarization amplitude due to the Hanle effect is relatively small (order of 10^{-4}).

In Table 2.2 are summarized the sensitivities of the spectrum lines above mentioned to magnetic fields through the Zeeman and Hanle effects.

2.3.2. Spectral lines for diagnostics of chromospheric dynamics

The chromosphere is pervaded by fast moving plasma structures. The measure of the dynamic properties of such structures requires not only spectral lines with great sensitivity to temperature variations at certain wavelengths but also short integration times. Since such observations are done typically with filter instruments with limited spectral bandwidths little contamination from nearby wavelengths is also desired. In this sense, the Mg II k/h spectral lines at around 2800 Å are suitable for the SUVIT in SOLAR-C. Their sensitivity to temperature variations is great in the upper chrmosphere because the opacity of these lines is very large at the line core. High temperature sensitivity lines also allow investigating heating processes in the chromosphere. Although the low photon budget at the spectral range of the Mg II lines is a limiting factor for the polarimetric measurement (Table 2.1 and Fig. 2.4), it is well enough to do high cadence spectroscopic observation (without polarimetry) with exposure times shorter than 0.1 sec.

Other spectral lines like the Ca II infrared triplet at about 850 nm and Ca II H and K lines are good candidates for tracking the dynamics of the various chromospheric events, by analyzing observed line profiles along with cloud modeling and/or forward modeling of the lines obtained from numerical simulation of the chromosphere (see Appendix A.3.1 and A.4).

2.4. Configuration of the instrument

A basic concept of the optical design of SUVIT on SOLAR-C is to use a similar configuration with the Solar Optical Telescope (SOT) on HINODE, which allows us to make use of the technical heritage that the Japanese solar physics group developed in HINODE/SOT (Tsuneta et al. 2008, Suematsu et al. 2008). A major difference is to expand the diameter of the aperture from 0.5 m to 1.5 m, which is aiming to collect one order of magnitude more photons than HINODE/SOT as well as angular resolution better than 0.1 arcsec. This is essential to achieve the high polarimetric sensitivity for chromospheric diagnostics. SUVIT consists of the telescope and focal plane instruments. The focal plane instruments are installed into two packages:

1) Spectrograph package
   It consists of an Echelle grating spectrograph for spectro-polarimetric observations and a correlation tracker for the image stabilization system.

2) Imager package
   It consists of a broadband filtergraph utilizing interference filters for monochromatic imaging observations and a narrowband filtergraph utilizing a tunable narrowband filter for imaging spectrograph allowing to make Dopplergrams and magnetograms.

The combination of the multiple instruments enables to cover wide variety of scientific targets. The optical block diagram of the instruments is shown in Fig. 2.6. The telescope collects incident lights and feeds into the focal plane packages. The tip-tilt mirror in the telescope is driven to remove attitude jitter of the spacecraft using signals of image displacements detected with the correlation tracker in the spectrograph package. Polarization modulators are to be installed in each focal plane package while polarization calibrator is possibly implemented in the telescope. Preliminary parameters of pixel scales and typical exposures are summarized in Table 2.3. Table 2.4 shows possible choices of the spectrum lines at each focal plane instrument. The combination of the spectrum lines provides the spectrum diagnostics completely covering from the photosphere through the middle to the upper chromosphere.

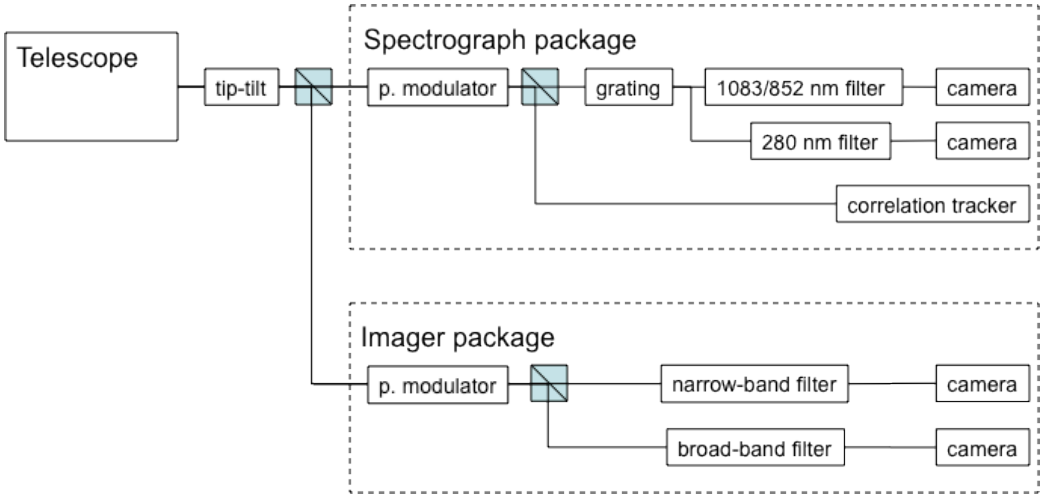

Fig. 2.6. Optical block diagram of the focal plane instruments.

Table 2.3. Configuration of the focal plane instruments.

	FOV	Pix scale	Exp.	Note
Correlation tracker (CT)	10”x10”	0.2”	< $2x10^{-3}$ sec	faster readout than 5kHz. 50x50 format
Spectro-polarimeter (SP)	184”×184”	0.09”	~1 sec	2 pix sampling of 0.18”res 2K pix along slit, S/N~10^3.
		0.18”	>10 sec	2x2 pix binning to reach S/N~10^4.
Broadband filtergraph (BF)	164”×164”	0.04”	<0.1 sec	2.5 pix sampling of 0.1” res 4K×4K detector
Narrowband filtergraph (NF)	205”×205”(1) 120”x120”(2)	0.05”	<1 sec	2 pix sampling of 0.1” res 4K×4K or 2Kx2K detector

(1) The optical configuration allows us to cover the FOV of 200” x 200” if a tunable filter has an aperture big enough to cover the FOV.

(2) The 120” x 120” FOV is available when the diameter of a Lyot filter-type tunable filter has a diamete of 50 mm at the F/40 telecentric focus. In order to accommodate larger FOV coverage in the NF, we need optics to convert magnification in the channel.

Table 2.4: Spectrum lines to be observed in SUVIT on SOLAR-C.

Spectrum lines		SP	BF	NF	Purpose
Mg II k	279 nm	x	x		T and V in the chromosphere
Continuum	TBD		x		Imaging and T in the photosphere
CN band	388 nm		x		Magnetic elements in the photosphere
Ca II K	393 nm		x		Structures in the chromosphere
Mg I b	517 nm			x	V and B in the low chromosphere
Na I D	589 nm			x	V and B in the low chromosphere
Fe I	525 nm or 630 nm			x	V and B in the photosphere
H I α	656 nm			x	Structures in the chromosphere
Ca II	854 nm	x		x	T, V, and B in the chromosphere
He I	1083 nm	x			V and B in the chromosphere

2.5. Optical telescope assembly

2.5.1. Optical design

The optical telescope assembly (OTA) of SUVIT employs the following basic characteristics in the baseline design for exploring its technical feasibilities:

- Aplanatic Gregorian 2 mirror telescope.
- Entrance aperture with the 1.5mφ diameter.
- Heat rejection mirror at the primary focus.
- Axial symmetric optics to give negligible instrumental polarization.
- Afocal interface between the telescope and the focal plane instruments.

The aperture size of the telescope is the most critical item in the concept of the telescope, which is driven by the scientific requirements. We are going to optimize the aperture size down to 1m according to future investigation of technical and scientific feasibilities. Another factor to design the telescope is a limitation of the length of the telescope to fit within a fairing of the launcher (JAXA H-IIA rocket). Based on a study of positional tolerance of the secondary mirror, the distance between the primary mirror (M1) and the secondary (M2) is decided to be 2.8 m as a baseline design. Basic parameters of the optical design of the telescope are summarized in Table 2.5, and its overall configuration is shown in Fig. 2.7. The afocal interface has an advantage to relax the positional tolerance between the telescope and the focal plane instruments. Because the wider wavelength coverage (280 nm to 1.1 μm) than Hinode is required in SUVIT-OTA, the refractive optical design to make a collimated beam in HINODE/SOT is not appropriate. Instead, we are going to realize it using a collimator mirror unit (CMU), which consists of three off-axis aspheric mirrors. The third mirror of the CMU can be used as a tip-tilt mirror for the image stabilization system. Optical performance of the telescope is shown in Fig. 2.8 as is evaluated with spot diagrams at the image plane focused with an ideal lens located at the exit pupil. The RMS spot radius is well within the spot size due to diffraction within the field of 200 arcsec.

There are two field stops in the telescope. One is a heat dump mirror (HDM) at the

focus of M1, which is 45-deg flat mirror with a central hole passing the beam of field of view of 300 arcsec (TBD), and to reflect the unnecessary solar illumination outside of the hole from the side of the telescope. The other is a secondary field stop (2FS) at the Gregorian focus, which is again to reflect the unnecessary solar illumination out of the field of 220x220 arcsec (TBD), which a bit oversizes the area of detectors in the focal plane instruments.

Table 2.5. Basic optical parameters of SUVIT-OTA.

		SOT-OTA (HINODE)	SUVIT-OTA (SOLAR-C)
Entrance pupil (mm)		500	1500
M1 – M2 distance (mm)		1500	2800
M1	outer diameter (mm)	560	1580
	clear aperture (mm)	509	1513
	curv. radius (focal) (mm)	2339.4 (1169.7)	4629.34 (2314.67)
	conic const.	-0.9706	-0.990927
M2	outer diameter (mm)	159	340
	clear aperture (mm)	147	320.5
	curv. radius (focal) (mm)	524.94 (262.47)	835.494 (417.747)
	conic const. (mm)	-0.3996	-0.54815
HDM outer radius (mm)		32.83	43.1
Eff. f-length at 2nd focus (mm)		4527 (F/9.05)	14300 (F/9.54)
CMU focal length (mm)		271	572
Exit pupil diameter (mm)		30	60

(note: The unit is in mm.)

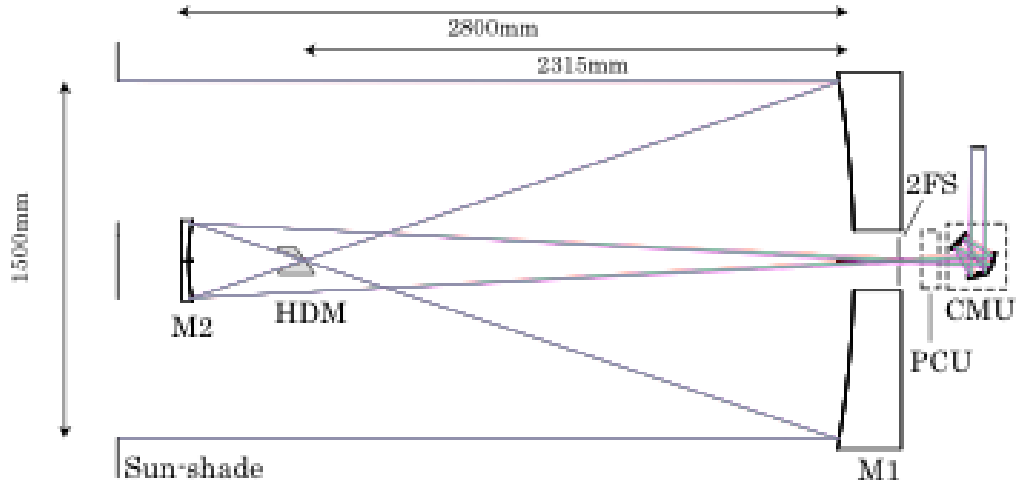

Fig. 2.7. The optical configuration of the telescope assembly of SUVIT. A polarization calibration unit (PCU) can be inserted after the Gregorian focus for calibrating polarization responses of the focal plane instruments.

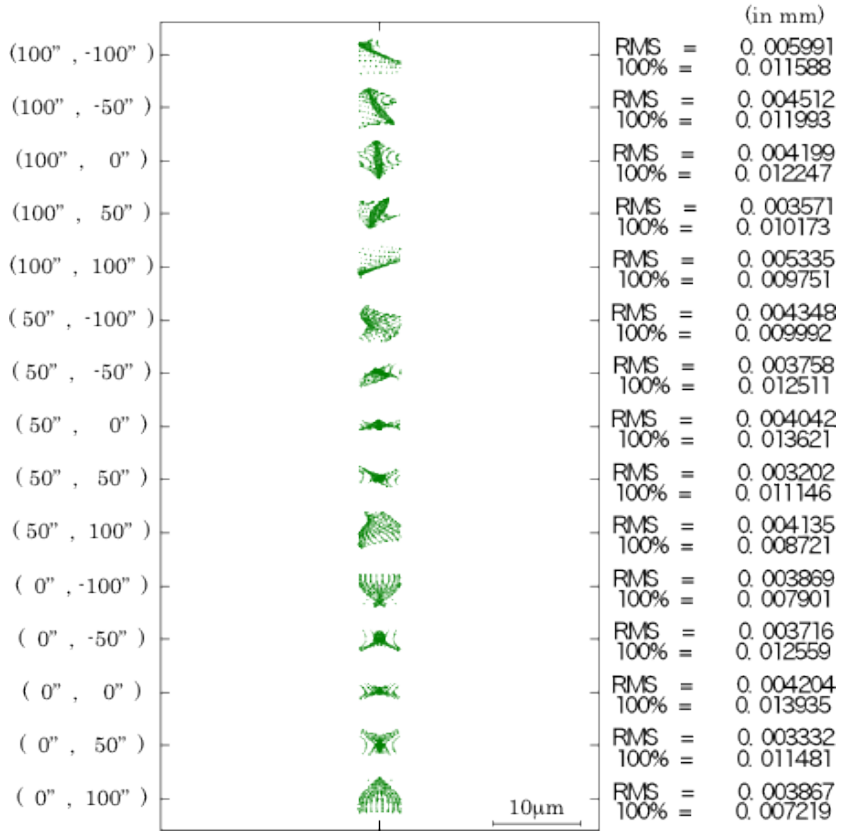

Fig. 2.8. Spot diagrams of the telescope evaluated at the image plane focused with the ideal lens located at the exit pupil. Note that the RMS spot radius due to diffraction is about 6 μm at 500 nm.

2.5.2. Mirror coating and photon budgets

In order to observe the spectrum lines prioritized based on the scientific point of view, it is essential to cover the wavelength range from 280 nm to 1.1μm. A coating design of the mirrors is critical not only to have higher throughputs for precise polarimetric measurements but also to minimize absorption of the solar illumination at the mirrors of the telescope. The silver-based reflective coating used in HINODE/SOT has high reflectivity in the visible and NIR wavelength range. But its reflectivity is very low in the UV wavelengths shorter than 350 nm. Aluminum coating is good alternative in UV although its reflectivity is slightly lower in visible and NIR (Fig. 2.9).

When we apply the aluminum coating to the mirrors in SUVIT-OTA, and if we assume efficiencies of the focal plane instruments, we can estimate the number of photons to be collected by the telescope per a resolution element and per unit time. Fig. 2.10 shows effective areas and efficiencies as a function of the wavelength, in which we assume that the spectrograph or filtergraph efficiency is 0.2, the quantum efficiency of the detector is 0.8 at λ>900nm, 0.5 at λ<300nm, and typical QE of CCD at 300nm<λ<900nm. The instrument has a total efficiency of about 0.1 in the observing wavelength range even when we use the aluminum coating, and the effective area is expected to be 1000 to 2500 cm^2 dependent on the wavelength. Fig. 2.11 shows the number of photons to be achieved with the telescope at major chromospheric lines

where we assume wavelength sampling of $\lambda/\Delta\lambda=2x10^5$, spatial sampling of 0.1" /pixel, and temporal sampling of 1 sec. The polarimetric diagnostics of chromospheric lines require the polarimetric sensitivity of 10^{-4}. This means that we have to collect 10^8 photons in a resolution element if the sensitivity is limited by a photon noise. The figure indicates that we can collect more than 10^6 photons at the line center of each spectrum line with the sampling mentioned above. It appears that we can collect 10^8 photons at the line center of He I 10830 Å and Ca II 8542 Å if we apply 2x2 pixel summing (i.e. 0.2" per pixel) and integrate for 10 to 20 seconds, that is short enough to temporally resolve the dynamics in the chromosphere.

As is shown above, the 1.5mφ aperture and the aluminum coating provides a good photon budget satisfying the scientific requirements at observing spectrum lines. For further improvements of the throughput and for helping a thermal design by minimizing the heat absorption at the mirrors of the telescope (see 2.5.4), it is desirable to develop a mirror coating with higher reflectivity in visible and NIR while keeping the reflectivity at 280 nm.

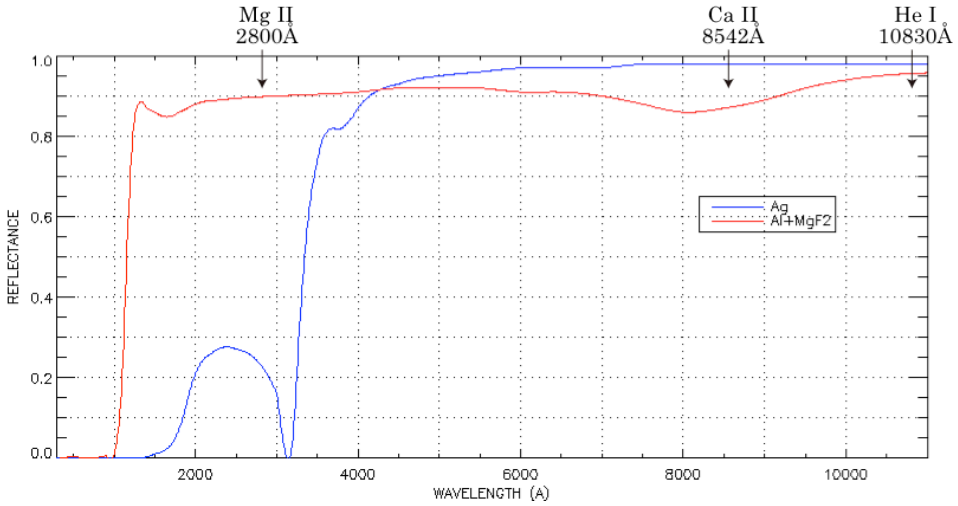

Fig. 2.9. Mirror reflectivities of the silver (Ag) coating and the aluminum (Al) coating with MgF2 over-coating.

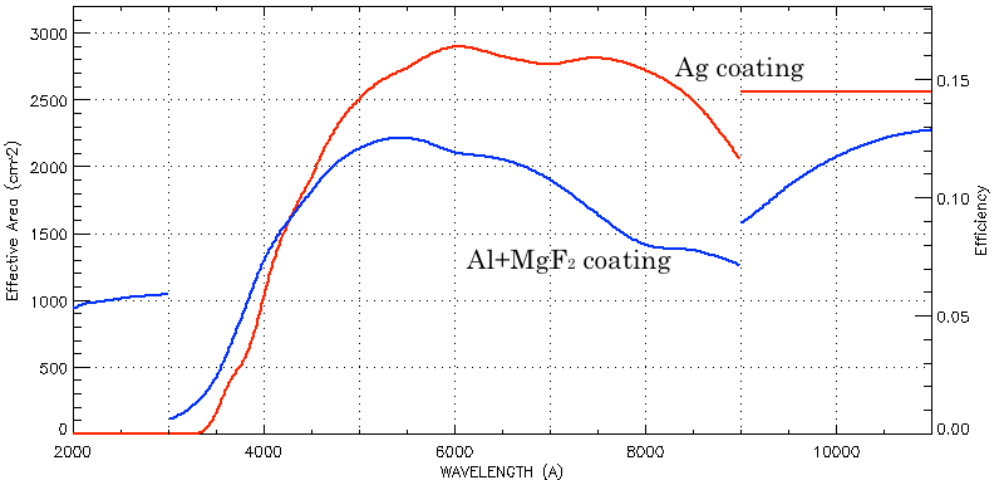

Fig. 2.10. Effective area of the SUVIT with the 1.5 mφ aperture. The telescope consists of 5 mirrors with Ag coating (red line) and Al + MgF2 coating (blue line).

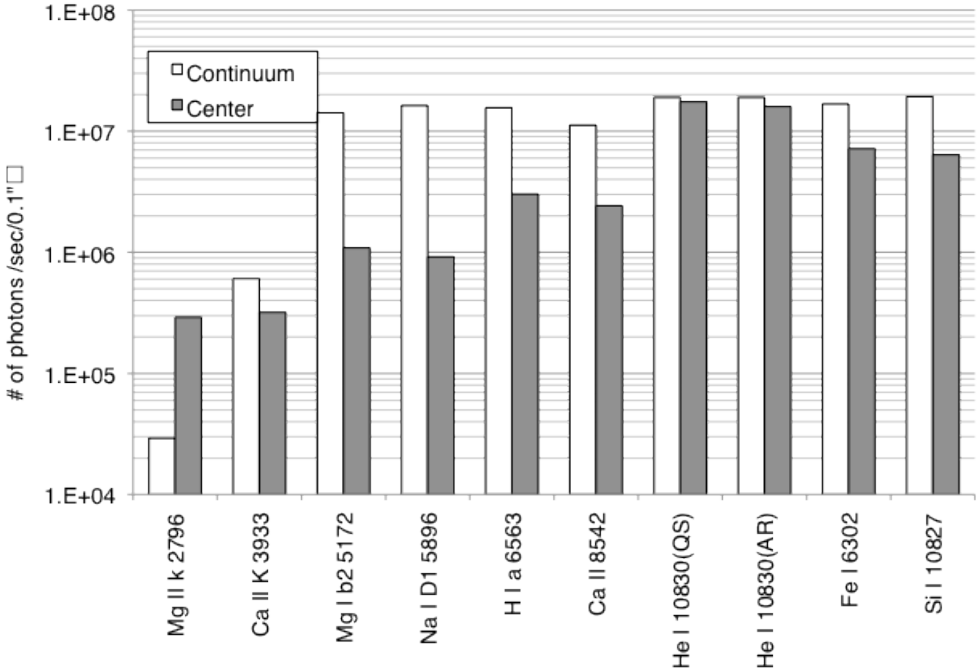

Fig. 2.11. The number of photons to be achieved with the telescope at observing chromospheric and photospheric lines. The gray bars represent the number of photons at the line core of each spectrum line while the white bars are at nearby continuums.

2.5.3. Structure design

The structural design of the SUVIT-OTA basically follows that of Hinode SOT. M1 and M2 for the aplanatic Gregorian are made of light-weighted low expansion material of either ULE or Zerodur. The light-weighting technology of telescope mirrors has been much advanced since Hinode OTA manufacturing era. We expect 90 % mass reduction with an open back mirror structure. Then the M1 of 1.5 m aperture would weigh less than 150 kg. The light-weighted mirrors are crucial not only from tight weight budget of satellite but also from ground testing of telescope optical performance because of small gravitational mirror deformation. The surface figures of the mirrors are ellipsoids as conic constants shown in Table 2.5. Since null correctors for these

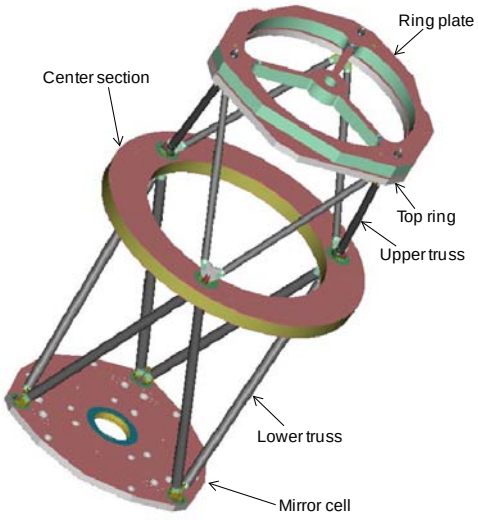

Fig. 2.12. CFRP truss structure of SOT-OTA in HINODE.

aspheric mirrors can contribute to inaccurate surface figures, we should include a M1-M2 combination test in the mirror polishing process. We note that flight-model supporting mechanism for M1 also should be used in the combination test so that the surface error due to the mounting can be corrected in the polishing process. The HDM and the 2FS at the primary and the Gregorian focus are to be made of aluminum alloy and to be coated with a silver coating.

The short Gregorian telescope demands small static mis-alignment tolerances for M1 and M2, on the order of a few tens microns for decenter and despace or several arcsec for tilt, and a micron-order de-space short-term stability on-orbit during observations (Table 2.6). To meet this tolerance, the telescope structure is made of a truss of ultra-low-expansion CFRP (Carbon Fiber Reinforced Plastics) pipes in a Graphite Cyanate matrix, whose CTE is proven to be smaller than 0.1 ppm/K, and the dimensional change due to moisture absorption is about 30 ppm, which is much smaller than conventional epoxy matrix composite pipes (Fig. 2.12). CFRP honeycomb sandwich panels are adhesively bonded with upper and lower truss pipes without any metal junctions to save weight and also to avoid differential CTE, which may cause unexpected thermal distortion.

Table 2.6. Mis-alignment sensitivity of SUVIT-OTA as contrasted with Hinode OTA.

Component		Aberration	SUVIT-OTA[1)] (SOLAR-C)	SOT-OTA[1)] (HINODE)
M1	Despace	Defocus	3.4 μm	8.3 μm
		Spherical	500 μm	2750 μm
	Decenter	Coma	48.5 μm[2)]	165 μm
	Tilt	Coma	4.3 arcsec[3)]	28.8 arcsec
M2	Despace	Defocus	3.3 μm	7.6 μm
		Spherical	500 μm	2800 μm
	Decenter	Coma	48.5 μm[4)]	165 μm
	Tilt	Coma	21 arcsec	111 arcsec

1) The positional and angular sensitivities to the mis-alignment of M1 and M2 are evaluated in the condition that a Strehl ratio is reduced to 0.8 from 1.0 at 633 nm (He-Ne laser) at the field center.
2) The coma aberration can be compensated by M2 tilt of 0.189°.
3) The coma aberration can be compensated by M2 tilt of 0.168°.
4) The coma aberration can be compensated by M2 tilt of 0.20°.

Mounting of M1 is one of the most critical parts in SUVIT-OTA. The primary mirror is supported by three stress-free mounting mechanisms seated on the CFRP bottom panel, interfaced with three superinvar pads bonded on the side of the mirror (Fig. 2.13). The pad interface of the mounting mechanism provides a kinematic mount for M1. The pad interface thus avoids stresses to the mirror resulting from dimensional errors in machining or temperature change. In order to make it sure, the mounting mechanisms are to be used in the wavefront error measurements of M1 and M2 as noted above. The only significant surface error of the primary mirror is caused by the difference of CTE between the superinvar pads and the ULE, which constrains the best-performance temperature range of the primary mirror to be between -15 to 55℃(TBD).

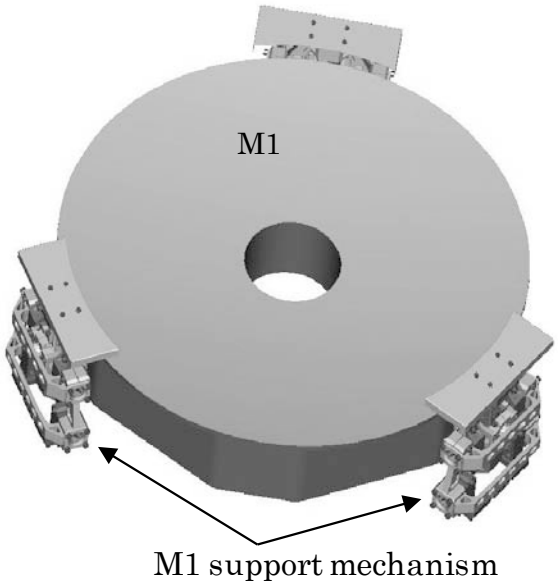

Fig. 2.13. Hinode OTA M1 and its supporting mechanism.

M2 is supported by a superinvar tripod-shaped pad of stress relief spring legs that are glued at the backside of M2. The surface error of the secondary mirror can be again caused by the CTE difference between the superinvar pad and the ULE, and it constrains the best-performance temperature range between 0 to 40℃(TBD). Since the positional tolerance of M2 is tighter than that of Hinode OTA, it is demanded to have in-flight alignment mechanism of M2 by occasional commanding from the ground. As shown in Table 2.6, the positional tolerances of M1 and M2 are much relaxed if M2 tilt adjustments are possible. We expect the mis-alignment of M2 does not occur frequently but does in post-launch and seasonal intervals. The amount of M2 tilt mis-alignment can be derived by analyzing a coma aberration of a wavefront error using a phase diversity method in one of the focal plane instruments.

2.5.4. Thermal design

Solar illumination of about 2 kW is inevitably impinged onto the primary mirror at the bottom of the SUVIT-OTA during solar observations from its aperture. It is critically important to make a thermal design to dump such a large heat load to space and maintain optical and structure components within allowable temperature ranges with small temperature fluctuation. In order to identify technical difficulties in the thermal design of the 1.5mφ telescope, we investigate thermal environment of the telescope using a scaled-up thermal model (Fig. 2.15) of Hinode SOT-OTA except higher solar absorption coefficient α of M1 and M2 with taking into account the lower reflectivity of the aluminum coating (α ~ 0.1 for Al coating while α ~ 0.05 for Ag coating at begin-of-life (BOL), see Table 2.7). The thermal design concept of Hinode SOT-OTA is summarized as follows:

1) Most of the incident energy is reflected back by M1 and dumped out to space by the

HDM through the heat dump window on the side of the telescope.

2) The sunshade has an optical solar reflector facing the Sun to keep it cold, while the upper area of the shield tube is used as a radiator.
3) The solar heat absorbed in M1 is radiatively transmitted to a telescope lower tube from its side and from a bottom cooling plate just beneath M1.
4) The solar heat absorbed by M2 is radiatively transmitted to the radiator from its backside.
5) The heat absorbed by the 2FS and CMU is conductively transferred to a mirror cell and also emitted out through their housings, and is finally radiatively transmitted to the lower tube.

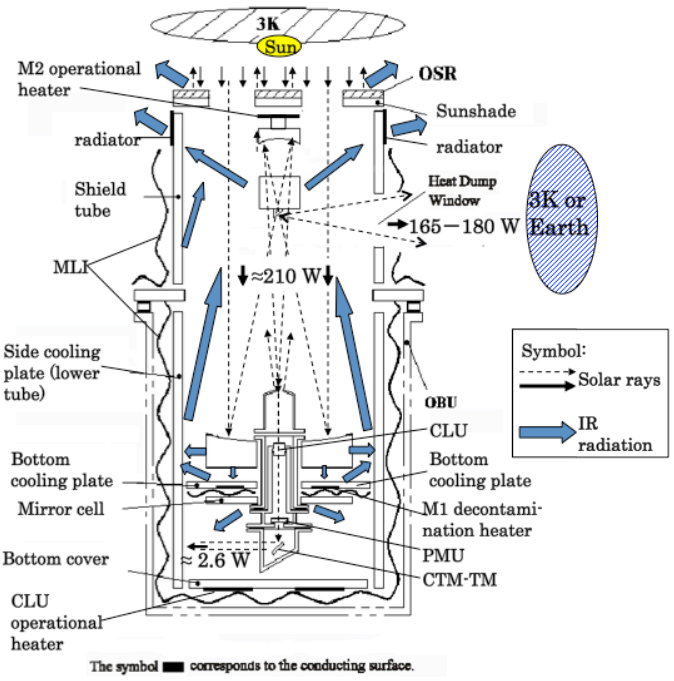

Fig. 2.14. Thermal design concept in the Hinode OTA.

6) The heat absorbed by the HDM is conductively transferred to the cylindrical structure supporting the HDM and outer spiders, and then radiatively transferred to the radiator on the shield tube and space through the heat dump window.
7) The heat of the lower tube and the shield tube is radiatively emitted directly to the space through the entrance aperture and indirectly via the radiator of the sunshade and upper shield tube.
8) The OTA is thermally insulated from the spacecraft. The OTA is physically connected to an optical bench unit (OBU) only by mounting legs of low-thermally conductive titanium and is radiatively de-coupled from the OBU.

Table 2.7. Solar light absorption coefficient and absorbed energy at begin-of-life (BOL).

Components	Absorption coeff. α	Incident radiation (W)	Absorbed radiation (W)
M1	0.12	2074.9	244.8
HDM	0.1	1830.1	175.4
M2	0.12	76.2	9.0
CMU	0.11	19.4	2.1
Total	---	----	431.4

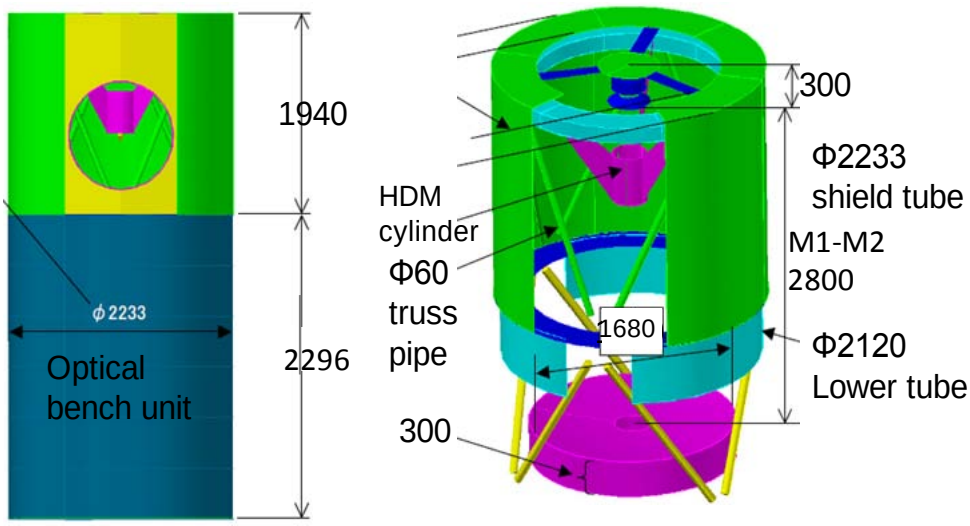

Fig. 2.15. Thermal math model for SUVIT-OTA.

Predicted temperatures of optical components at BOL are given in Table 2.8, where the orbit of the spacecraft is either the sun synchronous polar orbit (SSO) or the geo-synchronous orbit (GEO). The base model is simply a scaled-up model of Hinode SOT-OTA, and we find that it gives unacceptably high temperatures both for the primary mirror and HDM, especially in the case of SSO. When we increase the area of the radiator on the shield tube (Mod-1) and increase the conductivity between HDM and the HDM cylinder and increase the area of the HDM cylinder (Mod-2), it is possible to make the temperatures marginally within the acceptable range even in the case of SSO.

Table 2.8. Predicted temperatures of the components at BOL.

Components	Base model		Mod-1	Mod-2
	SSO	GEO	SSO	SSO
M1 surface	61	49	52	52
M2 surface	-2 ~ -7	-24	-12 ~ -8	-12 ~ -7
HDM surface	109 ~ 111	100	103 ~ 104	60 ~ 61
CMU	34 ~ 37	22 ~ 24	24 ~ 27	24 ~ 26

It turned out, however, that those modifications still cannot lower the temperature of M1, especially when the solar absorption coefficient αis degraded at end-of-life (EOL) and the heat absorption at M1 increases by about 100W (Table 2.9). To lower the temperature in this case, more drastic modifications are necessary, in which an additional heat dump system from M1 (e.g. change the bottom of OBU to a radiator) is accommodated (Mod-3). The prediction based on the modification indicates that we can obtain the acceptable temperatures lower than 50 ℃ even at EOL if the heat load of about 100W at M1 is dumped at the bottom of the telescope and is transferred toward the spacecraft bus (Table 2.10). It is described in section 5.5 that there is a feasible concept for transferring the heat load from the telescope to the spacecraft bus, and for dumping it from a radiator on the side surface of the bus.

It is clear from the thermal model investigation that GEO has an advantage to have

the moderate temperatures and lower temperature fluctuation because less affected by infrared radiation from the earth. Another possible solution for lowering the temperatures is to employ a mirror coating of high reflectivity in UV and low solar heat absorption like the silver coating (see 2.5.2), which is now under investigation.

Table 2.9. Solar light absorption coefficient and absorbed energy at end-of-life (EOL).

Components	Absorption coeff. α	Incident radiation (W)	Absorbed radiation (W)
M1	0.17	2074.9	348.6
HDM	0.1	1726.3	165.4
M2	0.17	71.9	12.1
CMU	0.11	18.6	2.0
Total	---	----	528.2

Table 2.10. Predicted temperatures of the components at EOL.

Components	Base model + Mod-2		Base model + Mod-2 + Mod-3	
	SSO	GEO	SSO	GEO
M1 surface	80	70	52	39
M2 surface	0 ~ 4	-17 ~ -16	-2 ~ 3	-18 ~ -17
HDM surface	63 ~ 64	51	61 ~ 62	47 ~ 48
CMU	41	29	19	4

2.6. Focal plane instruments

2.6.1. Interface with the telescope

The collimated beam from CMU is spitted by a 50:50 beam splitter (BS) inside the OTA, and is fed into the two focal plane packages (Fig. 2.16). The afocal interface between the telescope and the focal plane instruments helps to relax the positional tolerance in the alignment of the packages. The third mirror of CMU can be used as a tip-tilt mirror (TM) of the image stabilization system, and works to remove the attitude jitter of the spacecraft in both the beams going to the two packages. The polarization calibration unit (PCU) is to be inserted between the 2FS and CMU to produce specific polarization states for polarization calibration, where the polarization modulators are installed in each focal plane packages as is shown in Fig. 2.6.

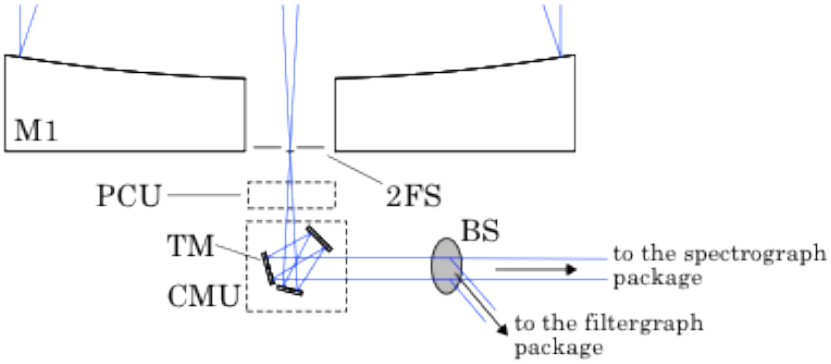

Fig. 2.16. Concept of the beam splitting inside OTA. The beam splitter is located behind the CMU, and feeds the collimated beam into the two focal plane packages.

2.6.2. Spectro-polarimeter

The spectrograph package consists of the spectro-polarimeter (SP) and the correlation tracker (CT). The SP is an instrument for obtaining full Stokes parameters of spectral line profiles, and provides precise polarimetric measurements of the chromospheric and photospheric lines to diagnose magnetic fields in the solar surface. The preliminary concept of the spectrograph is to employ a Littrow spectrograph configuration similar with the spectro-polarimeter (SP) of HINODE SOT. The optical configuration of the spectro-polarimeter is shown in Fig. 2.17 (*top*). The basic parameters are summarized in Table 2.11. It consists of an Echelle grating and an offset-aspheric mirror for collimating and reimaging the beam before and after the grating. In the current design, the spectrum bands around He I 1083 nm, Ca II 854 nm, and Mg II h/k 280 nm can be observed simultaneously in the same diffraction angle with different orders (Fig. 2.17 *bottom*). The observing bands include not only chromospheric lines but some photospheric lines in the observing wavelengths (e.g. Si I at 1082.7 nm) allowing simultaneous observation of both the photosphere and the chromosphere. Is to be switched by changing band-pass filters. Scanning over the FOV across the slit is done with a scan mirror located in front of the slit. In order to minimize scanning duration, a multi-slit configuration is considered, in which two or three slits are located with 60'' – 80'' separation to get spectra at multiple locations simultaneously (Fig. 2.17 *bottom*). A Wollaston prism is installed in front of the detector to measure the orthogonal polarization states simultaneously. In order to observe the He I line at 1083 nm, it is required to use an infrared detector instead of CCD. But infrared detectors generally require low temperatures environment to suppress noises due to dark currents. We are now investigating a possible usage of an HgCdTe detector with a 1.7 μm cut-off which can be operated with relatively higher temperatures (T~200K). The detector is also sensitive to 854 nm with a good efficiency. In order to observe Mg II h/k lines at 280 nm in SP, getting co-focus at the slit is optically difficult because the wavelength is very different from 1.1 μm and 854 nm. It is under investigation to make an optical design allowing observations at 280 nm in SP.

The precise polarimetric measurements for diagnostics of chromospheric fields require 10 – 20 sec integration at each slit position to achieve the 10^{-4} polarimetric sensitivity. In addition to the deep polarimetric observation, the instrument is to be

designed to support rapid scanning to make spectroscopic observations for study of chromospheric dynamics and a spectro-polarimetric observations for photospheric magnetic fields over the FOV with 0.1 sec – 1 sec integration at each slit position. Basic observing modes with the instrument are summarized in Table 2.12.

Table 2.11. Basic parameters of the spectrograph.

Type	Littrow spectrograph
Entrance pupil	60 mm
Focal length @ slit	1650 mm (F/27.5)
Detector size	2048 x 2048, 18μm/pixel
Pixel scale	0.09 arcsec /pixel
FOV along slit	184 arcsec
Blaze angle	63.4°
Groove	110 / mm
Slit width	TBD μm
Sampling dispersion	$\lambda/\Delta\lambda$=2.5 x10^5

Wavelength bands	1083 nm	854 nm	280 nm
Spectrum lines	He I	Ca II	Mg II
Order	15	19	58
Wavelength sampling	43 mÅ	34 mÅ	11 mÅ

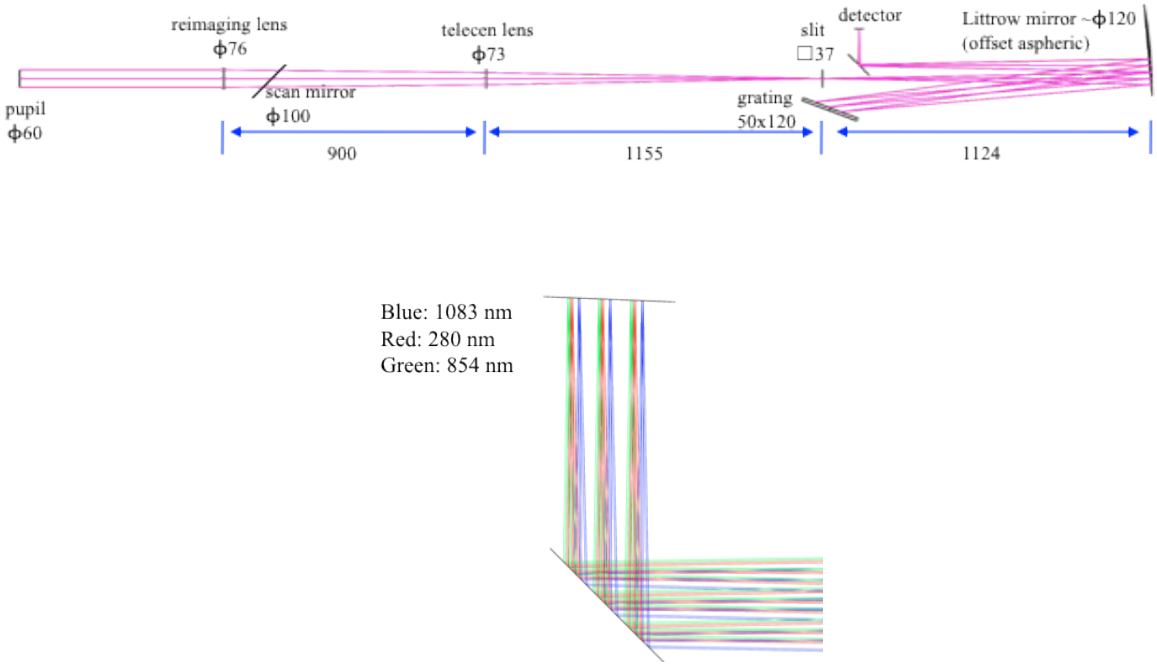

Fig. 2.17. Optical configuration of the spectro-polarimeter (*top*), which allows simultaneous observation of the three wavelength bands at around 1083 nm, 854nm, and 280 nm at the same diffraction angle (*bottom*). The figure shows optical rays at each spectral band when three slits are located at the image plane.

Table 2.12. Basic observing modes of SP in SUVIT.

Rapid mode	High-speed spectroscopic observation for studies of dynamics. − Spectral lines: Mg II h/k 280nm, Ca II 854 nm − Integration time: ~0.1 sec at each slit position. − Duration: ~2 minutes to scan 100 arcsec FOV.
Normal mode	Spectro-polarimetric observation for study of photospheric magnetic fields and chromospheric dynamics. − Spectral lines: He I 1083 nm, Si I 1082.7 nm, Ca II 854 nm − Integration time: ~1 sec at each slit position. − Duration: ~20 minutes to scan 100 arcsec FOV.
Deep mode	Spectro-polarimetric observation for study of chromospheric magnetic fields. − Spectral lines: He I 1083 nm, Si I 1082.7 nm, Ca II 854 nm − Integration time: 10 – 20 sec at each slit position. − Duration: 20 – 40 minutes to scan 10 arcsec FOV. (Sparse scanning is used to map wide FOV.)

2.6.3. Broad-band filtergraph

The purpose of the broad-band filtergraph (BF) is to get a monochromatic image of the solar photosphere and chromosphere using interference filters at the best possible spatial and temporal resolution. The optical design is very simple and is shown in Fig. 2.18, in which a filter wheel and a shutter are located in front of the detector. The basic optical parameters and candidates of the filter pass-bands are shown in Table 2.13. A key for developing the channel is to make an optical design allowing co-focus at around 280 nm and longer than 400 nm.

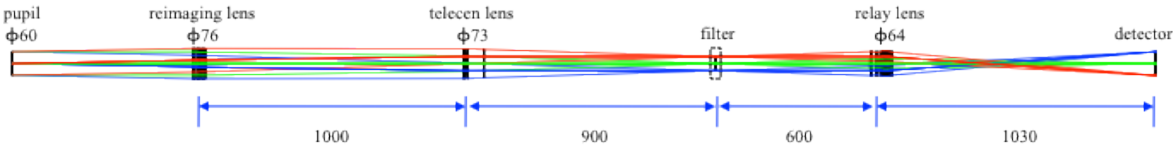

Fig. 2.18. Optical configuration of the broad-band imager.

Table 2.13. Basic parameters of the broad-band imager.

Entrance pupil	60 mm
Focal length	2475 mm (F/41.3)
Detector size	4096 x 4096, 12μm/pixel
Pixel scale	0.04 arcsec /pixel
FOV	164 arcsec x 164 arcsec

Pass-bands	279 nm	380 nm	393 nm	TBD
Spectrum lines	Mg II k/h	CN band	Ca II K	Contin.

2.6.4. Narrow-band filtergraph

The narrow-band filtergraph (NF) is an important instrument to get monochromatic imaging in chromospheric and photospheric lines, and to make Dopplergram and magnetogram observations with covering relatively wide field of view. A tunable filter (TF) is a key component in the narrowband filtergraph. There are two possible types of TF for SUVIT, (1) Lyot filter and (2) Fabry-Perot filter. The Lyot filter is a narrow-band filter using a birefringence of calcite blocks, where peak wavelengths of its transmission can be tuned with either rotating wave plates or liquid crystal variable retarders (LCVRs). There are two possible ways in the Fabry-Perot filter. One is to use two glass plates and adjust the gap between them to tune the central wavelength of the transmission (air space). The other is to use a plate made of ferroelectric crystal ($LiNbO_3$) and apply high voltages to tune the wavelength. There are advantages and disadvantages among them, which are summarized in Table 2.14, and a trade-off study is now under going.

Table 2.14. Comparison between Lyot filter and Fabry Perot filter for SUVIT.

	Lyot filter	Fabry Perot	
		Air space	$LiNbO_3$
Speed of incident beam	F ~ 40	F ~ 200	F~90
Necessary diameter D = 1.5m, FOV=2'φ D = 1.5m, FOV=3'φ	 ~36 mm ~54 mm	 ~180 mm ~270 mm	 ~81 mm ~120 mm
Transmission	~5 %	~70 %	~70 %
Simultaneous 2-pol.	impossible	possible	possible
Simultaneous multi λ	(in principle possible)	impossible	possible (y-cut)
Structure	complex	high accuracy	simple
Oil	necessary	free	free
Control device	rot. WP or LCVR	Piezo	$LiNbO_3$
Past experience	HINODE SOT	SOHO LASCO/C1	SUNRISE IMAX
Advantage	- Smaller aperture - Tolerant - Large FSR - Stable flat field	- Fast tuning - High throughput	- Light and simple - Smaller aperture (than air speace FP)
Disadvantage	- Many pol. elements - Need oil - Low throughput - Long	- Big and heavy - High precision - Unstable flat field - Small FSR	- High voltage - Slow tunig - Small FSR - Unstable flat field - Vulnerability

A possible optical design is shown in Fig. 2.19, where we use a Lyot filter as TF, and locate it in a telecentric beam of F/40 to make a uniform wavelength over the field of view. Several wavelength pass-bands can be switched by changing blocking filters located in front of TF. The reimaging lens is possibly shared with the broad-band filtergraph in the imager package. The basic parameters of the optical configuration are summarized in Table 2.15. Requirements on TF are summarized in Table 2.16. The FOV available with NF depends on how big the TF diameter can be fabricated. When the

diameter of the Lyot filter is 50 mmφ at the telecentric focus of F/40, the FOV is to be limited within 120” x 120”. In the case of the air-space Fabry-Perot filter at the telecentric focus of F/200, the FOV is to be limited within 90” x 90” when the diameter of the TF is 180 mmφ.

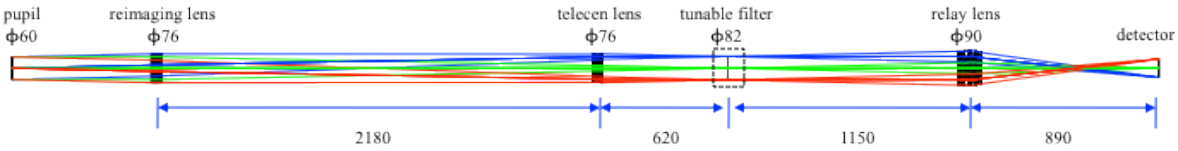

Fig. 2.19. Optical configuration of the narrow-band imager in the case when the Lyot filter is located at the telecentric beam of F/40.

Table 2.15. Basic parameters of the narrow-band imager.

Entrance pupil	60 mm
Telecentric beam	~F/40 (in the case of a Lyot filter) ~F/200 (in the case of a air-gap Fabry-Perot)
Focal length	1980 mm (F/33)
Detector size	4096 x 4096, 12μm/pixel
Pixel scale	0.05 arcsec /pixel
FOV	205 arcsec x 205 arcsec (1) 120 arcsec x 120 arcsec (2) 90 arcsec x 90 arcsec (3)

Pass-bands	517 nm	589 nm	630 nm	656 nm	854 nm
Spectrum lines	Mg I b	Na I D	Fe I	H I α	Ca II

(1) The optical configuration allows us to observe the FOV if the TF is big enough to cover the FOV.
(2) The FOV is available when the diameter of the Lyot filter is 50 mm φ at the F/40 telecentric focus.
(3) The FOV is available when the diameter of the Fabry-Perot filter is 180 mm φ at the F/200 telecentric focus.

Table 2.16. Requirements on TF.

wavelength range	500 – 870 nm
band width	~100 mÅ
Strehl ratio	>0.9
FOV	~200 arcsec
free spectral range	> 3 Å
tuning range	±3 Å
tuning speed	<5 s to scan FSR
tuning resolution	<5 mÅ
repeatability	<2 mÅ
uniformity	
wavelength	5 mÅ (TBD)
transmission	5 %
Stability	
wavelength	5 mÅ /day
transmission	1% /day
Parastic light	<2 %
Ghost	<1 %

2.7. Image stabilization system

In order to achieve high spatial resolution and precise polarimetric measurements in SUVIT of SOLAR-C, it is essential to achieve stable pointing of the telescope for solar images exposed on the detectors (see section 5.4 for more details). The image stabilization system (ISS) is to be implemented inside the telescope to reduce image displacements caused by attitude jitters of the spacecraft and disturbances generated by moving components (e.g. filter wheels, shutters, etc.). ISS consists of a correlation tracker (CT), which is installed in the spectrograph package and calculates image displacements by correlation tracking of solar granules, and a tip-tilt mirror (TM) to compensate the displacements, and servo control electronics. One of the mirrors in the collimator mirror unit (CMU) is to be used as the TM inside the SUVIT-OTA while the CT is to be installed in one of the focal plane packages, likely in the spectrograph package, because it is required to control behavior of the image stabilization system in coordination with slit-scanning observations of the spectro-polarimeter.

In HINODE SOT, we have developed ISS to remove residual pointing errors that the attitude control system cannot suppress in the frequency range lower than 14 Hz (Fig. 2.20 *left*), and achieved the pointing stability of 0.03 arcsec (3σ) as in-flight performance (Shimizu et al. 2008). It is expected to achieve better stability than 0.015 arcsec (3σ) in SOLAR-C SUVIT for the spatial resolution better than 0.1" and for the high polarimetric accuracy because pointing fluctuation during the polarization modulation introduces artificial polarization signals. High frequency disturbances induced by moving components and structural resonances are to be partially suppressed by extending the control bandwidth of ISS from 14Hz to about 100Hz (Table 2.17). It is a key to make use of a high-speed (faster than 5000 frames per second) camera with a CMOS device for correlation tracking of granule patterns. The simulated performance of ISS is shown in Fig. 2.20 (*right*).

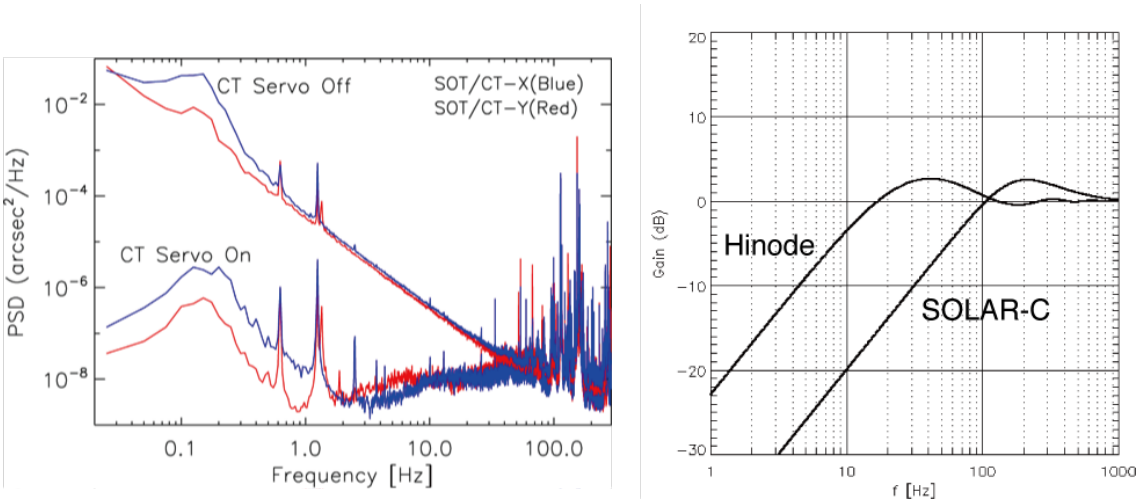

Fig. 2.20. Power spectrum densities of the pointing error signals measured with the CT in SOT (*left*). Simulated reduction performance of pointing error against input disturbances in SOLAR-C with the parameters given in Table 2.17 (*right*).

Table 2.17. Basic parameters of the servo-loop performance of ISS.

	HINODE SOT	SOLAR-C SUVIT
Cross-over frequency	14 Hz	> 100 Hz
Time const of TM drive	7.24×10^{-4} sec	$< 5 \times 10^{-4}$ sec
CT signal delay time	3.2×10^{-3} sec	$< 2 \times 10^{-4}$ sec

2.8. Contamination control

The contamination of the optical components becomes critical to carry out an observation in the UV wavelength range shorter than 400 nm. In the HINODE/SOT, gradual degradation of the throughput has been observed through its mission period. The degradation is supposed to be because of accumulation of molecular contaminants, which are out-gassed from organic components inside the telescope, on the surfaces of the primary mirror or the collimator lens unit. The decrease of the throughput is about 40% at 388 nm and about 50% at 396 nm 3 years after the launch. The corresponding throughput degradation at 280 nm is roughly estimated as ~20% if we scale an absorption coefficient of the contaminants to the shorter wavelength. In order to keep higher throughput in UV through the mission period, it is required to have more careful control of contamination environment in designing and developing the telescope. One possibility is to extend the period of bake-out of components in a vacuum chamber.

2.9. Integration and test plan

2.9.1. Integration and initial M1-M2 alignment

The SUVIT-OTA optical components are assembled in a dedicated integration and test tower structure having a dummy optical bench unit (OBU) that simulates a mounting interface of the spacecraft. The tower structure is capable of tilting the OTA from a vertical to horizontal configuration as well as rotating around the optical axis (Fig. 2.21). The integration is performed in the vertical configuration. After the CFRP truss structure is installed on the dummy OBU, M1 is installed on the mirror cell and its optical axis is aligned to the center of the mirror cell and the vertical line. Next, the ring plate assembled with the M2 and HDM units is installed on the top ring.

Then the OTA is tilted to the horizontal configuration. De-center, tilt and de-space of M2 with respect to M1 is adjusted using a Shack-Hartmann sensor attached to the mirror cell. The sensor can yield real-time coefficients of low-order Zernike polynomials such as focus (A20), primary astigmatism (A22, B22), coma (A31, B31) and spherical (A40) aberration. A high-precision folding flat mirror is set in front of the OTA entrance aperture. The Shack-Hartmann sensor is focused at the center of the secondary field stop, and the defocus and coma aberration is eliminated by adjusting positions and tilt of M2.

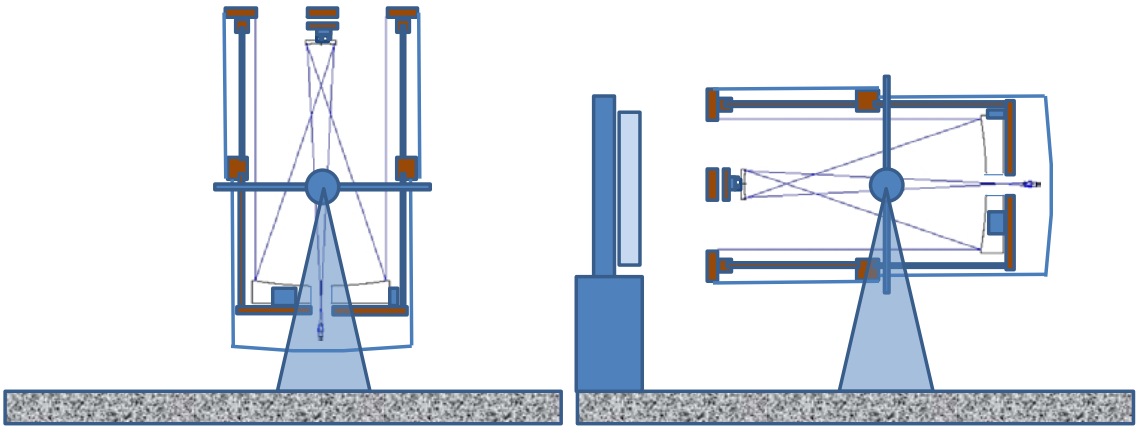

Fig. 2.21. OTA vertical configuration for telescope integration (*left*) and horizontal configuration for initial M1-M2 alignment with a Shack-Hartmann sensor and for optical performance test with an interferometer (*right*). By rotating the OTA around the optical axis in the horizontal configuration, it is possible to measure the wavefront error with canceling the gravity effect.

2.9.2. Zero-gravity optical performance test

The wavefront error of the OTA is measured in the horizontal configuration (+1 G condition) with an interferometer after integrating the CMU to the OTA. The interferometer sent a collimated beam into the OTA from the exit pupil. With the folding flat ahead the entrance pupil, the double-path wavefront error of the OTA is obtained. Next, rotating the OTA 180 degrees around the optical axis and setting the interferometer in the opposite side, the measurements for -1 G condition is performed. Averaging the -1 G and the +1 G wavefront errors can canceled out the effect of gravity. We can thus measure the wavefront error in the zero-gravity condition.

2.9.3. Opto-thermal test

The thermal model predicts that the OTA on orbit will inevitably have a large temperature gradient along the optical axis; the bottom part of telescope including M1 will reach a temperature from room temperature to higher than 50 ℃, while the upper structures supporting M2 will reach a temperature of 0 to 30 (TBD), depending on thermal conditions and its life phase. It is absolutely necessary, therefore, to verify the optical performance in such a temperature distribution even though the opto-mechanical design predicts that those temperatures are acceptable.

We will conduct opto-thermal testing of the OTA using a vacuum chamber dedicated for space environment tests of optical sensors. The configuration of the test setup is shown in Fig. 2.22. The OTA is mounted in a vacuum chamber in a horizontal configuration with a dummy OBU made of superinvar, and the folding flat mirror with a tilt and rotational stage is installed at one end of the chamber. Mounted on the side wall of the chamber, the interferometer looks into the OTA through an optical quality window. The vacuum chamber has upper and lower shrouds surrounding the entire OTA. By controlling temperatures of the shrouds, we can change the temperatures of upper and lower parts of the OTA independently, while the temperature of the folding flat mirror is always kept about the room temperature, using another temperature-controlled shroud.

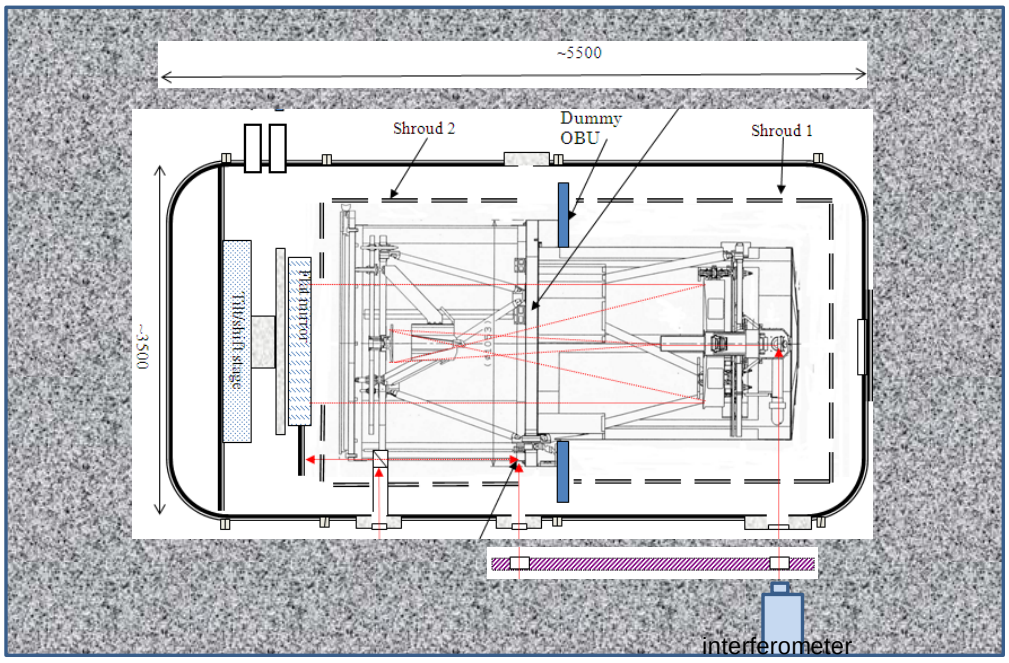

Fig. 2.22. Configuration to the OTA opto-thermal test.

Appendix A. Diagnostics of dynamics and magnetic fields in the chromosphere

A.1. Limitations in the Zeeman diagnostics

The only way to obtain quantitative information on magnetic fields in the solar atmosphere is via the measurement and physical interpretation of the emergent spectral line polarization. The approach commonly used is to analyze polarized line profiles due to the Zeeman effect. The polarization of the Zeeman effect is due to splitting of a spectral line in wavelength. An observational signature of the circular polarization produced by the longitudinal Zeeman effect is an anti-symmetric profile whose amplitude scales with the ratio, *R*, between the Zeeman splitting and the Doppler broadened line width.

$$R = \frac{1.4 \times 10^{-7} g_{eff} \lambda B}{\sqrt{1.663 \times 10^{-2} T / \mu + \xi^2}} \quad (1)$$

where g_{eff} is the effective Lande factor of the transition, μ is the atomic weight of the atom under consideration and λ is in Å, B in gauss, T in K and the non-thermal velocity ξ in km s^{-1}. The linear polarization amplitudes of the transverse Zeeman effect scale instead as R^2. The Zeeman effect produces significant amplitude of polarization when the line splitting is comparable with the line width, i.e. R~1, which is the case of photospheric lines. On the other hand, the Zeeman splitting is typically much smaller than the line width (i.e. R<<1) at the major chromospheric lines, because of relatively weaker field strength and larger line width in the chromosphere. This makes polarization amplitude smaller there especially in the linear polarization to obtain the transverse component of magnetic fields (Table 2.1 and Fig. 2.23). This is why we need high polarimetric sensitivity to diagnose magnetic field in the chromosphere.

A.2. Prospects of the Hanle diagnostics

There is another physical mechanism by means of which the magnetic fields of the solar atmosphere makes polarization of the emergent spectral line radiation: the Hanle effect. Anisotropic radiation pumping processes produce atomic level polarization (i.e., population imbalances and quantum coherences among the magnetic sublevels pertaining to any given degenerate energy level). The Hanle effect can be defined as any modification of the atomic level polarization due to the presence of a magnetic field. The Hanle effect makes changes in the polarized line profiles at magnetic strengths between ~$0.1B_H$ and ~$10B_H$ (Fig. 2.23), where the critical Hanle field strength (B_H, in gauss) is that for which the Zeeman splitting of the energy level under consideration is similar to its natural width:

$$B_H = 1.137 \times 10^{-7} / t_{life} g_J \quad (2)$$

with g_J the level's Landé factor and t_{life} its radiative lifetime in seconds. The critical Hanle field strength is typically from 1mG to 10 G dependent on the spectrum lines. This means that the Hanle effect is sensitive to weaker magnetic fields than the Zeeman effect (from at least 1 mG to 100 G), regardless of how large the line width due to Doppler broadening is. When the magnetic field is much stronger than the critical Hanle strength, the polarization amplitude does not depend on the field strength

(so-called Hanle saturation regime). Note that in the saturation regime the linear polarization signals created by atomic level polarization are still sensitive to the magnetic field orientation. When the field strength is strong enough, the linear polarization of chromospheric lines is generally due to the Hanle and transverse Zeeman effect (Fig. 2.23). Note also the circular polarization is always dominated by the longitudinal Zeeman effect, and the amplitude of the circular polarization provides information of the longitudinal field. The Hanle effect as a diagnostic tool is not limited to a narrow solar limb zone. In particular, in the forward scattering geometry of a solar disk center observation, the Hanle effect creates measurable linear polarization in the presence of an inclined magnetic field (Trujillo Bueno et al. 2002).

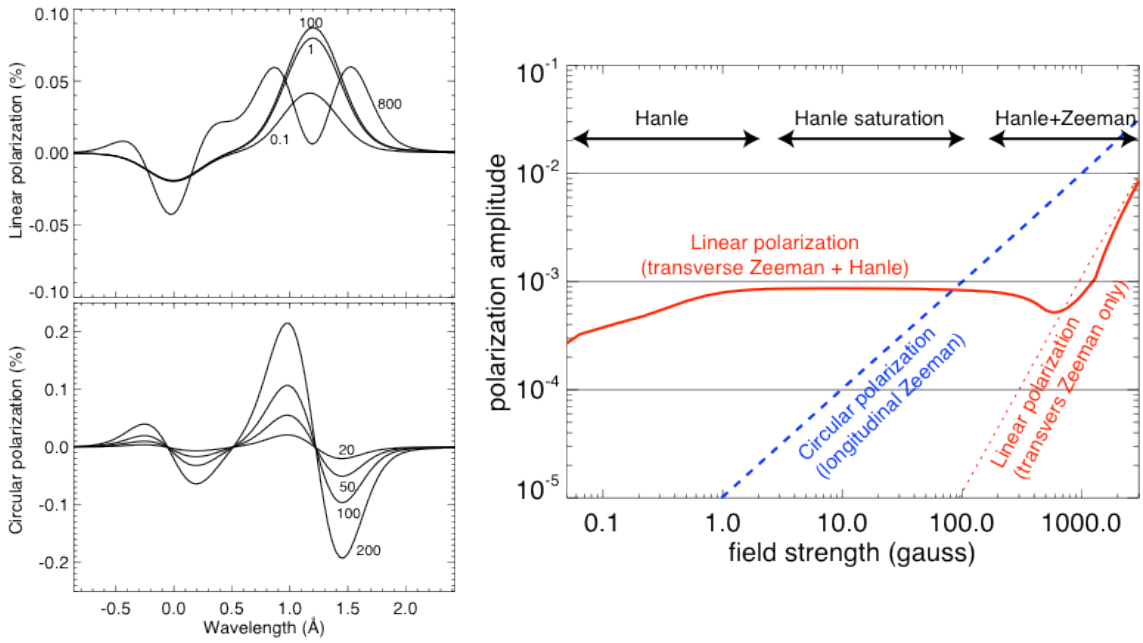

Fig. 2.23. (Left) Polarized spectrum line profiles at the He I 10830 Å for several field strengths (in gauss). The critical Hanle field strength B_H is about 0.8 gauss at the line. (Right) Polarization amplitude induced by joint action of the Zeeman and Hanle effect at He I 10830 Å as a function of the field strength (right). This is the case of forward scattering at the disk center and when the magnetic field is purely horizontal (for the linear polarization) or purely vertical (for the circular polarization). The Hanle effect allows us to diagnose transverse fields weaker than 100 gauss, which is not accessible with the transverse Zeeman effect only.

A.3. Inversion of chromospheric lines

The plasma velocities, temperatures, magnetic field vectors, and other interesting physical conditions in the solar atmosphere are not directly observable. In order to extract quantitative information on such conditions we need to make use of our knowledge on how the properties of the light are transformed as it propagates. A typical approach involves a non-linear fitting of observations of intensity and polarized spectrum profiles with synthetic ones obtained by solving the forward problem (i.e. radiative transfer) in a model atmosphere involving some unknown parameters. Because the chromosphere consists of complex fine structures organized by magnetic fields,

interpretation of chromospheric spectral lines requires simplification to restrict the number of unknown parameters that an observed line profile depends on.

A.3.1. Obtaining velocities and plasma parameters

One of the traditional methods to retrieve plasma parameters of chromospheric fine structures is so-called cloud modeling which describes the transfer of radiation through structures located higher up from the solar photosphere resembling clouds on earth's sky. Such cloud-like structures, when observed from above, absorb the radiation coming from below. The intensity line profiles mostly depends on transparency of the cloud to the incident radiation and also on the physical parameters in the cloud. Thus, in its most basic form cloud modeling delivers the four parameters, cloud optical thickness, cloud source function, cloud Dopplershift (i.e. velocity), and cloud Dopplerwidth, all four for a homogeneous cloud irradiated from below (see review by Tziotziou et al. 2007). The cloud source function can be converted into density and temperature through non-LTE calculation (e.g. Beckers 1972, Tsiropoula and Schmieder 1997) including static ionization equilibrium. Recent MHD simulations have shown that in chromosphere structures that suffer repetitive episodic heating, the actual populations of the atomic levels can be far from time-independent statistical equilibrium (Leenaarts et al. 2007). It is important to refine the cloud modeling to include time-dependent ionization as well as to compare data directly with numerical spectral line synthesis employing MHD simulations of time-dependent chromospheric structures.

A.3.2. Obtaining magnetic fields

Inversions of polarized Stokes profiles for photospheric lines have been developed and used routinely for over 20 years now to produce magnetic field maps. The simplest one is to use the Milne-Eddington method (e.g. Skumanich and Lites 1987) employing simplified assumption that all the physical parameters are constant in the line-formation region (except for the source function which varies linearly with optical depth) and has the advantage that the forward problem has an analytical solution, which makes the inversion robust and fast. The second method, the Stokes inversion based on response function (SIR, Ruiz Cobo and del Toro Iniesta 1992), is based on a full solution of the polarized LTE transfer in an arbitrarily one-dimensional atmosphere. It has the advantage that it is possible to determine the variation of physical parameters along the line of sight.

Similar tools for chromospheric inversions already exist and significant experience has been accumulated for nearly a decade now. There are several reasons why the analysis of chromospheric lines is more challenging. The biggest issue is that the radiative transfer in the chromosphere is non-LTE and there is not a universal solution. One needs to employ different techniques depending on the particular physical scenario under study (whether the polarization is originated by Zeeman effect or scattering, etc). They fall roughly into two different approaches. The He I triplet at 1083 nm forms over a very thin atmospheric slab because it forms by recombination of He II ions created by UV coronal illumination. The line formation allows us to use the Milne-Eddington type of approach as a valid approximation to derive accurate magnetic fields in the Zeeman regime (Lagg et al. 2004). The inversion code HAZEL (Hanle and Zeeman Light,

Asensio Ramos, Trujillo Bueno & Landi Degl'Innocenti 2008) is able to tackle the full problem including the Zeeman and Hanle effects self-consistently in such a slab (Fig. 2.24).

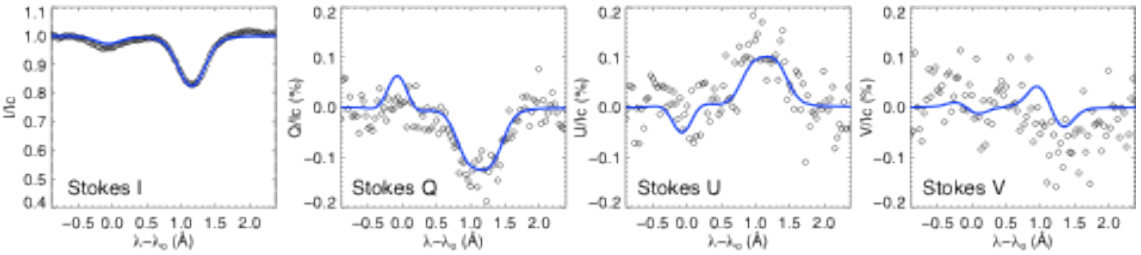

Fig. 2.24. Example of a spectro-polarimetric observation of He I 10830 Å line and non-linear fitting of the observed line profiles with HAZEL.

Another alternative is the generalization of SIR to non-LTE atmosphere (Socas-Navarro et al. 1998). In the current code, the polarization generation is restricted to the Zeeman regime only but the line formation is treated fully in non-LTE, with the assumptions of instantaneous ionization equilibrium and complete angle and frequency redistribution (CRD). The CRD approximation is valid for some lines such as those in the Ca II infrared triplet at around 850 nm (Uitenbroek 1989). The non-LTE inversion was successfully applied to spectro-polarimetric observations in the Ca II infrared triplet to get three-dimensional magnetic structures around a sunspot (Socas-Navarro et al. 2005). The validity of the inversion and the possible impact of ionization history and three-dimensional radiative transfer are currently been studied using numerical MHD simulations of the chromosphere (de la Cruz Rodriguez et al. 2010, Fig. 2.25) though these approximations affect only the determination of thermodynamical parameters but not the magnetic field vector and the line-of-sight velocity.

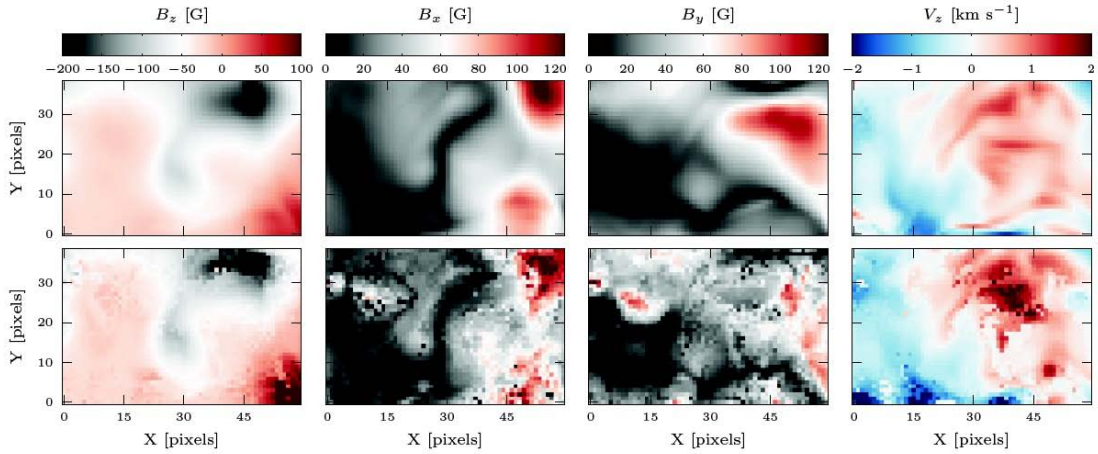

Fig. 2.25. Test of the non-LTE inversion in the Ca II 854 nm line using the numerical MHD simulation of the chromosphere (see A.4), where top panels show parameters from the simulation and bottom panels show parameters obtained with the inversion of the synthesized line profiles.

Because the non-LTE inversion requires lots of computational power, it is under investigation to apply pattern recognition techniques such as principal component

analysis (PCA, Casini et al. 2005) and artificial neural network (ANN, Socas-Navarro 2005) to the inversion of the chromospheric lines. The general idea behind the pattern-recognition approach is to create a sufficiently dense and uniform database of magnetic and atmospheric models that are relevant for the line formation characteristics in an observation. The computationally intensive forward-model step is thus pushed upfront to a one-time calculation of an adequate database of Stokes profiles, while the inversion problem is reduced to the search in that database of the best match to the observed line profiles.

A.4. Numerical modeling of the chromosphere

In order to fully exploit detailed chromospheric line observations, including their polarization measurements, a promising approach would incorporate comparisons of observed spectral line properties and dynamic phenomena with those seen in numerical MHD simulations of the same observables. This requires 3D models of the photosphere and the chromosphere including a realistic description of the important physics. From such models it is then necessary to calculate the observable spectral lines employing radiative transfer.

Although there are lots of complexities in the modeling, several codes exist within the description of single-fluid magnetohydrodynamics. They can treat the detailed radiative transfer, and their photospheric simulations reproduce detailed observations to remarkable detail (e.g. Stein and Nordlund 2006). In the chromosphere, scattering starts to play an important role, radiative losses in strong lines from calcium, magnesium and hydrogen, where non-LTE is crucial, and the hydrogen ionization balance is out of statistical equilibrium. Recently numerical codes have been developed that can treat all these effects and simulations have been produced where comparisons with observations start to become meaningful (Fig. 2.26, e.g. Leenaarts et al. 2009). Efforts are also underway to go beyond the single-fluid magnetohydrodynamic description of the chromosphere.

Once a realistic simulation exists it is necessary to calculate the observable radiation in order to compare with the observations. It is important that the employed radiative transfer codes are capable of handling partial frequency redistribution (PRD), which accounts for the coherence of the incoming and outgoing photons in scattering events in strong chromospheric spectral lines like the Mg II h/k and the Ca II H/K lines. In addition, to compare with observations of polarization in chromospheric lines, the radiative transfer codes should be able to calculate polarized line profiles from a given three-dimensional magnetic configuration in an MHD simulation. Several non-LTE transfer codes already exist that meet many of the requirements, and in the near future these efforts will be combined.

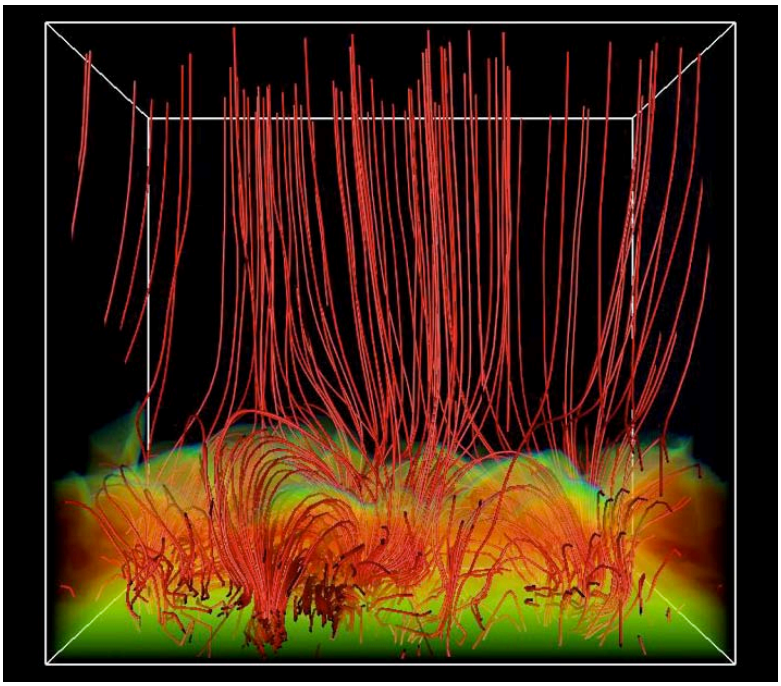

Fig. 2.26. Snapshot of a 3D radiative MHD simulation including the photosphere, chromosphere, and corona (courtesy of Carlsson and Hansteen).

Chapter 3: EUV/FUV High-Throughput Spectroscopic Telescope

3.1. Performance requirements for the spectrometer

The Solar-C mission provides an ideal platform for a EUV/FUV high-throughput high-resolution spectrometer (may be called EUVS hereafter). Performance requirements are summarized below for a breakthrough spectroscopic instrument, which can be realized with recent technology advancements.

1. *To operate in both spectroscopic and imaging modes with high temporal resolution (cadence).* This is required for quantitatively understanding the physics of dynamical phenomena. One order of improvement in effective area is required. Thus, the temporal resolution at a slit position can be shortened down to 0.5 sec for active region plasma and 1 sec for quiet Sun plasma.
2. *To perform EUV/FUV spectroscopy with high spatial resolution.* The spectrometer is required to resolve structures equal to 0.5" resolution or better. The target is 0.3 arcsec, which is roughly equivalent to the width of chromospheric spicules observed with Hinode/SOT.
3. *To observe a field of view as large as possible.* The best resolution may be restricted to ~5x5 arcmin^2 (a medium size active region), but lower resolution should cover a larger field of view.
4. *To perform EUV/FUV spectroscopy with high spectral resolution.* The spectrometer is required to determine Doppler velocities to an accuracy of ~ 2 km/s from spectral line shifts and non-thermal motions as small as 20 km/s from line widths.
5. *To make measurements with spectral lines from a broad temperature range and with adequate plasma diagnostics covering chromospheric, transition region, low corona and flare temperatures.* The observations must cover all relevant temperatures and structures in order to track the flow of energy from the chromosphere into the corona.
6. *To perform good observations with low-scattering optics.* This performance is needed to explore "faint" reconnection outflow regions, coronal holes, and off-limb observations.
7. *To ensure precise co-alignment with the data from other onboard telescopes.* Co-alignment must meet the high spatial resolution of the spectrometer.

The performance requirements summarized above are determined from the science goals in section 1. Table 3.1 summaries instrument performance required for the Solar-C spectrometer, compared with the previous spectrometers. It is obvious that the Solar-C spectrometer will have significant improvements on the temporal resolution, spatial resolution, and temperature coverage. Some of the performance required for the Solar-C spectrometer are discussed below to show possible discovery spaces and new sciences.

Table 3.1. Performance of Solar-C spectrometer in comparison with other spectrometers

	Solar-C spectrometer	Hinode/EIS	SoHO/SUMER
Temporal resolution for a slit position *1	0.5 - 10 sec for AR 1 -10 sec for QS	10 - 20 sec for AR 30 – 60 sec for QS	10 – 20 sec for AR line *2
Spatial resolution	~0.3 arcsec (target) ~0.16 arcsec (pixel size)	3-4 arcsec 1arcsec (pixel size)	2 arcsec 1arcsec (pixel size)
Primary temperature coverage ($\log_{10}$ K)	4.1 – 7.2	4.9, 5.6-7.2	4.1-5.8

*1 The values given here are typical exposure duration for multiple numbers of spectral lines covering a wide temperature range.

*2 SUMER can record spectral lines in only one of spectral windows at the same time. If spectral lines in another spectral window are measured, the grating is needed to move before the exposure.

3.1.1. Spatial resolution requirement

One of key tasks of EUVS is to precisely measure plasma conditions, such as temperature, density, and velocity of elementary structures of the magnetized atmosphere in all temperature regions from the chromosphere through transition region and into the corona. Such measurements made simultaneously with different spectral lines allow us to trace the flow of energy from the chromosphere up into the corona. In the photosphere the energy is observed to be in plasma structures with a scale length of about 0.3″ or about 200 km. Movies made in the Ca II H-line from Hinode SOT clearly reveal that the chromosphere is dominated by a multitude of thin (~200 km), dynamical, jet-like extrusions called spicules. Since SOT can carry out only imaging observations for the chromosphere without spectroscopic capabilities, the proposed spectrometer will be the first instrument to diagnose the plasma properties of these thin, dynamical structures and to follow these structures upwards through the atmosphere into the corona. As the magnetic field may expand with height, the overall size of structures may increase as they rise above the chromosphere/transition region, but the width of spicules may be preserved into the transition region and corona. Coronal loops are well-known coronal magnetic structures, but elementary structures are not yet fully resolved in the corona with the currently existing imaging telescopes (0.″5 at the highest resolution). Spectroscopic measurements in the EUV have suggested that only 10% of the volume of coronal loops is filled with hot plasma, when they are observed with the spatial resolution of 2-3 arcsec (pixel size 1 arcsec) (Warren et al. 2008). Thus, measuring the plasma parameters with 0.3 arcsec, i.e., 10% of the 1 arcsec volume, can fully resolve elementary structures hidden in the magnetic loops. Understanding the magnetic sub-structure implied by the small filling factor is crucial for determining energy flow in coronal loops and ultimately for understanding the physics of coronal heating.

In addition to its own scientific contribution, the spectrometer observations shall have close scientific synergy with the other proposed telescopes. One of the important science goals is to understand the roles of waves propagating through the atmosphere in heating and activating dynamical motions in the plasma. It is important to determine whether or not sufficient energy remains in the waves that penetrate all the way to the corona to make a substantial contribution to the heating budget of the solar corona and/or to the acceleration of the solar wind. It is also critical to identify propagating MHD waves and their modes. For this purpose, observations of magnetic field fluctuations are required in addition to observations of intensity and velocity fluctuations. The proposed spectrometer can provide the observation of intensity and velocity fluctuations. Magnetic field measurements are available only for the low atmosphere, i.e., in the photosphere and chromosphere, and they will be provided by the

UV-Visible-IR telescope with a spatial resolution of 0.2″ or better. The UV-Visible-IR telescope is designed to determine the modes and amplitudes of waves in the low atmosphere just after the excitation of the waves, and the proposed spectrometer can continue to trace their propagation into the transition region and corona. With these coordinated observations, we will explore for the first time the mode conversion in waves, which is expected in the atmospheric layer where the plasma beta is unity. Since the plasma beta changes from high ($\beta>1$) in photosphere and low chromosphere to low ($\beta << 1$) in the corona, we can observe how the waves are evolved as a function of height in the stratified atmosphere. With having high spatial resolution never achieved so far, we can newly explore behaviors of waves and turbulence in small scale, which are useful information for physically understanding roles of waves in the atmosphere. We may have new information concerning turbulent cascade and phase mixing of Alfvenic waves.

Considering these new discovery spaces, the proposed spectrometer should have the capability of resolving structures with scales smaller than 350 km (0.5″). Ideally, it would be better to resolve even smaller structures, say, 0.3″ or ~200 km.

3.1.2. Temporal resolution requirement

Since the structures to be resolved with EUVS are small and dynamic, a high time cadence is necessary and consequently a high-throughput instrument is required. As a goal of the instrument design, the effective area of the spectrometer is set to be at least 10 times larger than previous instruments (EIS onboard Hinode, SUMER and CDS onboard SoHO). This means an improvement of at least an order of magnitude in temporal resolution if observing with the same sampling scale (~1″ arcsec). There is also an improvement even when observing with higher spatial resolution (0.5″ arcsec) than achieved with previous instruments. In the case of EIS observations, typical integration times of an exposure are 10 to 20 s for active region emission lines and 30-60 s for the quiet Sun (Note that shorter exposures are possible in very limited numbers of brighter lines). SUMER observations are carried out with 10 to 20 s integration times (shorter exposures would be possible in the brighter lines but the exposure time is limited by the available telemetry rate). With having high throughput performance and bright spectral lines, the integration times of the proposed spectrometer can be shortened down to 1-0.5 s. The sit-and-stare measurements at a slit position provide time series of spectral data with temporal resolution of 0.5-1 s. The field of view with 15 arcsec width can be repeatedly measured with 25-50 sec cadence, if the slit step is 0.3 arcsec. The spectral maps for 100 arcsec field of view are available every ~200 s, if the slit is stepped per 0.6 arcsec.

As discussed in section 1, numerical simulations suggest that low-frequency (<5mHz) magnetoacoustic waves may provide a significant source of the energy necessary for maintaining the chromosphere. Moreover, the outgoing low-frequency (<1mHz) Alfven waves may provide a major contribution to the heating and acceleration of the plasma as a result of the nonlinear generation of the compressive waves and shocks in the corona. Observationally, various kinds of oscillations and waves have been detected with Hinode data. For example, with analyzing EIS spectral data, upwardly propagating and standing slow magnetoacoustic waves are reported in active regions (Kitagawa et al. 2010) and coronal holes (Banerjee et al. 2009). When the waves propagates along a coronal loop with the sound speed (~150 km/s in the corona), the proposed spectrometer can scan the entire coronal loop about 5 times with 0.6 arcsec step during the time when the waves propagates from one end to the other end of the loop. Thus, such data will allow us to trace the waves from the excitation to the dissipation. The speed of Alfven waves is much higher than the sound speed in the

transition region and corona, but the scan speed of the proposed spectrometer can allow us to explore the properties of propagating Alfven waves, if we choose slit scan step size properly. Moreover, owing to higher temporal resolution, we will search for higher frequency waves (~1Hz) that cannot be explored with the currently existing spectrometers. If higher frequency waves are found in the transition region and corona with sufficient flux, high frequency waves may be a possible candidate for making the bright corona in active regions.

High temporal cadence performance with high spatial resolution has the potential to resolve fine dynamical structures in the coronal loops. Hinode EIS has revealed excess non-thermal line broadening at the footpoints of coronal loops, which is interpreted as the existence of highly blue-shifted small-scale flows at the base of coronal loops (Hara et al. 2008). Non-thermal line broadening is known in spectral lines from the transition region and corona, and we guess that the broadening is created by turbulent nature in coronal loops. Having short integration time is definitely useful to distinguish each of turbulent flows, providing new information on interpreting non-thermal line broadening.

Higher temporal cadence would provide strong tools in exploring coronal holes. Existing spectrometers need much longer integration times to meaningfully record spectral data in coronal holes, where the FUV and EUV coronal emissions are much fainter than in active regions. It is important to identify the source region of the fast solar wind in polar coronal holes. Because of very long integration times (several minutes for a slit position and several hours for mapping a region), it is difficult with existing instruments to confidently identify the source regions. A substantial improvement in the throughput performance can much reduce the time needed to spectrally map a region, getting closer to the timescales for the evolution of the structures. Also, waves with periods from 7 to 20 min have been detected in plumes and inter-plumes above the limb in the polar regions (DeForest & Gurman 1998; Ofman et al. 2000; Banerjee et al. 2000, 2009). A high throughout performance could allow a search for higher frequency waves in coronal holes and a search for wave signatures in line widths and velocity.

3.1.3. Broad temperature coverage

As one of the top-level science goals, we will attempt to understand how the energy is transported through elementary magnetic structures from the chromosphere to the transition region, and from the transition region into the corona. Furthermore, magnetic energy dissipation events are well observed over the entire solar atmosphere, not only in the outer corona which is filled with fully ionized, collisionless plasma, but also in the chromosphere which consists of weakly ionized plasma. In order to capture the entire picture observationally, it is important to measure the plasma conditions and behaviors in different temperature layers simultaneously.

SoHO/SUMER records spectral lines at longer wavelengths in the FUV, where many spectral lines originating from the transition region and chromosphere are available, while only few coronal lines are observed. In contrast, Hinode EIS observes spectral lines at shorter wavelength in the EUV, where many spectral lines from the corona and flare plasma are available but the number of spectral lines is limited for exploring the transition region and chromosphere. Extensive coordinated observations by the two instruments have been obtained since the launch of Hinode, providing significant new results. However, we realize that it is impossible to achieve high accuracy in the co-alignment of the spectral data from SUMER and EIS. Also, since the spectral data are acquired for a single slit position and it takes a long time to map a large field-of-view, it is nearly impossible for two different slit spectrographs to obtain data at the same location on the Sun and at the same time. However, observations at

the same locations and times are critical for understanding the dynamical behavior and evolution of the plasma in the observed targets, because the timescales for the evolution of structures are quite short.

Therefore, it is a requirement that the next generation advanced EUV/FUV spectrometer capture spectral data over the entire temperature domain of the solar atmosphere at the same locations and times. This performance can much improve and ensure accurate co-alignment among different spectral lines. With this improvement, we can discuss with high confidence the relationships among the observational signatures at different temperatures. Elementary magnetic structures of the order of 0.3″ seen in the chromosphere can then be traced into the transition region and corona. It is also possible to trace the flow of energy through static elementary magnetic structures over the solar atmosphere and quantitatively investigate the role of waves as a transporter of energy for heating the corona and energizing the solar wind.

3.1.4. Necessity of low scattering optics

Low-scattering optics should be considered when the spectrometer is designed and fabricated to allow us to accurately record low intensity data. A single-mirror, off-axis telescope is mandatory for off-limb observations, to avoid stray light from the bright solar disk. Many important science discoveries may be hidden in low emission measure areas such as reconnection outflow regions, which are much fainter than flare loops. As another example, low intensity emission in coronal holes observed off-limb may hold the key for understanding solar wind acceleration and shock formation in the high corona.

The reconnection region science discussed in section 1.3.4.2 is an excellent example for stressing the importance of low-scattering performance. Probing the reconnection region itself is not easy because intense flare loops are formed near the reconnection region due to chromospheric evaporation. According to the model calculation given in section 1.3.4.2, the total intensity of the reconnection outflow region is about one thousandths of the total intensity of the bright post-flare loops, when observed in spectral lines from Fe^{+17} to Fe^{+23}. This estimate tells us that low-scattering optics are necessary for investigating the flare reconnection outflow region.

3.1.5. Substantial jump expected from the NASA IRIS mission

IRIS (Interface Region Imaging Spectrograph) is a NASA SMEX mission selected for launch in December 2012. This spectrograph observes several spectral lines in the 120 to 280 nm range with high spatial resolution (0.3″) and high cadence (1 to 5 sec), to discover how the outer atmosphere is energized. The spectral lines observed with IRIS are suitable for exploring the interface between the upper chromosphere and lower transition region, and the IRIS mission is expected to open a window of discovery into a crucial gap in current solar observational capabilities.

However, the spectrometer proposed here would provide a substantial step forward from IRIS observations, because the Solar-C Plan B mission can provide unique observations that have never been realized, allowing us to progress beyond the chromosphere-transition region interface into the entire transition region and corona. The proposed spectrometer will be able to observe spectral lines in the EUV and FUV that seamlessly cover all the temperatures from the chromospheric to the corona with high spatial resolution (0.5″ or better) and high cadence (1 to 5 s). Observations of this completeness are necessary for understanding coronal heating and the formation of the solar wind. In addition, the proposed spectrometer observes several spectral lines that originate from high temperature plasma in the 10^6-10^7 K temperature range,

and these spectral lines are useful for diagnosing flares and active region dynamics in the corona. Thirdly, and more important, is that EUV and FUV spectroscopic observations can be carried out simultaneously with quantitative measurements of magnetic fields in the chromosphere and photosphere with 0.1″ to 0.2″, taken by the UV-Visible-IR telescope. This would be an enormous help in associating an accurate magnetic geometry with the EUV-FUV spectra. Finally, unlike IRIS, the single-mirror off-axis design of the telescope allows us to observe faint structures in the corona far from the solar disk.

3.2. Technical feasibility of each key element

The strawman instrumentation draws heavily on current technology under development by the international EUV/FUV spectroscopic community. Technical feasibility of each key technology is briefly described below.

3.2.1. Two element optical layout

In order to improve throughput performance, minimizing the number of optical elements is essential; the spectrograph consists of two optical elements, i.e., an off-axis parabola primary mirror and a concave grating. The two-element spectrograph design was first developed and flown for EIS onboard Hinode and it has since been refined to meet various requirements for RAISE, VERIS and EUNIS rocket payloads.

3.2.2. The telescope mirror and mirror coating

For off-limb solar observations the single-mirror telescope greatly reduces stray light, as compared to an on-axis, double-mirror design. In addition, a secondary mirror would not only reduce throughput by adding another reflection but would also be vulnerable to degradation due exposure to very high solar flux. Thus the decision is made for a single-mirror telescope.

Increasing the size of the primary mirror gives a significant improvement in throughput. If the diameter of the mirror can be increased twice, the effective area is improved by a factor 4. 30 cm or larger diameter gives 4 times or larger throughput, as compared with EIS (diameter 15cm).

Driven by requirements for EUV photolithography, EUV optics with very low scatter and diffraction limited performance are available. For example, the optics developed for the MET EUV photolithographic system have a slope error of 0.3 to 1.0 microradians, and microroughness of 0.1 to 0.2 nm over spatial frequencies from 9 nm to 4 mm (Goldberg et al. 2005).

A single coating on the primary mirror – without division in sections for EUV and FUV ranges - results in good performance across a broad wavelength range. The suggested coating is described in Figure 3.1. It consists of a broadband Si/Mo multilayer with a 5 nm B_4C topcoat. The B_4C topcoat is semi-transparent in the EUV but gives reasonable reflectance at longer wavelengths as shown in Figure 3.1 (left). The single coating minimizes risk and complexity for the primary mirror associated with dividing the solar illuminated mirror into segments with different coatings. Recent advances in stabilizing multilayer for higher temperature performance will be incorporated into the multilayer coating design.

3.2.3. Grating and grating coating

To realize seamless temperature coverage in the 10^4 to 10^7 K range, the spectrometer needs to cover between 2 and 4 wavelength bandpasses over a range from 10 nm to 120 nm. To accommodate this broad wavelength range, the grating is divided into two segments. The ruling density, groove geometry and figure of each segment is optimized for the specific wavelength range. Each grating segment is coated individually. A process is envisioned where each coated grating segment would be contacted/cemented to a common plate. This plate would then be installed into the instrument.

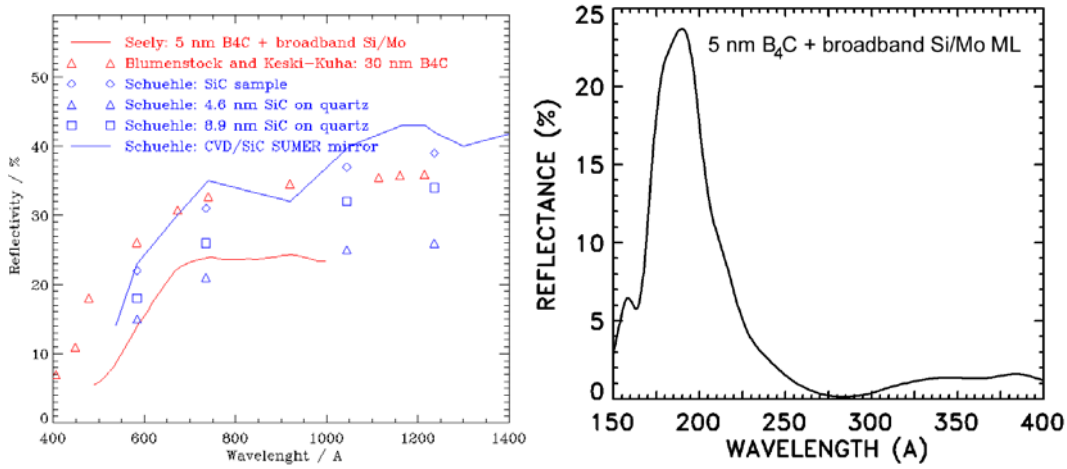

Figure 3.1. Reflectivity of the proposed primary mirror coating. The red curve in the left panel shows the performance of the coating from 50 to 120 nm. The right panel gives the EUV coating performance.

3.2.4. Solar blind detectors for EUVS

Enhanced technology detectors with larger format and faster readout are under development for space flight. The intensified (CMOS-APS) active pixel sensor (flown on NASA's EUNIS and RAISE rocket flights) has the promise of exceptionally fast image readout with quick access to specific pixel areas. The intensifier with opaque anode ensures that the detector is "solar blind" and focal plane filters, to suppress visible solar radiation, are not needed. The opaque photocathode on the microchannel plates will ensure very high sensitivity in selected spectral ranges.

At shorter wavelengths (in the EUV), back side thinned, large format, fast readout silicon based CCD and APS detectors are highly efficient, low-noise, fast-readout detectors. The backside illuminated detectors will be fitted with focal plane filters to provide rejection of the visible solar radiation scattered from the grating. The performance of currently available intensified CCD and EUV backside illuminated CCDs are suitable for the EUVS mission while similar CMOS-APS sensors are presently under development.

3.2.5. Removal of metal filters and thermal control concept

To achieve low scatter, higher throughput and broad wavelength coverage, the EUVS strawman design has no prefilters in the front aperture. These prefilters have historically been used to protect the multilayers from the incident solar radiation. With one solar constant illuminating the primary mirror, the temperature of the mirror is expected to increase to 50 °C

or 60 °C provided that a passively cooled plate is provided. Similar systems for NEXUS instrument (proposed as a SMEX) and SUMER (flown on SOHO) have had very reasonable properties, but a more detailed solution has yet to be found. A heat rejection mirror will be placed in front of the slit plane to reject the majority of the solar radiation before the slit.

3.3. Strawman Instrument

3.3.1. Optical Design

The EUVS instrument schematic is shown in Figure 3.2. As shown in the schematic, solar radiation is incident on the EUVS off-axis paraboloid primary mirror (ϕ~40cm). The primary mirror focuses an image of the solar disk on the entrance slit and reflective slit jaws. Solar radiation falling outside the instrument field of view is redirected out the front of the instrument with a heat rejection mirror following a similar design used for the SUMER/SOHO and the NEXUS instruments. A slit selection mechanism interchanges and precisely places various slits in the telescope focal plane.

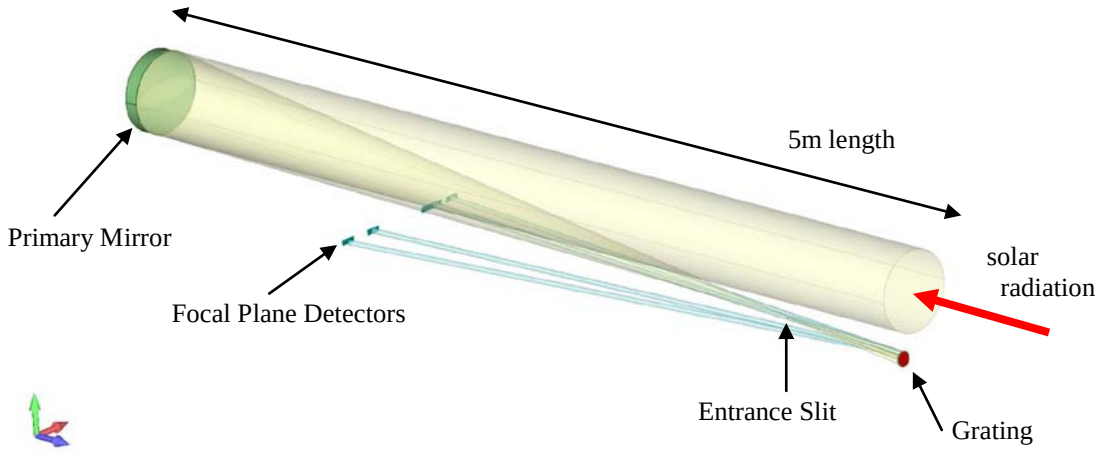

Figure 3.2. EUVS strawman instrument schematic

Solar radiation passing through the slit is reflected and dispersed by the elliptical, variable line space grating onto the various focal plane detectors. The grating may be divided into as many as four separate gratings to cover the various wavelength bands. The figure, ruling, and coating of each grating segment are optimized to meet the requirements of the particular wavelength range. The spectra are recorded by large format, electronic detectors.

3.3.2. Effective Area

Results from a conservative first order effective area calculation for the strawman instrument are given in Figure 3.3. The effective area was calculated using the expected performance of a next-generation, broadband multilayer reflection coating for both mirror and grating. A groove efficiency of 0.40 and detector efficiency of 0.5 were assumed. Each

channel used 0.25 of the mirror total area. The calculated effective area is a factor of >10 higher than previous instrumentation as shown below. Further optimization and refinement of this calculation would likely show considerable improvement. In particular, the use of only two grating sections for the EUV and the FUV ranges will enhance by a factor two the throughput.

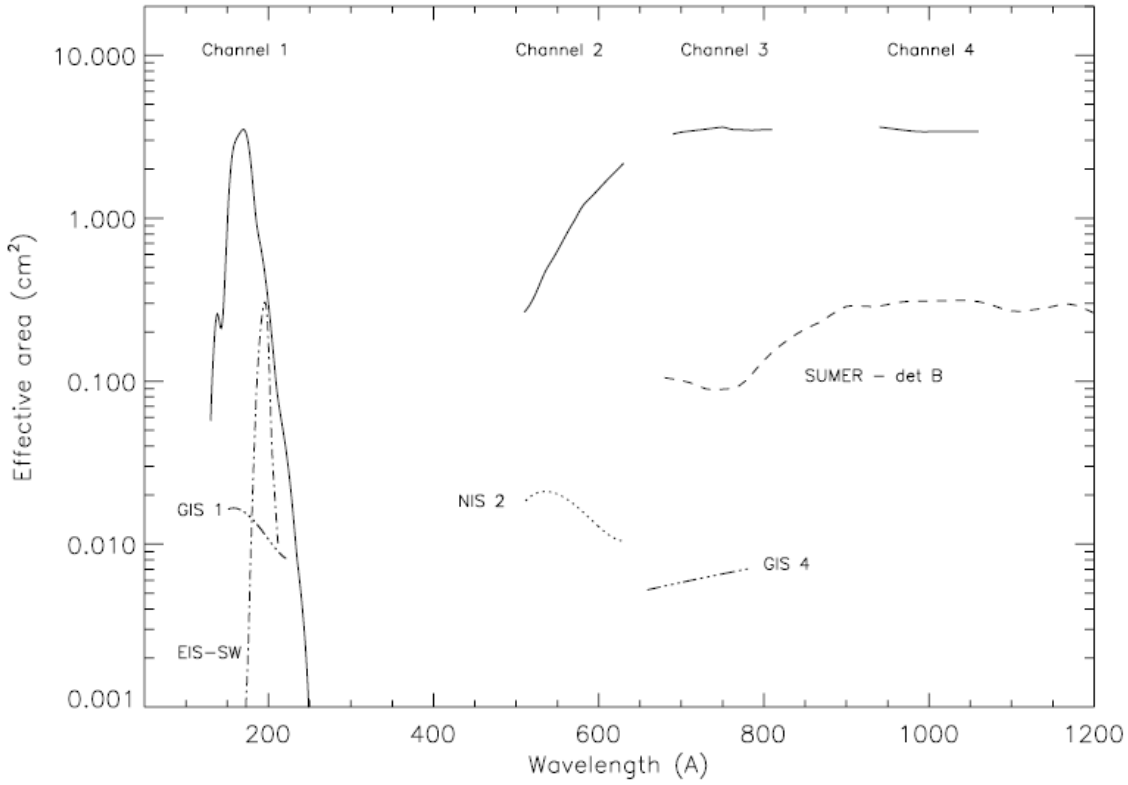

Figure 3.3. Effective area of the EUVS strawman instrument. Previous comparable effective areas for EIS, CDS and SUMER are plotted for comparison.

3.3.3. Selection of wavelength bands

Four spectral bands were chosen as representative for the purpose of developing the strawman design. The bandpasses will be further optimized to meet the specific Solar-C scientific requirements.

3.3.4. Expected count rates and Temperature Coverage

The expected count rates for the emission lines in the four channels have been calculated and are given in Appendix 3-A. The temperature coverage of the bandpasses is superb as shown in Figure 3.4. The total counts in each line for quiet Sun, active regions and flares are given for a spatial sampling of 0.33". Count rates larger than 100 counts/s will allow rastering of quiet-Sun plasmas with 1-s exposure times in the hydrogen H I and the carbon C III lines. Spatial binning and slightly longer integrations allow rapid scanning in a wide variety of fainter lines (C II, He I, O V, Ne VIII, Fe IX, Fe X, etc.) and will yield extraordinary

spectroscopic images of the quiet Sun. Active region count rates of several hundred counts/s with 0.33" spatial resolution enable spectroscopic imaging of active region flows and dynamics. The EUVS line list includes high temperature, well isolated emission lines in flares and active region plasmas.

Figure 3.5 compares the count rates expected for the Solar-C spectrometer with the currently operating SoHO/SUMER and Hinode/EIS and planned IRIS. It is obvious that the Solar-C spectrometer collects much more numbers of photons in 1 sec integration time, even though the spatial resolution is 0.33 arcsec.

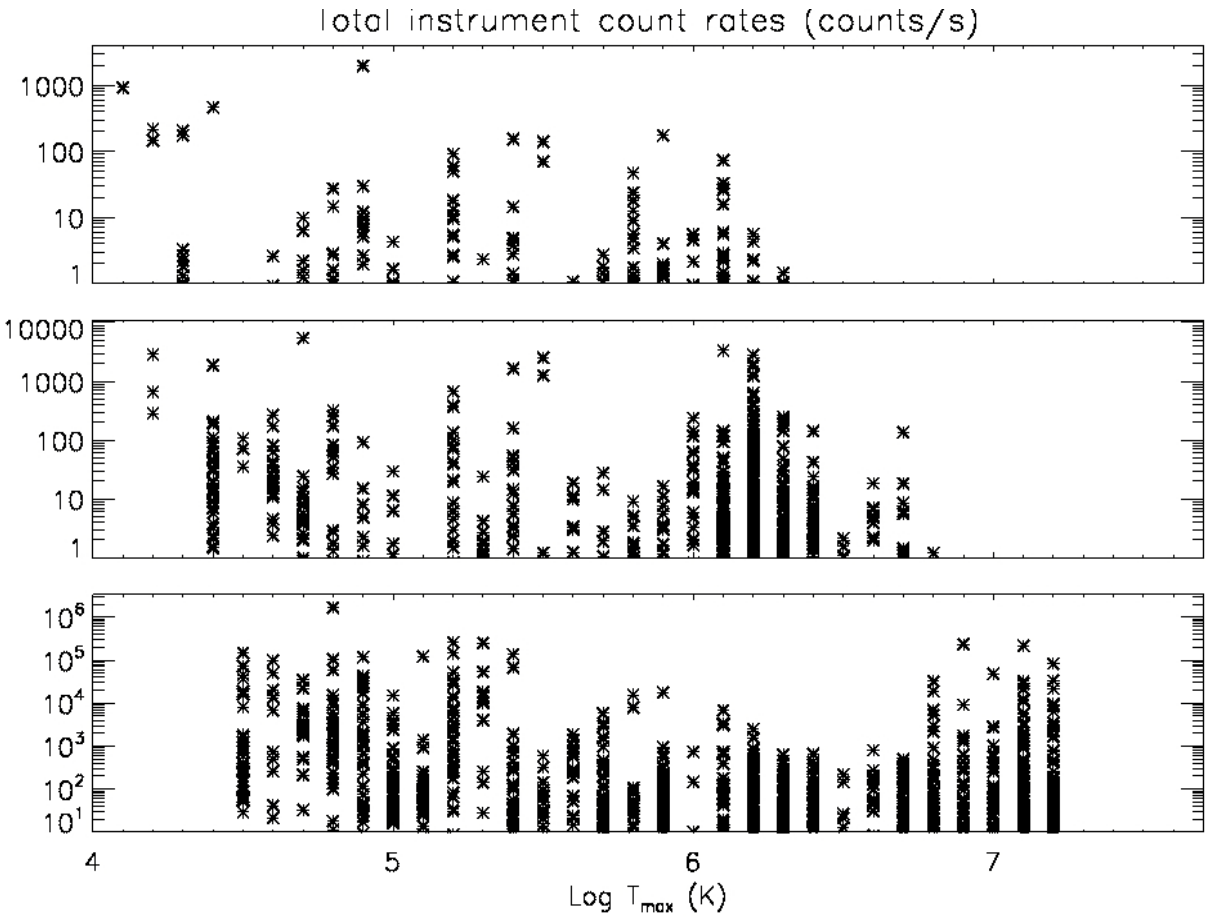

Figure 3.4. Expected Count Rates. The expected count rates are plotted as a function of ionization temperature for a spatial sampling of 0.33". The plots show total counts in each line plotted at their ionization temperature. Each asterisk corresponds to a specific emission line. The top panel corresponds to typical quiet Sun; the middle panel shows typical active region count rates, and the bottom panel shows flare plasma count rates.

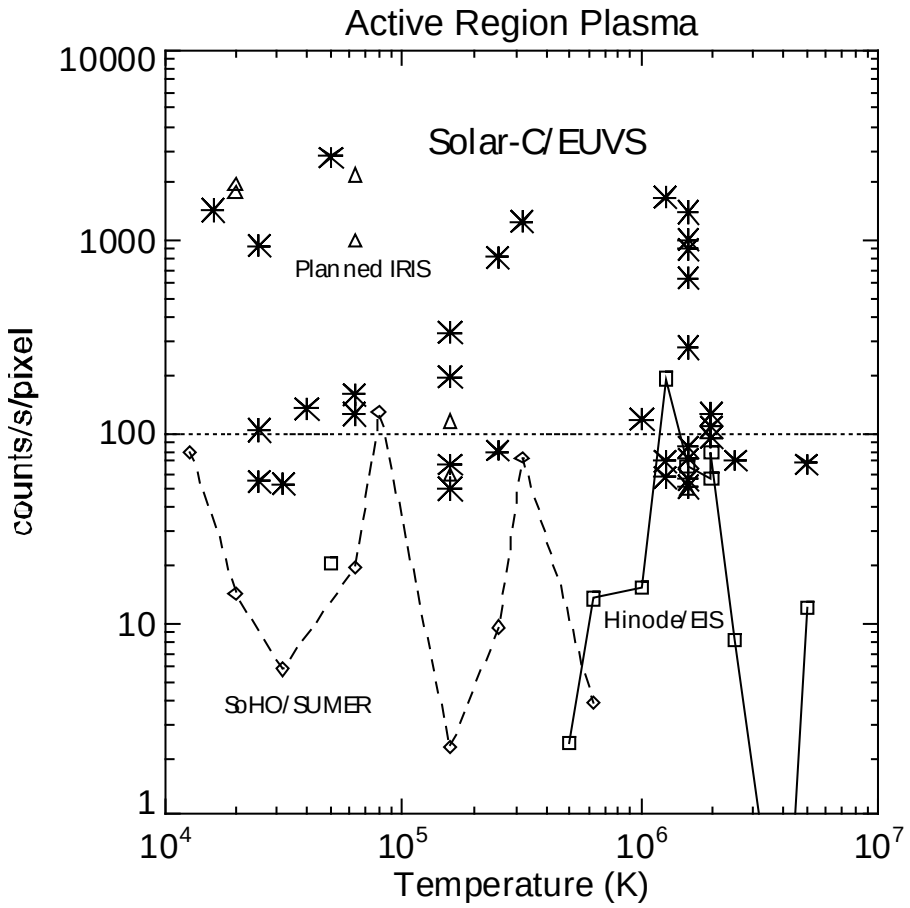

Figure 3.5. Count rates for typical active regions. The Solar-C spectrometer is compared with currently operating SUMER and EIS and planned IRIS. The expected count rates are plotted as a function of ionization temperature for the spatial sampling of each spectometer. Each asterisk corresponds to a specific emission line observed with the Solar-C spectrometer. Triangles, diamonds, and squares are for IRIS, SUMER, and EIS, respectively.

3.3.5. Improvements over previous instrumentation

Critical improvements over previous instrumentation are obtained with this strawman design as follows:

- >18 improvement in spatially resolved area on the solar disk
- >10 improvement in effective area
- complete temperature coverage ($10^4 – 10^7$ K in active regions with $\Delta(\log T) < 0.3$)

A summary table of the EUVS scientific characteristics is given in Table 3.2.

Table 3.2. EUVS scientific summary characteristics.

Plate scale	~0.16"/pixel (sampling comparable to Hinode SOT)
Simultaneous field of view	Slit: 0.16", 0.32", 0.96"; Slot: 10", 40", 200" Slit/slot length: 200" nominal, >300" extended
Maximum raster width	+/- 75" nominal, +/- 200" extended
Wavelength range	four channels (Å):130-250; 510-630; 690-810; 940-1060;
Exposure times	1-5 s with 0.33" spatial sampling 0.1-0.5 s in active regions with 1.0" spatial sampling
Velocity resolution	Doppler (centroid) shift measurement accuracy <3km/s Turbulent velocity (width) <10km/s
Temperature coverage	$10^4 - 10^7$ in active regions with $\Delta(\log T) < 0.3$

3.4. Strawman design details

Further details of the strawman design are given in Table 3.3. Provisions have been made in the strawman design for a slit jaw camera imaging system and a possible closed loop servo-control system using a correlation tracker system and an articulated primary mirror for image stabilization. Solar image rastering is accomplished by tilting the primary mirror.

Table 3.3. EUVS strawman design – nominal performance

Telescope	**Baseline or nominal value**
Type	off-axis paraboloid mirror, single coating optimized for both long and short bands.
optical properties	40cm usable aperture diameter, 400cm focal length, 30cm off-axis distance, <λ/80rms, <0.5nm microroughness, 19.4 microns/arcsecond plate scale.
Mirror blank	Lightweighted premium grade zerodur blank (or equivalent).
Stabilization	<0.03 arcsecond jitter suppression, >5Hz bandwidth possible
Geometric blur	~0.26" at 75" roughly circular field of view, ~0.52" at 150" roughly circular field of view
Slit/slot assembly	**Baseline or nominal value**
General	6 slits/slot positions, front face with reflective coating, >327" length
selected widths	Slits: 0.16", 0.32", 0.96"; Slots: 10", 40", 200"
Slit jaw imaging	**Baseline or nominal value**
General	Projecting a high-quality image of the slit jaws onto a CCD camera. Feeds a CCD camera used for correlation tracker system.
Design char.	field of view: 400" x 400"; plate scale: 0.2"/pixel; CCD format: 2K x 2K.
Filter bandpass	Possible selections include: Ly-α line (121.6 nm), Tmin(160 nm), Mg II line (280 nm), Ca II (393 nm), G-band (430.5 nm), Hα line (656.3 nm), TiO band (705.7 nm).
Correlation tracker system	If implemented is expected to be similar to that used on Hinode/SOT bandwidth (10-30 Hz). Dedicated small-format CCD camera.
Spectrograph characteristics	**Baseline or nominal value**
General	Optimized single reflection EUV spectrograph, elliptical substrate with variable line spacing as required, grating figure and ruling individually optimized for the bandpass/quadrant. Typical blur: <1 pixel over majority of wavelength range for +/- 50" at slit center. Coating selected and optimized for each quadrant. Detector optimized for the bandpass/quadrant
EUV1 bandpass (130-250Å)	detector: 12kx2k mosaic CCD/APS, backside illuminated, 13.5 μm pixel size. stray light rejection: thin film metallic filter with supporting mesh. spatial plate scale: 0.16"/pixel. spectral plate scale: 0.010 Å/pixel, 17.7 km/s-pixel@170Å. Grating: m~4.35, elliptical figure, 4000line/mm VLS ruling, -1 order.

EUV2 bandpass (510-630Å)	detector: 5kx2k CCD/APS, 17 μm pixel size with MCP intensifier with KBr photocathode. stray light rejection: solar-blind intensifier spatial plate scale: 0.20"/pixel. spectral plate scale: 0.026 Å/pixel, 13.7 km/s-pixel@570 Å. grating: m~4.35, elliptical figure, 2000line/mm VLS ruling, +1st order.
EUV3 bandpass (690-810Å)	detector: 5kx2k CCD/APS, 17μm pixel size with MCP intensifier with KBr photocathode. stray light rejection: solar-blind intensifier. spatial plate scale: ~0.20"/pixel spectral plate scale: ~0.025 Å/pixel, 10.0 km/second-pixel @ 750Å. grating: m~4.35, elliptical figure, 2000line/mm VLS ruling, -1st order.
EUV4 bandpass (940-1060Å)	detector: 5kx2k CCD/APS, 17 μm pixel size with MCP intensifier with KBr photocathode. stray light rejection: solar-blind intensifier. spatial plate scale: ~0.20"/pixel. spectral plate scale: ~0.024 Å/pixel,7.2 km/s-pixel@1000 Å. Grating: m~4.35, elliptical figure, 2000line/mm VLS ruling, +1st order.

3.5. Further optimization for better instrument

Considerable optimization activities remain for the spectrograph instrument. Science goals and associated measurement requirements need further definition. The trades relating to instrument wavelength ranges need further definition. The number of channels drives instrument complexity. The wavelength ranges should be placed more conveniently on various detectors. The size and f# of the primary mirror strongly drive the instrument mass and envelope. The primary mirror size also drives the design of the articulated mirror mechanism and associated requirements. The optical design may be further optimized for the wavelength ranges and detectors selected. The coatings of the mirror and gratings could also be optimized for the particular application.

Appendix 3-A. EUVS count rates for the brightest lines

Count rates were calculated for the EUVS instrument using the CHIANTI spectral code for the quiet Sun, active region and flare plasmas. The counts listed are for the total emission line in a 0.33" spatial bin. The emission lines are sorted by channel and ionization temperature. The ion and associated ionization temperature are included for reference. For the quiet Sun, all lines with a total count rate of >10 counts/s are included. For active regions, emission lines with a total count/s of >50 were tabulated. For flare plasmas, those emission lines with count rates >10000 counts/s are included. Many valuable faint diagnostic lines have not been tabulated.

QUIET SUN INTENSITIES

Ion	Wvl.(A)	Tmax	Count/s
Fe IX	171.073	5.90	86.9
Fe X	174.531	6.10	36.4
Fe X	177.240	6.10	16.4
Fe XI	180.408	6.10	14.1
He I	584.335	4.40	230.7
O V	629.732	5.40	76.5
Mg X	609.794	6.10	13.0
O III	703.854	4.90	14.7
N IV	765.147	5.20	29.5
O IV	787.710	5.20	24.9
O IV	790.199	5.20	45.1
Ne VIII	770.410	5.80	23.5
Ne VIII	780.325	5.80	11.9
H I	949.745	4.20	71.2
H I	972.538	4.20	107.3
H I	1025.724	4.10	453.1
C II	1036.339	4.30	87.5
C II	1037.020	4.30	102.2
C III	977.020	4.90	98.9
N III	991.577	4.80	13.6
O VI	1031.914	5.50	69.6
O VI	1037.615	5.50	34.9

The lines counted in this table have all a count rate greater than 10.0000

ACTIVE REGION INTENSITIES

Ion	Wvl.(A)	Tmax	Count/s
Fe VIII	167.486	6.00	71.0
Fe VIII	168.173	6.00	118.0
Fe VIII	168.544	6.00	58.7
Fe IX *	168.647	6.10	59.8
Fe IX	171.073	6.10	1671.6
Ni XI	148.374	6.20	56.3
Ni XII	152.154	6.20	73.4
Ni XII	154.162	6.20	50.4
Ni XIII	157.729	6.30	125.3
Ni XIII	164.150	6.30	90.8
Ni XIV	170.500	6.30	72.2
Ni XIV	171.370	6.30	108.2
Fe X	174.531	6.20	1408.2
Fe X	175.263	6.20	153.2
Ni XV	176.741	6.40	71.2
Fe X	177.240	6.20	637.8
Fe XI	178.060	6.20	57.7
Fe XI	180.408	6.20	900.6
Fe X	180.441	6.20	62.9
Fe XI	181.137	6.20	59.0
Fe XI	182.169	6.20	128.8
Fe X	184.537	6.20	110.7
Fe XII	186.887	6.20	91.5
Fe XI	188.232	6.20	195.6
Fe XI	188.299	6.20	71.0
Fe XII	192.394	6.20	108.4
Fe XII	193.509	6.20	212.0
Fe XII	195.119	6.20	277.7
Fe XIII	202.044	6.20	85.1
He I	584.335	4.40	936.4
O IV	554.513	5.20	50.4
O V	629.732	5.40	822.3
Si XII	520.666	6.30	94.8
Si XI	580.920	6.20	51.6
Mg X	609.794	6.20	1010.1
Mg X	624.943	6.20	613.9
O III	703.854	4.80	125.8
O II	718.506	4.60	134.1
O II	718.568	4.60	86.7
O V	760.446	5.40	80.1
N IV	765.147	5.20	195.3
S V	786.470	5.20	67.6
O IV	787.710	5.20	184.4
O IV	790.199	5.20	334.0
Mg IX	706.036	6.10	70.6
Ne VIII	770.410	6.20	636.5
Ne VIII	780.325	6.20	319.7
H I	949.745	4.20	143.0
H I	972.538	4.20	336.1
H I	1025.724	4.20	1441.1
C II	1036.339	4.40	95.0
C II	1037.020	4.40	103.3
S II	1045.765	4.40	54.8

C III	977.020	4.70	2728.3
N III	989.799	4.80	86.6
N III	991.577	4.80	159.3
C II	1010.373	4.50	53.1
O VI	1031.914	5.50	1258.7
O VI	1037.615	5.50	631.0
Si VIII	944.467	6.10	57.7
Fe XVIII	974.860	6.70	68.3

The lines counted in this table have all a count rate greater than 50.0000

FLARE INTENSITIES

Ion	Wvl.(A)	Tmax	Count/s
Fe XXIII	132.906	7.20	16711.9
Fe XXII	135.791	7.10	10684.5
Fe XXII	156.019	7.20	10742.9
Fe XXIV	192.029	7.20	41466.6
He I	584.335	4.50	22806.8
O III	599.590	4.90	21647.0
O IV	554.513	5.20	16856.3
O IV	609.829	5.20	13597.1
O V	629.732	5.30	123868.6
Mg X	609.794	6.80	15972.9
Fe XX	567.867	7.10	14098.6
Fe XIX	592.236	7.00	24262.3
O III	702.337	4.90	15646.4
O III	702.838	4.90	14272.3
O III	702.896	4.90	12071.4
O III	702.900	4.90	19085.9
O III	703.851	4.90	19602.9
O III	703.854	4.90	58808.9
O II	718.506	4.70	17162.6
O II	718.568	4.70	11081.7
N IV	765.147	5.10	61374.2
O V	760.446	5.30	26905.2
S V	786.470	5.20	26186.6
O IV	787.710	5.20	71908.2
O IV	790.112	5.20	13861.8
O IV	790.199	5.20	128603.8
Fe XX	721.559	7.10	108802.5
Fe XXI	786.162	7.10	16011.5
H I	972.538	4.50	18466.2
C III	977.020	4.80	834613.1
N III	989.799	4.80	29670.6
N III	991.577	4.80	52456.0
C II	1010.373	4.60	10053.1
H I	1025.724	4.50	72905.9
H I	1025.725	4.50	36616.4
C II	1036.339	4.60	24846.7
C II	1037.020	4.60	49448.2
O VI	1031.914	5.40	67592.8
O VI	1037.615	5.40	33837.3
Fe XVIII	974.860	6.90	116048.3

The lines counted in this table have all a count rate greater than 10000.0

Chapter 4: X-ray Imaging (Spectroscopic) Telescope

4.1. X-ray Telescope for the Overall Solar-C/Plan-B Science

In addition to its own scientific standpoint, the X-ray Imaging (Spectroscopic) Telescope shall have close scientific synergy with other Solar-C/Plan-B instruments to maximize outcome from the Solar-C observatory as a whole. While SUVIT and EUVS chiefly observe lower layers of solar atmosphere, the X-ray Imaging (Spectroscopic) Telescope observes the uppermost layer of the Sun, the corona, to achieve comprehensive understanding on magneto-hydrodynamic processes across the entire layers of solar atmosphere with various degrees of ionization. Science with Solar-C/Plan-B relevant to the corona shall address (a) forms and mechanisms of storage and dissipation of energy that was transferred upwards through photosphere and chromosphere, (b) quantitative understanding on the physics of magnetic reconnection which is believed to be the central engine for converting magnetic energy to thermal and kinetic energy of coronal plasmas, and possibly, (c) diagnostics on wave phenomena along magnetic field lines. Investigation of mechanism(s) for explosive energy release may also have relevance to space weather studies.

In pursuing such science capabilities, we consider the following two possibilities for the Solar-C/Plan-B X-ray Imaging Telescope:

(1) Photon-counting imaging spectroscopy X-ray telescope
(2) Ultra-high spatial resolution normal incidence EUV telescope

The photon-counting telescope adopts grazing-incidence optics and aims to perform imaging-spectroscopy of the soft X-ray corona from below 1 keV up to ~5 keV with its main scientific target being quantitative investigation of dissipation processes that act in the corona such as heating of active region corona and magnetic reconnection in flares. The upper-end of the energy range can be increased up to ~10 keV if we adopt a smaller grazing-incidence angle (~5 keV with 0.9 degrees while ~10 keV with 0.45 degrees) as will be described in the subsequent part of this report. The energy coverage up to ~10 keV will be particularly powerful in investigating heating and acceleration of plasmas in the reconnecting magnetic field structure in flares.

While the photon-counting telescope should be powerful in studying energy dissipation processes in the corona, it may have less overlap with the other Solar-C/Plan-B instruments (SUVIT and EUVS) in terms of temperature coverage (hence less overlap in the atmospheric layers of the Sun) and spatial resolution because of its grazing-incidence optics. Taking this point into account, the other possibility, the ultra-high spatial resolution normal incidence telescope has been considered. The normal incidence telescope puts its emphasis on delivering complementary observables for EUVS, providing context imagery information for EUVS with higher spatial

resolution than EUVS, with a wide field-of-view and with overlapping temperature coverage thus aims to investigate connection between transition region and the low corona.

4.2. Photon-Counting Imaging Spectroscopy X-ray Telescope

4.2.1. Scientific Objectives

The photon-counting imaging spectroscopy X-ray telescope will provide the first-ever opportunity to perform imaging-spectroscopic investigation of the corona in soft X-ray wavelength range, from below 1 keV up to ~5 keV (Figure 4.1).

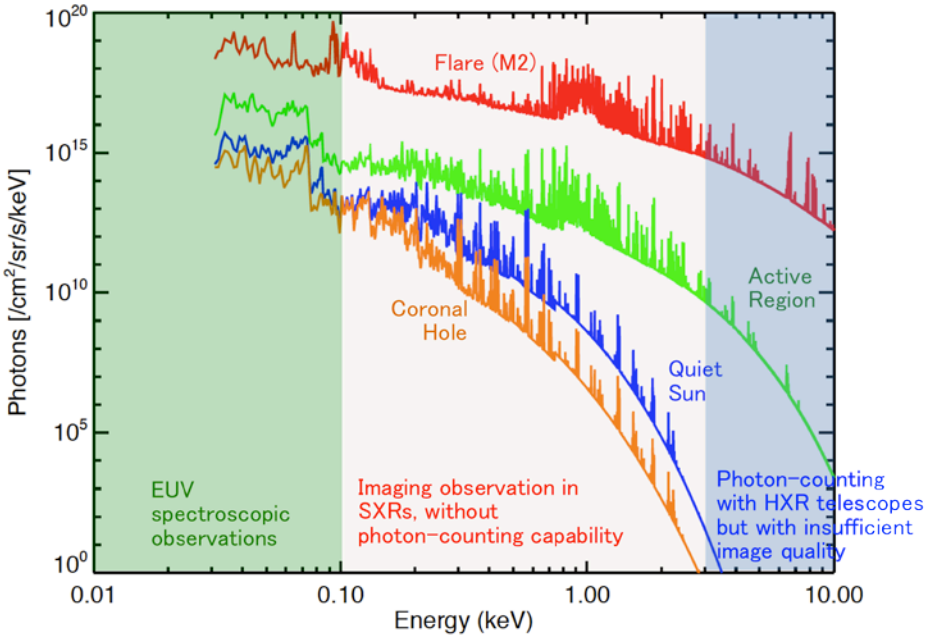

Figure 4.1. Status of past imaging-spectroscopic investigation in EUV/X-ray wavelengths overlaid with model solar spectra synthesized with CHIANTI Ver. 6. Imaging-spectroscopic investigation of the soft X-ray corona has so far remained totally unexplored.

Among Plan-B science goals detailed in Section 2, two main scientific targets of this telescope with photon-counting capability is summarized as follows:

(1) Quantitative investigation of structure and dynamics of magnetized plasmas around the site of magnetic reconnection.

It is widely perceived, based on imaging observations with *Yohkoh*, that magnetic reconnection is the engine for liberating magnetic energy for plasma heating and particle acceleration in solar flares. Nevertheless, one has to say that understanding of the reconnection process, such as structures of slow and fast shocks, and temperatures and heating status of upstream and downstream plasma flows around the shocks, still

remains almost unclear. The most critical piece of information that has been missing to tackle this problem is spatially-resolved spectral information in the reconnecting magnetic structure. Previous X-ray telescopes (*Yohkoh* SXT and *Hinode* XRT) could only provide a single 'representative' temperature in the form of filter-ratio temperature which is more like a mean temperature weighted by the differential emission measure (DEM) distribution over the line-of-sight plasmas (Acton, Weston, and Bruner 1999). This feature of filter-ratio temperatures tends to smear out any spectral features across coronal structures unless the bulk of plasmas (namely, those with the largest fraction of DEM) changes its spectral shape. The photon-counting imaging-spectroscopy of reconnecting magnetic structure will characterize plasma status upstream and downstream of shock structures associated with magnetic reconnection. This would, in turn, identify location and structure of the reconnection shocks. Spectral information with low-scattering focusing optics for a variety of flares should provide key clues in quantitatively understanding the physics of magnetic reconnection.

While the photon-counting X-ray telescope can derive electron temperatures as the continuum Bremsstrahlung emission, emission-line diagnostic with EUVS can deliver information on ion temperatures. One remarkable possibility is that the combination of spatially-resolved electron and ion temperatures will provide us with significantly powerful tool for studying electron and ion heating especially in the downstream of the shocks.

(2) Investigate temperature structure of active region corona, in particular that for high temperatures (above ~5 MK)

One of the key information necessary for unravelling the mechanism(s) of coronal heating, in particular the hot corona around active regions, is to identify evolution of spectral structures together with their distribution across lateral (across active regions) or in vertical (hight distribution) extents. This will enable one to locate site of heat input (hence dissipation site) across the area and subsequent heat flow that results in generating the hot corona. This approach may be particularly effective if the heating is intermittent (*i.e.*, by nano-flares). The non-dispersive nature of photon-counting imaging-spectroscopy, in contrast to dispersive, scanning, instruments will be effective in identifying such heat input and subsequent flow in the corona by measuring spectral evolution taken simultaneously across a wide field-of-view. Instruments that utilize EUV wavelengths may not be suitable for this investigation due to lack of strong EUV emission lines at high temperatures from active regions.

Discovery space with imaging spectroscopy of an extended energy range

In this report, the X-ray grazing-incidence angle to the mirror of 0.9 degrees set as the baseline. While this grazing-incidence angle provides certain capability for performing imaging-spectroscopic observations of active regions (see below for details), the highest energy available for flare observations would be limited to ~5 keV (Figure 4.13). An interesting possibility which greatly enhances observation capability for flares, with decreased capability for active regions, is to go to an even smaller incidence angle. For example, the grazing-incidence angle of 0.45 degrees will increase the highest energy

available for flare observations to as high as ~10 keV (Figure 4.14).

The small incidence angle (*e.g.*, 0.45 degrees) for the photon-counting telescope will enable imaging spectroscopy in the energy range of a few to ~10 keV. This performance provides the following discovery space for flare sciences in the field of reconnection study:

(1a) Identification of high-temperature plasmas in the flaring magnetic field structure

The increase in the energy range up to ~10 keV will enable one to observe Fe (~6.7 keV) and Fe/Ni (~8 keV) line complexes together with thermal-bremsstrahlung continuum from high temperature plasmas in energy spectra of flares. When combined with the expected imaging-spectroscopic performance of the telescope shown in Figure 4.15, this means that we'll be able to track spatial distribution and its evolution of super-hot (> ~30 MK) plasmas with angular scale and temporal resolution combination of 2" with every 5 s (or 1" with every 20 s). Imaging spectroscopy with such fine spatial scale and temporal resolution will enable us to identify site of in-situ heating and to discuss heating of plasmas in the reconnecting magnetic field structure.

(1b) Evolution of non-thermal (or supra-thermal) electron population

The extended energy coverage should also provide breakthrough in understanding particle acceleration mechanism(s) in solar flares. It is generally believed that initial particle acceleration takes place inside the reconnection region (forming reconnection outflows), followed by transport to and further acceleration somewhere at the outer part of it (see Tsuneta & Naito (1998) for the case of fast-shock acceleration). However, it has so far remained unclear, or even unexplored, where and how particles (ions and electrons) are accelerated in the reconnecting structure. While soft X-ray imaging-spectroscopy of the reconnecting magnetic structure should naturally be powerful in identifying, and tracing the evolution of, e.g., shock structures associated with magnetic reconnection, observations with the extended energy range of up to ~10 keV (as compared to ~5 keV in the baseline design) would provide enourmous leap in unravelling the nature of particle acceleration in flares. This is because the observations will deliver information on how and where supra-thermal electron distributions (manifest themselves as power-law X-ray spectra) grow out of the ambient thermal electron distribution, especially near the onset of particle acceleration where soft X-ray emission from thermal plasmas along the line of sight is yet to be dominated. As the mean energy of thermal electrons is typically 2-3 keV, X-ray emission by supra-thermal electrons can be well identified in the ~5-10 keV range. Note there has been a number of observations reported since 1980's that non-thermal X-ray emission from flares may extend down below 10 keV. Furthermore, there is related observational support from in situ observations of the Earth's magnetosphere that supra-thermal electrons appear in energy spectra around 4 times as large as thermal energy (2 keV) near the reconnection region (see, e.g., Imada et al. 2007). Thus, the extended energy coverage, coupled with high dynamic-range imagery with soft X-ray focusing optics, will give us a unique opportunity to locate the site of electron acceleration and to study the nature of the acceleration in relationship with the reconnecting magnetic field structures such as

shocks.

Table 4.1. Key parameters of the photon-counting X-ray telescope.

Item	Description	Remarks
Overall description	Perform imaging investigation of the X-ray corona with the following two modes. Two modes selectable (not simultaneously). (1) Photon-counting mode: Imaging spectroscopy for a limited region of interest. (2) Photon-integration mode: Imagery with the entire, or part of, the imaging array. Walter Type I (-like) grazing-incidence telescope with a segment mirror. A CMOS-APS detector to be used as the focal-plane imaging array.	
Envelope dimensions of the telescope	~40cm × 40cm × 4.5m (TBD)	Telescope plus the focal-plane camera. Includes housings.
Angular resolution & Temporal resolution for photon counting	For photon-integration mode: ~1" (~0.5"/pixel) For photon-counting mode: For active regions and flares, generate an X-ray spectrum for spatial area whose size* ~< 2"×2" (goal) / ~4"×4" (min.) within every < 10 s (goal) / 30 s (min.)	* Spatial area size in which a spectrum with good counting statistics can be synthesized with reasonable integration time.
Field of view	For photon-integration mode*: ~13'×13' For photon-counting mode**: >~3'×3' (goal) ~80"×80" (nom.) ~40"×40" (min.) 'Elongated' FOV (such as ~40"×13') is possibile	* Off-axis image blur not taken into account. ** Area with which photon-counting analysis can be performed.
Energy range	~0.5-5 keV* (baseline) ~0.5-~10 keV* (under study)	* Energy range above 2 keV available during flares, with photon-counting mode.
Energy resolution	ΔE (FWHM)*: ~130 eV (goal), 150 eV (nom.) @ 5.9 keV ~74 eV (goal) @ 1.5 keV Readout noise: ~43 eV FWHM (goal)	* Includes readout noise.
Data rate	(With the event processing in Section 6.2.3.4) max. 110 Mbps for 512×512 photon-counting area max. 6.9 Mbps for 128×128 photon-counting area	No data compression assumed. For 10-bits A/D conversion.
Pre-filter	Same as Hinode/XRT.	Entrance filter for rejecting visible light and heat input to the telescope.
Visible-light optics	TBD	
X-ray flux monitor	TBD; for controlling X-ray flux attenuation filters.	

Besides photon-counting capability, the telescope will also be capable of providing images of soft X-ray corona (with conventional photon-integration, or 'flux mode') with the highest angular resolution of 1 arcsec (0.5 arcsec pixel size) as a solar X-ray imager. Such images will deliver context information for other Plan-B instruments.

By adopting an X-ray CMOS active-pixel sensor (APS) device for the focal-plane imaging array, the photon-counting X-ray telescope will be free from "spill-over" of signal charges for over-exposed images which is often seen with soft X-ray imagers employing CCDs without anti-blooming pixel architecture, including *Hinode* XRT and *Yohkoh* SXT. The spill-over-free feature of the telescope, combined with high dynamic-range focusing optics imagery, should be particularly powerful for the soft X-ray corona, in detecting faint features that could be present right next to a bright feature, such as material flows and ejecta associated with magnetic reconnection.

With the advent of recent progress in high-speed, low noise, CMOS-APS detectors, the photon-counting X-ray telescope for Solar-C/Plan-B should provide breakthrough in our understanding on energy storage and dissipation in the corona, including the physics of magnetic reconnection. Key parameters of the photon-counting telescope are given in Table 4.1.

4.2.2 Required Specification for the Instrument

4.2.2.1 Optics

Photon-counting imagery in X-rays needs be done with grazing-incidence optics that can cover, continuously, a wide spectral range of X-ray emission from the corona. Normal-incidence imagers may not be suitable for the photon-counting purpose because (1) they can image only a narrow wavelength range for each passband, and (2) since the wavelengths for normal-incidence imagers are in the EUV range whose photon energies below ~100 eV, silicon detectors such as CMOS-APS, whose best-expected FWHM energy resolution would be around ~50 eV at those energies, are not sufficient for resolving fine spectral features in the EUV range. A grazing incidence telescope is chosen to utilize the sensitivity to the hotter plasmas and the associated spectral lines, in soft X-rays.

4.2.2.2 Angular Resolution

It has been suggested by recent *Hinode* EIS observations (Hara *et al.* 2008) that sub-arcsecond structures in coronal loops may be important in understanding elementary processes of coronal heating for active regions. In this regard, pixel size of less than 1", say, 0.5", would be preferable for photon-integration imagery. For photon-counting imaging spectroscopy, while angular resolution of, *e.g.*, 5" (that is, energy spectra with every 5" square; half-resolution pixel size of *Yohkoh* SXT) could still provide new spectroscopic information on the hot corona, especially for large magnetic structures such as reconnecting loop structure seen in long-duration flares (LDEs), higher angular resolution even beyond that (*e.g.*, 2" square or even higher) would be much desired in investigating spectral features in active region loops and in

reconnecting magnetic structures in flares.

4.2.2.3 Temporal Resolution / Cadence

From photon counting viewpoint, capability of generating an energy spectrum every 30 s or shorter should be necessary for active regions to see their thermal evolution. For flares, temporal resolution for generating energy spectra of 10 s, or shorter, should be desired.

4.2.2.4 Energy Range and Energy Resolution

Imaging-spectroscopic capability for hot corona should be essential for investigating flare science such as reconnecting structures. This leads to a requirement that the telescope should be sensitive beyond 2 keV (which is the upper limit for *Hinode* XRT), to several keV's. Also, sensitivity below 1 keV is desired for imagery with photon integration to image quiet Sun and coronal holes. Regarding energy resolution for photon-counting observations, FWHM resolution of ~150 eV is needed to observe higher end of the energy range (several keV's). For low-energy range of around 1 keV, necessary energy resolution is currently under investigation. As is discussed in Section 4.2.4, a combination of 5 electrons (rms) read-out noise and Fano-limited energy resolution (with Fano factor F = 0.12 for silicon) provides comfortable energy resolution for observing emission lines in the ~1 to 2 keV range.

4.2.3 Baseline Instrumentation

4.2.3.1 Overview

In response to specifications based on scientific requirements, we propose a photon-counting soft X-ray telescope whose observational performance summarized in Table 4.1. In this Section, we explain key items for the proposed telescope.

(a) Optics System

Figure 4.2 indicates a preliminary sketch of the grazing-incidence telescope with photon-counting capability. The telescope consists of (1) a pre-filter in front of the entrance aperture, (2) front-end grazing-incidence mirror of Walter Type I (-like) design, (3) focal-plane CMOS image sensor, (4) analysis/attenuation filters in front of the CMOS detector, (5) focal-plane shutter, and (6) camera control & event processing electronics (items (1), (5) and (6) not shown in Figure 4.2). There may be an aperture adjustment mechanism under consideration that is to be mounted in front of the telescope aperture to reduce incident flux to an appropriate level when performing photon-counting observations. The telescope will have ~4 m of focal length.

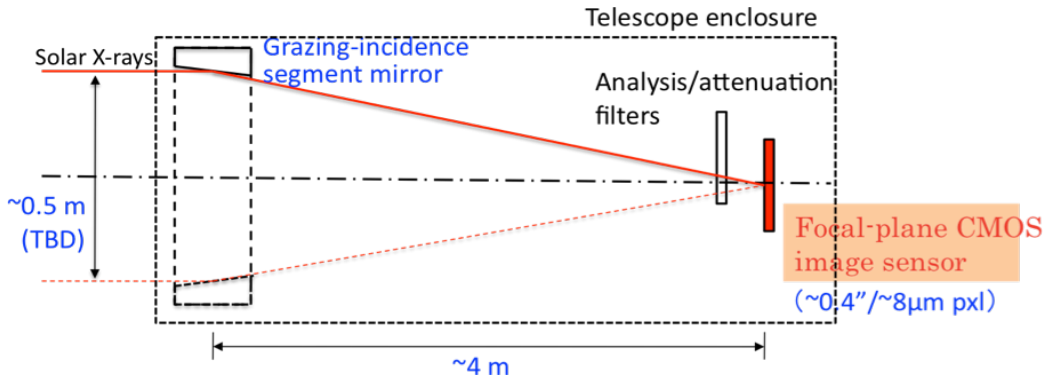

Figure 4.2. Schematic illustration of a preliminary photon-counting telescope concept.

(b) Event Processing System

In addition to the optical performance of the grazing-incidence mirror, accurate measurement of energy and position on the detector for each detected photon, with avoiding significant pulse pile-up effect, is a crucial key for the success of this instrument. Figure 4.3 presents a preliminary diagram for event processing under photon-counting measurement.

Besides the function blocks indicated in Figure 4.3, the telescope should employ appropriate attenuation filter or aperture size in response to the incident flux level.

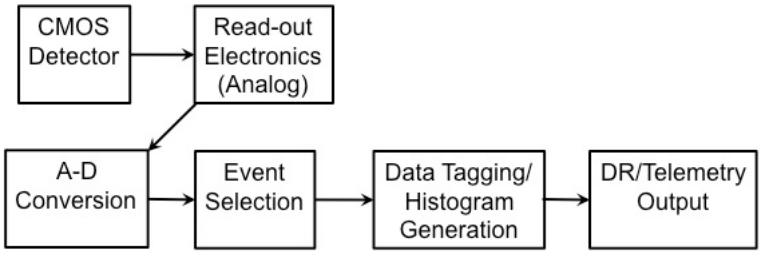

Figure 4.3. A preliminary block diagram describing the event processing scheme for detected X-ray photons under photon-counting measurement.

4.2.3.2 Optics/Mirror

A piece of grazing-incidence segment mirror, consisting of 1/8 of an entire circle, will be adopted for the X-ray mirror of the telescope. The mirror employs a Walter-I (-like) design with 2 reflections, with the length (in optics axis direction) of the first reflection segment designed to be 40 mm (TBD). While the radius of the mirror r (radius of an entire circle along which the segment mirror is laid), located at f = 4 m in front of the detector, changes with different grazing incidence angle to the mirror θ_i with the following relation

$$r = f \times 4\theta_i \,,$$

we take θ_i = 0.9 degrees as the baseline to perform imaging-spectroscopy both for active regions and flares. Grazing angles of 0.45, 1.35, and 1.8 degrees have also been studied. Besides the baseline incidence angle, θ_i = 0.45 degrees could be an interesting option for flare sciences (Section 4.2.4.3) but with penalty of poor observational performance for active regions. The baseline diameter of the mirror with the grazing incidence angle of 0.9 degrees is 50.3 cm.

Unlike *Hinode* XRT, the mirror must be coated with iridium (Ir) to attain high reflectivity, hence sensitivity of the telescope, for keV X-rays.

A conceptual schematics of the segment mirror mount is shown in Figure 4.4, with a drawing for the mirror-detector package in Figure 4.5.

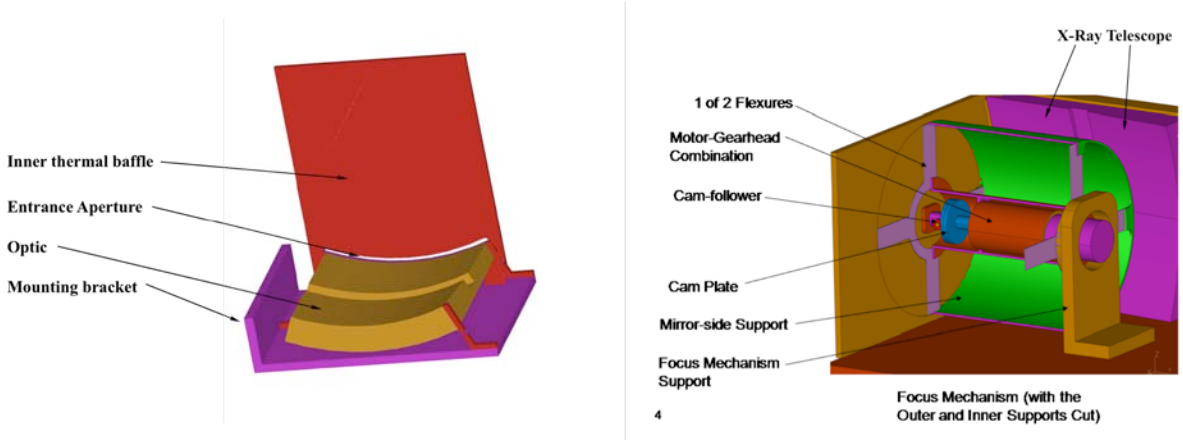

Figure 4.4. *Left:* Close-up of a segment mirror unit consisting of primary and secondary reflecting surfaces, having 1/8 segment of the entire circle. *Right:* Preliminary conceptual illustration on the focus mechanism which moves the mirror segment along the direction of the optics axis.

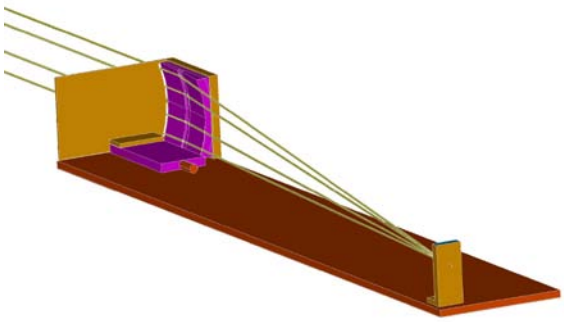

Figure 4.5. An illustration indicating segment mirror unit (left) and the focal-plane detector (right). Ray paths for X-rays from the Sun also shown in the figure.

A preliminary set of baseline parameters for the X-ray mirror is summarized in Table 4.2. A key requirement to the grazing-incidence mirror is that it should keep very small figure error (deviation from ideal mirror surface profile) to achieve 1 arcsec resolution (0.5 arcsec pixel size) while maintaining small micro-roughness for suppressing X-ray

scattering from other (bright) features on the Sun. A first-cut, rough estimate indicates that the figure error of ~10 nm P-V (TBD) would be needed to have Half-Power Diameter of 0.5 arcsec for angular resolution and micro-roughness of 3-4 Å r.m.s. (TBD) to suppress off-axis scattering wing level down to ~10^{-5} of the core at 1 arcmin off-axis at Al-K.

While fabrication of a mirror with the above specification is challenging, development of the mirror with Japanese domestic partners is currently under investigation which might provide possible solution for the fabrication.

Table 4.2. Baseline parameters for the X-ray mirror (preliminary).

Item	Description	Remarks
Mirror type	Walter Type I (-like) grazing incidence mirror, with two reflections at the primary and the secondary reflection segments.	
Length of the reflection segment	40 mm for the primary reflection segment. TBD mm (~50 mm) for the secondary reflection segment.	TBD; May be increased depending on tolerance for abberation.
Annular segment profile	1/8 of the entire circle.	
Grazing incidence angle	0.9 degrees	Baseline value.
Annular radius of curvature	251.3 mm	For grazing-incidence angle of 0.9 degrees.
Mirror surface	Coated with iridium (Ir)	Coating is a must for science performance of the telescope.
Focal length	4.0 m	
Plate scale	0.41"/8μm (0.5"/10μm)	8-10 μm corresponds to the pixel size of the baseline detector.
Angular resolution performance		
Core	Figure error of the mirror ~10 nm P-V (TBD) to have 0.5 arcsec HPD (Half-Power Diameter).	
Wing	Mirror micro-roughness 3-4 Å r.m.s. (TBD) to sufficiently suppress off-axis scattering wing level down to ~10^{-5} of the core at 1-arcmin off-axis at Al-K.	

4.2.3.3 Focal-Plane Detector

Table 4.3 summarizes baseline specifications for the focal-plane detector to meet the instrument performance tabulated in Table 4.1. In order to achieve high frame readout at the focal-plane detector, we identify CMOS image sensors as the most appropriate for our purpose. There are several active-pixel detectors under development besides CMOS which aim pixel-based spectroscopy on X-ray photons, such as DEPFET for *IXO* X-ray observatory (former *XEUS*; Strüder *et al.* 2003, 2004, Treis *et al.* 2005, Strüder 2008) and pixel detectors for high-energy particle accelerator applications such as for LHC

(*e.g.*, Llopart *et al.* 2007), these detectors mostly have large pixel size of typically ~50 μm, with the smallest one at most ~25 μm. The large pixel size of these detectors, unfortunately, is not consistent with the required angular size of a pixel of ~0.5" unless the telescope has significantly large focal length exceeding 10 m.

Recently, there has been remarkable development in CMOS active-pixel image sensors which appear to be best suited as our photon-counting detector because of their small pixel size (can easily be smaller than 10 μm) and their potential of high frame readout capability.

Table 4.3. Baseline specification for the focal-plane detector (preliminary).

Item	Description	Remarks
Device type	CMOS-APS	Device from e2v considered to be the baseline.
Format	2k×2k or larger	
Pixel size	8-10 μm	
Photon-counting area	512×512 (goal) 100×100 (minimum)	Should be changeable over the imaging area.
Frame readout rate for photon counting	1000 fps	
Pixel gain	>a few × 10 (>50) μV/e^- for photon-counting pixels a few μV/e^- for photon-integration pixels	Should be switchable over the imaging area.
Low-energy X-ray sensitivity	Back-illuminated device, or thin (~<1 μm) SiO_2 absorption layer if a front-illuminated device is employed.	
Readout noise	5 e^- rms (TBD; goal) ≤50 eV FWHM (minimum)	
Energy resolution	Fano-limited (F=0.12) (goal) ≤150 eV FWHM (minimum)	
Charge spreading	At least 3-σ electron cloud diameter smaller than 3 pixels.	
Pulse-height A/D conversion	≥10 bits	

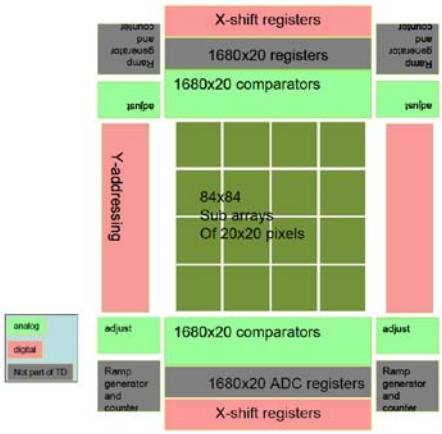

Figure 4.6. Envisaged CMOS-APS for WFS whose development ongoing at e2v. An area of 1680×1680 pixels is planned to be read out with a frame rate of 700 fps (nominal) and with readout noise of ~3 e^- r.m.s. Figure courtesy of e2v.

As of this writing, the most promising series of devices along the line of our need is those which could be provided by e2v Technologies, U.K. A large-format wavefront sensor (WFS) for night astronomy is currently under development by e2v (Figure 4.6). The target specification for the WFS is to read out 1.6k × 1.6k pixels (24 μm pixel size) area at a frame rate of 700 fps (nominal) with low readout noise (a few e^- r.m.s.), backside illumination with bulk depletion using high-resistivity epitaxial silicon. They have recently successfully completed demonstration of their approach on pixel architecture to achieve low readout noise together with high frame rate, and are now quite confident that most, if not all (except the largest case of the photon-counting area), of baseline specifications in Table 4.3 can be met with their pixel architecture developed for the WFS. Figure 4.7 depicts possible readout of the photon-counting area among the 2k × 2k imaging area (pixel size 8-10 μm) based on the existing architecture at e2v with the background of WFS heritage. Final pixel size will be determined considering effect of charge spreading by X-ray photons on event detection efficiency.

The extended readout area in the horizontal direction in the figure would be particularly effective when considering the possibility of flexible spacecraft roll to be mentioned in Chapter 5 in such a way that the horizontally-extended area can serve as a vertual 'slit' along which imaging spectroscopy can be performed.

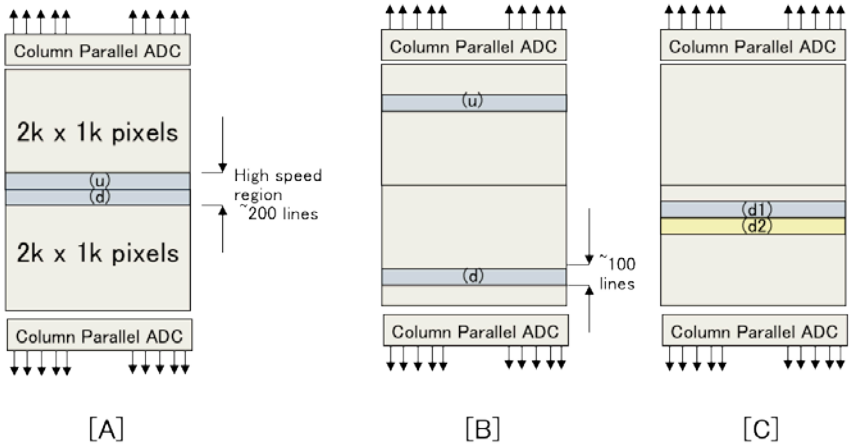

Figure 4.7. Possible readout scheme of photon-counting area in the 2k×2k array with the existing pixel architecture at e2v. In the figure, areas labelled as '(u)' are read out from the upper side of the detector while those with '(d)' from the lower side, each with 1000 fps. [A] 2k×200 area in the middle of the imaing area to be read out with 1000 fps. [B] Two separate 2k×100 areas to be read out. [C] Switch read out of area (d1) and (d2) each other so that a total of 2k×200 area in the lower half of the detector be read out at 500 fps, which may be useful for observing weak sources extending large spatial extent. Figure courtesy of e2v.

In parallel to the development of high frame-rate readout, back-thinning of CMOS-APS is also being extensively promoted at e2v, using high resistivity (~1 kΩ-cm) epitaxial silicon to have the bulk silicon depleted instead of depleting only a limited portion around the p-n junction of the photo-diode in each pixel thus attaining a depletion layer thickness of ~10 μm or even more. A sample of such back-thinned CMOS-APS is said to become commercially available next year (2011). A prototype WFS device with ~800×600 pixels and with a readout rate of 700 fps (1000 fps max.)

for the entire area is scheduled to appear in 2012, again with back-thinning and with high-resistivity silicon.

As for spreading of signal charges by incident X-ray photons, only limited results have so far been available with e2v CMOS-APS devices. Nonetheless, results from X-ray illumination with Mn target (that emits Mn Kα and Kβ lines besides Bremsstrahlung continuum) for a front-illuminated device performed at Centre for Electronic Imaging at The Open University indicates the X-ray signals are contained within 3×3 pixels area with ~20% of Mn Kα (5.9 keV) events resulting in single-pixel events even with a small pixel size of 5.8 μm and with low resistivity silicon (hence shallow depletion layer). This result suggests promising prospects that the extent of charge spreading (and also fraction of single-pixel events) would even be better with a larger pixel size of 8-10 μm and with high resistivity silicon.

To summarize, at this very moment there is no CMOS-APS device present that immediately meets the baseline specifications for the photon counting. However, with the rapid development of CMOS-APS currently ongoing towards the desired direction of (1) high-speed and low-noise readout capability and (2) good soft X-ray spectroscopic capability, the photon-counting detector is expected to become even more realistic within the upcoming 1-2 years.

In the subsequent section of this Report, we assume back-illuminated CMOS device from e2v, with 10 μm-thick depletion layer and with 8 μm pixel size for assessing science capability of the photon-counting telescope.

4.2.3.4 Flux Attenuation System

For performing photon-counting observations for flares and active regions, it is deemed necessary to employ attenuation system for the incident X-ray flux so as to avoid event pile-up on the focal-plane detector. Either a set of attenuation filters mounted on a filter wheel(s) or an aperture adustment mechanism would be employed for the flux attenuation system with the former may be more suited to observe higher end of the spectrum because the attenuation filters absorpt lower-energy X-ray photons. While logic for selecting certain attenuation filter or a particular aperture size (with probably using signals from a separate flux monitor) needs be elaborated, observations with the baseline geo-stationary orbit (see Section 5) could provide a remarkable chance of performing such attenuation on true real-time basis.

4.2.4 Expected Capability

4.2.4.1 Introduction

Figure 4.8 shows effective area profiles of the telescope for the four grazing-incidence angles θ_i studied (θ_i = 0.45, 0.9, 1.35, and 1.8 degrees), with θ_i = 0.9 degrees being considered as the baseline. The effective area profiles include (1) X-ray transmission of the pre-filter (same material design as *Hinode* XRT, namely, 1200 Å of

aluminum on 2500 Å polyimide assumed), (2) reflectivity of the grazing-incidence mirror, (3) projected QE of the focal-plane CMOS detector, and (4) geometrical area of the telescope that is determined by the aperture size of the first reflecting segment of the mirror, when viewed from the Sun.

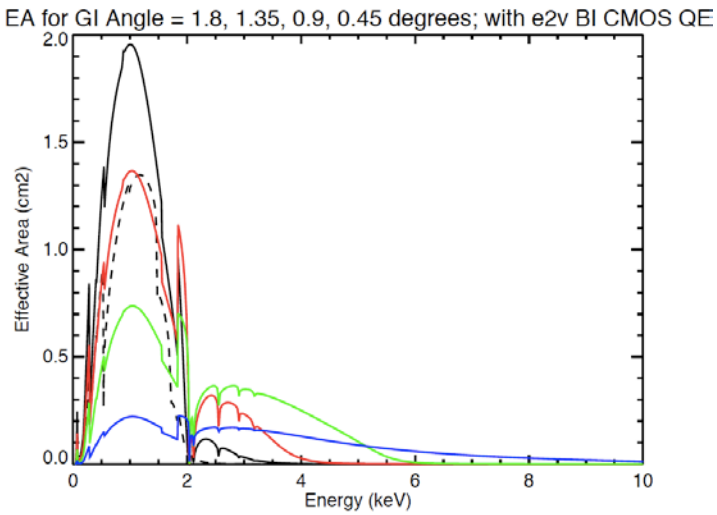

Figure 4.8. Effective area profiles for grazing incidence angles of 1.8 (black), 1.35 (red), 0.9 (green), and 0.45 (blue) degrees. The effective area profile for Hinode XRT (without Ir coating on the mirror surface) is also shown for comparison (black dashed line). QE profile for the back-illuminated e2v CMOS device assumed for all the four grazing incidence angle profiles.

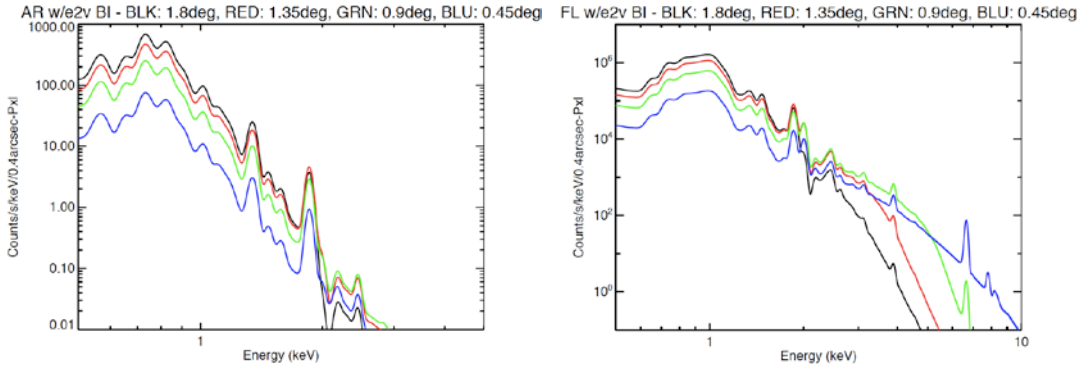

Figure 4.9. *Left:* X-ray count spectra for a model active region with CHIANTI V6.0, for four grazing-incidence angles, 1.8, 1.35, 0.9, and 0.45 degrees (in black, red, gree, and blue, respectively). No attenuation filters assumed to be present. *Right:* Those for a model flare (GOES class M2). Again without attenuation filters.

Figure 4.9 indicates X-ray count spectra for a model active region (left panel) and a model flare (right panel) from CHIANTI V6.0 (Dere *et al.* 2009), without focal-plane filters. Readout noise and energy resolution indicated as "goal" in Table 6.2-4 are used for generating these plots. Note with the back-illuminated CMOS neither active region nor flare count spectra can be observed as they are in the photon-counting mode because incident X-ray count rates will be too high (*e.g.*, in the flare case, ~3×10^5 cts/s/pixel for θ_i = 0.9 deg.) to perform any meaningful photon counting avoiding pulse

pile-up. For this reason, focal-plane attenuation filters should be necessary. The attenuation filters will make count spectra to be actually measured different from those in Figure 4.9, with low-keV portion to be significantly attenuated. In the photon-integration mode, such attenuation filters will not be necessary but analysis filters for performing filter-ratio analysis may be employed.

Signal count rates to the focal-plane detector of the telescope without attenuation filters (nor focal-plane analysis filters) is summarized in Table 4.4. Here, the baseline back-illuminated CMOS detector is assumed for estimating signal count rates.

Table 4.4. Estimated signal count rate for the telescope, with the baseline detector and the grazing-incidence angle of 0.9°.

Target(1)	Flare (M2)	Active Region	Quiet Sun	Coronal Hole
Photon count rate (cts/s/pxl)	3.1×10^{5} (2)	2.2×10^{2} (2)	7.9	1.7
Electron rate (e^-/s/pxl)	7.4×10^{7}	1.8×10^{4}	1.9×10^{2}	3.5×10^{1}
Exposure time for photon-integration(3)	1.0 ms	4.2 s	3.9×10^{2} s	2.1×10^{3} s

(1) Emission spectrum from each target created from CHIANTI V6.0.
(2) Attenuation filters (and/or aperture adjuster) need be inserted in order to perform photon-counting spectroscopy.
(3) Time for generating 75 ke^-, which is half the nominal full-well capacity of the CCD for *Hinode* XRT.

4.2.4.2 Active Regions

Figure 4.10 presents simulated photon count spectra to be detected with the photon-counting mode of the telescope, with the baseline grazing-incidence angle of θ_i = 0.9 degrees. A model DEM for active region (Vernazza and Reeves 1978) with CHIANTI V6.0 emission code is used for obtaining solar emission from a "typical" active region. The spectra assumes 1024 energy bins between 30 eV to 10 keV, with binning made in such a way that count rate from each summed-bin has at least 5-σ statistical significance against Poisson errors (only photon counts are considered here as the source of the error), with an imposed limitation that the maximum number of binning be 20. A set of readout noise of 5 electrons r.m.s. and Fano-limited energy resolution (with Fano factor F = 0.12) is adopted here to produce the spectra. This set of readout noise and energy resolution is listed as goal for the detector specification in Table 4.3.

Left panel of Figure 4.10 shows a spectrum with 262 s net integration time while the right panel 654 s net integration. Here, net integration time stands for the total of integration time from each pixel that contributes for generating a single energy spectrum. For example, for generating the left-side spectrum of the figure, it will take 16 s with 4×4 pixels (1.6" square).

As seen in the figure, an emission line complex of Mg may be detected around 1.34 keV even with the 262 s net integration case with positive, or marginal, indication of another emission line complex of Si around 1.85 keV. As the contribution curves for these emission line complexes peak at 5-8 MK, any deviation of measured emision line complexes from Figure 4.10 immediately give us information on distribution and

evolution of high-temperature (≥5 MK) plasmas that has never been provided before.

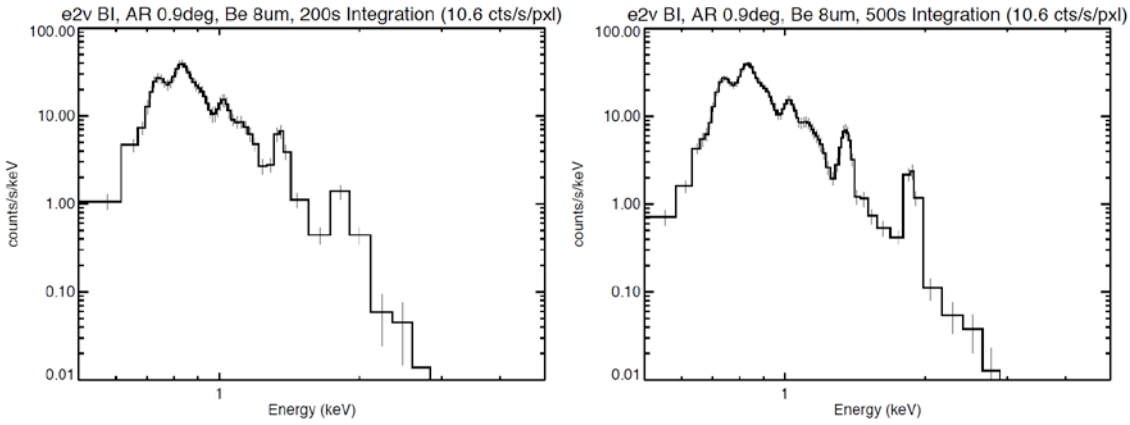

Figure 4.10. Simulated photon count spectra for a "typical" active region with the baseline grazing-incidence angle of 0.9 degrees and with the baseline CMOS detector. *Left:* With net integration time of 262 s. *Right:* Net integration time 654 s.

If we concentrate on the low-temperature emission in the energy range below ~1 keV, energy spectra in that energy range can be generated even quickly. Figure 4.11 shows an example of active region spectrum with 2 μm-thick Be filter employed as the attenuation filter (yielding incident photon count rate of 39.1 counts/s/pixel to the detector) with net integration time of 130 s. This means the spectrum in the figure would be obtained every 14 s with 3×3 pixels (1.2" square).

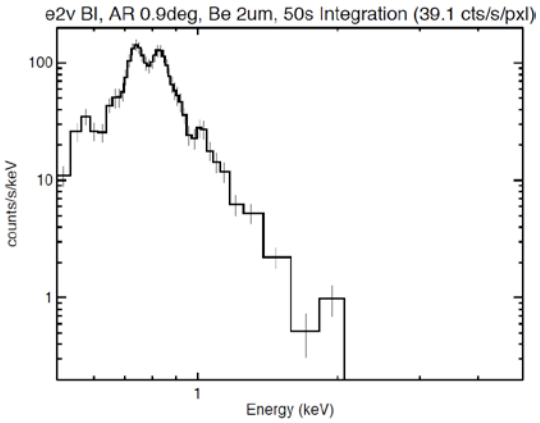

Figure 4.11. Simulated photon count spectra for a "typical" active region with the baseline grazing-incidence angle of 0.9 degrees and with the baseline CMOS detector, with net integration time of 130 s.

Apart from thermal emission so far studied, if non-thermal emission were to extend down to, say a few keV range, at the early phase of a flare, such non-thermal emission is likely to be well detected as continuum component in the spectra, in a spatially-revolved way. Note detection of such non-thermal components would not be available with EUV spectrographs since they manifest themselves as continuum emission, and can be done only with the X-ray imaging-spectroscopic approach. So far, spatially-resolved observations of non-thermal components down to a few-keV range have not been performed except for very limited cases (Krucker *et al.* 2002, Hannah *et al.* 2008).

Observations with the photon-counting X-ray telescope will provide crucial information on physical condition of the corona that triggers explosive energy release in flares.

4.2.4.3 Flares

In the case of flares (with a model flare of GOES class M2 studied with CHIANTI spectral code), attenuation filters are necessary to reduce incident rate of X-ray photons to the detector in order to avoid excess photon pile-up, down to a level of several times 10 photons/s/pixel. Energy spectra thus observed will therefore undergo significant attenuation of low-keV energy components by the attenuation filters. Figure 4.12 shows expected photon count spectrum profiles for a model flare of GOES M2 class to be detected with the photon-counting mode of the telescope, for different grazing-incidence angles, with an attenuation filter (beryllium assumed) inserted in each case to reduce the incident photon count rate down to ~40 photons/s/pixel. As seen in the figure, peak position of the spectrum changes with different grazing-incidence angles. Note in actual observations (with limited integration time for a spectrum) count rates down to roughly 2 orders of magnitude lower than the peak would give a practical lower limit for meaningful spectra with good, or reasonable, photon statistics. Hence energy range that can be explored differs with different grazing-incident angles.

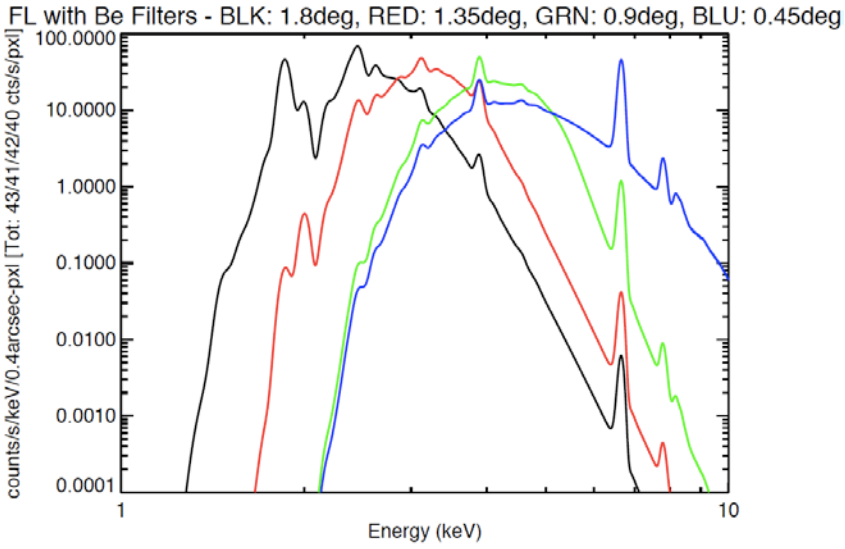

Figure 4.12. Photon count spectrum profiles expected from a model GOES M2 flare for the four different grazing-incident angles. An attenuation filter made of beryllium assumed for each profile; thickness 0.42 mm for θ_i = 1.8°, 0.8 mm for θ_i = 1.35°, 1.5 mm for θ_i = 0.9°, and 1.5 mm for θ_i = 0.45° so that each spectrum has a similar total count rate of ~40 counts/s/pixel. Note the profiles are ideal ones with infinitely-good photon statistics.

Figure 4.13 presents simulated photon count spectra with the photon-counting mode of the telescope, with the baseline grazing-incidence angle of θ_i = 0.9 degrees. A focal-plane attenuation filter of 1.5 mm-thick beryllium is inserted to reduce incident count rate down to 42.3 counts/s/pixel. A model DEM for a GOES M2-class flare (Dere and Cook, 1979) with CHIANTI V6.0 emission code is used for obtaining solar

emission for this flare case. For displaying flare count spectra, binning was made so that count rate from each summed-bin has at least 10-σ statistical significance against Poisson errors (only photon counts are considered here as the source of the error), with the maximum number of binning set to be 20. The left panel of the figure corresponds to 140 s net integration while the right panel 840 s. Even with the 140 s net integration time (that means 15.6 s integration for a 1.2"×1.2" area (3×3 pixels)), signature of Ca XIX emission (emission from 20 MK plasma) at ~3.9 keV can be seen in addition to the continuum thermal emission. Note these spectra only reflect thermal emission from flare plasmas; any non-thermal emission, if present, can be overlapped to these spectra.

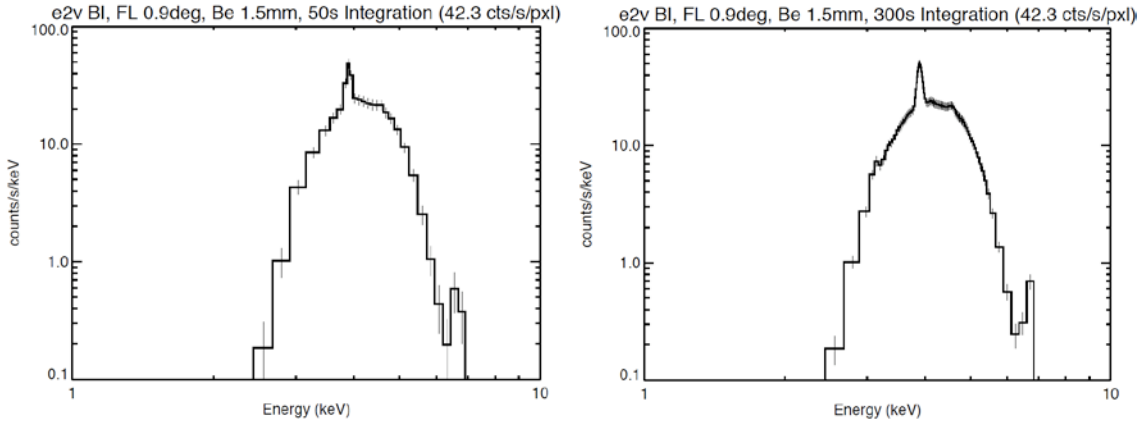

Figure 4.13. Simulated photon count spectra for a model flare of GOES M2 class with the photon-counting mode of the telescope of θ_i = 0.9°. *Left:* Net integration time 140 s. *Right:* Net integration time 840 s.

As supplementary information, Figure 4.14 shows simulated flare spectra with grazing-incidence angle of θ_i = 0.45 degrees. This grazing angle could provide an interesting possibility that, in addition to the Ca XIX emission Fe and Fe/Ni emission complexes around 6.7 keV and 8 keV, respectively, may also be detected.

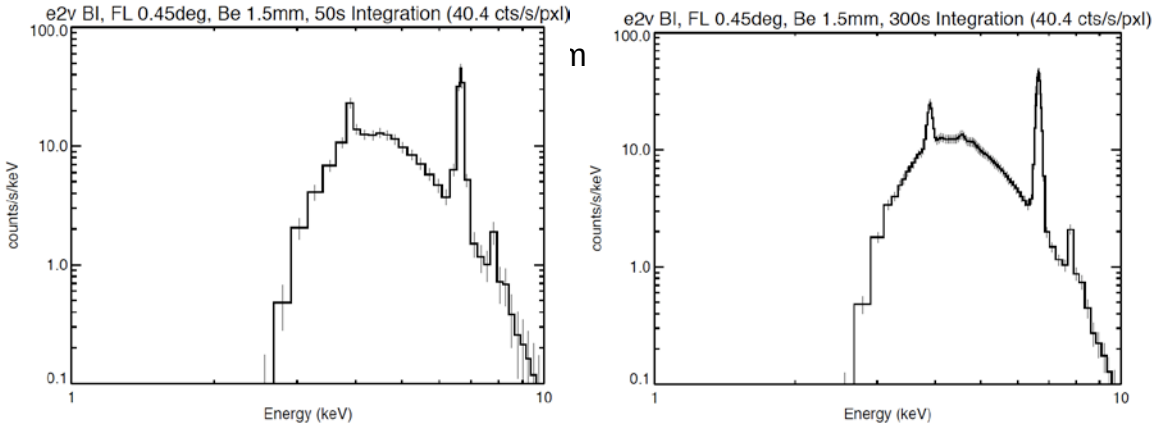

Figure 4.14. Simulated photon count spectra for a model flare of GOES M2 class with the photon-counting mode of the telescope of θ_i = 0.45°. *Left:* Net integration time 133 s. *Right:* Net integration time 800 s. 1.5 mm-thick Be filter assumed as the attenuation filter so that the incident photon count rate to the detector reduced to 40.4 counts/s/pixel.

Based on the above observation capability for active regions and flares, imaging-spectroscopic performance of the photon-counting telescope is schematically illustrated in Figure 4.15. The figure presents angular size (in arcsec) of observation target versus temporal resolution that can be attained with the baseline photon-counting telescope. (Here, 'baseline' refers to instrument capability summarized in Table 4.2 and 4.4.) Lower-left direction in the figure corresponds to smaller target (angular resolution) with higher temporal cadence hence preferable for observations. For performing

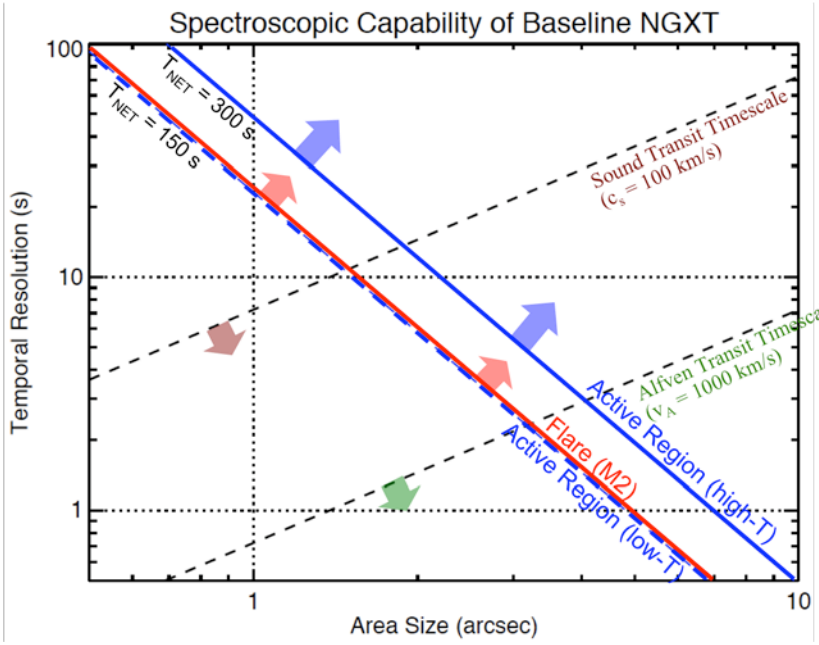

Figure 4.15. Imaging-spectroscopic capability expected for the baseline photon-counting telescope. See text for details.

imaging-spectroscopy on high temperature emission in the range of 1-2 keV, upper-right side region from the solid blue line (with label 'Active Region (high-T)') can be addressed by the instrument, while angular size-temporal resolution combination in the left-side region would result in insufficient photon statistics for generating soft X-ray energy spectra. On the other hand, for imaging spectroscopy on low temperature emission in the range below 1 keV, upper-right side region from the blue dashed line (with label 'Active Region (low-T)') can be addressed.

For flare observations, the border is shown in solid red line (with label 'Flare (M2)'), and imaging-spectroscopic observations can be performed with good photon statistics for the region upper-right of the border. If we could have small charge spreading (less than 3×3 pixels), or could adopt a better event selection method (if it exists) other than the one discussed in the Appendix, the border would be further pushed down towards lower-left direction in the figure, enabling us to investigate spectroscopically smaller region with higher temporal cadence.

In Figure 4.15, two dashed lines from lower-left to upper-right, one roughly indicating sound transit time scale (with sound velocity set as c_s = 100 km/s) and the other Alfven transit time scale, are shown. With the baseline imaging-spectroscopic

performance of the photon-counting telescope, physical processes with sound time scale in active regions would be observed with angular resolution (size) of 2" and temporal resolution of ~10 s, while those with Alfven time scale in flares with angular resolution (size) of ~3" and temporal resolution of ~2 s.

4.3 Ultra-High Spatial Resolution Normal Incidence EUV Telescope

As demonstrated by *Hinode* observations, activities in the lower atmosphere of the Sun, such as those of spicules in the chromoshere, and their consequences to the upper atmosphere, may hold the key to understand energy transfer and subsequent dissipation (heating) into the corona. While dynamics of the transition region and the lower corona will be extensively studied quantitatively by EUVS, combination with an imaging telescope with the following features as compared to EUVS should further enhance science output on the dynamics, energy transfer and dissipation in the transition region and the low corona.

(1) Temperature overlap
(2) Higher spatial resolution
(3) Higher exposure cadence
(4) Wider field of view

Data from *Hinode* EIS has clearly indicated that there is structure and velocity component present whose spatial scale below the instrument resolution. A similar case could happen with the EUVS instrument under which full interpretation of observed data, such as line profiles, would confront difficulty. An imaging telescope with the above-listed features should provide context information for EUVS and would greatly help to understand what is going on in their data.

As the spatial resolution of the EUVS instrument will be ~0.3" (~0.16" pixel size), that for the imaging telescope should be equal to, or better than, 0.2"-0.3" (~0.1" pixel size). The need of ultra-high spatial resolution together with temperature overlap with EUVS leads to the choice of EUV normal incidence optics.

While EUV image data should be quite useful to observe structure, motions and magnetic environment of coronal phenomena, the image data by themselves would be not suited to derive physical quantities such as density, actual temperature and velocity of coronal plasmas. Nevertheless, with the spatial resolution of 0.2"-0.3", the EUV normal incidence telescope, when combined with EUVS, is expected to contribute in Solar-C/Plan-B science in the following aspects: (1) Resolve fine, hopefully elemental, structures and study plasma flows, magneto-acoustic waves and small-scale heatings in coronal temperature range, (2) investigate transfer and dissipation mechanism of magnetic energy, and (3) understand how corona reacts to activities that occurred in the lower atmosphere. Furthermore, the movement of the localized particle-acceleration site can be also investigated by observing the EUV flare kernel with high spatial and temporal resolution (Figure 4.16).

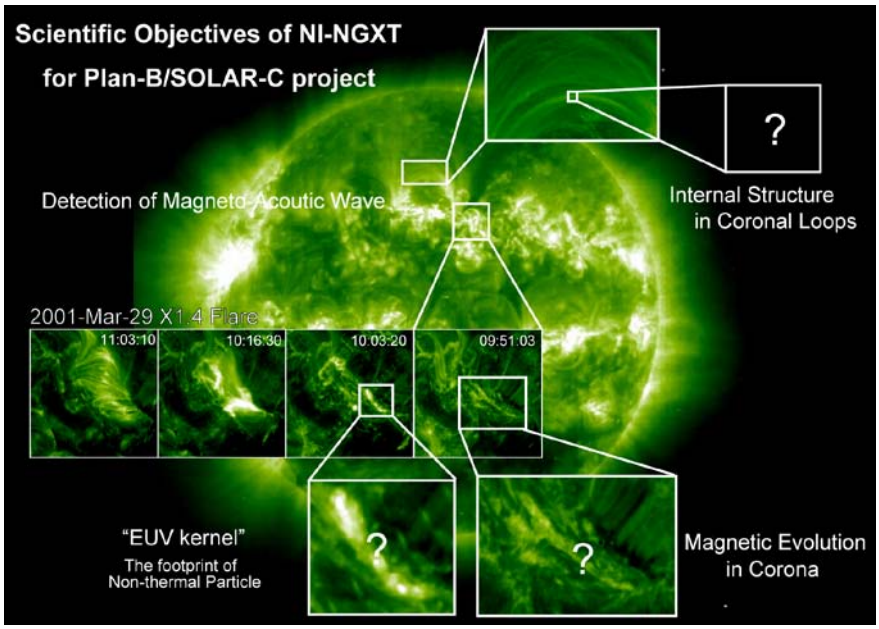

Figure 4.16. Target structures and phenomena of the ultra-high spatial resolution normal incidence EUV telescope.

4.3.1 Scientific Requirements for the Instrument

The primary goal of the ultra high-spatial resolution normal incidence EUV telescope for Solar-C/Plan-B mission is to give support in understanding physics of magnetic energy storage and release in coronal plasmas by investigating how corona reacts to activities that occurred in lower atmosphere. Based on the science goal, scientific requirements on the EUV telescope are summarized below to deliver largest synergy with EUVS.

1. The telescope should have higher angular resolution than EUVS, that is, to resolve structure with 0.2"-0.3" resolution with 0.1" detector pixel for resolving fine coronal structures to give aid in understanding elemental processes in corona.

2. Exposure cadence should exceed that for EUVS. As exposure time for EUVS is 1-5 s for active regions with 0.33" spatial sampling while that for the EUV telescope for active regions and flares can be as short as 1 s and 0.1 s, respectively, the requirement on cadence can be reasonably met.

3. Field of view should well cover that for EUVS (that is 200" nominal, >300" extended). This results in the telescope field of view requirement of ~400"×400". Note this size covers even outer structures of an active region.

4. Temperature range should well overlap that for EUVS. This could imply multiple normal-incidence channels for the telescope. The temperature overlap would also help in co-aligning image data with EUVS. A UV band for the telescope may also

be useful for co-alignment with SUVIT data.

5. To perform observations with low-scattering optics. In order to observe faint structures in the corona, such as long loops in active regions, plume in coronal holes and structures on the limb, scatter light of the telescope has to be low.

4.3.2 Strawman Instrument Concept

The following depicts preliminary, strawman instrument concept of the EUV telescope. Specifications of the instrument design should be elaborated in coordination with the EUVS instrument.

4.3.2.1 Optical design

The instrument will consist of two telescopes. The telescopes have the same optical design except the optical bandpass. The optical design of the telescope is a Ritchey-Chrétien form of Cassegrain. The primary and secondary mirrors are divided to three sectors and each sector is coated by the different multi-layer coatings for focusing in 3 different wavelengths by one optical system.

At the front aperture of each telescope, there are entrance filters and an aperture selector. The aperture selector conceals two third of the aperture and solar EUV light incidents only on one sector of the primary mirror. The light then travels the telescope tube to the primary mirror, where it is reflected back toward the secondary. The secondary is mounted on an active structure that is actuated to remove the instrument pointing errors and focus the system. Light reflects off the secondary, and toward the focal plane. There is a shutter and filter wheel near the focal plane. The shutter controls the exposure time. The filter wheel places the desired filter in the light path, thus controlling the spectral content of the incoming light. Since the mirror coatings act as narrow bandpass filters, the focal plane filters effectively select which channel of the telescope is sending light to the detector. The telescope has the guide telescope for tracking the position of the sun and measuring the instrument pointing error that is used for image stability compensation. The optical design and the guide telescope system are similar to that of the AIA/SDO and the TRACE.

4.3.2.2 Exposure time and the diameter of the primary mirror

Based on the refractivity of the mirrors, the transmission of the filters and the quantum efficiency of the CCD used in the AIA/SDO, we expected the effective areas for EUV lines of the instrument, and predicted the exposure times for accumulating 200 photons/pixel. The threshold count rate "200 photons/pixel" is needed to decrease the error of the count ratio between the X/EUV bands to less than 10%. The count ratio is useful for the temperature analysis of corona. Fig 4.17 shows an example of the results.

Recently, there has been remarkable development in CMOS active-pixel image sensors which appear to be best suited as our photon-counting detector because of their small pixel size (can easily be smaller than 10 μm) and their potential of high frame readout capability.

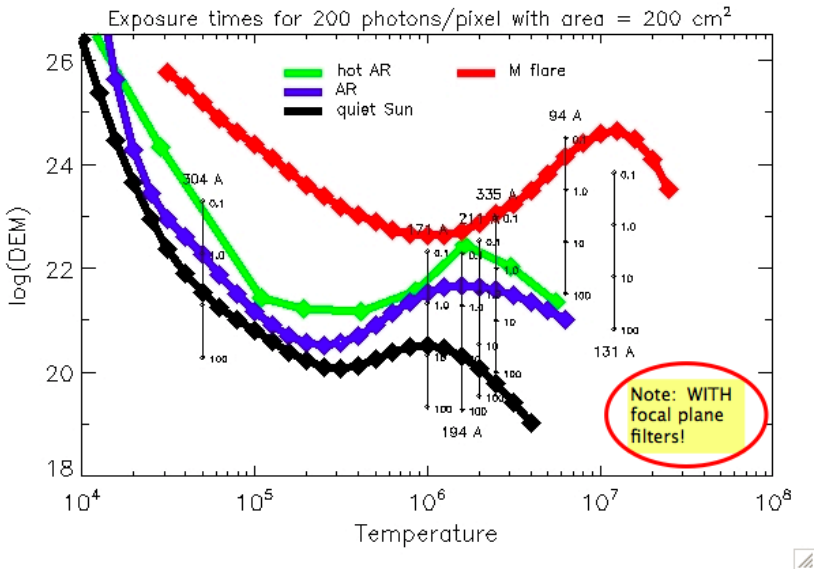

Figure 4.17. The Differential Emission Measures and the predicted exposure time for the EUV lines. The vertical bar indicates the exposure time for each EUV lines if the geometric area of the mirror for each EUV line is 200 cm^2.

4.3.2.3 Selection of wavelength and temperature coverage

The strawman instrument has 5 narrow EUV bands and one broad UV band. In order to observe the corona with continues temperature coverage, the five EUV bands are chosen for the instrument based on our knowledge of the solar EUV image taken by the EIT/SOHO, the TRACE and the AIA/SDO.

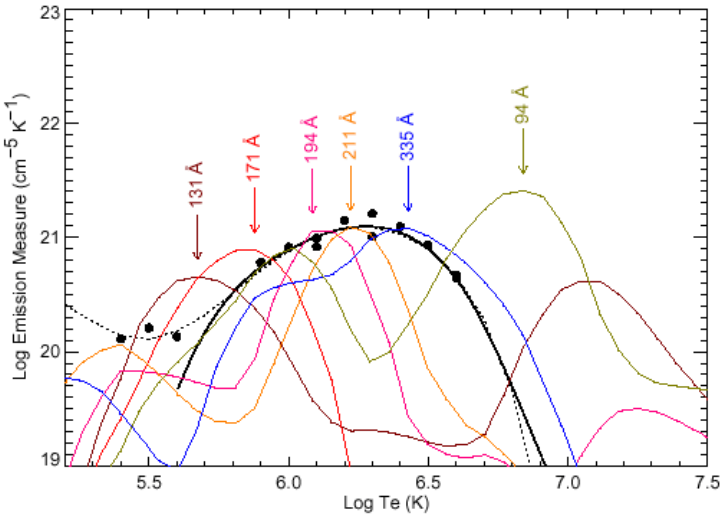

Fig 4.18. The temperature coverage of the AIA. (Adopted from the "AIA Concept Study Report" written by AIA Science Team.)

Selected band (main EUV line) : Temperature range (Log_{10} T)

- 171Å (Fe IX) : ~5.9
- 195Å (Fe XII) : ~6.1
- 211Å (Fe XIV) : ~6.3
- 335Å (Fe XVI) : ~6.5
- 94Å (Fe XVIII) : ~6.9 for a flare (blended with 6.0 component.)

The selected bands include the strong EUV lines and they have already been observed with 1" spatial resolution by AIA/SDO. The UV band of the instrument is similar to the UV band of SDO and TRACE. The 1600 Å and 1700 Å continuum images are taken with the band.

Table 4.5. Scientific summary of the instrument's characteristics

Spatial Resolution	0.2"-0.3" with 0.1"/pixel
Field of View	~400" × 400"
Wavelength Bands	171 Å, 195 Å, 211 Å, 335 Å, 94 Å and broad-UV band
Exposure time	1 s for an active region 0.1 s for a flare
Cadence	< 10 s

4.3.3 Strawman design details

Details of the strawman design are shown in Table 4.6.

Table 4.6. The strawman design details of the instrument.

Telescope	**Baseline or nomical value**
Number of telescopes	Two telescopes
Telescope type	Ritchey-Chrétien form of Cassegrain
Length of the telescope	< 400 cm
Optical properties	32 cm apartre diameter, TBD cm focal length, TBD microns/arcsecond plate scale
Design char.	Field of view: 400"x400", Platescale: 0.1"/pixel, Detector format: 4Kx4K
Mirror coating	Multi-layer coating by Mo, Si, SiC, Y and Al for 171Å, 195Å, 211Å, 335Å, 94Å and broad UV bands.
Stablization	The image stabilization system is constructed from the guid telescope and the tip-tilt secondary mirror.
Focus mechanism	Moves the secondary mirror. The tip-tilt secondary mirror is mounted on the focus mechanism.
Filters	**Baseline or nomical value**
Entrance filters for the X/EUV bands	Must block 10^{-6} of out of bandwidth radioation. The thin-metal filters made from Al or Zr.
Entrance filter for the UV band	The filters is made from the bandpass filter on MgF2
Focal plane filters	The thin-metal filters for the X/EUV bands are made from Al and Zr . The filters for the UV band are made from MgF2.
Detector	**Baseline or nomical value**
Detector Type	Back side illuminated CCD
Pixel size	TBD microns
Detector format	4K x 4K pixels

4.3.4 Technical feasibility for realizing the ultra-high spatial resolution

Many elements of the strawman instrument are flight-proven by AIA/SDO and TRACE. However, the instrument will have 5-6 times better spatial resolution than the existing telescopes. In order to realize such ultra-high spatial resolution of the instrument, one should further assess the following issues.

- Micro-roughness of the mirrors.
- Influence of the boundaries between different multi-layer coatings on each mirror.
- Stabilization system for the ultra-high spatial resolution.
- Vibration levels of the movable elements, especially those of the aperture selectors.
- Stray lights in the telescope tubes.
- Influence of high energy particles in the geo-synchronous orbit.

4.3.5 Further optimization for a better instrument

The optimization of the instrument design is not completed by the NGXT science group. The science goal and the requirements for the instrument should further be defined in detail in association with EUVS. Trade-off for wavelength selection should further be investigated. Number of telescopes, number of wavelength sectors on each mirror, types of multilayer coating and the diameter of the primary mirrors are closely related to this issue. The optical design may be further optimized for suitable observations of the corona in the Solar-C mission.

Appendix 4.A Event Processing

Since it is highly likely that electrons generated by an incident X-ray photon will spread over the pixel of incidence, it is indispensable to perform post-detection event processing to reconstruct correctly energy of incident photons by summing up electrons distributed over several pixels. Furthermore, since there is possibility that two photons incident to the same pixel, or to two adjacent pixels, in a single frame resulting in pulse pile-up (which then results in over-estimated X-ray energies), such pile-up should be avoided as much as possible with the post-detection event processing. As illustrated in Figure 4.3, this event processing is to be performed on digitized pixel data, namely, after analog voltage from each pixel signal is digitized with A/D conversion.

We here assume that all X-ray photons detected by the telescope generate electron clouds whose size (3-σ diameter in Gaussian profile) less than 3 detector pixels. With this assumption, events whose signals contained within 3×3 pixel area but not extending beyond that, such as those shown in Figure 4.19(a) are to be identified as "valid events", and signals from the central 3×3 pixels collected to reconstruct the energy of *an* incident X-ray photon. Note in the right-most panel of Figure 4.19(a) represents a situation that two-photon incidence cannot be excluded in this particular case hence would result in inclusion of a pile-up event. However, as will be demonstrated later, probability of occurrence of such case is sufficiently low.

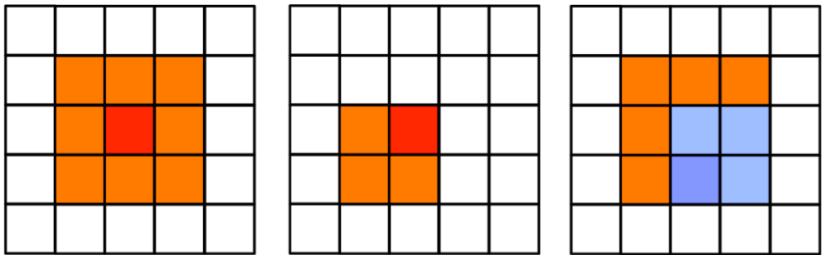

Figure 4.19(a). Example of events (indicating charge spreading across pixels) that are considered to be "valid" with 5×5 pixel-area event processing. In each panel, red pixel indicates the X-ray-incident pixel (5×5 area taken to set the red pixel at its center) while orange pixels indicate pixels with signals due to charge spreading. The right panel denotes the situation that another X-ray photon was incident (into the dark-purple pixel) in a single frame resulting in a mixture of signal charges in the 3×3 area. The right panel case cannot be excluded by the event processing.

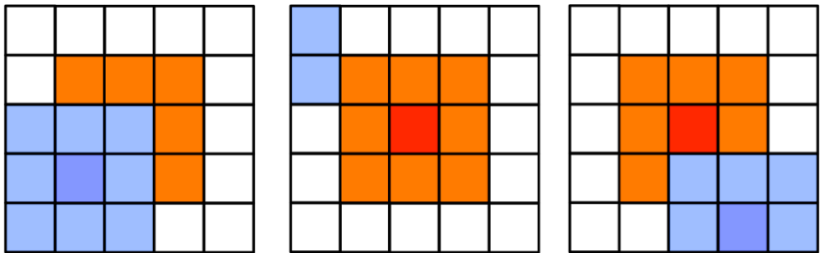

Figure 4.19(b). Example of events that are to be rejected because of possible contamination by the second photon in a frame. Pixel of the second-photon incidence is shown in dark purple with light-blue pixels denote pixels with signals from the charge spreading from the second photon. The middle panel represents a case where the second photon was incident outside the 5×5 pixel area but some of its spread charge present in the 5×5 area.

Figure 4.19(b) shows examples of "invalid events" with possibility that the central 3×3 pixel area is contaminated by charge from the second photon, due to signal distribution extending beyond the 3×3 area. Hence these events are to be rejected by the event processing.

Such post-detection event processing has been a standard technique for photon-counting CCD detectors in modern X-ray astronomy satellites such as *ASCA* and *Suzaku* (*e.g.*, Koyama *et al.* 2007), and the same, or very similar, scheme can be applied to our photon-counting solar X-ray telescope as well. A big difference here is, however, necessary event processing speed (as determined from level of X-ray flux), is usually 1-2 orders of magnitude higher in the case of solar application than X-ray astronomy; in the latter case, a typical pixel-processing speed is ~1 Mpixels/s (Dotani, T., private communication) while the pixel-processing speed necessary for the photon-counting telescope would be 65 Mpixels/s for photon-counting area of 256×256 pixels and 262 Mpixels/s for 512×512 pixels, with 1000 fps frame readout rate. While this difference is certainly a technical challenge for realizing photon-counting imagery on the X-ray solar corona, there has been effort in the X-ray astronomy community to achieve higher-speed pixel processing for the need of observing bright celestial objects. Anabuki *et al.* (2002) reported that the pixel-processing speed of 10 Mpixels/s with 5×5 pixel-area method was achieved with an FPGA by introducing a noble pipeline scheme for processing series of pixel data. Considering technical progress in FPGAs after 2002, having pixel-processing speed of a few to ~10 times larger than this value would not be totally unrealistic. Note parallel event processing using multiple FPGA units is a viable possibility to reduce processing speed for each unit.

Now let us consider what fraction of the incident photons is detected as "valid events" by the event processing method with 5×5 pixels. Suppose average number of photon incident for each frame sample, for each pixel, is p (photons/pixel/sample). As the photon incidence events follow Poisson statistics, the probability P_{tot} of having a valid event (which contains cases such as the right panel of Figure 4.19(a)) is given by

$$P_{tot} = (1 - e^{-p}) \times e^{-24p}.$$

This probability includes cases of, not only pure single event, but also multiple events (pile-up events) whose charge distribution happened to be contained in a single 3×3 pixel area. Since the single-event probability P_1 for the central pixel is expressed as

$$P_1 = p \times e^{-25p} ,$$

ratio of single events among detected valid events R_1 is

$$R_1 = \frac{P_1}{P_{tot}} = \frac{p}{e^p - 1} .$$

Figure 4.20 presents P_{tot}, P_1, and R_1 as a function of p. P_{tot} takes the maximum value of 0.015 at p = 0.041 photons/pixel/sample. This means, with N = 1000 fps frame readout, 15.0 counts/s/pixel is detected as valid events out of photon incidence rate of 41 counts/s/pixel. Single-event fraction R_1 exceeds 90% for $p \leq 0.2$ photons/pixel /sample. Figure 4.21 shows valid-event detection rate, in terms of counts/s/pixel (*i.e.*, in every seconds, instead of every sample) as function of average photon incidence rate to the detector (in terms of photons/s/pixel) and frame readout rate (fps). Obviously, fraction of valid events against incident photons decreases as the incident photon rate increases, because of increased probability of multiple photon incidence in a single

frame. This is an important aspect of photon-counting observations that excessive incident photon rate simply results in few number of single-events that are useful for generating energy spectra. Namely, the incident photon count rate has to be adjusted to an appropriate level so as to have good number of single-events detections.

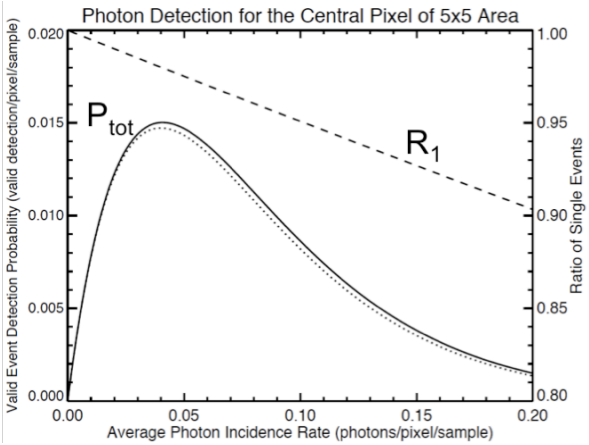

Figure 4.20. Profiles of valid-event detection probability P_{tot} (solid curve) and single-event fraction R_1 as function of average photon count rate p (photons/pixel/sample). Scales on the left Y axis apply to P_{tot} while those on the right Y axis to R_1. Probability of being a single event (P_1) is also shown in the figure as a dotted curve.

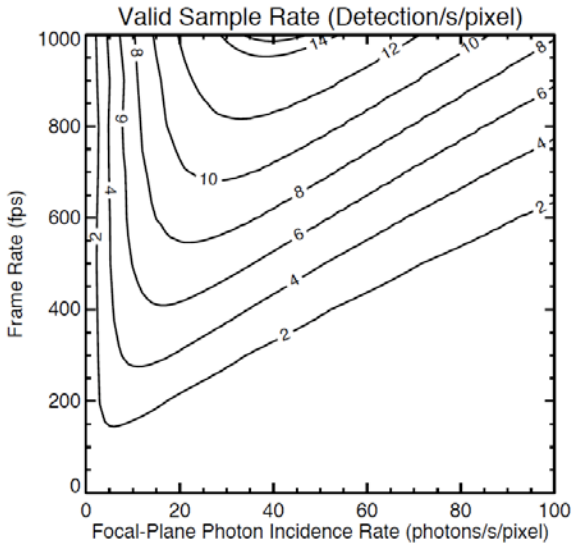

Figure 4.21. Valid-event detection rate (in terms of counts/s/pixel) with respect to average photon count (incidence) rate (photons/s/pixel) and frame readout rate (fps). Profile of P_{tot} in Figure 6.A-2 corresponds to a horizontal cut at the frame rate of 1000 fps in this figure.

Chapter 5: Spacecraft and Mission Design

The spacecraft characteristics as the baseline are summarized in Table 5.1. Key items of the characteristics are described in following sections.

Table 5.1. Characteristics of the baseline spacecraft.

Spacecraft layout	Telescopes mounted on the optical bench, which is on the Bus module. See Figure 7.1.
Weight	4930 kg (at liftoff), 2330 kg (dry weight)
Size	3.2 m x 3.2 m x 7.4 m, excluding solar array paddles
Launch vehicle	JAXA H-IIA (type 202)
Orbit	An inclined geo-synchronous orbit (Baseline) A sun-synchronous polar orbit (optional)
Power	~3,500 W (maximum)
Command & Telemetry	Uplink and housekeeping downlink: S-band Downlink: X-band 16-QAM (16Mbps) Ka-band QPSK (80Mbps, optional)
Attitude control	3-axis body pointing with high accuracy Image stabilization system in some telescopes A function to change the pointing around Z-axis for matching spectrograph slit direction to the observing target.
Science operations	Hinode operation scheme, with a final target selection around 10 to 15 minutes before the uplink in cases where this is essential for the science.

Two candidates exist for the X-ray imaging telescope. Here we assume the photon-counting grazing-incidence telescope, because it will require larger size and mass and higher telemetry rate.

5.1. Spacecraft Layout

The layout concept of the Solar-C Plan-B spacecraft is shown in Figure 5.1. Technical heritage acquired with the development of the Hinode (Solar-B) spacecraft is used as much as possible, including the design concept of the spacecraft structural layout. The three telescopes are mounted with mounting legs on the spacecraft OBU (Optical Bench Unit), which is a CFRP-made cylindrical structure providing stable condition to the telescopes. The telescope portion of the UV-Visible-IR telescope (SUVIT) is equipped inside the OBU cylinder. Its focal plane instruments and the other two telescopes are mounted on the external wall of the OBU. The mounting legs are made from low-thermal expansion materials, and provide 6-axis freedom kinematic mount to the telescopes. The OBU is mounted on the spacecraft bus module with a truss structure in order to isolate the OBU and telescopes from the influence of the thermal deformation of the bus module.

It is important to minimize co-alignment changes among the three telescopes and the attitude sensors against the launch load and the in-flight thermal environment. The

three telescopes and the attitude sensors (UFSS and IRU) are mounted on the same structural component, i.e., OBU, to achieve precise co-alignment among them.

The size and mass of the telescopes used for the initial design are listed in Table 5.2. The values in this table are the initial guess based on the aperture size and focal length currently under consideration for each telescope. The values contain significant uncertainty and will be revised as the design is in progress.

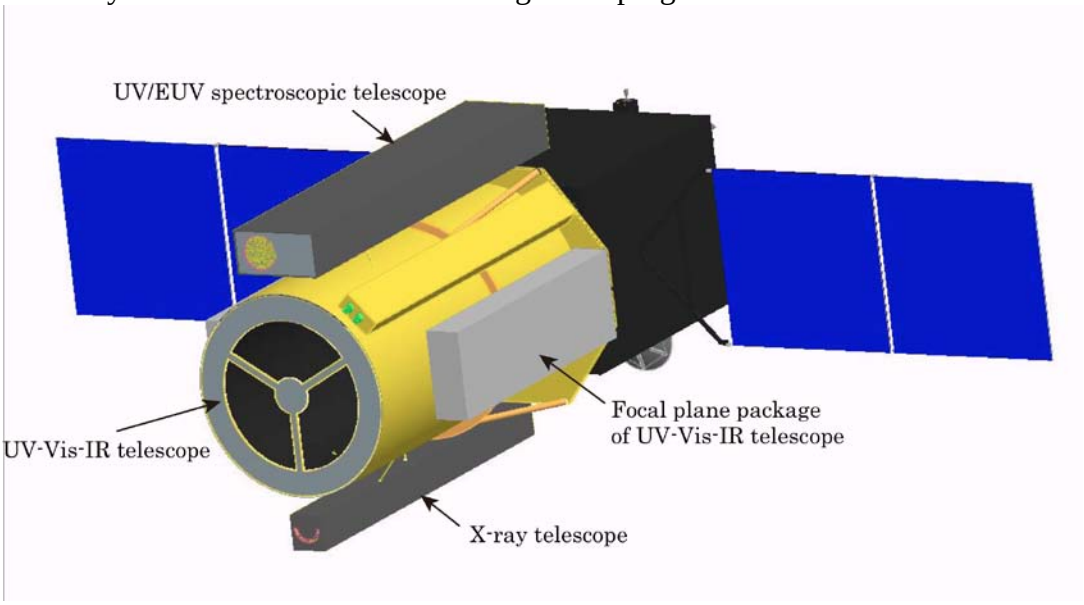

Figure 5.1. SOLAR-C plan-B spacecraft

Table 5.2. Size and weight of the telescopes used as the initial parameters.

Instruments		Size (mm)	Weight (kg)
UV-Vis-IR telescope	Telescope	φ2300 x 4300	500
	Spectrograph	1000 x 400 x 3200	100
	Imager	1000 x 400 x 3200	100
UV/EUV spectroscopic telescope		1000 x 500 x 5000	150
X-ray telescope (photon counting)		400 x 400 x 4500	150
Total			1000

The initial mass estimate result is shown in Table 5.3. The total mass of all the telescopes (1,000 kg) is a very rough value (upper-side value) and this will be revised as the telescope design is in progress. The spacecraft bus system is about 1,260 kg. The propellant for moving the spacecraft from a geo-transfer orbit (GTO) into an inclined geo-synchronous orbit (GEO) and maintaining the GEO orbit is counted as about 2,300 kg, which is the initial guess based on the information available on the website of Michibiki (QZSS), which has an inclined geo-synchronous orbit (GEO). The reasons why we are considering a GEO orbit as the primary option can be found later.

JAXA H-IIA 202 rocket is assumed as the baseline launch vehicle. This rocket is capable of installing a 4-ton spacecraft into a GTO orbit. The initial mass estimate shows about 500 kg over the 4-ton, and we will need to make efforts to reduce the mass by looking at the accuracy of mass estimates. Note that H-IIA 204 rocket, with four solid rocket boosters, can install a 6-ton spacecraft into a GTO orbit, although it is much

more expensive.

Figure 5.2 shows the dimension of the spacecraft, which can be fitted in the Model-4S fairing envelopes. The height is about 7.4m. The front-end position of the X-ray and UV/EUV telescopes may be located much below the front position of the UV-Visible-IR telescope, if the 4S fairing is used. This may give a contamination risk to the UV/EUV and X-ray telescopes, because these telescopes entrance views the outer side surface of the UV-Visible-IR telescope. In the design phase, we should carefully evaluate this layout and contamination issue in order to minimize the contamination risk.

Table 5.3. Initial mass estimate result.

Components		Weight (kg)	Remarks
Mission instruments		1000	Table 7.2
Structures	Bus module	340	Based on a standard Bus module
	Optical Bench	70	Sizing from Hinode optical bench
Thermal control system		100	
Data handling (space wire) system		10	Based on Astro-H (space wire) system
Communication	S and X-band	21	Based on Section 7.2.3.
	Ka-band (optional)	TBD	
Electric power system		142	
Solar array paddles		120	2 wings, 2 panels for each wing.
Attitude & Orbit control system		100	Including MIB (momentum wheel isolation bench, 30kg)
Chemical propulsion system		170	Including apogee kick motor (~500N thruster, section 7.3)
Other peripheral hardware, such as electrical cables and mechanical parts		185	
Total (dry weight)		2258	
Propellant		2300	Based on the information available on the Michibiki (QZSS) website.
Total (at liftoff)		4558	

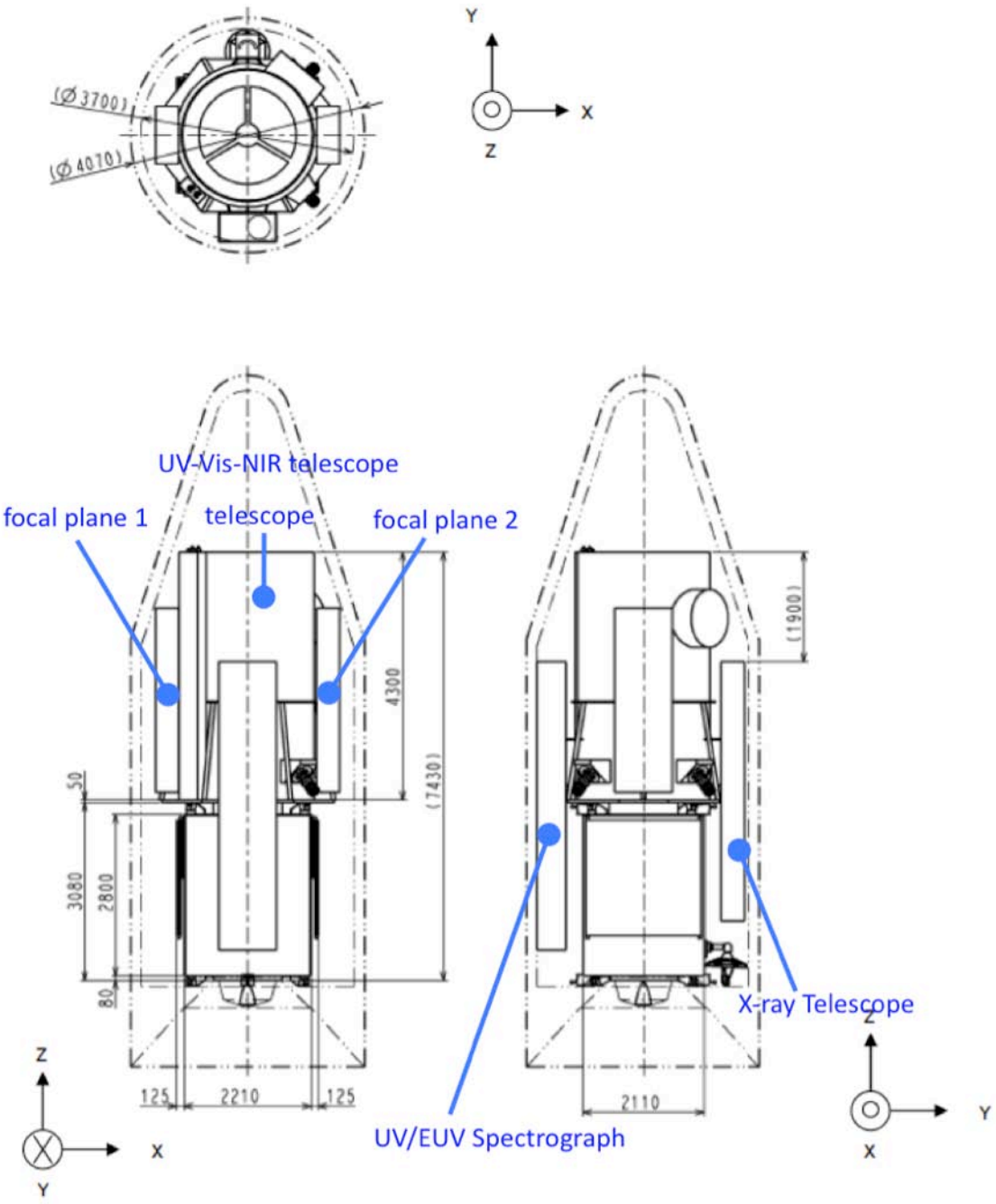

Figure 5.2. The spacecraft layout in the 4S fairing of the JAXA H-IIA rocket

5.2. Science Telemetry

5.2.1. Data rate estimate

Table 5.4 summarizes the data rates estimated from the three mission instruments. This is the initial guess based on the preliminary science design including the format size of detectors and typical exposure cadence. Details of the estimate can be found in Appendix 7-A. The table tells that high rate science telemetry is required to acquire spectroscopic and polarimetric data with high cadence and resolution. “Standard” case is for continuous observations without interruption, producing data with a constant rate. “Burst” case means that the data is produced with highest data rate, but the duration of such observations is limited.

The minimum requirement is that *the data can be acquired constantly with the data rate (the rate after compression) of about 8 Mbps in total*. According to evaluation of Hinode data, lossy compression is acceptable to most science cases, excepting X-ray telescope’s photon counting data, although the effect from lossy compression needs to be evaluated in the future. Thus, we assume to apply lossy compression to the data.

Also, much higher rate needs to be handled on board to have burst case observations. Assuming lossy compression can be used for burst case, the data output with 570 Mbps (before compression) and 143 Mbps (after compression) should be handled properly on board.

Table 5.4. Estimated data output rates from the mission instruments.

Instruments		data rate (Mbps)		
		no comp.	lossless comp.	lossy comp.
Solar UV-Vis-IR telescope	standard	14.4	6.1	2.5
	burst	320	128	48
UV/EUV spectroscopic telescope	standard	7.0	3.0	1.5
	burst	140	60	30
X-ray telescope (photon counting)	standard	6.9	3.5	
	burst	110	55	
Total	standard	28.3	12.6	7.5
	burst	570	243	143

5.2.2. Data handling on board and data recorder

The overall flow of the science data on board is described in Figure 5.3. It is the baseline that data compression is performed in each telescope before producing the data into the spacecraft bus. Since different types of data products (imaging, spectroscopic, and photon counting) are generated in the three mission instruments, it would be good to use different compression algorithms more suitable for the properties of data products. After compressing and packetizing the data, each instrument sends compressed data to the spacecraft. SpaceWire may be used for the data interface between the telescopes and spacecraft. There is no mission data processor, which is different from Hinode science

data handling system.

When we run continuous (i.e. 24 hours every day) observations with the 8Mbps data generation rate, *the total data amount is about 700 Gbits per day*. Since the maximum duration of the ground station support at USC may be less than 8 hours, the data needs to be recorded in the data recorder. The capacity of the data recorder should be enough to allow us to have continuous observations for 24 hours every day. Moreover, the data recorder allows us to run the burst observations; Data produced burstly is stored in the data recorder, followed by downloading the stored data after the acquisition when the spacecraft is linked to a ground station. The capacity of the data recorder will be determined by considering the observation plans and the capacity reality.

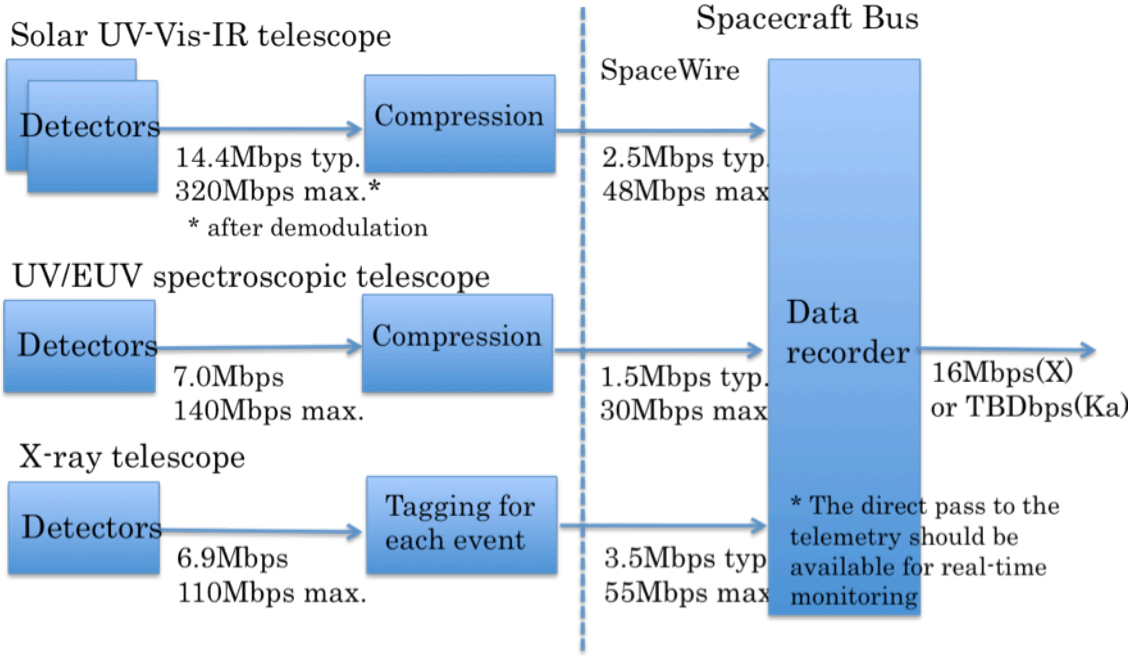

Figure 5.3. Overall data flow estimate

5.2.3. Science Telemetry System

The high-speed telemetry channel is absolutely required for the Solar-C Plan B mission to transfer the huge amount of data expected from the onboard telescopes. The requirement is to design the telemetry and data storage system to enable downloading the volume of the data produced constantly with the rate of about 8 Mbps.

An initial trade-off study suggests either an X-band telemetry system (16Mbps, 16-QAM modulation, with semi-directional low-gain antennas), or Ka-band telemetry system (80[TBD]Mbps, QPSK modulation, with directional high-gain parabola antenna), or the both of them. Each telemetry system is briefly described below.

X-band telemetry system (Figure 5.4)

X-band telemetry is easy to handle, but the problem is that the allowable bandwidth is restricted within 10MHz for near-earth space science applications in X-band frequency band, according to a recommendation by the ITU's SFCG (Space Frequency Coordination Group). If we use the QPSK (phase shift keying) modulation, same as Hinode's X-band modulator, the telemetry speed needs to be below about 8 Mbps to meet the signal bandwidth restriction. Instead, the 16-QAM (quadrature amplitude modulation), which is widely used on the ground communication and will be tested in one of Japanese technology demonstration satellites, can increase the telemetry speed to 16 Mbps.

If we have 12 hours for the telemetry downlink in total per day, the telemetry system can transfer all the data acquired with 8Mbps continuously for 24 hours. We assume USC 34m antenna as the primary antenna, and the system can be designed to have a positive link margin. Considering other spacecraft operations at USC 34m, the duration of downlink may be restricted below 8 hours. Thus it would be helpful to have additional downlinks on NASA and ESA stations, if antennas are available in Asia, Oceania, and Pacific Ocean area. It is also noted that a huge mass memory (recorder) is needed to record the data taken during non-contact period.

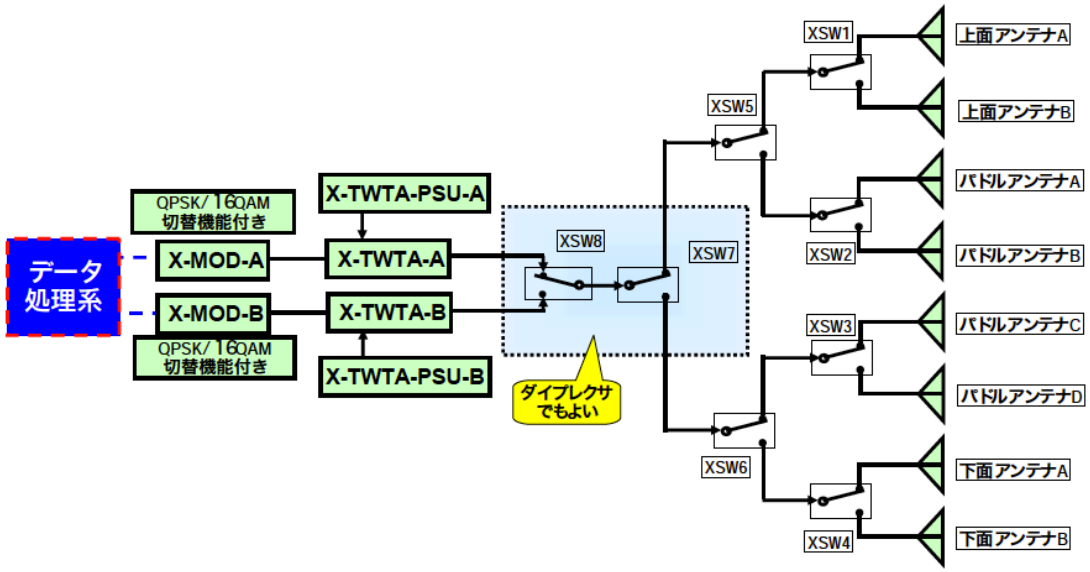

Figure 5.4. X-band telemetry system

Ka-band telemetry system

Another possibility is to newly explore the usage of Ka-band in Japan. Higher telemetry rate is possible because a wider bandwidth can be utilized in the Ka band by a spacecraft. Two candidate bands are identified; 1) ~17GHz, a portion of ground equipments available at USC can be used to minimize the cost. 2) ~26GHz, this band is used at the Near Earth Network (NEN) of NASA. It is needed to newly prepare the system for receiving signals at this band in Japan, if the telemetry is received at Japan. When the bandwidth is 100 MHz, 80 Mbps is achieved with QPSK. The downlink

duration can be reduced to a few hours, although a more huge mass memory (recorder) is needed.

A concern is that attenuation of signals due to bad weather (rains and heavy clouds) in Japan affects quality of the data and gives complication to real-time daily operations.

The both X-band and Ka-band systems work in case of the GEO orbit; X-band 16-QAM (16Mbps) as a baseline and Ka-band QPSK (80Mbps) as an option, though we have to implement the Ka-band capability at a ground station. However, it is impossible to adapt the X-band system if the spacecraft is in a sun-synchronous polar orbit, because about 15 passes are too small to download all the data. The only way is to adapt the Ka-band system, but a Ka-band antenna is required in the polar region, such as at Svalbard. At least 144 minutes are needed as the total contact duration to download all the data with 80Mbps and this duration corresponds to about 12 station contacts. During each contact (duration ~ 12 minutes), the Ka-band high-gain antenna is quickly moved to direct to the ground station, resulting in a concern of micro-vibration from the antenna mount mechanism. More details of the downlink system for the GEO orbit are summarized below:

1. GEO/X-band (baseline)
   - The 16-QAM modulator, which is under development for the ASNARO mission
   - The bit rate is 16 Mbps, which occupies the band width ~10MHz
   - Semi-directional low-gain antenna (angle ~ 60°, 0dbi), which is used in HAYABUSA. At least 6 (TBD) antennas are mounted to cover any direction, one of which is selected by switch.
   - 50W TWTA amplifier, which is under development for the ASTRO-G mission.
   - The link margin is XXX dB for USC 34m.
   - It is necessary to implement the X-band 16-QAM demodulator at the USC.
2. GEO/Ka-band (optional)
   - The QPSK modulator and the bit rate is 80 Mbps (band width=100MHz)
   - φ 0.3m high-gain antenna (32dbi) + 0.5W SSPA, whose pointing is driven by a two-axis mount mechanism.
   - The link margin is XXX dB for USC 34m.
   - It is necessary to make the Ka-band (17GHz) at the USC available. Another possibility is to make use of Ka-band (26GHz) with NASA or ESA ground station.

5.3. Orbit

As briefly discussed in section 5.2.3, two orbit candidates are considered for the Plan B spacecraft. Currently, an inclined geo-synchronous orbit (GEO) is considered as the baseline, with a sun-synchronous polar orbit (SSO) as the backup.

<u>Geo-synchronous orbit (GEO):</u>

- Same as Solar Dynamic Observatory (NASA)

- Altitude: 36000km, inclination: <30°, period: 1 day

Sun-synchronous polar orbit (SSO):

- Same as Hinode, TRACE, and IRIS.
- Altitude: 680-800 km, inclination: 97-98°, period: 98 min

The GEO orbit would provide much more advantages than the SSO orbit, although a demerit on the weight of the spacecraft. Advantages are listed below:

- X-band telemetry can be utilized to download the data volume required for observations, though the duration of contacts is fairly long (8 hours or longer per day).
- Thermal environment is colder in GEO than in SSO because of lower influence of infrared radiation from the earth, which much helps the thermal design of the optical telescope (see section 4.3.4).
- GEO is thermally very stable, providing less orbital variation of thermal environment. This would reduce structural deformation, resulting in less orbital variation in pointing stability (section 5.4.1) and temperature fluctuation of telescope optics.
- A new type of methodology for science operations (section 5.7) can be adapted, which would much help the narrow field-of-view spectroscopic telescopes to perform optimized observations
- Eclipse seasons are shorter in GEO than in SSO. SSO has eclipse season with about 20 mins (at maximum) duration every 98 mins orbital period and the season continues three months every year. The GEO's eclipse is about 72 mins (at maximum) duration per day and it continues only one month, twice every year (see Figure 5.5). A potential demerit is to need a large capacity of the battery for keeping some components warm without solar heat input.

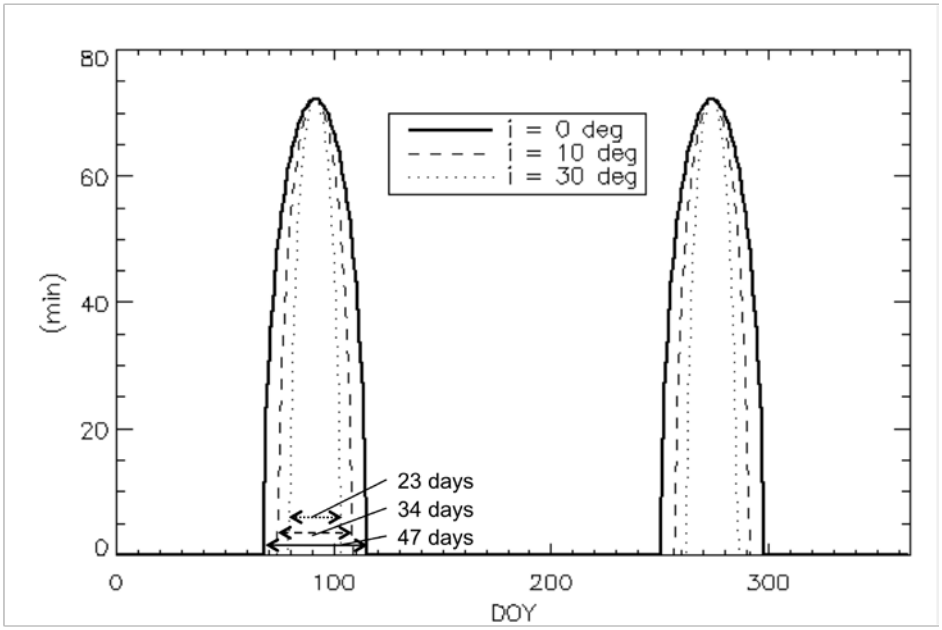

Figure 5.5. Eclipse duration in the case of GEO. The maximum duration is 72 mins per day. The eclipse season happens twice every year around the equinox. The duration of

the eclipse season depends on the inclination angle of the orbit.

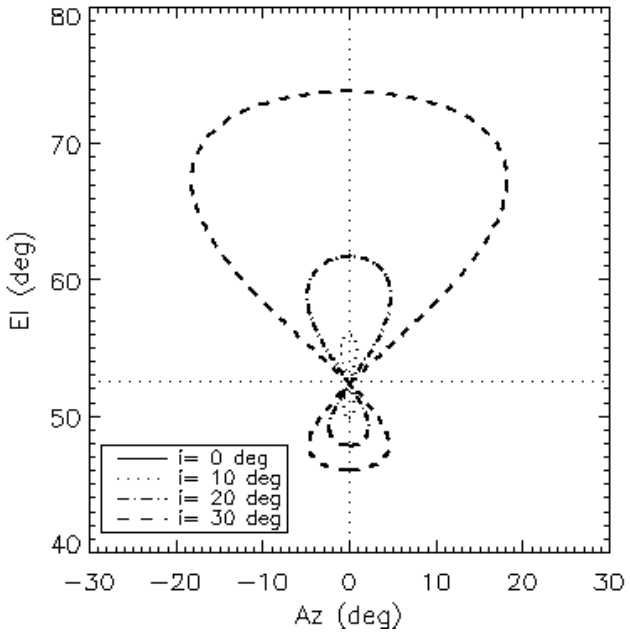

Figure 5.5: Visibility of the spacecraft from USC that is located at latitude of 30°N when the spacecraft is in GEO with inclinations.

It is not necessary to install the spacecraft into the geostationary orbit (GSO) in which the spacecraft is located directly above the equator where the inclination angle is 0°. When the orbit is at non-zero inclination, the duration of the eclipse season can be made shorter than one month (Figure 5.5). The spacecraft is no longer stationary when viewed from a ground station at the non-zero inclination. The spacecraft is always visible at an elevation angle higher than 45° at USC (latitude 31°N) when the inclination angle is less than 30° (Figure 5.6), which is high enough for continuous contact without interruption.

The most critical issue of GEO is that an apogee kick motor is required to install the spacecraft from GTO to GEO. The engine and its propellant take half of the total weight at the lift-off as is shown in Table 5.3.

5.4. Pointing Stability and Attitude Control

5.4.1. Requirements on the pointing stability

We set targets of angular resolution better than 0.1 arcsec in the Solar Ultraviolet-Visible-IR telescope, and better than 0.2 - 0.5 arcsec in the UV/EUV and X-ray telescopes. The angular resolution requires high stability of the body pointing, otherwise images are blurred due to residual pointing jitter. The requirements on the

pointing stability are thus derived based on the requirements on the angular resolution and exposure duration to obtain a data set (an image or set of images), and are summarized in Table 5.5. In Figure 5.7, the requirements on the pointing stability for both HINODE and SOLAR-C are indicated and compared as a function of frequency.

Table 5.5. Requirements on the pointing stability of the mission instruments.

Instruments		Time scale	Requirements (θx/θy)	Unit
Solar UV-Vis-IR telescope (*)		1 sec	0.015	arcsec 3σ
		10 sec	0.015	arcsec 3σ
		1 hour	2	arcsec 0-p
		Mission life	20	arcsec 0-p
UV/EUV spectroscopic telescope		0.5 sec	0.3	arcsec 3σ
		5 sec	0.3	arcsec 3σ
		1 hour	2	arcsec 0-p
		Mission life	32	arcsec 0-p
X-ray telescope	Normal incidence (*)	1 sec	0.1	arcsec 3σ
		10 sec	0.1	arcsec 3σ
	Grazing incidence	1 sec	0.3	arcsec 3σ
		1 min	0.7	arcsec 3σ
		1 hour	8	arcsec 0-p
		Mission life	32	arcsec 0-p

Instruments		Time scale	Requirements (θz)	Unit
Solar UV-Vis-IR Telescope		1 hour	50	arcsec 0-p
UV/EUV spectroscopic telescope		1 hour	100	arcsec 0-p
X-ray telescope	Normal incidence	1 hour	50	arcsec 0-p
	Grazing incidence	1 hour	100	arcsec 0-p

(*) The pointing stabilities are to be achieved with the usage of an image stabilization system inside the telescopes.

It is important to identify critical items to achieve the pointing stability requirements by comparing on-orbit pointing performance of HINODE that achieved the highest pointing stability in Japanese space missions. We evaluate the pointing stability of HINODE in the frequency domain using telemetry data taken with the Ultra Fine Sun Sensor (UFSS) and the mechanical gyroscope (Inertia Reference Unit, IRU) that are components of the attitude and orbit control system (AOCS) on-board HINODE. They provide residual pointing errors with a temporal sampling of 0.5 sec, which provides the pointing stability in the frequency domain lower than 1 Hz. The correlation tracker (CT) on-board HINODE provides signals of pointing errors with a temporal sampling of 580Hz, which is used to evaluate high frequency disturbances in the frequency range between 0.1 Hz and 290 Hz. The on-orbit pointing stability evaluated with UFSS, IRU, and CT of HINODE is shown in Figure 5.7, as comparison with the requirements on the pointing stability for HINODE (top) and SOLAR-C (bottom). It is found that the AOCS on-board HINODE delivers better performance than the requirements in the frequency range lower than 0.1 Hz (upper limit of the AOCS control

band). It is important to note that, without the image stabilization system, it is difficult to realize the good spatial resolution with SOT because the pointing stability of about 0.1 arcsec (0-p) at 0.1 Hz achieved with the AOCS is worse than the requirements of SOT. The image stabilization system has a crucial role in the reduction of the attitude jitter in the frequency range between 10^{-2} Hz and 10 Hz.

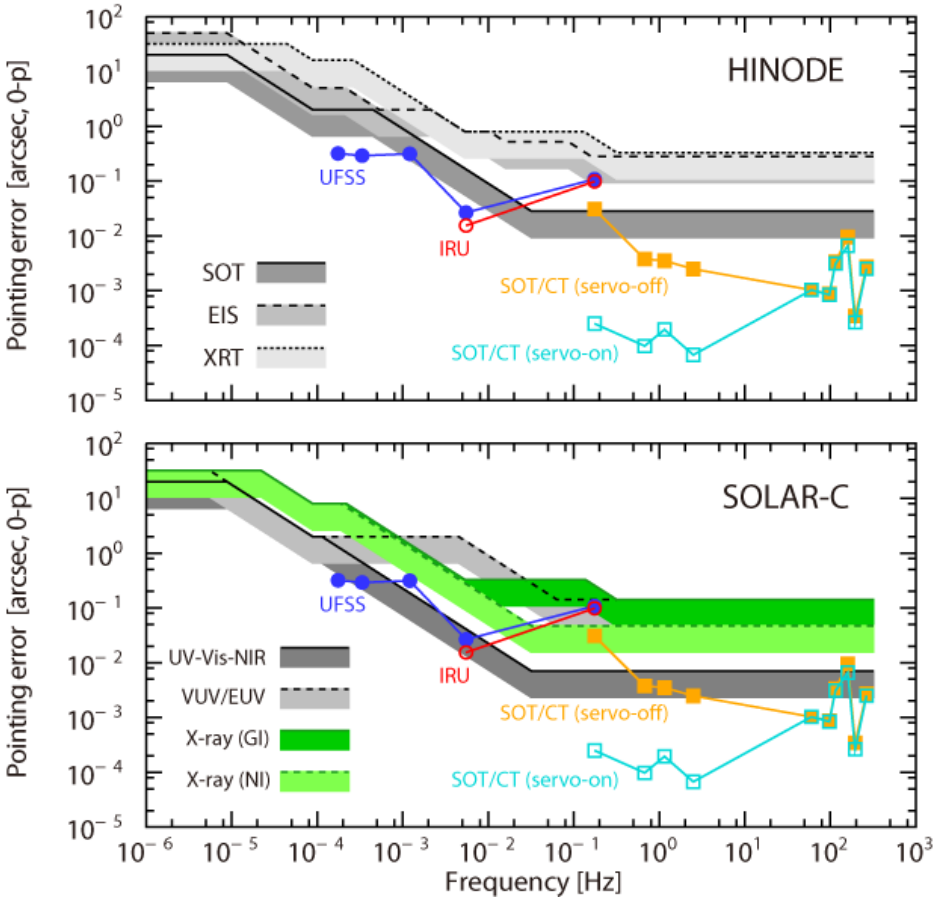

Figure 5.6. On-orbit performance of the pointing stability in HINODE in comparison with the requirements of the pointing stability for the mission instruments aboard HINODE (*top*) and SOLAR-C (*bottom*). The thick, dashed and dotted lines represent the requirements as a function of frequencies while the lower boundaries of the shaded belts indicate conditionally acceptable level, which is defined as one third of the requirements. The blue filled circles show the pointing stability evaluated with UFSS, the red open circles are that with IRU. The open cyan squares indicate the pointing stability evaluated with CT in the case of servo-on, and filled orange squares are that in the case of servo-off.

By comparing the on-orbit pointing performance of HINODE with the requirements for SOLAR-C, we have identified three critical items for further improvements necessary in the Plan B spacecraft:

(1) Orbital variation (10^{-3} – 10^{-5} Hz)

It is caused by misalignment between the attitude sensors and the telescopes due to thermal deformation of structures supporting them. In the case of SSO, temperature fluctuation is mainly induced by significant influence of infrared radiation from the earth. In SOLAR-C, the orbital variation is to be reduced significantly thanks to the lower temperature fluctuation at GEO.

(2) Degradation of the pointing stability at around 0.1 Hz

There is an unexpected degradation at around 0.1Hz in the on-orbit pointing performance of HINODE. The frequency of 0.1 Hz corresponds to the upper limit of controllable frequency of the AOCS. The stability is 0.1 arcsec (0-p), which is not enough to achieve the spatial resolution better than about 0.3 arcsec. It is necessary to clarify the cause and to improve the AOCS not to induce the degradation in SOLAR-C. If it is difficult to improve the pointing stability at around 0.1Hz only with the AOCS, the mission instruments have to be equipped with an image stabilization system inside them.

(3) High-frequency disturbances (>100 Hz)

The disturbances at the frequencies higher than 100 Hz have to be suppressed to achieve the resolution of 0.1 arcsec in SUVIT of SOLAR-C. They are induced by structural resonance between the telescope structures and disturbances of momentum wheels (MWs) and mechanical gyros. Because the image stabilization system aboard HINODE is not effective to such high-frequency (>20 Hz) disturbances, one possible approach is to improve the image stabilization system to have a broader response in the frequency as high as 100-200 Hz. The other approach is to suppress generation or transmission of the disturbances from MWs and the mechanical gyroscopes, which is technically possible if MWs are mounted on a vibration isolation bench.

5.4.2. Attitude control system

The attitude control system provides three-axis stabilization of the spacecraft to point to an observing target on the solar surface. We can basically use the same configuration as HINODE, which achieved the highest pointing stability in Japanese space missions, but some modification is necessary in order to improve the items required for further improvements of the pointing stability described in section 5.4.1. Major components in the attitude control system are listed below.

- Attitude and orbital control processor (AOCP)
  - The attitude computer is based on Hinode and other JAXA spacecrafts.
- Ultra Fine Sun Sensor (UFSS)
  - The sensor precisely measures the direction of the Sun with sub arc second accuracy.
  - The performance of UFSS on-board HINDOE is enough for the Solar-C requirements.

- Fine Sun Sensor (FSS)
  - The planned sensor has been used on Planet-C and so on.
- Star Tracker (STT)
  - The start tracker measures the roll around the direction of the Sun.
  - The performance of the star trackers used in other spacecrafts meets the Solar-C requirements.
- Tuned Dry Gyroscope (TDG)
  - The gyroscope measures the angle change of the spacecraft attitude as an inertia reference unit (IRU).
  - TDG has been used in many space missions in Japan. We have to investigate the possibility to reduce the disturbances caused by the mechanical gyroscope.
  - As an alternate option, fiber optic gyroscope (FOG) is considered for a disturbance-free gyroscope.
- Geomagnetic Aspect Sensor (GAS)
  - The sensor may be purchased from an aerospace company.
- Momentum wheels (MW)
  - Momentum wheels are used as actuators of the spacecraft attitude.
  - The baseline for momentum wheels is same as used in Hinode.
  - For suppressing transmission of the micro-vibration disturbances, vibration isolation bench may be required to mount momentum wheels.
- Magnetic torquer (MTQ)
  - The sensor may be purchased from an aerospace company (following the previous missions).

5.4.3. Flexibility on the role attitude

In the Hinode case, the spacecraft role is always fixed to align the spacecraft Y-axis, i.e., Y direction of CCD detectors, to the solar North-South direction. For the Solar-C Plan B mission, it would be useful to allow changing the spacecraft role attitude, depending on the nature of observing target. For example, when the slit of spectroscopic telescopes is placed along a coronal loop structure, the spectroscopic telescopes can record spectral lines as a function of spatial position along the loop structure with very limited number of slit scan positions (or in sit-and-stare mode). This can provide high cadence of observations, allowing us to track energy flows along magnetic fields.

This capability will be considered in the AOCS functional design. It would be not difficult in implementing this capability from viewpoint of AOCS. However, this capability would give complication to the command uplink and telemetry downlink operations. We may need more number of onboard antennas to cover any directions for the communication link with a ground station. Or, insufficient communication link level may be given depending on the roll angle.

5.5. Spacecraft thermal design to dump heat load from 1.5m telescope

In the thermal design of the spacecraft system, we basically follow the same concept as adapted in HINODE, which is summarized in the following:

- The OBU is made of low-thermal expansion and high-thermally conductive CFRP.
- The telescopes are thermally isolated from OBU and the spacecraft bus.
- The OBU is thermally isolated from the spacecraft bus.

However, as described in section 4.3.4, some part of the large heat load given to the primary mirror (M1) of the UV-Visible-IR telescope (SUVIT) needs to be transferred toward the spacecraft bus direction (-Z direction). With having the heat path toward the bus direction, the temperature of M1 can be kept well within the acceptable temperature range. Thus, a thermal interface is required between the SUVIT's primary mirror and the spacecraft. A preliminary thermal concept is to have heat pipes to transfer the heat to the radiators equipped at the bus side (Figure 5.8). The heat load at M1 is dumped to a cold plate located behind M1 with radiation. Heat pipes connect the cold plate to the radiators on the side of the bus or OBU structure. The heat load of about 100 – 200 W is required to transfer via heat pipes. A preliminary study shows that the size of the radiators necessary for 100-200W heat dump can be accommodated either on the side of the bus module or OBU structure.

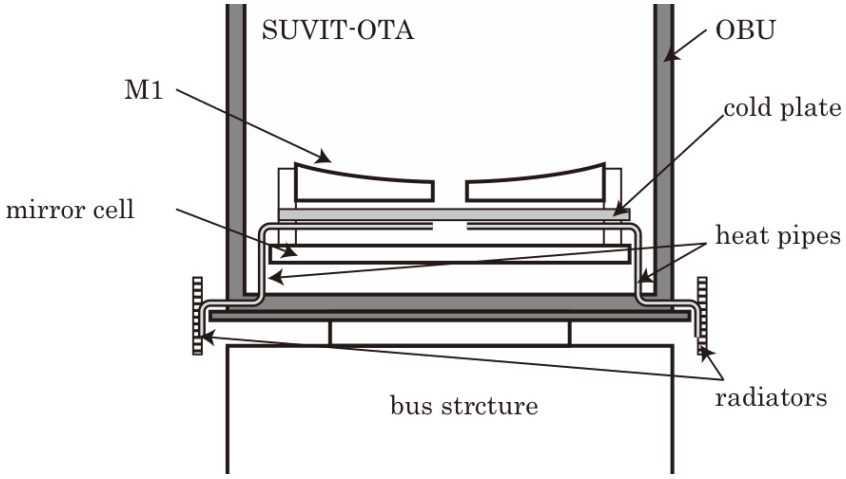

Figure 5.7. Thermal design concept to dump the heat load from M1 of the SUVIT-OTA.

5.6. Spacecraft power system

The spacecraft has solar array panels that generate the electric power. Considering the size of the Bus module and telescopes, 4 solar array panels would be a baseline. They are attached on the Bus; either two wings, each of which has two panels, as shown in Figure 5.1, or 4 panels (wings) at each face of the Bus module.

The 4 panels can generate the power up to ~3500W. The power budget will be evaluated in the design phase, but we will have no critical concerns on the power budget, from our former experience on Hinode (~1100W).

The proposed orbit provides a long continuous duration of non-eclipse condition. For eclipse periods and initial launch operation, the power system needs a power battery to provide the electrical power to the onboard components. The size of buttery will be determined after the initial evaluation of power budget in the design phase.

The power system provides an unregulated 50V power to all the components on board; 50-52 V in non-eclipse period and 30-49V in the eclipse period, which is same as used in Hinode.

5.7. Science operations

Since the spacecraft is viewed for a long duration from a ground station (USC), science daily operations may become more flexible than Hinode's operation. The following methodology may be added to the science planning scheme; an observer in the operation room checks images in real time, and make commands for adjusting the telescope pointing to the small area of interest, and then the operator uplinks the commands to the spacecraft during a contact (Figure 5.9). This kind of operations would be very powerful, because telescopes may have the field of view smaller than Hinode and the slit position for spectroscopic telescopes is very critical to capture the phenomena of interest.

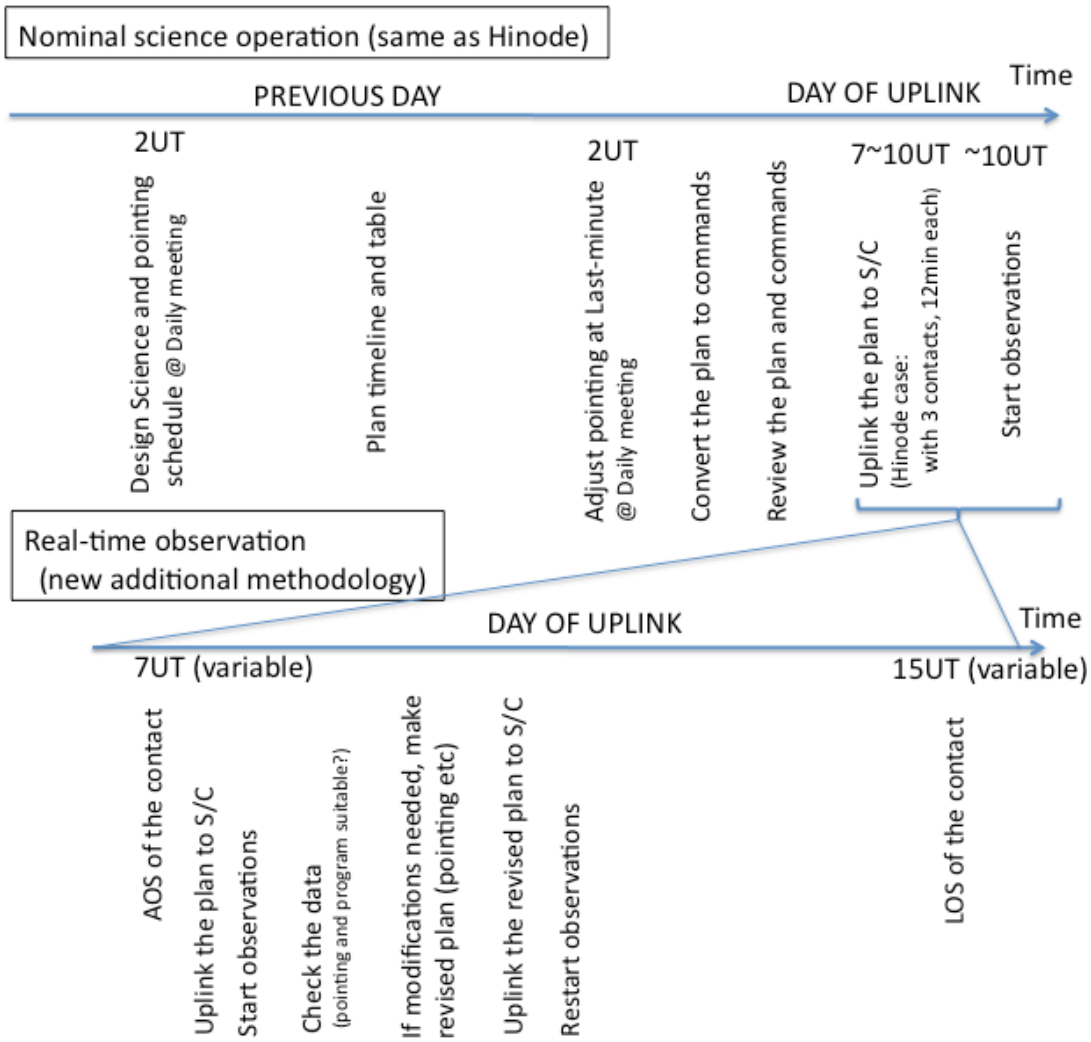

Figure 5.8. A new methodology of science operations that can be considered in the GEO case

Appendix 5-A. Data rate estimate

We here estimate data production rates from the mission instruments using their preliminary design including formats of their detectors and typical exposure duration in order to clarify how much telemetry rate is required to download the data from the spacecraft to the ground. We define two typical observing cases for each instrument; one is for continuous observations without interruption ("standard case"), which produces a lower data rate, and the other is for short-term burst observations ("burst case"), which produces a higher data rate. In the estimation, we assume a bit depth of their data products, and how much the data amount can be shrunk with lossless and lossy compression algorithms. Details are summarized in the following.

- Solar UV-Vis-IR telescope (SUVIT) / Spectrograph package
  - Standard case:
    - In this case, we can achieve high signal-to-noise ratio of about 10^4 with deep integration for measuring chromospheric magnetic fields.
    - Number of pixels of an image set:
      1024 (spatial) x 512 (wavelength) x 4 (Stokes) x 2 (orthogonal pol.)
      = 4 Mpixel
    - Bit depth:
      16bit/pixel (no comp.), 7bit/pix (lossless comp.), 3bit/pix (lossy comp.)
    - Temporal cadence:
      10 sec at each slit position

    → 6.4 Mbps (no comp.), 2.8 Mbps (lossless comp.), 1.2 Mbps (lossy comp.)

  - Burst case:
    - In this case, we can achieve standard signal-to-noise ratio of about $2x10^3$ with 1 sec integration for rapid slit scanning.
    - Number of pixels of an image set:
      2048 (spatial) x 1024 (wavelength) x 4 (Stokes) x 2 (orthogonal pol.)
      = 8Mpixel
    - Bit depth:
      16bit/pixel (no comp.), 6bit/pix (lossless comp.), 2bit/pix (lossy comp.)
    - Temporal cadence:
      1 sec at each slit position

    → 128.0 Mbps (no comp.), 48.0 Mbps (lossless comp.), 16.0 Mbps (lossy comp.)

- Solar UV-Vis-IR telescope (SUVIT) / Imager package
  - Standard case:
    - In this case, we get minimum wavelength sampling for Dopplergrams with the narrow-band filtergraph with reduced spatial and temporal sampling.
    - Number of pixels of an image set:
      2048 x 2048 (spatial) x 5 (wavelength)
      = 20 Mpixel

- Bit depth:
  12bit/pixel (no comp.), 5bit/pix (lossless comp.), 2bit/pix (lossy comp.)
- Temporal cadence:
  30 sec for each wavelength scan

→ 8.0 Mbps (no comp.), 3.3 Mbps (lossless comp.), 1.3 Mbps (lossy comp.)

➢ Burst case:
- In this case, we get full wavelength sampling of a spectrum line for imaging-spectroscopic observations with the narrow-band filtergraph with full spatial and temporal sampling.
- Number of pixels of an image set:
  4096 x 4096 (spatial) x 10 (wavelength)
  = 160 Mpixel
- Bit depth:
  12bit/pixel (no comp.), 5bit/pix (lossless comp.), 2bit/pix (lossy comp.)
- Temporal cadence:
  10 sec for each wavelength scan

→ 192.0 Mbps (no comp.), 80.0 Mbps (lossless comp.), 32.0 Mbps (lossy comp.)

● UV/EUV high-throughput spectroscopic telescope

➢ Standard case:
- In this case, we get a reduced set of spectrum lines with deep integration.
- Number of pixels of an image set:
  2048 (spatial) x 128 x 10 (wavelength)
  = 2.5 Mpixel
- Bit depth:
  14bit/pixel (no comp.), 6bit/pix (lossless comp.), 3bit/pix (lossy comp.)
- Temporal cadence:
  5 sec at each slit position

→ 7.0 Mbps (no comp.), 3.0 Mbps (lossless comp.), 1.5 Mbps (lossy comp.)

➢ Burst case:
- In this case, we get a full set of spectrum lines with shorter integration for rapid slit scanning.
- Number of pixels of an image set:
  2048 (spatial) x 256 x 20 (wavelength)
  = 10 Mpixel
- Bit depth:
  14bit/pixel (no comp.), 6bit/pix (lossless comp.), 3bit/pix (lossy comp.)
- Temporal cadence:
  1 sec at each slit position

→ 140.0 Mbps (no comp.), 60.0 Mbps (lossless comp.), 30.0 Mbps (lossy comp.)

- X-ray imaging (spectroscopic) telescope
  - Assumptions:
    - Perform tagging for each photon-incident event
    - Tagging information
      - ✓ Pixel address (X, Y)
      - ✓ Photon energy
      - ✓ Incident time
    - No on-chip/on-board pixel summing. Perform on ground if necessary.
    - Data compression may be possible, which reduces data rate to half.

  - Standard case:
    - In this case, we get photon counting imaging spectroscopy in 128 x 128 pixels ROI.
    - Pixel address (X, Y):
      7 bits x 2 = 14 bits (for 0–127)
    - Photon energy:
      10 bits (0–1023 ch)
    - Exposure time:
      every 1 ms
    - Ratio of event pixels:
      2 % (i.e., 128^2 x 10% = 327.7 pixels contain events)

    → 6.9 Mbps (no comp.), 3.5 Mbps (comp.)

  - Burst case:
    - In this case, we get photon counting imaging spectroscopy in 512 x 512 pixels ROI.
    - Pixel address (X, Y):
      9 bits x 2 = 18 bits (for 0–511)
    - Photon energy:
      10 bits (0–1023 ch)
    - Exposure time:
      every 1 ms
    - Ratio of event pixels:
      10 % (i.e., 512^2 x 10% = 6553.6 pixels contain events)

    → 110.0 Mbps (no comp.), 55.0 Mbps (comp.)

References

Acton, L.W. et al.: Deriving solar X ray irradiance from Yohkoh observations, 1999, J. Geophys. Res., 104(A7), 14827.

Anabuki, N. et al.: High-speed on-board data processing for x-ray CCD camera, 2002, Proc. SPIE, 4497, 158.

Asai, A. et al.: Strongly Blueshifted Phenomena Observed with Hinode EIS in the 2006 December 13 Solar Flare, 2008, ApJ, 685, 622.

Aschwanden, M. J. and Nightingale, R. W.: Elementary Loop Structures in the Solar Corona Analyzed from TRACE Triple-Filter Images, 2005, ApJ, 633, 499.

Aschwanden, M. J. et al.: Electron Trapping Times and Trap Densities in Solar Flare Loops Measured with Compton and YOHKOH, 1997, ApJ, 487, 936.

Aschwanden, M., Nightingale, R. and Alexander, D.: Evidence for Nonuniform Heating of Coronal Loops Inferred from Multithread Modeling of TRACE Data, 2000, ApJ, 541, 1059.

Asensio Ramos, A. et al.: Advanced Forward Modeling and Inversion of Stokes Profiles Resulting from the Joint Action of the Hanle and Zeeman Effects, 2008, ApJ, 683, 542.

Baker, D. et al.: Magnetic Reconnection along Quasi-separatrix Layers as a Driver of Ubiquitous Active Region Outflows, 2009, ApJ, 705, 926.

Banerjee, D. et al.: Long-Period Oscillations in Polar Plumes as Observed by cds on Soho, 2000, Solar Phys., 196, 63.

Banerjee, D. et al.: Polar Plumes and Inter-plume regions as observed by SUMER on SOHO, 2000, Solar Phys., 194, 43.

Banerjee, D. et al.: Propagating waves in polar coronal holes as seen by SUMER & EIS, 2009, A & A, 499, 29.

Barnes, G. and Leka, K. D.: Evaluating the Performance of Solar Flare Forecasting Methods, 2008, ApJ, 688, 107.

Baum, P. J. and Bratenahl, A.: Mass motion and heating in a magnetic neutral point system, 1974, Journal of Plasma Physics, 11, 93-98.

Baumjohann, W. et al.: Substorm dipolarization and recovery, 1999, J. Geophys. Res., 104, 24995.

Beckers, J. M.: Solar Spicules, 1972, Annual Review of Astronomy and Astrophysics, 10, 73.

Berger, T. E. et al.: Hinode SOT Observations of Solar Quiescent Prominence Dynamics, 2008, ApJ, 676, 89.

Bogdan, T. J. et al.: Waves in the Magnetized Solar Atmosphere. II. Waves from Localized Sources in Magnetic Flux Concentrations, 2003, ApJ, 599, 626.

Brandenburg, A. and Zweibel, E. G.: The formation of sharp structures by ambipolar diffusion, 1994, ApJ, 427, L91.

Brooks, D. H. et al.: Flows and Motions in Moss in the Core of a Flaring Active Region: Evidence for Steady Heating, 2009, ApJ, 703, L10.

Carlsson, M. and Stein, R. F.: Formation of Solar Calcium H and K Bright Grains, 1997, ApJ, 481, 500.

Carlsson, M. et al.: Can High Frequency Acoustic Waves Heat the Quiet Sun Chromosphere?, 2007, PASJ, 59, 663.

Carlsson, M. et al.: Chromospheric heating and structure as determined from high resolution 3D simulations, 2010, Memorie della Societa Astronomica Italiana, 81, 582.

Casalbuoni, S. et al.: Coronal plumes and the expansion of pressure-balanced structures in the fast solar wind, 1999, J. Geophys. Res., 104, 9947.

Casini, R., Bevilacqua, R., Lopez Ariste, A.: Principal Component Analysis of the He I D3 Polarization Profiles from Solar Prominences, 2005, ApJ, 622, 1265.

Cauzzi, G. et al.: Acoustic Shocks in the Quiet Solar Chromosphere, 2007, The Physics of Chromospheric Plasmas ASP Conference Series, 368, Proceedings of the conference held 9-13 October, 2006 at the University of Coimbra in Coimbra, Portugal. Edited by P. Heinzel, I. Dorotovič, and R. J. Rutten. San Francisco: Astronomical Society of the Pacific, 127.

Centino, R. et al.: Emergence of Small-Scale Magnetic Loops in the Quiet-Sun Internetwork, 2007, ApJ, 666, L137.

Cheung, M. C. M. et al.: Solar Surface Emerging Flux Regions: A Comparative Study of Radiative MHD Modeling and Hinode SOT Observations, 2008, ApJ, 687, 1373.

Chiueh, T.: Ambipolar Diffusion--driven Tearing Instability in a Steepening Background Magnetic Field, 1998, ApJ, 494, 90.

Cirtain, J. et al.: Evidence for Alfvén Waves in Solar X-ray Jets, 2007, Science, 318, 1580.

DeForest, C. E. and Gurman, J. B.: Observation of Quasi-periodic Compressive Waves in Solar Polar Plumes, 1998, ApJ, 501, L217.

De Pontieu, B. et al.: A Tale of Two Spicules: The Impact of Spicules on the Magnetic Chromosphere, 2007, PASJ, 59, 655.

De Pontieu, B. et al.: Chromospheric Alfvénic Waves Strong Enough to Power the Solar Wind, 2007, Science, 318, 1574.

De Pontieu, B. et al.: Observing the Roots of Solar Coronal Heating-in the Chromosphere, 2009, ApJ, 701, L1.

De Pontieu, B., et al.: The Origins of Hot Plasma in the Solar Corona, 2011, Science, 331, 55.

de la Cruz Rodríguez, J., et al.: Observation and analysis of chromospheric magnetic fields, 2010, Memorie della Societa Astronomica Italiana, 81, 716.

Del Zanna, L. et al.: An MHD model for solar coronal plumes, 1997, A & A, 318, 963.

DeRosa, M. C. et al.: A Critical Assessment of Nonlinear Force-Free Field Modeling of the Solar Corona for Active Region 10953, 2009, ApJ, 696, 1780.

Doschek, G. A. et al.: Bright Points and Jets in Polar Coronal Holes Observed by the Extreme-Ultraviolet Imaging Spectrometer on Hinode, 2010, ApJ, 710, 1806.

Dupree, A. K. et al.: He i 10830 Angstrom Wing Asymmetry in Polar Coronal Holes: Evidence for Radial Outflows, 1996, ApJ, 467, L121.

Dere, K. P. and Cook, J. W.: The decay of the 1973 August 9 flare, 1979, ApJ, 229, 772.

Dere, K. P. et al.: CHIANTI - an atomic database for emission lines. IX. Ionization rates, recombination rates, ionization equilibria for the elements hydrogen through zinc and updated atomic data, 2009, A&A, 498, 915.

Fossum, A. and Carlsson, M.: High-frequency acoustic waves are not sufficient to heat the solar chromosphere, 2005, Nature, 435, 919.

Fujimura, D. and Tsuneta, S.: Properties of Magnetohydrodynamic Waves in the Solar Photosphere Obtained with Hinode, 2009, ApJ, 702, 1443.

Gabriel, A. H. et al.: Solar Wind Outflow in Polar Plumes from 1.05 to 2.4 Rsolar, 2005, ApJ, 635, 185.

Gabriel, A. H. et al.: The Contribution of Polar Plumes to the Fast Solar Wind, 2003, ApJ, 589, 623.

Georgoulis, M. K. et al.: Statistics, Morphology, and Energetics of Ellerman Bombs, 2002, ApJ, 575, 506.

Giordano, S. et al.: Identification of the Coronal Sources of the Fast Solar Wind, 2000, ApJ, 531, 79.

Goldberg, K. A. et al.: Ultra-high accuracy optical testing: creating diffraction-limited short-wavelength optical systems, 2005, Optics for EUV, X-Ray, and Gamma-Ray Astronomy II. Edited by Citterio, Oberto; O'Dell, Stephen L. Proceedings of the SPIE, 5900, 114.

Green, L. M. and Kliem, B.: Flux Rope Formation Preceding Coronal Mass Ejection Onset, 2009, ApJ, 700, L83.

Hannah, I. G. et al.: An intriguing solar microflare observed with RHESSI, Hinode, and TRACE, 2008, A&A, 481, L45.

Hannah, I. G. et al: RHESSI Microflare Statistics. II. X-Ray Imaging, Spectroscopy, and Energy Distributions, 2008, ApJ, 677, 704.

Hara, H. et al.: Coronal Plasma Motions near Footpoints of Active Region Loops Revealed from Spectroscopic Observations with Hinode EIS, 2008, ApJ, 678, 67.

Harra, L. K. et al.: Coronal Nonthermal Velocity Following Helicity Injection Before an X-Class Flare, 2009, ApJ, 691, L99.

Harra, L. K. et al.: Response of the Solar Atmosphere to the Emergence of `Serpentine' Magnetic Field, 2010, Solar Phys., 263, 105.

Hassler, D. M. et al.: Solar Wind Outflow and the Chromospheric Magnetic Network, 1999, Science, 283, 810.

Hones, E. W., Jr.: Transient phenomena in the magnetotail and their relation to substorms, 1979, Space Science Reviews, 23, 393.

Hori, K. et al.: Pseudo--Two-dimensional Hydrodynamic Modeling of Solar Flare Loops, 1997, ApJ, 489, 426.

Imada, S. et al.: Average profiles of energetic and thermal electrons in the magnetotail reconnection regions, 2005, Geophys. Res. L., 32, L09101.

Imada, S. et al.: Energetic electron acceleration in the downstream reconnection outflow region, 2007, J. Geophys. Res., 112, A03202.

Imada, S. et al.: Ion Temperature and Non-Thermal Velocity in a Solar Active Region: Using Emission Lines of Different Atomic Species, 2009, ApJ, 705, L208.

Imada, S. et al.: Non-Gaussian Line Profiles in a Large Solar Flare Observed on 2006 December 13, 2008, ApJ, 679, 155.

Imada, S. et al.: The dawn-dusk asymmetry of energetic electron in the Earth's magnetotail: Observation and transport models, 2008, J. Geophys. Res., 113, A11201.

Innes, D. E. et al.: Bursts of Explosive Events in the Solar Network, 1997, Solar Phys., 175, 341.

Ishikawa, R. et al.: Relationships between magnetic foot points and G-band bright structures, 2007, A & A, 472, 911.

Ishikawa, R., et al.: Transient horizontal magnetic fields in solar plage regions, 2008, A&A, 481, 25.

Isobe, H. et al.: Convection-driven Emergence of Small-Scale Magnetic Fields and their Role in Coronal Heating and Solar Wind Acceleration, 2008, ApJ, 679, 79.

Jefferies et al.: Magnetoacoustic Portals and the Basal Heating of the Solar Chromosphere, 2006, ApJ, 648, 151.

Ji, H. et al.: Experimental Test of the Sweet-Parker Model of Magnetic Reconnection, 1998, Physical Review Letters, 80, 3256.

Jing, J. et al.: Changes of Magnetic Structure in Three Dimensions Associated with the X3.4 Flare of 2006 December 13, 2008, ApJ, 676, 81.

Kataoka, R. et al.: Three-dimensional MHD modeling of the solar wind structures associated with 13 December 2006 coronal mass ejection, 2009, J. Geophys. Res., 114, A10102.

Katsukawa, Y. et al.: Small-Scale Jetlike Features in Penumbral Chromospheres, 2007, Science, 318, 1594.

Kilpua, E. K. J. et al.: Small Solar Wind Transients and Their Connection to the Large-Scale Coronal Structure, 2009, Solar Phys., 256, 327.

Kitagawa, N. et al.: Mode Identification of MHD Waves in an Active Region Observed with Hinode/EIS, 2010, ApJ, 721, 744.

Klimchuk, J. A.: On Solving the Coronal Heating Problem, 2006, Solar Phys., 234, 41.

Koyama, K. et al.: X-Ray Imaging Spectrometer (XIS) on Board Suzaku, 2007, PASJ, 59, S23.

Krieger, A. S. et al.: A Coronal Hole and Its Identification as the Source of a High Velocity Solar Wind Stream, 1973, Solar Phys., 29, 505.

Krucker, S. et al.: Hard X-ray Microflares down to 3 keV, 2002, Solar Phys., 210, 445.

Kubo, M. et al.: Hinode Observations of a Vector Magnetic Field Change Associated with a Flare on 2006 December 13, 2007, PASJ, 59, 779.

Kubo, M., Low, B. C., and Lites, B. W.: Granular-scale Magnetic Flux Cancellations in the Photosphere, 2010, ApJ, 712, 1321.

Lagg, A. et al.: Retrieval of the full magnetic vector with the He I multiplet at 1083 nm. Maps of an emerging flux region, 2004, A&A, 414, 1109.

Leenaarts, J. et al.: Non-equilibrium hydrogen ionization in 2D simulations of the solar atmosphere, 2007, A&A, 473, 625.

Leenaarts, J. et al.: Three-Dimensional Non-LTE Radiative Transfer Computation of the CA 8542 Infrared Line From a Radiation-MHD Simulation, 2009, ApJ, 694, L128.

Leka, K. D. and Barnes, G.: Photospheric Magnetic Field Properties of Flaring versus Flare-quiet Active Regions. IV. A Statistically Significant Sample, 2007, ApJ, 656, 1173.

Li, H. et al.: Response of Solar Atmosphere to Magnetic Flux Emergence from Hinode Observation, 2007, PASJ, 59, 643.

Lites, B. et al.: Hinode Observations of Horizontal Quiet Sun Magnetic Flux and the ``Hidden Turbulent Magnetic Flux", 2007, PASJ, 59, 571.

Lites, B., et al.: The Horizontal Magnetic Flux of the Quiet-Sun Internetwork as Observed with the Hinode Spectro-Polarimeter, 2008, ApJ, 672, 1237.

Lites, B., et al.: Emergence of Helical Flux and the Formation of an Active Region Filament Channel, 2010, ApJ, 718, 474.

Llopart, X., Ballabriga, R., Campbell, M., Tlustos, L., and Wong, W.: 2007, NIM-A, 581, 485.

Magara, T. and Tsuneta, S.: Hinode's Observational Result on the Saturation of Magnetic Helicity Injected into the Solar Atmosphere and Its Relation to the Occurrence of a Solar Flare, 2008, PASJ, 60, 1181.

Manso Sainz, R. and Trujillo Bueno, J.: Scattering Polarization of the Ca II IR Triplet for Probing the Quiet Solar Chromosphere, 2010, ApJ, 722, 1416.

Masuda, S. et al.: A loop-top hard X-ray source in a compact solar flare as evidence for magnetic reconnection, 1994, Nature, 371, 495.

Matsumoto, T. and Shibata, K.: Nonlinear Propagation of Alfvén Waves Driven by Observed Photospheric Motions: Application to the Coronal Heating and Spicule Formation, 2010, ApJ, 710, 1857.

Matsumoto, T. et al.: Cooperative Observation of Ellerman Bombs between the Solar Optical Telescope aboard Hinode and Hida/Domeless Solar Telescope, 2008, PASJ, 60, 577.

Matsuzaki, K. et al.: Hot and Cool Loops Composing the Corona of the Quiet Sun, 2007, PASJ, 59, 683.

McIntosh, S. W. and De Pontieu, B: High-Speed Transition Region and Coronal Upflows in the Quiet Sun, 2009, ApJ, 707, 524.

McKenzie, D. E. and Canfield, R. C.: Hinode XRT observations of a long-lasting coronal sigmoid, 2008, A & A, 481, 65.

Merenda, L. et al.: A Magnetic Map of a Solar Filament, 2007, The Physics of Chromospheric Plasmas ASP Conference Series, 368, Proceedings of the conference held 9-13 October, 2006 at the University of Coimbra in Coimbra, Portugal. Edited by P. Heinzel, I. Dorotovič, and R. J. Rutten. San Francisco: Astronomical Society of the Pacific, 2007, 347.

Minoshima et al.: Multiwavelength Observation of Electron Acceleration in the 2006 December 13 Flare, 2009, ApJ, 697, 843.

Nagai, T. et al.: Geotail observations of the Hall current system: Evidence of magnetic reconnection in the magnetotail, 2001, J. Geophys. Res., 106, 25929.

Nagai, T. et al.: Structure and dynamics of magnetic reconnection for substorm onsets with Geotail observations, 1998, J. Geophys. Res., 103, 4419.

Nagata, S. et al.: Formation of Solar Magnetic Flux Tubes with Kilogauss Field Strength Induced by Convective Instability, 2008, ApJ, 677, 145.

Nakariakov, V. M. et al.: TRACE observation of damped coronal loop oscillations: Implications for coronal heating, 1999, Science, 285, 862.

Nishizuka, N. et al.: Giant Chromospheric Anemone Jet Observed with Hinode and Comparison with Magnetohydrodynamic Simulations: Evidence of Propagating Alfvén Waves and Magnetic Reconnection, 2008, ApJ, 683, 83.

Ofman, L. et al.: Ultraviolet Coronagraph Spectrometer Observations of Density Fluctuations in the Solar Wind, 1997, ApJL, 491, 111.

Ofman, L. et al.: UVCS WLC Observations of Compressional Waves in the South Polar Coronal Hole, 2000, ApJ, 529, 592.

Oieroset, M. et al.: Evidence for Electron Acceleration up to ~300 keV in the Magnetic Reconnection Diffusion Region of Earth's Magnetotail, 2002, Physical Review Letters, 89, 195001.

Okamoto, T. J. et al.: Coronal Transverse Magnetohydrodynamic Waves in a Solar Prominence, 2007, Science, 318, 1577.

Okamoto , T. J. et al.: Prominence Formation Associated with an Emerging Helical Flux Rope, 2009, ApJ, 697, 913.

Ono, Y. et al.: Experimental Investigation of Three-Component Magnetic Reconnection by Use of Merging Spheromaks and Tokamaks, 1997, Physics of Plasmas, 4, 1953.

Orozco Suárez, D. et al.: Quiet-Sun Internetwork Magnetic Fields from the Inversion of Hinode Measurements, 2007, ApJ, 670, 610.

Parker, E. N. et al.: Solar and Stellar Magnetic Fields and Atmospheric Structures - Theory, 1989, Solar Phys., 12, 271.

Raouafi, N. E. et al.: Evidence for Polar Jets as Precursors of Polar Plume Formation, 2008, ApJ, 682, 137.

Raouafi, N. E. et al.: Properties of Solar Polar Coronal Plumes Constrained by Ultraviolet Coronagraph Spectrometer Data 2007, ApJ, 658, 643.

Reeves, K. K. and Warren H. P.: Modeling the Cooling of Postflare Loops, 2002, ApJ, 578, 590.

Reeves, K. K. et al: Theoretical Predictions of X-Ray and Extreme-UV Flare Emissions Using a Loss-of-Equilibrium Model of Solar Eruptions, 2007, ApJ, 668, 1210.

Roberts, B.: Waves and Oscillations in the Corona, 2000, Solar Phys., 193, 139.

Ruiz Cobo, B. and del Toro Iniesta, J. C.: Inversion of Stokes profiles, 1992, ApJ, 398, 375.

Rust, D. M. and Kumar, A: Evidence for Helically Kinked Magnetic Flux Ropes in Solar Eruptions, 1996, ApJ, 464, L199.

Rutten, R. J.: Observing the Solar Chromosphere, 2007, ASP Conference Series, 368, 27.

Sanchez-Almeida, J. et al.: Search for photospheric footpoints of quiet Sun transition region loops, 2007, A & A, 475, 1101.

Savcheva, A. and van Ballegooijen, A.: Nonlinear Force-free Modeling of a Long-lasting Coronal

Sigmoid, 2009, ApJ, 703, 1766.

Schmieder, B. et al.: Emerging Flux and the Heating of Coronal Loops, 2004, ApJ, 601, 530.

Seely, J. F. et al.: Observation of nonthermal energy distributions during the impulsive phase of solar flares, 1987, ApJ, 319, 541.

Shibata, K. et al.: Chromospheric Anemone Jets as Evidence of Ubiquitous Reconnection, 2007, Science, 318, 1591.

Shimizu, T. et al.: Image Stabilization System for Hinode (Solar-B) Solar Optical Telescope, 2008, Solar Phys., 249, 221.

Shimizu, T. et al.: Frequent Occurrence of High-Speed Local Mass Downflows on the Solar Surface, 2008, ApJ, 680, 1467.

Shimizu, T. et al.: Hinode Observation of the Magnetic Fields in a Sunspot Light Bridge Accompanied by Long-Lasting Chromospheric Plasma Ejections, 2009, ApJ, 696, L66.

Shimojo, M. and Tsuneta, S.: The Relation Between Magnetic Fields and Coronal Activities in the Polar Coronal Hole, 2009, ApJ, 706, L145.

Singh, K. A. P. and Krishan, V.: Alfvén-like mode in partially ionized solar atmosphere, 2010, New Astronomy, 15, 119.

Skumanich, A. and Lites, B. W.: Stokes profile analysis and vector magnetic fields. I - Inversion of photospheric lines, 1987, ApJ, 322, 473.

Socas-Navarro, H. et al.: Non-LTE Inversion of Line Profiles, 1998, ApJ, 507, 470.

Socas-Navarro, H. and Manso Sainz, R.: Shocks in the Quiet Solar Photosphere: A Rather Common Occurrence, 2005, ApJ, 620, 71.

Socas-Navarro, H.: Strategies for Spectral Profile Inversion Using Artificial Neural Networks, 2005, ApJ, 621, 545.

Stein, R. F. et al.: Supergranule scale convection simulations, 2006, ApJ, 642, 1246.

Strüder, L. et al. 2003: in "X-ray Evolving-Universe Spectroscopy - The XEUS Instruments", ESA SP-1273, Chapter 3.

Strüder, L. et al.: XEUS wide-field imager: first experimental results with the x-ray active pixel sensor DEPFET, 2004, Proc. SPIE, 5165, 10.

Suematsu, Y.: Influence of Photospheric 5-Minute Oscillations on the Formation of Chromospheric Fine Structures, 1990, Progress of Seismology of the Sun and Stars, Proceedings of the Oji International Seminar Held at Hakone, Japan, 11-14 December 1989. Lecture Notes in Physics, 367, edited by Y. Osaki and H. Shibahashi. Springer-Verlag, Berlin Heidelberg New York, p.211

Suematsu, Y. et al.: The Solar Optical Telescope of Solar-B (Hinode): The Optical Telescope Assembly, 2008, Solar Phys., 249, 197.

Suzuki, T. K. and Inutsuka, S.: Making the Corona and the Fast Solar Wind: A Self-consistent Simulation for the Low-Frequency Alfvén Waves from the Photosphere to 0.3 AU, 2005, ApJ, 632, 49.

Teriaca, L. et al.: The Nascent Solar Wind: Origin and Acceleration, 2003, ApJ, 588, 566.

Titov, V. S. and Demoulin, P.: Basic topology of twisted magnetic configurations in solar flares,

1999, A & A, 351, 707.

Tomczyk, S. et al.: Alfvén Waves in the Solar Corona, 2007, Science, 317, 1192.

Treis, J., Fischer, P., Hälker, O., Harter, M., Herrmann, S., Kohrs, R., Krüger, H., Lechner, P., Lutz, G., Peric, I., Porro, M., Richter, R. H., Strüder, L., Trimpl, M., and Wermes, N. 2005 : IEEE Trans. Nucl. Sci. 52, 1083.

Trujillo Bueno, J. et al.: Selective absorption processes as the origin of puzzling spectral line polarization from the Sun, 2002, Nature, 415, 403.

Tsiropoula, G. and Schmieder, B.: Determination of physical parameters in dark mottles, 1997, A&A, 324, 1183.

Tsuneta, S. et al.: Hot and Superhot Plasmas above an Impulsive Flare Loop, 1997, ApJ, 478, 787.

Tsuneta and Naito: Fermi Acceleration at the Fast Shock in a Solar Flare and the Impulsive Loop-Top Hard X-Ray Source, 1998, ApJ, 495, 67.

Tsuneta, S. et al.: The Magnetic Landscape of the Sun's Polar Region, 2008, ApJ, 688, 1374.

Tsuneta, S. et al.: The Solar Optical Telescope for the Hinode Mission: An Overview, 2008, Solar Phys., 249, 167.

Tu, C.-Y. et al.: Solar Wind Origin in Coronal Funnels, 2005, Science, 308, 519-523.

Tziotziou, K.: Chromospheric Cloud-Model Inversion Techniques, 2007, ASP Conference Series, 368, 217.

Uitenbroek, H.: Operator perturbation method for multi-level line transfer with partial redistribution, 1989, A&A, 213, 360.

Uitenbroek, H.: Chromospheric Diagnostics, 2006, ASP Conference Series, 354, 313.

Vecchio, A. et al.: Solar atmospheric oscillations and the chromospheric magnetic topology, 2007, A & A, 461, 1.

Vernazza, J. E. and Reeves, E. M.: Extreme ultraviolet composite spectra of representative solar features, 1978, ApJ Suppl., 37, 485.

Warren, H. P. and Doschek, G. A.: Reconciling Hydrodynamic Simulations with Spectroscopic Observations of Solar Flares, 2005, ApJ, 618, 157.

Warren, H. P. et al.: Observations of Active Region Loops with the EUV Imaging Spectrometer on Hinode, 2008, ApJ, 686, 131.

Watanabe, K. et al.: G-band and Hard X-ray Emissions of the 2006 December 14 Flare Observed by Hinode/SOT and Rhessi, 2010, ApJ, 715, 651.

Watanabe, T. et al.: Temperature and Density Structures of Solar Corona - A Test of Iron Line Diagnostic Capability of EIS Instrument on board Hinode, 2007, PASJ, 59, 669.

Wiegelmann, T. et al.: Can We Improve the Preprocessing of Photospheric Vector Magnetograms by the Inclusion of Chromospheric Observations?, 2008, Solar Phys., 247, 249.

Wilhelm, K. et al.: On the source regions of the fast solar wind in polar coronal holes, 2000, A & A, 353, 749.

Wilhelm, K.: Solar coronal-hole plasma densities and temperatures, 2006, A & A, 455, 697.

Yamada, M. et al.: dentification of Y-Shaped and O-Shaped Diffusion Regions During Magnetic Reconnection in a Laboratory Plasma, 1997, Physical Review Letters, 78, 3117.

Zweibel, E. G.: Ambipolar diffusion drifts and dynamos in turbulent gases, 1988, ApJ, 329, 384.

Zweibel, E. G.: Magnetic reconnection in partially ionized gases, 1989, ApJ, 340, 550.

Acronyms

16-QAM	16 Quadrature Amplitude Modulation
2FS	Secondary Field Stop
3D	Three dimensional
A/D	Analog to Digital
AIA	Atmospheric Imaging Assembly, SDO
ANN	artificial neural network
AOCS	Attitude and Orbit Control System
APS	Active Pixel Sensor
AR	Active region
ASNARO	Advanced Satellite with New System Architecture for Observation
BF	Broadband filtergraph
BOL	Beginning of life
BS	Beam splitter
CCD	Charge Coupled Device
CDS	Coronal Diagnostic Spectrometer, SOHO
CFRP	Carbon Fiber Reinforced Plastics
CH	Coronal hole
CHIANTI	An Atomic Database for Spectroscopic Diagnostics of Astrophysical Plasmas
CME	Coronal Mass Ejection
CMOS	Complementary Metal Oxide Semiconductor
CMU	Collimator Mirror Unit
CRD	complete angle and frequency redistribution
CT	Correlation Tracker
CTE	Coefficient of thermal expansion
DEM	Differential Emission Measure
EIS	Extreme ultraviolet Imaging Spectrometer, Hinode
EIT	EUV Imaging Telescope, SoHO
EOL	End of life
EQ	Equilibrium

ESA	European Space Agency
EUNIS	Extreme Ultraviolet Normal Incidence Spectrograph
EUV	Extreme Ultraviolet
EUVS	EUV/FUV high-throughput spectrometer
FOV	Field of View
FPGA	Field-Programmable Gate Array
FUV	Far Ultraviolet
FWHM	Full width half maximum
GEO, GSO	Geo-Synchronous Orbit
GOES	Geostationary Operational Environment Satellite
GTO	Geo-Transfer Orbit
HAZEL	Hanle and Zeeman Light (Inversion code)
HDM	Heat Dump Mirror
HPD	Half power diameter
IR	Infrared
IRU	Inertial Reference Unit
IRIS	Interface Region Imaging Spectrograph
ISS	Image stabilization system
ITU	International Telecommunication Union
JAXA	Japan Aerospace Exploration Agency
kG	kilo Gauss
LDE	Long-duration flare event
LVCR	Liquid crystal variable retarder
M1	Primary mirror
M2	Secondary mirror
MET	Microfield Exposure Tool
MHD	Magneto-Hydro-Dynamics
MIB	Momentum wheel Isolation Bench
MK	Million Kelvin
MW	Momentum Wheel
NASA	National Aeronautics and Space Administration

NEN	Near Earth Network
NF	Narrowband filtergraph
NGXT	Next generation X-ray telescope
NI	Normal incident
NIR	Near infrared
NLFFF	non-linear force free field
OBU	Optical Bench Unit
OTA	Optical Telescope Assembly
PC	Photon counting
PCA	Principal component analysis
PCU	Polarization Calibration Unit
QE	Quantum efficiency
QPSK	Quadrature Phase Shift Keying
QS	Quiet Sun
RAISE	Rapid Acquisition Imaging Spectrograph Experiment
RHESSI	Reuven Ramaty High Energy Solar Spectroscopic Imager
RMS	Root mean square
SDO	Solar Dynamics Observatory
SFCG	Space Frequency Coordination Group
SIR	Stokes inversion based on response function
SMEX	Small Explorer
S/N	Signal-to-Noise
SOHO	Solar and Heliospheric Observatory
SOT	Solar Optical Telescope, Hinode
SP	Spectro-Polarimeter
SSO	Sun-synchronous polar orbit
SSPA	Solid State Power Amplifier
STEREO	Solar TErrestrial RElations Observatory
SUMER	Solar Ultraviolet Measurements of Emitted Radiation, SOHO
SUVIT	Solar UV-Visible-IR Telescope
SXT	Yohkoh Soft X-ray Telescope

TBD	To be determined
TF	Tunable filter
TRACE	The Transition Region and Coronal Explorer
LTE	Local thermodynamic equilibrium
TM	Tip-tilt mirror
TR	Transition Region
TRACE	Transition Region and Coronal Explorer
TWTA	Travelling Wave Tube Amplifier
UFSS	Ultra Fine Sun Sensor
USC	Uchinoura Space Center
UV	Ultraviolet
UVCS	Ultraviolet Coronagraph Spectrometer, SOHO
VERIS	VEry high angular Resolution Imaging Spectrometer
WFS	Wavefront sensor
WP	Wave plate
XIT	X-ray Imaging Telescope
XRT	X-ray Telescope, Hinode